DNA-based Artificial Systems for Mimicking Membrane-Related Mechanisms and Targeted Delivery

Samet Kocabey

München 2016

DNA-based Artificial Systems for Mimicking Membrane-Related Mechanisms and Targeted Delivery

Samet Kocabey

Dissertation

durchgeführt an der Fakultät für Physik

der Ludwig-Maximilians-Universität

München

vorgelegt von

Samet Kocabey

aus Eskisehir, Türkei

München, den 31.10.2016

Erstgutachter: Prof. Dr. Tim Liedl

Zweitgutachter: Dr. Markus Rehberg

Tag der Mündlichen Prüfung: 16 December 2016

Contents

List of Figures

Zusammenfassung

Im Laufe der letzten zehn Jahre hat sich DNA durch die Selbstorganisation komplementärer Sequenz als sehr vielseitiges Baumaterial auf der Nanometer Skala bewährt. Die Struktur der DNA erlaubt die Konstruktion von beliebig geformten, nanometergroßen Objekten und die Modifizierung mit einer Vielzahl an (Bio-)Molekülen mit Nanometer Genauigkeit, definierter Orientierung und kontrollierbarer Stöchiometrie. In dieser Dissertation wurden DNA-basierte Nanostrukturen für die Nachahmung membranbedingter biologischer Ereignisse und zielgerichteter Transportapplikationen vorgestellt.

Im ersten Teil der Arbeit wurden das Potenzial zur gezielten Verabreichung und die Stabilität der entworfenen DNA-Nanostrukturen in zellulärer Umgebung untersucht. Zu diesem Zweck wurden DNA-Nanoröhren durch ein einzelsträngiges DNA-Kachel-Anordnungs hergestellt und mit Folat-Molekülen und siRNA funktionalisiert um spezifisch Gene in Krebszellen, die den Folatrezeptor überexprimieren abzuschalten. In dieser Studie beobachteten wir, dass DNA-Nanoröhrchen zum Endosom geleitet wurden, aber nicht zum Cytosol der Krebszellen. Übereinstimmend mit dieser Beobachtung, konnte kein Abschalten der Zielgene detektiert werden. Darüber hinaus stießen wir auf einige Herausforderungen hinsichtlich der Stabilität der Strukturen, die bei der Anwendung *in vivo* berücksichtigt werden müssen.

Im zweiten Teil wurde die hierarchische Anordnung von membrangebundenen DNA-Origami-Strukturen untersucht. Dazu wurden dreischichtige DNA-Origami-Blockstrukturen über Cholesterin-Moleküle an die Lipiddoppelschichten gebunden, die frei auf den Membranen diffundierten. Eindimensionale Polymere und zweidimensionale Gitter wurden durch programmierten Selbstorganisation der Strukturen auf den Membranen unter Verwendung verschiedener Sätze von Verbindungsoligonukleotiden gebildet. Weiterhin wurden DNA-Origami-Triskelione zu sechseckigen Gittern zusammengebaut, die der Bildung von Clathrin- Vesikeln während der Endozytose glichen. Darüber hinaus führt die Gitterbildung zu einer Verformung der Lipidmembranen, die auf das Potential des Systems für eine kontrollierbare Formgebung der Membranen aufzeigt. Die Studie zeigte, dass selbstorganisierte DNA-Origami-Strukturen die hierarchische Assemblierung von Multiproteinkomplexen auf zytoplasmatischen Membranen nachahmen könnte.

Im letzten Teil wurde die Verwendung von DNA-Nanoröhrchen untersucht, eine Immunreaktion *in vivo* zu induzieren oder zu unterdrücken. In der ersten Studie wurden DNA-Nanoröhren mit unmethylierten Cytosin-Phosphat-Guanin-Oligodesoxynukleotiden (CpG-ODNs) funktionalisiert und in den Skelettmuskel anästhesierter Mäuse injiziert, um eine Immunstimulation gezielt herbeizuführen. Wir beobachteten, dass DNA-Nanoröhren durch gewebsständige Makrophagen internalisiert wurden und in den Endosomen akkumulierten. Nur Mikroinjektion von CpG-funktionalisierten DNA-Nanoröhren, aber nicht undekorierte Nanoröhren oder CpG-ODNs induzierte eine signifikante Rekrutierung von Leukozyten zur Injektionsstelle sowie eine Aktivierung des NF-κB-Signalweges. In der zweiten Studie wurden DNA-Nanoröhren mit dem anti-inflammatorischem Wirkstoff Dexamethason über i-Motivsequenz funktionalisiert. Wir haben gezeigt, dass die Strukturen die Leukozyten-Rekrutierung in das entzündete Gewebe aufgrund der i-Motiv-abhängigen Freisetzung von Dexamethason hemmen.

Abstract

Over the last decade, DNA has proven to be an extremely versatile building material through the self-assembly of complementary oligonucleotides. The structure of DNA allows the construction of arbitrarily shaped objects in nanoscale which can be modified with a variety of (bio)molecules with nanometer precision, defined orientation and fully controlled stoichiometry. In this dissertation, DNA-based nanostructures were demonstrated for mimicking membrane-related biological events and targeted delivery applications.

In the first part of the thesis, targeted delivery and the stability of the designed DNA nanostructures in the cellular environment were investigated. For this purpose, DNA nanotubes were produced via the single-stranded tile assembly method and functionalized with folate molecules and siRNA to specifically silence genes in folate receptor over-expressing cancer cells. In this study, we observed that DNA nanotubes reached to the endosome but not to the cytosol of the cancer cells. Consistent with this observation, no silencing of the targeted gene could be detected. Furthermore, we encountered several challenges concerning the stability of the structures that have to be taken into account during *in vivo* delivery applications.

In the second part, the hierarchical assembly of membrane-bound DNA origami structures was investigated. For this, three-layer DNA origami block structures were attached to the lipid bilayers via cholesterol molecules and diffused freely on the membranes. One-dimensional polymers and two-dimensional lattices were formed upon the programmed self-assembly of the structures on the membranes using different sets of connector oligonucleotides. DNA origami triskelions further assembled into hexagonal lattices that resembled the formation of clathrin-coated pits during endocytosis. Moreover, the lattice formation leads to deformation of the lipid membranes that indicates the potential of the system towards controllable sculpting of the membranes. The study demonstrated that self-assembled DNA origami structures could mimic the hierarchical assembly of multi-protein complexes on cytoplasmic membranes.

In the last part, we investigated the use of DNA nanotubes to induce or suppress the immune reactions *in vivo*. In the first study, DNA nanotubes were functionalized with unmethylated cytosine-phsophate-guanine oligodeoxynucleotides (CpG ODNs) and microinjected into the skeletal muscle of anesthetized mice to induce immune stimulation. We observed that DNA nanotubes were internalized by tissue-resident macrophages and accumulated in their endosomes. Only microinjection of CpG functionalized DNA nanotubes but not of plain nanotubes or unfolded CpG ODNs induced the significant recruitment of leukocytes to the injection site as well as the activation of the NF-κB pathway. In the second study, DNA nanotubes were functionalized with the anti-inflammatory drug dexamethasone via an i-motif sequence. We demonstrated that these structures inhibited the leukocyte recruitment into the inflammed tissue due to the i-motif dependent release of dexamethasone.

1. Introduction to DNA Nanotechnology

1.1 DNA Structure and Properties

Deoxyribonucleic acid (DNA) is the molecule that carries the genetic information of all living organisms and many viruses. DNA was first isolated by Friedrich Miescher in 1869 and its molecular structure was discovered by James Watson and Francis Crick in 1953 where the model building is based on the X-ray data acquired by Rosalind Franklin and Maurice Wilkins [1-4]. The discovery is awarded with the Nobel Prize in Physiology or Medicine in 1962. DNA structure is a long polymer made from repeating units of nucleotides. Two complementary chains hybridize to form right-handed DNA double helical structure where the distance between following nucleotides is 0.34 nm and a helical pitch of 10.5 nucleotides [5]. (Figure 1.1A) The diameter of a double helix is 2 nm. DNA exists in several conformations including right-handed B-DNA, A-DNA and left-handed Z-DNA depend on the conditions such as base sequence, type and concentration of metal ions and direction of supercoiling [6]. B-DNA is the most common one found under cell conditions. A DNA nucleotide is composed of one of four bases including Adenine (A), Thymine (T), Guanine (G) and Cytosine (C) which are connected to a sugar group, 2-deoxyribose, and a phosphate group. The sugars are joined together by phosphate groups that form phosphodiester bonds between the third and fifth carbon atoms of adjacent sugar rings. These asymmetric bonds lead to a chemical polarity and give a direction to each polynucleotide strand with a terminal phosphate group at the 5' end and a terminal hydroxyl group at the 3' end of the DNA strand. DNA strands form the double helix structure through the hydrogen bonds between nucleotide pairs known as Watson-Crick base pair which are adenine-thymine and guanine-cytosine [7-9]. (Figure 1.1B) Hydrogen bonds between base pairs and stacking interaction between aromatic nucleobases drive the formation of double helix structure. The asymmetric arrangement of DNA strands leads the formation of two grooves with different sizes as a result of the non-diametrical glycosilic bonds of the base pairs: a major groove with a width of 2.2 nm and a minor groove with a width of 1.2 nm.

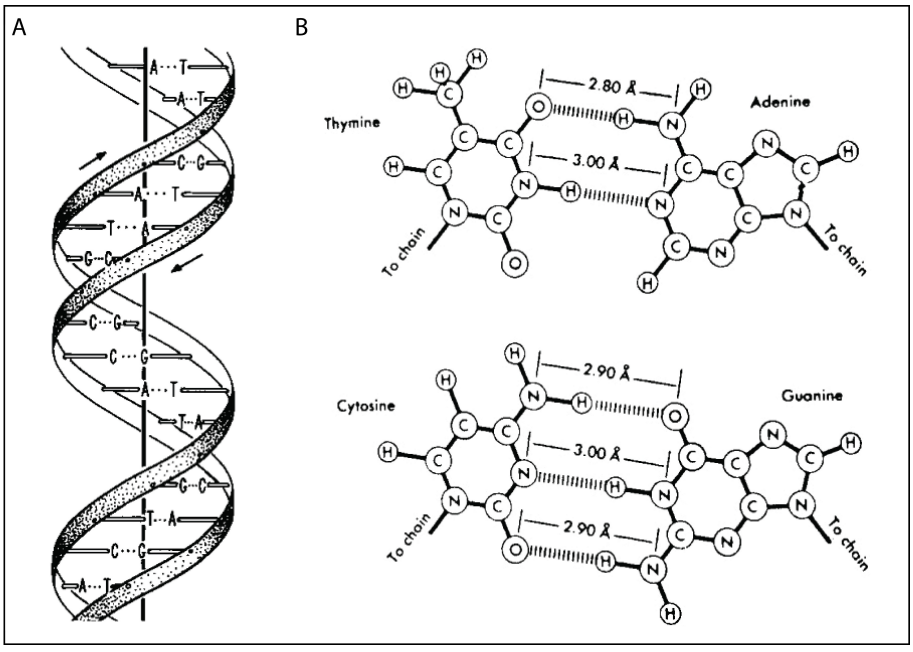

Figure 1.1: DNA double helix structure. A) Schematic illustration of DNA double helix. Reprinted with permission from [7, 9]. Copyright 2004 Elsevier. B) Watson-Crick base pairs showing the two hydrogen bonds between Adenine and Thymine, and three hydrogen bonds between Guanine and Cytosine. Reprinted with the permission from ref. [8, 9]. Copyright 2004 Elsevier.

The four nucleobases are classified into two types according to the number of aromatic rings: purines are A and G, which are formed by the fusion of five- and six-membered heterocyclic rings and pyrimidines are, C and T, which only have six-membered rings. The Watson-Crick base pairs have different number of hydrogen bonds between purines and pyrimidines, in which adenine binds to thymine with two hydrogen bonds, and cytosine binds to guanine with three hydrogen bonds. This makes a DNA with high GC content more stable than a DNA with low GC content [10]. Since the base pairing is based on hydrogen bonding (5-30 kJ/mole binding energy) that is relatively weak compared to covalent bonding (100 kJ/mole binding energy), the strands could be separated and rejoined by high temperature and mechanical forces. The stability of DNA is depend on the GC content, sequence (base stacking) and length which is measured by the melting temperature; the temperature at which 50% of the double stranded DNA molecules are converted to single stranded DNA molecules [11]. The melting temperature is dependent on ionic strength and the concentration of DNA. In addition to Watson-Crick base pairs, DNA sequences that are rich in guanine or cytosine also form alternative tertiary structures such as G-quadruplex or i-motif via different hydrogen bonding mechanisms where the tertiary structures are stabilized by the presence of cations.

1.2 DNA Nanotechnology

DNA Nanotechnology was first introduced by Ned Seeman´s groundbreaking vision of self-assembled six-arm branched junctions into a three dimensional lattices with the purpose of accurately positioning proteins for crystallography studies during early eighties [12, 13]. (Figure 1.2A) The field is based on using nucleic acids as non-biological engineering materials rather than as genetic information carriers. In 1991, Seeman experimentally constructed the first DNA object which is topologically equivalent to a cube [13, 14]. (Figure 1.2B) Since then the field rapidly evolved into an interdisciplinary field crossing with physics, chemistry, biology, materials science and computer science. Starting with the Seeman´s cube distinct DNA nanostructures have been developed such as polyhedra, nanotubes, 1D and 2D periodic lattices and 3D complex arbitrary shapes as well as molecular machines and DNA computers.

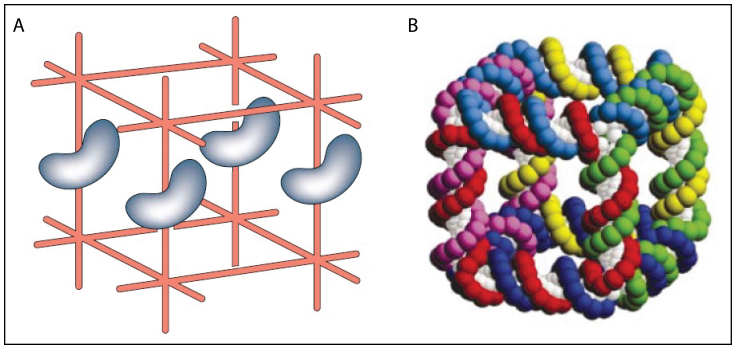

Figure 1.2: Origin of DNA nanotechnology. A) Scaffolding biological macromolecules using DNA crystals. Macromolecules are oriented parallel to each other for the structure determination by X-ray crystallography. B) Self-assembled DNA cube using six single stranded DNA strands first introduced by Seeman in 1991. Reprinted by permission from Macmillan Publishers Ltd: Nature ref. [13], copyright 2003.

1.2.1 DNA as Building Material

DNA is a unique building block for nanotechnology applications for many reasons. First of all, DNA has a nanometer scale structural geometry, a 2 nm diameter and 3.4 nm of helical pitch as previously mentioned. Second, DNA has programmable and predictable intra- and intermolecular interactions, adenine and thymine (A-T) and guanine and cytosine (G-C) base pairs which hybridization energies could be estimated. Single stranded overhangs and sticky ends are programmable to connect double helical domains. Third, DNA has combined stiffness and flexibility. The persistence length of a double-stranded DNA is 53 nm which is stiff enough to build constructs in the nanometer range [15]. Moreover, the flexible angles at a bend in any branched structure tolerate the small strains and allow folding of arbitrary designs. Lastly, DNA can be synthesized using phosphoramidite chemistry and modified by enzymes that allow labeling, ligation or cleavage.

In order to create stable DNA constructs in multiple dimensions, programmed branched DNA molecules must self-assemble into lattices and compact structures. The Holliday junction allows the formation of such lattices and structures via hybridization. Named after the molecular biologist Robin Holliday, in 1964, the Holliday junction is a branched DNA molecule contains four double-stranded arms joined together [16]. The Holliday Junction occurs in the process of genetic recombination as well as double-strand break repair mechanisms. During this process, since the junctions have homologous sequences the branch point slides over the branched DNA molecule in which the process called as “branch migration” [17]. Synthetic DNA nanotechnology takes the advantage of using asymmetric sequences to avoid branch migration and immobile Holliday junctions allow the formation of specific designed geometries with high degree of structural rigidity. Moreover, the oligonucleotide synthesis allows the formation of multi-armed junctions such as three, five or six armed junctions [18, 19].

1.2.2 DNA Tile-Based Assembly

DNA tile assembly is based on the idea of combining sticky-end cohesion and branched DNA junctions to build geometric objects and periodic 2D or 3D lattices which could be seen for the first time in Seeman´s cube design. The same group later developed double crossover (DX) molecule by joining two double helices through strand exchange which is two times stiffer than linear double stranded DNA [20-22]. Then, triple crossover (TX) molecules were developed where single DNA strand connects three parallel helices in one plane [23]. These molecules self-assembled into periodic 2D lattices using proper sticky ends [24-26]. Like these molecules, four-helix, eight-helix and twelve-helix tiles were later shown that can self-assemble into 2D arrays and nanotubes [27, 28]. Moreover, Mao group developed the concept of sequence symmetry by utilizing several tile designs such as cross-

shape, triangular or three-point star motifs which were shown to self-assemble into large 2D assemblies with hexagonal or triangular cavities [29]. The sequence symmetry minimized the number of unique single DNA strands and avoids any unpredictable distortion which allows the formation of larger periodic 2D arrays up to millimeter range. Apart from the periodic lattices, aperiodic lattices were also developed via the directed nucleation DNA DX tiles along around a long scaffold [30]. A modification of DX tile, DX-J tile motif, which carries an extra domain perpendicular to the plane, was used together with DX tile to visualize the formation of barcoded tiles into 2D arrays by atomic force microscopy.

In the following years, tiles with different sequences of sticky ends were used in order to create different geometric shapes such as octahedron, tetrahedron, polyhedra, icosahedron and addressable finite-sized arrays [31-35]. In 2008, DNA nanotubes and ribbons with programmable circumferences were developed via single stranded tile (SST)-based assembly [36]. Monodisperse DNA nanotubes with various circumferences (4,5,6,7,8,10 and 20 helices) were self-assembled using this technique. The design is based on 42-base long single stranded DNA motif which has 10 and 11 base domains complementary to neighboring tiles. (Figure 1.3A and Figure 1.4A) This technique was used in associated publications P1 and P3. In order to form more complex structures the SST approach was extended by using 362 distinct tiles [37]. Complex 2D shapes and tubes were assembled from a self-assembled rectangle that serves as a molecular canvas in which the exclusion of corresponding tiles from the canvas allows the formation any desired shape. (Figure 1.3B) Using the similar SST approach, based on 32-base long single stranded DNA motifs with 8 base-long domains, complex three-dimensional shapes were self-assembled from hundreds of distinctive DNA sequences [38]. Moreover, by introducing uniform curvature into the repeating units of single stranded tiles DNA nanorings were self-assembled from 4 and 6 helix DNA bundle units [39].

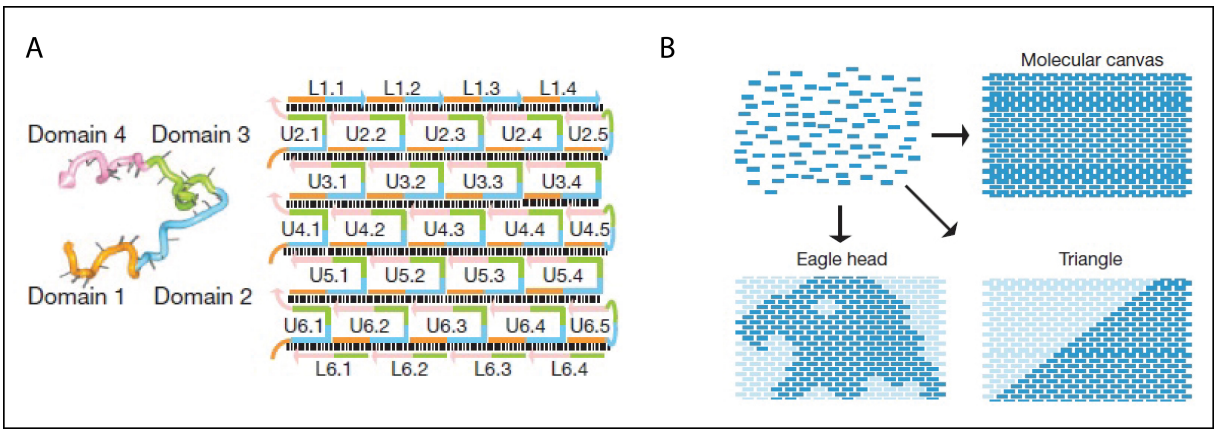

Figure 1.3: Self-assembly of molecular shapes using single-stranded tiles. A) Single-stranded tile motif and design of an SST structure using 42-base long standard tiles (labelled U) and 21-base long half tiles (labelled L). B) Design of arbitrary two-dimensional shapes from molecular canvas. Reprinted by permission from Macmillan Publishers Ltd: Nature ref. [37], copyright 2012.

1.2.3 DNA Origami

In 2006, Paul Rothemund revolutionized the field of DNA Nanotechnology with the breakthrough technique called DNA origami [40]. Named after Japanese art of paper folding, the technique is based on the folding of the long single stranded DNA (derived from the genomic DNA of M13mp18) using over 200 complementary short oligonucleotide staple strands. (Figure 1.4B) Using this technique, Rothemund showed that self assembly of single stranded DNA with short single stranded oligonucleotides in a single pot thermal annealing reaction resulted in arbitrary shaped 2D DNA origami structures with 100 nm diameter and 6 nm spatial resolution such as squares, stars, triangles and smiley faces. (Figure 1.5A) He also further showed the structures can be programmed to form complex images and words on the structures using hairpins at determined positions and form larger assemblies like periodic lattices or a hexamer of triangles using connector sticky ends. The advantage of this technique in compare to previously shown DNA tile based assembly technique is avoiding the stoichiometry and purification related problems that commonly occurred in the methods required many short DNA strands.

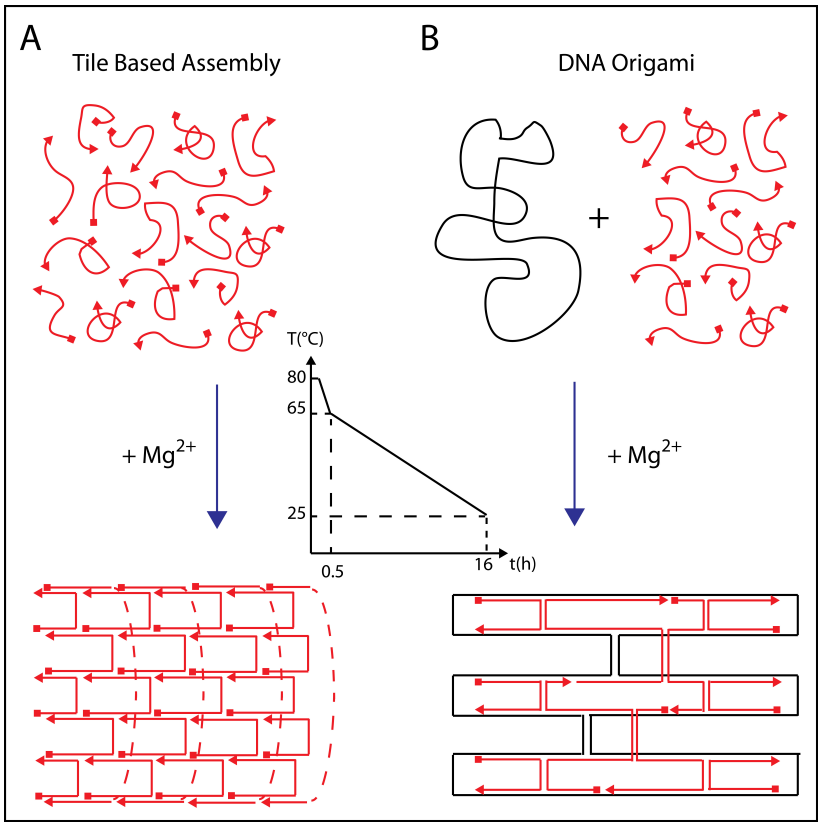

Figure 1.4: DNA self-assembly techniques. A) Programmed single-stranded tiles self-assemble into 6-helix DNA nanotubes during thermal annealing in the presence of Mg^{2+}. B) In DNA origami method, staple strands fold the single-stranded scaffold DNA into a predesigned shape.

3 years after the successful demonstration of two dimensional DNA origami assemblies, Shih group developed three-dimensional DNA origami objects using honeycomb lattice arrangement of DNA double helices [41]. (Figure 1.5B) In this technique each inner

helix are connected to three neighbor helices by the staple cross-overs at distances of multiples of every 7 base pairs which leads to angles 0°, 120° and 240° between the crossovers when assuming one full turn (360°) of B-form DNA consists of 10.5 bases. To enable more close-packed and flat edge structures, same group developed another way of folding of DNA origami structures based on a square lattice arrangement of DNA double helices [42]. In compare to honeycomb lattice where 1 full turn of DNA consists of 10.5 bp, the square lattice forces 1 full turn at every 10.67 bp (or 3 turns at 32 bp) which leads to angles 0°, 90°, 180° and 270° (or staple cross-over at every 8 bp) between the cross-overs of adjacent DNA double helices. Both honeycomb and square lattice folding techniques can be used and desired DNA origami designs can be produced using caDNAno [43], a graphical-interface based computer-aided design program developed by Shawn Douglas. DNA origami structures can also be intentionally curved or twisted by forcing cross-overs into the structure at non-natural intervals via targeted insertions and deletions. Dietz et al. showed that the degree of curvature could be controlled with a minimal radius of curvature of 6 nm using this technique [44]. In this technique which DNA double helices arranged into honeycomb lattice, the deletion of a base pair (cross-overs forced to be < 7 bp) results local stretching and overwinding which leads the shortening and a left-handed torque. Conversely, the insertion of a base pair (when the full turn is forced to be > 7 bp) results under-winding and compressive strain which leads the lengthening and a right-handed torque. Intricate DNA origami structures were developed such as wireframe beach balls, gears and spirals with this approach. (Figure 1.5C) In addition to these approaches, different design tools were also developed by researchers to form distinct DNA origami structures such as DNA boxes, DNA tensegrity and DNA gridiron structures [45-47]. (Figure 1.5D-F) Most recently, with the help of computer design software DNA scaffold can be routed from the arbitrary polygonal meshes to form any kind of DNA origami structures[48]. (Figure 1.5G)

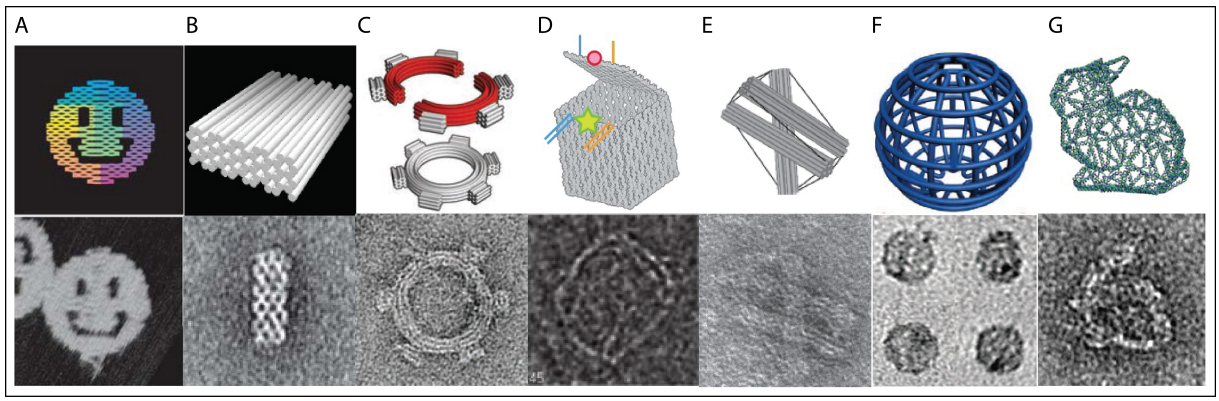

Figure 1.5: DNA origami structures. Top: Schemes of structures. Bottom: Designed structures imaged by AFM (A) and TEM (B-G). The size of the structures: 30-100 nm. A) One of the first DNA origami structures developed by Rothemund: a disk with three holes which resembles a smiley face. Reprinted by permission from Macmillan Publishers Ltd: Nature [40] Copyright 2006. B) 3D DNA origami structure by Shih and co-workers. Reprinted by permission from Macmillan Publishers Ltd: Nature [41] Copyright 2009. C) Curved structure by Dietz et al. From [44]. Reprinted with permission from AAAS. D) DNA origami box with a controllable lid by Andersen et al. Reprinted by permission from Macmillan Publishers Ltd: Nature [46] Copyright 2009. E) DNA tensegrity structure by Liedl

et al. Reprinted by permission from Macmillan Publishers Ltd: Nature [47] Copyright 2010. F) DNA origami sphere by Yan and co-workers. From [45]. Reprinted with permission from AAAS. G) 3D mesh of a Stanford bunny rendered in DNA by Högberg and co-workers. Reprinted by permission from Macmillan Publishers Ltd: Nature [48] Copyright 2015.

Today, the realization of the power of programmable DNA self-assembly and the ability of DNA functionalization with nanometer precision with a wide range of molecules allow the use of DNA nanotechnology by researchers in many diverse research areas including plasmonics, nanoelectronics, biophysics and biomedicine. DNA structures often function as template to position flurophores [49], gold nanoparticles [50], quantum dots [51], polymers [52], proteins and other biomolecules [53]. During the course of my work, I focused on using DNA nanostructures which are functionalized with a variety of biomolecules for mimicking membrane related biological events and cellular delivery applications.

The successful delivery of DNA based nanostructures is composed of three main steps that have to be completed. First, the designed structures should maintain the structural and functional integrity in the biological fluid. Second, the functionalized structures should specifically target and interact with the cellular membrane which is a selective barrier that separates cell from the outer environment. Third, the structures should reach the cytoplasm to perform the desired action such as delivery of the payload. In the light of this sequence of events, three different projects were presented in this dissertation as three parts. In the first part, we demonstrated the importance of structural integrity of the designed structures for the functionality and targeted delivery. In the second part of the thesis, we successfully demonstrated how the interaction of DNA nanostructures with lipid membranes could be achieved to form hierarchical structures resembling the formation of clathrin coated pits during endocytosis. The technique showed here could be further implemented on the biological membranes. In the last part, we successfully demonstrated the delivery of CpG oligonucleotides and drug molecules *in vivo* using DNA nanostructures.

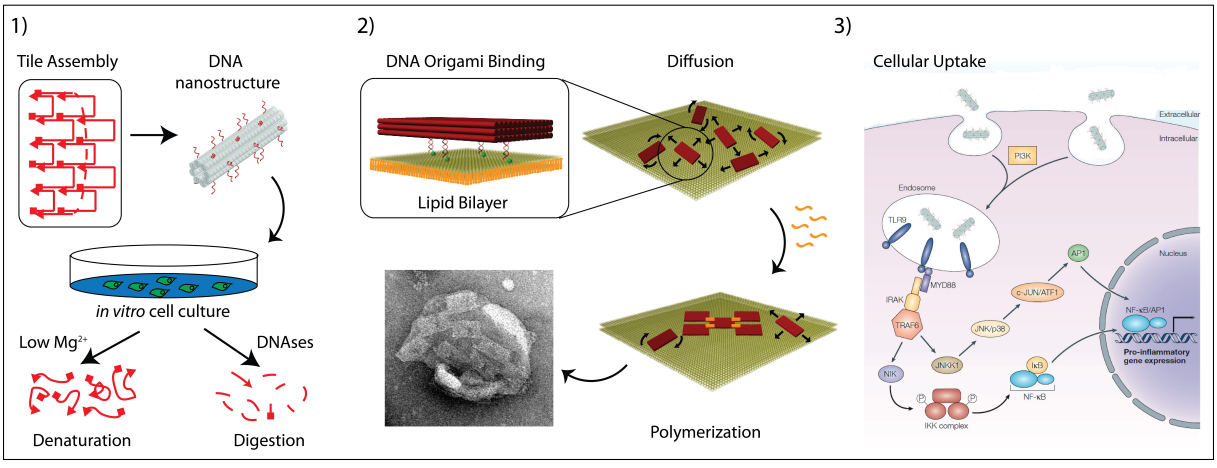

Figure 1.6: Towards the delivery of DNA-based nanostructures. 1) The stability of DNA nanostructures in the biological fluid. 2) Membrane-assisted polymerization of DNA origami structures after cholesterol-mediated binding and lateral diffusion. 3) Cellular uptake of CpG decorated DNA nanotubes and subsequent expression of pro-inflammatory genes.

2 DNA-based Nanostructures for Cellular Delivery

2.1 DNA Carrier Systems for Cellular Delivery

DNA structure allows the precise control of the shape of the building material upon self-assembly and spatial arrangement of any kind of molecule (e.g. drugs, small molecules, antibodies, proteins) on the material which is not possible for other common delivery systems such as liposomes, polymers and inorganic materials. It has also potential for drug loading in high density and tunable release properties with environmental changes (e.g. pH) based on the sequence programmability. Since DNA is constitutively found inside the cells it is also inherently biocompatible material. Therefore, DNA-based nanostructures offer a great potential as delivery agents.

Up to now, DNA nanostructures have been functionalized with wide range of bioactive molecules such as proteins, antibodies, anticancer drugs, synthetic oligonucleotides or small-interfering RNAs to elicit different therapeutic effects *in vivo*. To enable the desired therapeutic effects of DNA nanostructures, most of the time, they need to overcome the first biological barrier which is lipophilic membrane to gain access to cytosol and then reach the targeted cellular compartments including nucleus and mitochondria. Due to the anionic nature nucleic acid molecules are often impermeable to cellular membranes. Several studies reported that gene delivery vectors such as plasmids or antisense oligonucleotides are considered as using different cell entry mechanisms including receptor mediated endocytosis, pinocytosis or through interaction of cell membrane nucleic acid channels [54, 55]. One common approach used for the uptake of DNA nanostructures is specifically targeting cell surface receptors which lead the receptor mediated endocytosis of the DNA nanostructures that are functionalized with proteins, antibodies or small molecules. Mao et al. showed that folate conjugated DNA nanotubes are designed to target folate receptors that are overexpressed on many cancer cell types can enter ovarian cancer cells [56]. The modification of nanotubes with fluorescent dyes showed that the structures or their fragments are internalized upon receptor binding. Modi et al. designed two different DNA nanodevices which are respectively targeting furin and transferrin receptors on the cell membrane to investigate the pH change of the furine retrogate endocytic pathway and the transferring endocytic/recycling pathway simultaneously on the same cancer cell line [57]. Most recently, transferrin receptors were also targeted using 2D DNA origami nanostructures. The study presented by Okholm et al. showed that increasing the number of transferring molecules on the nanostructure correlates with the cellular uptake of the structures [58]. DNA nanodevices were also used to target specific tissues *in vivo*. For this reason, the Krishnan group designed pH sensitive DNA nanodevice called I-switch which was microinjected to multicellular organism, *Caenorhabtidis elegans* [59]. Upon injection, the nanodevice was targeted to specific scavenger cells that present cell-surface anionic ligand-binding receptors and upon internalization they showed that the device could map the endosomal maturation.

DNA based nanostructures were also used to modulate cellular activities externally by targeting cell surface receptors, eg. membrane proteins. The interaction between cellular membrane receptors and DNA nanostructures could be established via functionalizing DNA

structures with aptamers, antibodies, proteins or carbohydrates. One striking example of such an approach is a logic-gated DNA origami nanorobot developed by Douglas et. al. [60]. (Figure 2.1A) The barrel-like nanorobots were loaded with fluorescently labeled antibody fragments against human leukocyte antigen (HLA-A/B/C) which are controlled by the aptamer encoded logic gates. The structures are only opened if the cell surface markers expressed on the cells that are recognized by the aptamers and then presented antibodies are available to bind to antigens. Using different aptamer combinations they tested the structures on 6 different cell lines which express different profiles of antigens. Furthermore, they showed that it is also possible to use nanorobots to selectively bind to a single cell type in a mixed cell population. DNA nanostructures are also capable of spatial orientation of ligands to investigate certain cellular pathways. Nanocalipers developed by Shaw et. al. demonstrated the well-positioned Ephrin ligands on the structure directed the levels of EphA2 receptor activation in human breast cancer cell lines [61]. (Figure 2.1B) Recently, the study presented by Sut et al. showed that DNA tile structures can be functionalized with lactose molecules to target lectin receptors, which are carbohydrate binding receptors and highly expressed in many cancer cell types [62]. They found that the functionalization of DNA structures with lactose increased the intracellular uptake efficiency of the structures in compare to unmodified tiles and release of doxorubicin, anti-cancer drug, to the cancer cells.

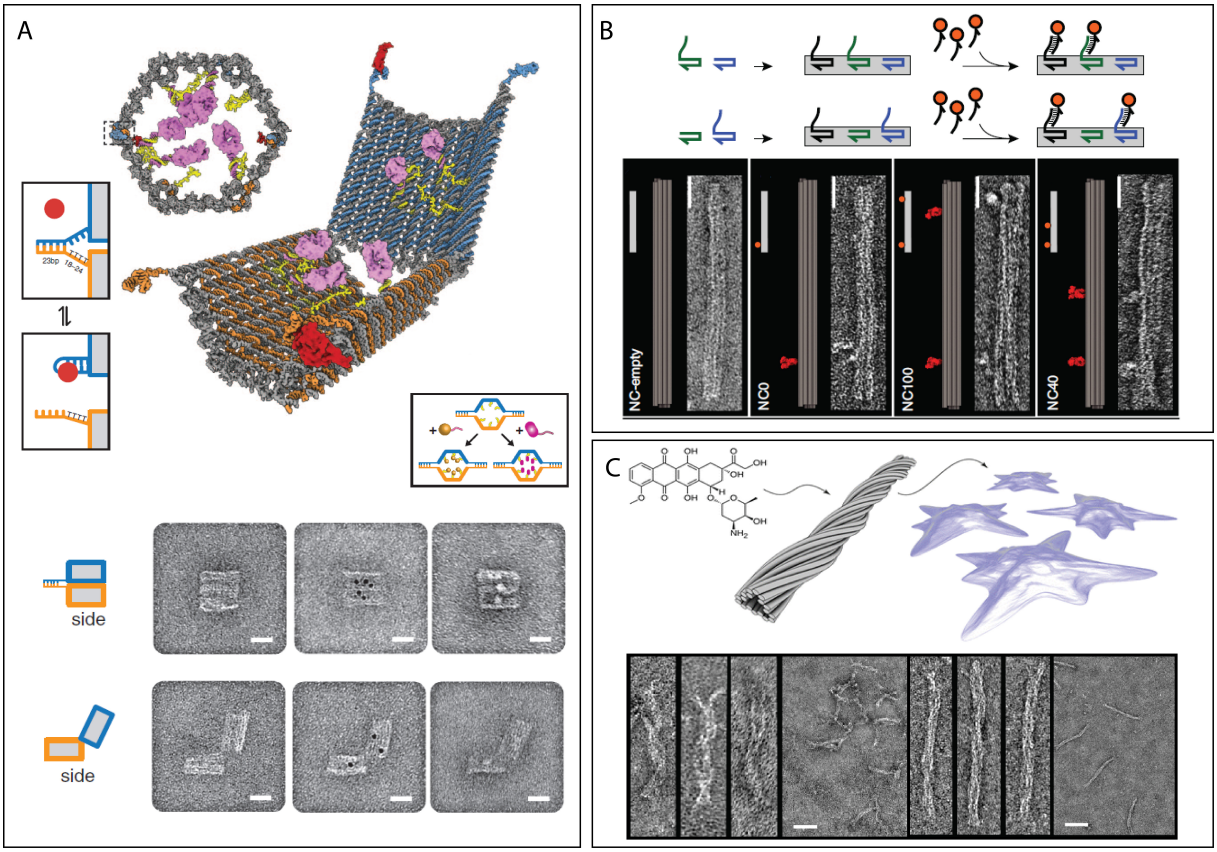

Figure 2.1: DNA-based structures for cellular targeting and delivery**.** A) A logic-gated DNA origami nanorobot to target cells and subsequently displyay molecular payload. From [60]. Reprinted with permission from AAAS. B) DNA origami nanocaliper to position two Ephrin ligands either 40 nm or 100 nm apart from each other. Reprinted by permission from Macmillan Publishers Ltd: Nature Methods [61] Copyright 2014. C) Twisted rod-like DNA

origami nanostructure for doxorubicin delivery. Reprinted with permission from [63]. Copyright 2012 American Chemical Society.

DNA nanostructures have been also used as drug delivery vehicles to deliver anticancer drugs such as doxorubicin. Doxorubicin is a cytotoxic drug commonly used in cancer therapeutics and since doxorubicin intercalates in the major groove of DNA it is an optimum delivery agent for DNA based vehicles. Moreover, doxorubicin can able to cross the lipid bilayer membranes. Even though DNA nanostructures more likely trapped in the endosome, they can release the doxorubicin to cytosol which can then go to nucleus eventually. Chang et al. showed for the first time that DNA icosahedra modified with an aptamer that recognizing MUC1 receptors were internalized by human breast cancer cells and released doxorubicin upon internalization [64]. Using 2D origami triangle and 3D origami tubes, Jiang et. al. observed enhanced drug loading and delivery in compare to unfolded structures. Drug loaded structures had more cytotoxic effect on drug-resistant cancer cells compare to the unloaded structures or free drug controls due to the uptake and slow release in lysosome. [65]. Shortly after, the Högberg group developed a twisted DNA origami which enables tunable release of doxorubicin. [63]. (Figure 2.1C) Another drug delivery study using Daunoribicin also showed efficient uptake and drug release to the drug resistant acute promyelocytic leukemica cells [66]. Finally, Zhang et al. studied anti-tumor effect of doxorubicin intercalated DNA origami triangles by injecting the structure into the teil vein of tumor-bearing mice [67]. They found that doxorubicin loaded DNA origami structures possessed enhanced tumor passive targeting and long-lasting accumulation properties at tumor region.

In the following study where the results are presented in associated publication P1, we investigated the targeted delivery of DNA nanotubes in several cancer cell lines which over express folate receptors. DNA nanotube structures were folded using single-stranded tile assembly method which was mentioned in detail in section 1. To target folate receptors, the structures were conjugated with folate molecule by using click chemistry. Moreover, DNA nanotubes were hybridized with siRNA molecules that are against *GFP*, a model gene, that are stably expressed in the targeted cells.

2.2 Folate Receptor-Mediated Delivery of siRNA conjugated DNA Nanotubes

Folate (folic acid) is a vitamin which has high affinity to folate receptor proteins that are highly expressed on the many cancer cell types [68, 69]. Since the folate molecule is involved in several metabolic pathways and required for biosynthesis of nucleotides it is highly consumed by proliferating cells. The accessibility of the folate receptors is also limited on the regular cells due to its location on the apical membrane. Due to its high binding affinity, ease of modification, small size and low immunogenicity it becomes a promising targeting agent in cancer therapies in recent years [70]. Folate receptors are membrane associated proteins attached to the glycosylphosphatidylinositol (GPI) anchor. Folate binding to its receptor initiates cellular uptake via receptor-mediated endocytosis upon formation of sub-micron size lipid rafts/receptor rich domains which are devoid of caveolae but rich in sphingolipid and cholesterol [71].

Small interfering RNA (siRNA) has become one of the most common drug targets in cancer therapy since its nobel prize-winning discovery in 2006 by Fire and Mello [72]. This 20-25 bp RNA duplex is first recognized and cleaved by the enzyme Dicer and then each double stranded RNA are spliced into guided and passenger strand. The guided strand is incorporated into the RNA-induced silencing complex (RISC) while the passenger strand is degraded. Then, RISC complex hybridize the guided strand to the complementary sequence in the target messenger RNA (mRNA) which triggers the cleavage and post transcriptional silencing of the gene. Using siRNA is highly advantageous in cancer therapies since multiple gene targeting is possible simultaneously.

In this project, we developed 6-helix tile tubes carrying folate molecules for cancer cell targeting, siRNA for gene silencing and flourescence molecules for visualization. DNA tube assembly, folate conjugation, siRNA duplex formation, and characterization of the folded structures are depicted in the Figure 2.2.

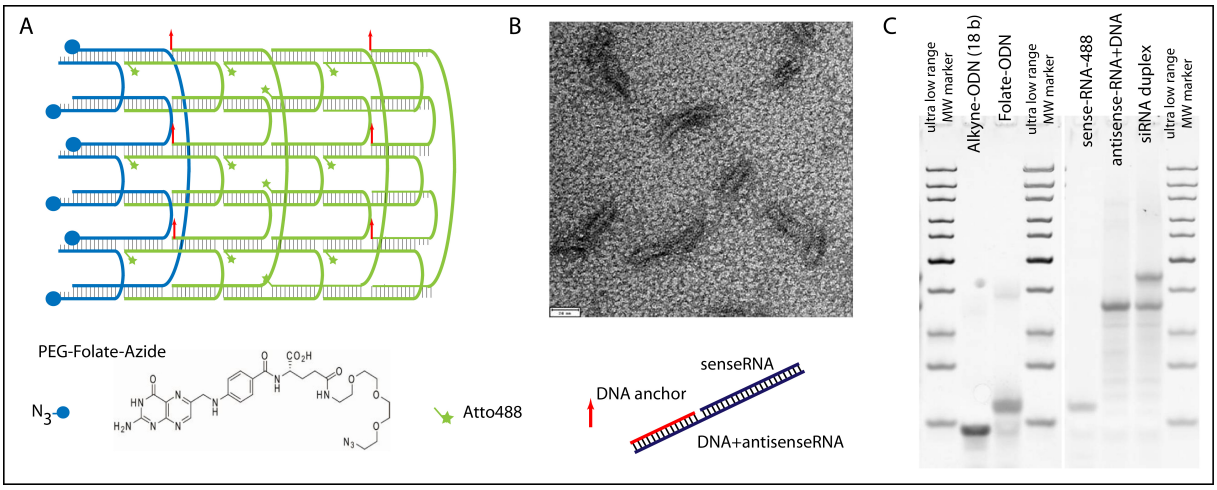

Figure 2.2: Design and characterization of 6-helix nanotubes for folate targeted delivery. A) 6-helix DNA nanotube design carrying folate molecules, Atto488 fluorophores and DNA anchors for siRNA conjugation. B) TEM image of DNA nanotubes. (scale bar: 20 nm) C) 20% native PAGE gel analysis of folate and siRNA conjugation.

In our experiments, the confocal microscopy results showed that nanotubes are delivered to the endosome but not reached to the cytosol to induce gene silencing and the uptake of the structures were not elevated by the presence of folate molecule. From these experiments, we realized several challenges that need to be considered and improved during *in vitro* and *in vivo* experiments.

First of all, DNA nanostructures have tendency to disintegrate in cell culture conditions (DMEM medium with ~1 mM Mg^{2+}, 135 mM Na^{+}) since the folding of the DNA nanostructures require high salt concentration (~ 20 mM Mg^{2+}). DNA nanotubes used in these experiments were stable up to 8 hr in the medium when there is no siRNA on the structure, however they degraded in 1 hr when they have siRNA extension. This is mainly because of the distorted stacking of the last base before extension and electrostatic repulsion between the extended sequence and the structure. Mg^{2+} depletion-dependent disintegration of several DNA origami structures was also observed in similar works [73, 74]. (Figure 2.3A) However,

employing 84-nt long tiles instead of 42-nt long ones enhanced the life-time in the cell medium drastically. In addition to using longer DNA strands, Benson *et al*. showed with their DNA polyhedral meshes that designing structures which consist of loosely packed single helices, enhances the stability of the structures in biologically relevant buffers such as PBS or DMEM at low salt concentrations and elevated temperatures [48].

DNAse activity is the other most important drawback for the stability of DNA nanostructures in biological applications. Since DNA nanostructures are tightly packed with Mg^{2+} the stability against DNAse are higher in compare to double stranded DNA. Castro et al. showed that enzymatic degradation of DNA origami bundles was significantly slower than the bare double stranded DNA by incubating structures with T7 endonuclease 1 or DNAse 1 [75]. In our work, we have also observed the cleavage of fluorescent dye molecules from the structure when the dye modified oligonucleotides were hybridized to the extended handles from the structure. The cleaved dyes were located in the cytoplasm near the mitochondria when the structures were incubated in the serum (e.g. FCS) containing media. However, we observed the endosomal colocalization of the fluorophores instead of mitochondria when they enzymatically labeled to the 3´ end of the single tiles.

Although we observed the uptake and colocalization of DNA nanotubes in endosome, similar uptake levels of single stranded DNA tiles carrying fluorophores were also detected after 8 hrs of incubation. Since the structures showed the stability in the serum containing media up to 8 hrs we assume that they are uptaken during this time. However, similar uptake levels of single stranded tiles measured by fluorescence data could be related with the degradation of tiles during this time and accumulation of dyes in the endosome.

In this study and other cellular delivery studies of DNA nanostructures it is shown that DNA structures are uptaken by cells up to some extent however the transfection efficiency is still low. By quantifying the DNA scaffold using quantitative polymerase chain reaction (qPCR) method, Okholm et al. recently showed that planar DNA origami structures were uptaken by cells however the amount of uptake was an order of magnitude lower than the structures incubated with lipofectamine [76]. This could be explained with the high negative charge density on the DNA nanostructures. Therefore the transfection efficiency of DNA structures could be improved using modifications such as cationic peptides, polymers or lipids. Recently developed virus mimicking particles covering DNA structures showed enhanced stability and uptake of the structures. Perrault et al. encapsulated DNA origami octahedrons in the PEGylated (polyethylene glycol conjugated) lipid membranes [77]. (Figure 2.3B) They showed that increasing the number of outer handles for the lipid envelope formation protected the structures against nuclease attack for 24 hrs. Almost 85 % of the structures, which are formed using 48 outer handles for lipid conjugation, remained stable after incubation with 20 units of DNAse I enzyme. Moreover, the encapsulated DNA octahedrons showed 17 times greater half-life in compare to DNA oligonucleotides and bare octahedrons. Encapsulated DNA octahedrons were fluorescently visible for 2 hrs all over the mice body whereas the control samples were accumulated in the bladder. In an alternative work, Mikkilä et al. combined virus capsid proteins with DNA origami structures [78]. All these works showed enhanced uptake and stability against DNAses. Alternatively, the

stability of the DNA nanostructures could be improved by chemical modifications of DNA nucleobases using click chemistry. Cassinelli et al. showed that single stranded tiles in the 6-helix nanotubes could be interlocked by applying click reaction between 3′ and 5′ ends of the same tile [79]. (Figure 2.3C) Strikingly, the 6-helix tube structures, which consist of 24 oligonucleotides, are stable against high temperature (95 °C), exonuclease I, and low salt concentrated mediums like DMEM when all strands were interlocked by click reaction. Another strategy to increase the stability of DNA structures is the formation of disulfide bonds between adjacent DNA strands. The Gothelf group showed that DAE tiles are stable under heating conditions (65 °C) and in the presence of denaturing agents [80]. The strategy used here is also reversible under reducing environments like cytoplasm of the cells which could be exploited for the cellular application such as cargo delivery of the DNA nanostructures.

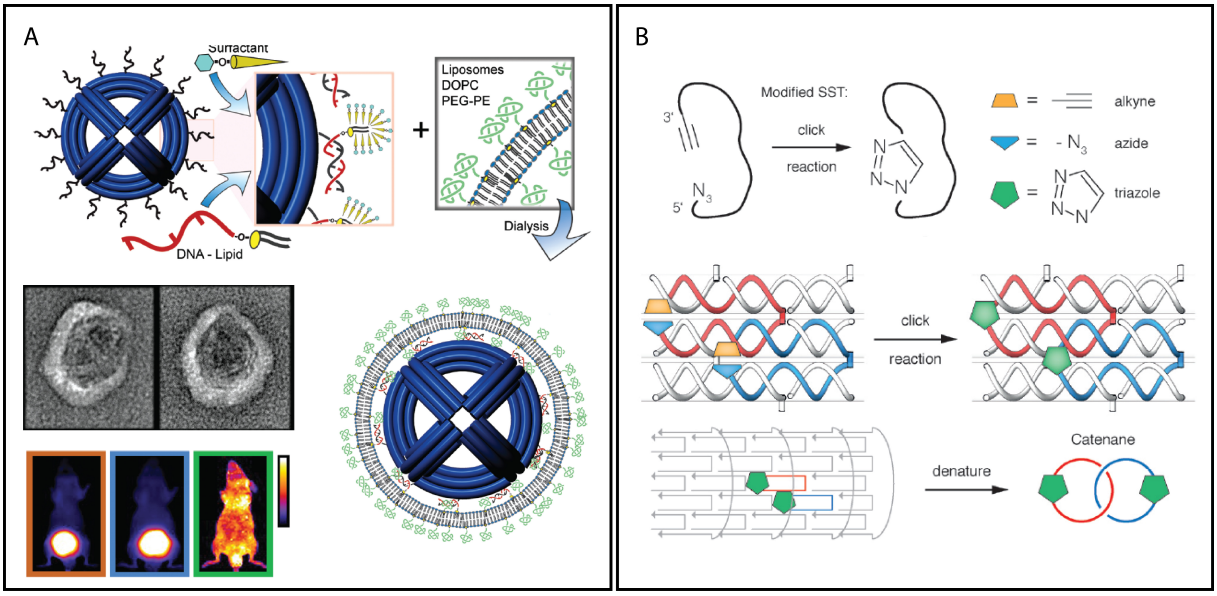

Figure 2.3: Increasing the stability of DNA nanostructures. A) A virus-inspired membrane-encapsulated spherical DNA origami structure enhancing the stability and pharmacokinetic bioavailability. Reprinted with permission from [77]. Copyright 2014 American Chemical Society. B) Increasing the stability of tile-assembled DNA nanotubes by click reaction. Reprinted with permission from [79]. Copyright 2015 John Wiley and Sons.

The surface properties of the DNA nanostructures could be altered using specific DNA intercalators to enhance the transfection efficiency of DNA nanostructures. The enhanced uptake of aforementioned DNA-based drug delivery systems including Doxorubicin and Daunorubicin could be related with the altered surface properties of DNA structures. To change the surface property of the DNA origami structures several groups also used cationic polymers to coat the structures [81]. Most recently, Chopra et al. demonstrated that DNA origami structures can be folded in Mg free buffer solutions containing low (< 1mM) concentrations of a condensing agent spermidine [82]. These structures are stable in cell lysate and in the presence of high electric field pulse which allows the transfection with electroporation.

To summarize, we found out in this study that for the efficient delivery of the DNA based nanostructures, the structures assembled in specific folding solution should maintain structural and functional integrity inside the biological fluid. One possible direction could be using condensation agents such as polyamines which can fold the structures with a salt independent manner while at the same time allow the accessibility and functionalization of DNA molecules. After surviving the biological fluid then the structures could reach their targets on the cellular membranes.

2.3 Associated Publication P1

Cellular Uptake of Tile-Assembled DNA Nanotubes

by

Samet Kocabey, Hanna Meinl, Iain S. MacPherson, Valentina Cassinelli, Antonio Manetto, Simon Rothenfusser, Tim Liedl and Felix S. Lichtenegger

published in

Nanomaterials 2015, 5(1), 47-60

Nanomaterials **2015**, *5*, 47-60; doi:10.3390/nano5010047

OPEN ACCESS

nanomaterials

ISSN 2079-4991

www.mdpi.com/journal/nanomaterials

Article

Cellular Uptake of Tile-Assembled DNA Nanotubes

Samet Kocabey [1], Hanna Meinl [2], Iain S. MacPherson [1], Valentina Cassinelli [3], Antonio Manetto [3], Simon Rothenfusser [2], Tim Liedl [1] and Felix S. Lichtenegger [2,4,*]

[1] Faculty of Physics and Center for Nanoscience, Ludwig-Maximilians University, Munich 80799, Germany; E-Mails: samet.kocabey@physik.lmu.de (S.K.); iainmacpherson@gmail.com (I.S.M.); tim.liedl@physik.lmu.de (T.L.)

[2] Division of Clinical Pharmacology, Department of Internal Medicine IV, Klinikum der Universität München, Munich 80336, Germany; E-Mails: hanna.meinl@outlook.com (H.M.); simon.rothenfusser@med.uni-muenchen.de (S.R.)

[3] Baseclick GmbH, Tutzing 82327, Germany; E-Mails: v.cassinelli@baseclick.eu (V.C.); a.manetto@baseclick.eu (A.M.)

[4] Department of Internal Medicine III, Klinikum der Universität München, Munich 81377, Germany

* Author to whom correspondence should be addressed;
E-Mail: felix.lichtenegger@med.uni-muenchen.de; Tel.: +49-89-4400-57300;
Fax: +49-89-4400-57330.

Received: 2 December 2014 / Accepted: 22 December 2014 / Published: 30 December 2014

Abstract: DNA-based nanostructures have received great attention as molecular vehicles for cellular delivery of biomolecules and cancer drugs. Here, we report on the cellular uptake of tubule-like DNA tile-assembled nanostructures 27 nm in length and 8 nm in diameter that carry siRNA molecules, folic acid and fluorescent dyes. In our observations, the DNA structures are delivered to the endosome and do not reach the cytosol of the *GFP*-expressing HeLa cells that were used in the experiments. Consistent with this observation, no elevated silencing of the *GFP* gene could be detected. Furthermore, the presence of up to six molecules of folic acid on the carrier surface did not alter the uptake behavior and gene silencing. We further observed several challenges that have to be considered when performing *in vitro* and *in vivo* experiments with DNA structures: (i) DNA tile tubes consisting of 42 nt-long oligonucleotides and carrying single- or double-stranded extensions degrade within one hour in cell medium at 37 °C, while the same tubes without extensions are stable for up to eight hours. The degradation is caused mainly by the low concentration of divalent ions in the media. The lifetime in cell medium can be increased drastically by employing DNA tiles that are 84 nt long. (ii) Dyes may get cleaved from the oligonucleotides and then accumulate inside the cell close to the

mitochondria, which can lead to misinterpretation of data generated by flow cytometry and fluorescence microscopy. (iii) Single-stranded DNA carrying fluorescent dyes are internalized at similar levels as the DNA tile-assembled tubes used here.

Keywords: DNA nanotechnology; DNA tile; siRNA delivery; stability; folate; cation

1. Introduction

Therapeutic agents must overcome multiple barriers to reach their target [1,2]. For example, siRNAs have to reach the target tissue, enter the cells, be released from the endosomal compartment and, finally, silence the target gene via the RISC complex [3]. Up to now, researchers have developed a variety of nanoparticle carrier systems to overcome these barriers, such as polymers [4], liposomes [5] or conjugates [6], with various levels of efficiency and toxicity. Most recently, with improvements in the DNA nanotechnology field, DNA-based nanostructures were developed as carrier systems for a variety of active components, including siRNAs [7], antibodies [8], immunostimulants [9,10] and cancer drugs [11,12]. DNA nanostructures are promising for delivery applications because they can be easily modified with a variety of (bio)chemical moieties for targeting purposes at nanoscale precision; they are monodisperse with well-defined sizes and are non-cytotoxic [10,13–18]. To date, several groups have investigated the targeted delivery of DNA-based nanostructures using different targeting agents, such as cell penetrating peptides or small molecules. Among them, folate is a commonly-used molecule, due to the high expression of its receptors on certain cancer cells. Efficient folate-mediated uptake has been demonstrated using various DNA-based structures, such as DNA nanotubes built from a single palindromic DNA strand [19] or Y-shaped DNA nanostructures prepared by rolling circle amplification [20]. Although the DNA-based nanostructures are promising for targeted delivery applications, as exemplified above, the stability of these structures at 37 °C in blood or tissue is one of the main issues to be considered. In a recent study, the stability of a variety of DNA origami structures with different designs, such as octahedron, six-helix bundle tubes or 24-helix bundle rods, were investigated using *in vitro* conditions, and time-and shape-dependent denaturation and digestion were observed due to the Mg^{2+} depletion in the media and the DNase activity of the serum [21]. As an alternative to the DNA origami method [14,15] and shape-specific designs, such as DNA cubes [22], tetrahedrons [23] or octahedrons [24], single-stranded tile assembly has recently proven to be a versatile and modular design strategy to build a wide variety of two- and three-dimensional shapes [25,26]. In this study, we intended to show efficient folate-mediated uptake and subsequent gene silencing by tile-assembled DNA nanotubes carrying GFP siRNAs *in vitro*. However, we were not able to demonstrate the sought-after effects, but instead observed untimely disassembly of our constructs under certain *in vitro* conditions and, therefore, investigated strategies to maintain the structural integrity in relevant environments. We examined the stability of tile-assembled structures under limited divalent cations and in the presence of nucleases in buffer and in cell media. We then describe a number of artifacts that should be taken into consideration during experiments with DNA-based nanostructures *in vitro*.

2. Results and Discussion

2.1. Design and Self-Assembly of Six-Helix DNA Nanotubes

We designed tubule-like DNA nanostructures consisting of 24 oligonucleotides that self-assemble into six parallel helices using the single-stranded DNA tile assembly method introduced by Yin *et al.* (Scheme 1 and Table S1) [25,27]. Six of the oligonucleotides were alkyne-modified during synthesis and conjugated in-house with PEG-folate-azide (Baseclick GmbH, Tutzing, Germany) by a click reaction. Reversed phase high performance chromatography (RP-HPLC) analysis and matrix-assisted laser desorption/ionization (MALDI) mass spectrometry revealed the almost quantitatively conjugation of folate molecules to the alkyne-oligonucleotides. (Figures S1 and S2, Table S2). Another set of six oligonucleotides was extended by an 18 nt-long sequence at the 3' end to allow the attachment via hybridization of six siRNA molecules that potentially silence the expression of GFP upon delivery. To visualize the DNA nanotubes *in vitro*, two different labeling strategies were employed. In the first approach, Atto488-dUTP was enzymatically labeled to the 3' end of a set of 12 tile oligonucleotides using terminal transferase. In the second approach, the same set of oligonucleotides was extended with another 18 nt-long sequence allowing attachment via hybridization of 12 Atto647-modified (via NHS chemistry) oligonucleotides. The nanotubes have a designed length of ~27 nm and an expected diameter of ~6 nm for the dried sample. Note that the tube diameter of a six-helix bundle increases in buffer to 8 nm and that tubes decorated with additional molecules will have a larger effective diameter [28].

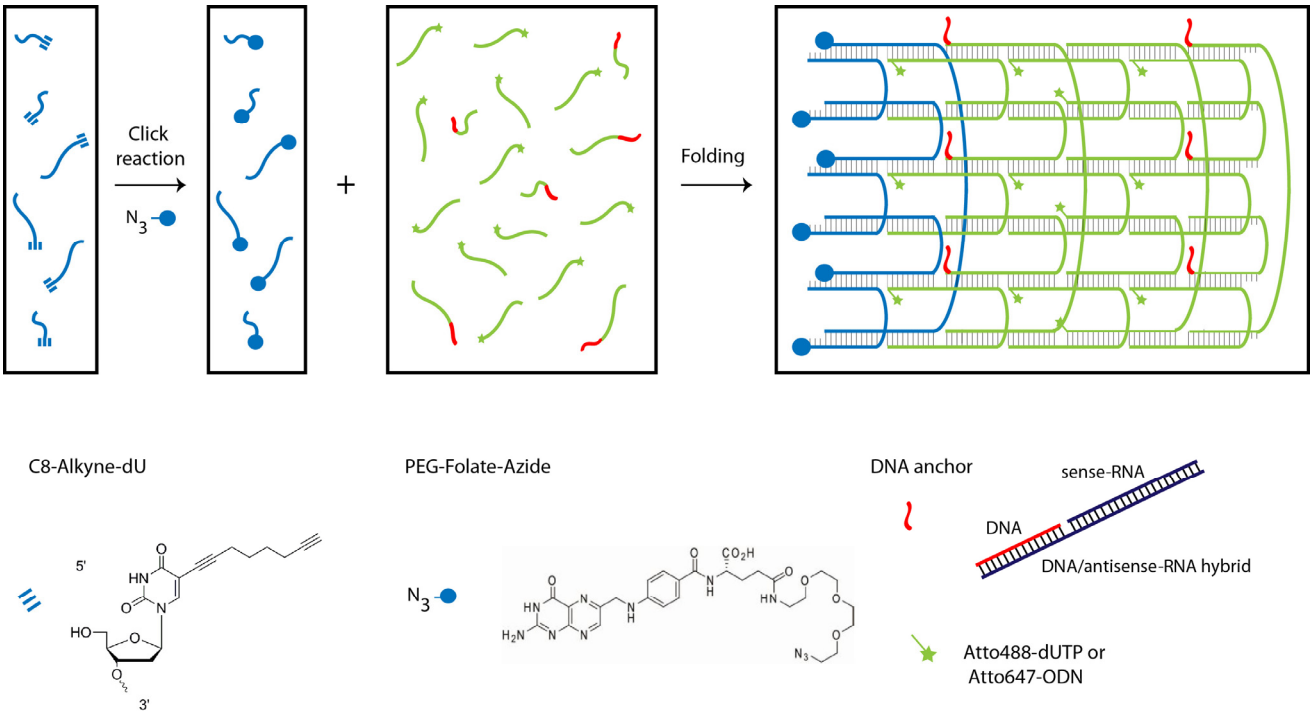

Scheme 1. DNA nanotube assembly. (**Left**) Click reaction of alkyne-modified oligonucleotides with azide-modified PEGylated folate. (**Right**) Self-assembly of 24 oligonucleotides into a six-helix tube after a 17-h annealing process.

The nanotube structures containing the desired subsets of oligonucleotides and modifications were folded in TE-buffer containing 20 mM Mg^{2+} during a thermal annealing process starting at 80 °C and cooling down to room temperature over the course of 17 h. Analysis by gel electrophoresis analysis showed for all designs prominent bands representing the folded structures (Lanes 2 + 3 + 4 in Figure 1). Conjugation of folate and folate + siRNA (Lanes 3 and 4, respectively) to the DNA nanotubes leads to a decrease of their mobility in comparison to nanotubes without folate and siRNA (Lane 2). Transmission electron microscopy (TEM) demonstrates the correct assembly of the nanotubes and the monodispersity of the samples. The measured length of 27 ± 1 nm and the measured diameter of 6 ± 1 nm perfectly match the expected dimensions (Figure 1B–D).

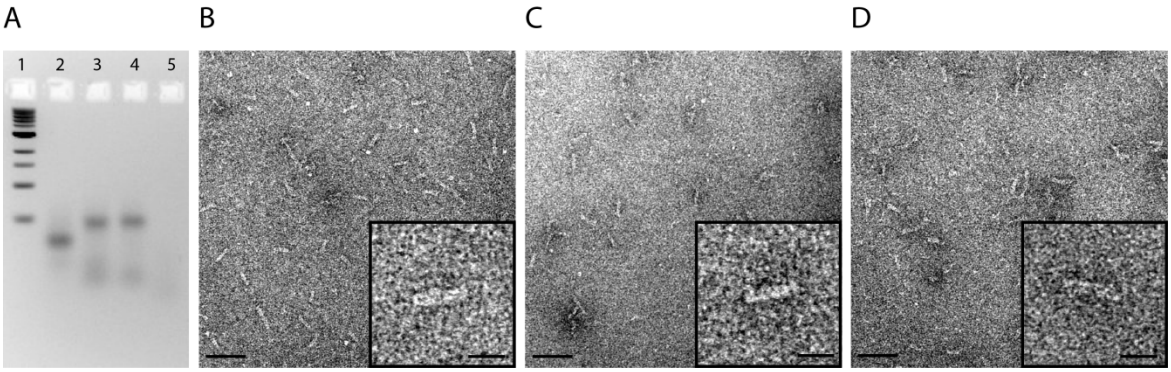

Figure 1. Characterization of nanotubes. (**a**) Gel electrophoresis analysis of assembled nanotubes: (1) 1-kb ladder, (2) nanotube, (3) nanotube + folate, (4) nanotube + folate + siRNA, and (5) individual oligonucleotide. Electron micrographs of (**b**) Nanotubes; (**c**) Nanotubes with folate; and (**d**) Nanotubes with folate and siRNA (scale bars: 50 nm; insets: 20 nm).

2.2. Tubule-Like Tile-Assembled DNA Nanostructures Are Delivered to the Endosome of HeLa Cells Independently of Folic Acid and Are Not Capable of Releasing siRNA into the Cytosol

DNA nanotubes labeled with Atto488 via enzymatic labeling were added to HeLa cell cultures at 10 nM, together with dextran-AF647 as a marker for endosomal uptake. At various time points thereafter, confocal microscopy was performed to evaluate the localization of the construct. After 24 h, we found clear co-localization of the nanotubes with dextran (Figure 2A–C). Observations for up to 72 h did not show any change in localization (Figure S3C,D).

To determine a potential effect of uptake via the folate receptor, which is highly expressed on the surface of HeLa cells, nanotubes with and without folic acid were compared side by side. No influence on the endosomal staining pattern was noticed in the fluorescence microscopy images, neither after 24 h nor after 72 h (Figure S3). For a quantitative analysis of the uptake, we conducted flow cytometry-based measurements of the HeLa cells at different time points after the addition of fluorophore-labeled nanotubes (Figure 2D). A minor signal was already detected after 4 h, which further increased in the course of 24 h. No significant difference was found between the uptake of nanotubes with or without folate.

On a functional level, we tested if the nanostructures released their siRNA cargo successfully to the cytoplasm by analyzing the knockdown capacity of siRNA molecules bound to the DNA nanotube.

Stably *GFP*-transfected HeLa cell lines were used together with siRNA directed against *GFP* (siGFP). The siGFP was either bound to the nanostructure via hybridization or transfected into the cytoplasm by lipofection as a positive control. The GFP signal of the cells was measured by flow cytometry after 96 h (Figure 2E). In the condition with lipofection of GFP-targeting siRNAs, the fluorochrome signal was markedly decreased compared to lipofection of a control siRNA (siCTRL). However, the addition of siGFP to the nanotubes did not result in *GFP*-knockdown, independent of folate labeling, consistent with endosomal trapping of the whole structure, including their siRNA cargo.

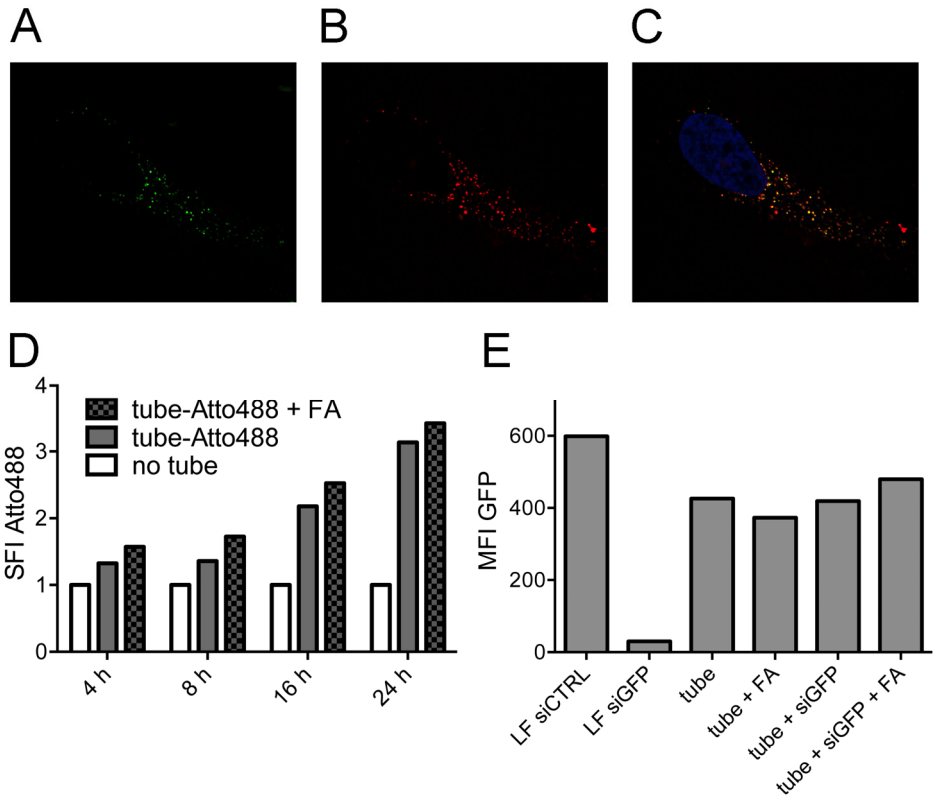

Figure 2. Endosomal uptake of nanotubes in HeLa cells. Endosomal staining of nanotubes with dextran. (**a**) Nanotubes; (**b**) Dextran; (**c**) Merged image from (**a**), (**b**) and a third channel (DAPI, blue). (**d**) Flow cytometry analysis of folate-dependent uptake of Atto488-labeled nanotubes over 24 h. Untreated cells act as the control, and the specific fluorescence intensity (SFI) of the dye is depicted. (**e**) Fluorescence intensity of stably GFP-expressing Hela cells upon the addition of nanotubes carrying *GFP*-targeting siRNAs or upon transfection of a *GFP*-targeting siRNA and a non-targeting siRNA, respectively, as controls using lipofection (LF). The median fluorescence intensity (MFI) of GFP is depicted.

2.3. Stability of DNA Nanotubes Differs in Various Conditions In Vitro

To address the stability of tile-assembled DNA nanostructures *in vitro*, we incubated them in different buffers and cell media. First, we incubated the nanotubes in PBS with different Mg^{2+} concentrations at 37 °C for 2 h. We used PBS as a buffer to simulate the cell media conditions, as both cell media and PBS possess several monovalent and divalent cations at isotonic concentrations. Importantly, for the assembly and stabilization of the DNA nanostructures, usually Mg^{2+} concentrations

much higher than those found in PBS and cell media are used. While folding of DNA nanostructures can also be achieved at high Na^+ concentrations [29], the 135 mM NaCl present in PBS are not sufficient to stabilize DNA nanotubes at 37 °C, if the individual DNA tiles are 42 nt long. Gel analysis revealed that the nanotubes without extensions were stable down to 1 mM Mg^{2+}, whereas the nanotubes carrying siRNA started to degrade already below 4 mM Mg^{2+} (Figure 3A,B). This indicates that the addition of extension sequences protruding from the DNA nanotubes destabilizes the structure, which may be explained by distorted stacking of the last base before the extension and with an increase of electrostatic repulsion between the elongated tail and the DNA duplexes in the nanotube [30]. Next, we compared the stability of nanotubes against DNases and incubated the structures in cell medium containing 10% FCS. Gel analysis showed that under these conditions, the plain nanotubes are stable up to 8 h (Figure 3C). However, nanotubes carrying siRNA were degraded in 1 h when the structures were incubated in media containing 10% FCS. These nanotubes were also degraded slightly during 8 h in DMEM medium without FCS, likely due to Mg^{2+} depletion (in all cell media experiments, the concentration of Mg^{2+} was 1.8 mM).

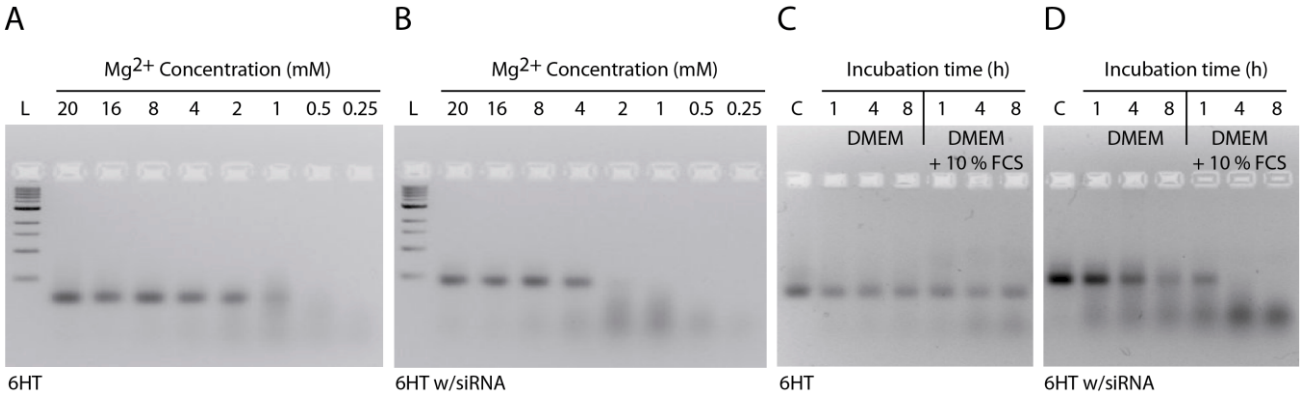

Figure 3. Stability of nanotubes. (**a**) Stability of nanotubes in PBS with different Mg^{2+} concentrations; (**b**) Stability of nanotubes carrying siRNA in PBS with different Mg^{2+} concentrations; (**c**) Stability of nanotubes in DMEM medium in the absence or presence of FCS; (**d**) Stability of nanotubes carrying siRNA in DMEM medium in the absence or presence of FCS (L: 1 kb ladder; C: control. All samples were incubated at 37 °C).

To overcome the problem of premature degradation, DNA tile tubes were assembled from 84 nt-long oligonucleotides. This design allows longer complementary regions (21 bp for the 84mers instead of 10 bp and 11 bp for the 42mers) within the tile assembly, which, in turn, yields much higher thermal stability, but also higher resistance to Mg^{2+} depletion (Figure 4). Our results show that the stability of tile-assembled nanotubes is dependent on sequence design, temperature, salt concentration and structural modifications, such as the addition of single- or double-stranded extensions to the DNA tiles.

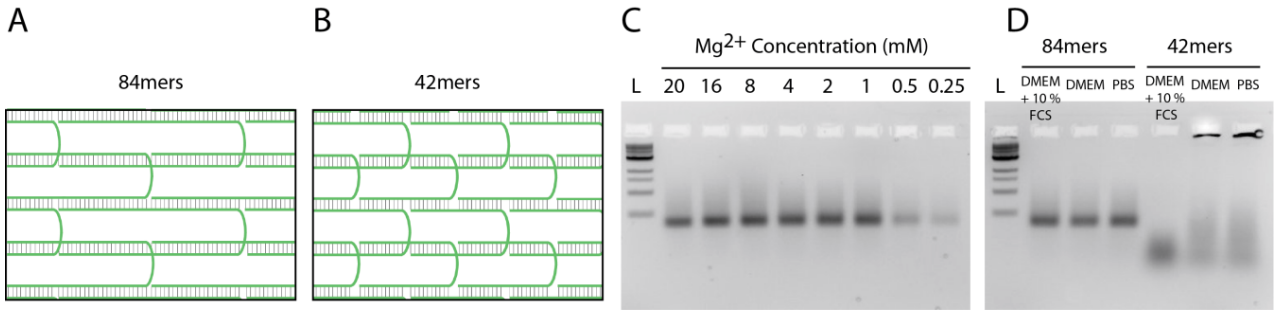

Figure 4. Stability of nanotubes assembled from 84 nt-long oligonucleotides. (**a**) Schematic depiction of a section of the 6HT demonstrating the hybridization of 84mers; (**b**) Schematic depiction of a section of the 6HT demonstrating the hybridization of 42mers; (**c**) Stability of nanotubes (84mers) in PBS with different Mg^{2+} concentrations; (**d**) Stability of nanotubes (84mers and 42mers) in DMEM + 10% FCS, DMEM and PBS. Nanotubes were incubated at 45 °C for 2 h (L: 1 kb ladder; C: control).

2.4. Strong Extra-Endosomal Uptake Can Be Feigned by Dye Cleavage

When nanostructures labeled with Atto647 via hybridization were incubated with HeLa cells, we repeatedly observed a very high fluorescence level in the cells during microscopy- or flow cytometry-based analysis. Furthermore, the fluorochrome did not co-localize with dextran as an endosomal marker (Figure 5A), but instead, mitochondrial localization was detected (Figure 5B). The level of uptake and the mitochondrial staining pattern were associated with the addition of serum to the culture medium (Figure S4). Similarly, when only the oligonucleotide labeled with Atto647 (via NHS chemistry) was added to the HeLa cells, we observed a rapid and strong staining of the cells only in the case when serum was added (Figure 5C). This effect was not observed when the fluorophores were attached via enzymatic binding. We therefore conclude that Atto647 is cleaved off the DNA by some component in the serum and is taken up independently of the nanostructure.

2.5. Single-Stranded DNA Molecules, But Not Deoxynucleotide Triphosphates, Are Internalized at Similar Levels as the Tile-Assembled Nanotube Structures

Specific uptake of the tubule-like tile-assembled DNA nanostructures was analyzed by direct comparison with oligonucleotides and deoxynucleotide triphosphates. All three molecules were labeled with Atto488 and incubated at identical molar concentrations with HeLa cells. Fluorochrome uptake was measured by flow cytometry at various time points (Figure 5D). No intracellular staining was found in the deoxynucleotide triphosphate condition. However, we observed similar uptake of the fluorochrome with the oligonucleotide as with the nanostructure.

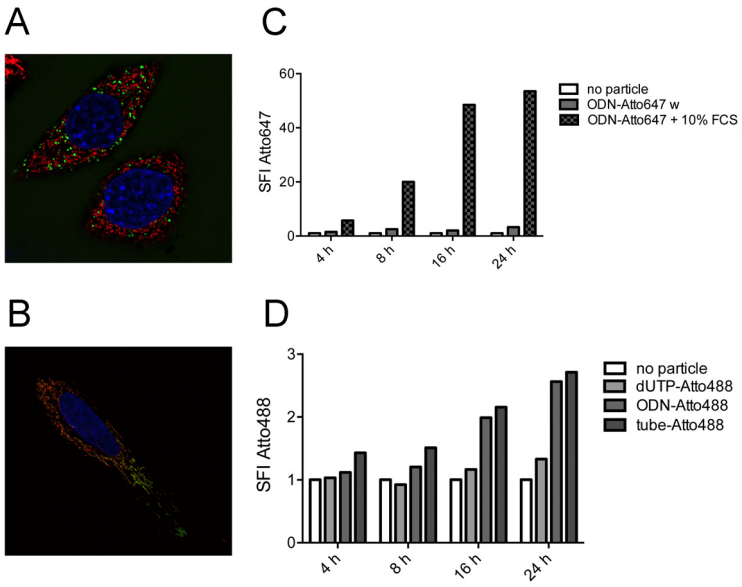

Figure 5. Effect of dye cleavage on cellular uptake. (**a**) Endosomal staining using Alexa Fluor 488-coupled dextran (shown in green) of HeLa cells treated with oligodeoxynucleotide (ODN)-Atto647 (shown in red); (**b**) Mitochondrial colocalization of Atto647 (shown in red) in HeLa cells stained with the mitochondrial dye MitoTracker Green (shown in green). Nuclei are stained with Hoechst 33342; (**c**) Flow cytometry analysis of fluorescence intensity of cells treated with ODN-Atto647 in the absence or presence of FCS; (**d**) Flow cytometry analysis of fluorescence intensity of cells treated with Atto488-dUTP, ODN-Atto488 and nanotube labeled with Atto488. Untreated cells act as the control, and the specific fluorescence intensity (SFI) of the dye is depicted.

3. Experimental Section

3.1. DNA Nanotube Design

DNA nanotubes were designed using Yin's single-strand tile (SST) method [27]. Each tile oligonucleotide is 42 bases long and consists of four domains with ten or eleven bases. Twenty four individual oligonucleotides were used to form 6 helix nanotube. The domains at the ends of the nanotube contain non-pairing poly-A sequences to prevent polymerization. siRNA hybridization to the nanotubes was done by extending 3' ends of six tiles with an 18-nt long overhang sequence (5'-AGGATGTAGGTGGTAGAG-3'). The used siRNA sequences for *GFP* silencing were sense: 5'-GCCACAACGUCUAUAUCAU-3', and antisense: 5'-AUGAUAUAGACGUUGUGGC CTCTACCACCTACATCCT-3'. Six oligonucleotides were modified with PEG-folate azide (Baseclick GmbH, Tutzing, Germany) using click reactions. The underlined sequence shows the complementary overhang. All oligonucleotides were purchased from Eurofins (Ebersberg, Germany) with HPSF or HPLC purification.

3.2. Folate Conjugation and Characterization of Oligonucleotides

Each of the six alkyne-modified oligonucleotides (Baseclick GmbH) were submitted to click reaction, using CuBr as the Cu(I) source. Ten microliters of a freshly prepared CuBr (0.1 M)/THPTA (0.1 M) solution in a 1:2 *v*/*v* ratio were added to a 50-µL (0.1 mM, 5 nmol) solution of each alkyne-oligonucleotide. The addition of folate-PEG3-azide (2.5 µL, 10 mM in DMSO) completed the click reaction cocktail. The mixture was mixed for 1.5 h at 45 °C. Finally, the solution was purified via ethanol precipitation. Folate-conjugated oligonucleotides were analyzed by analytical RP-HPLC (e2695 system, Waters, Milford, MA, USA) coupled with a photodiode array detector (PDA 2998, Waters) using a reversed phase XBridge OST C18 column (4.6 mm × 50 mm, Waters). Before injection in RP-HPLC, samples were diluted to 10 µM concentration in HPLC-grade H_2O. Samples (2 µL) were desalted against ddH_2O using a nitrocellulose membrane (MerckMillipore, Frankfurt, Germany), and 0.4 µL were spotted onto a MALDI plate (Bruker Corporation, Millerica, MA, USA) along with 0.4 µL of 3-hydroxypicolinic acid (HPA, Sigma Aldrich, St. Luis, MO, USA). Measurements were carried out with the Autoflex MALDI-TOF (Bruker Corporation).

3.3. Dye Labeling of DNA Nanotubes

Fluorescent dyes were conjugated to the 12 oligonucleotides with two different approaches before the nanotube assembly. In the first approach, 3' ends of twelve tiles were extended by 18 nt-long overhang sequences to hybridize the dye-modified sequence: (Atto647 TTCATTCTCCTATTACTACC). In the second approach, the 3' ends of the same tiles were enzymatically labeled with Atto488-dUTP (Jena Bioscience, Jena, Germany). For this, Atto488-dUTP (80 µM), $CoCl_2$ (5 mM), terminal transferase enzyme (16 U/µL, Roche, Penzberg, Germany) and all DNA tiles (400 pmol) were mixed in a 20 µL, 1× TdT reaction buffer and then incubated at 37 °C for 30 min. Then, 2.5 µL of NaOAc (3 M) were added, and the solution was filled up to 80 µL with ice-cooled ethanol (99%). After 1 h of incubation at −20 °C, samples were centrifuged at 13,000× *g* for 30 min. Then, samples were washed with 70% ethanol for 10 min again, and the supernatant was discarded. The remaining pellet was dissolved in distilled water.

3.4. DNA Nanotube Assembly and Purification

For DNA nanotube assembly, 400 nM of dye and folate modified tiles, 800 nM of antisense-ODN and 1.6 µM of sense-ODN were mixed in a folding buffer (10 mM Tris-HCl, 1 mM EDTA, pH 8.0, 20 mM $MgCl_2$). For the plain nanotube assembly, 1 µM of unmodified tiles was used. The DNA nanotubes were folded over the course of 16 h (5 min at 80 °C, cooling down to 65 °C at 1 °C/min, cooling down to 25 °C at 2.5 °C/h). Purification of the assembled DNA nanotubes was done using 30K Amicon Ultra 0.5-mL centrifuge filters (30000 MWCO, Millipore, Schwalbach, Germany) to remove excess strands that were not folded into the structures. One hundred microliters of assembled DNA nanotube solution were mixed with 400 µL of folding buffer, filled into the centrifuge filter, and centrifuged 3 times at 13,000× *g* for 6 min. After every centrifuge step, the flow-through was removed and the filter was refilled up to 500 µL with buffer. After final centrifugation, the remaining solution at

the bottom of the filter (~50 µL) was pipetted out, and the concentration of nanotubes was determined by measuring the optical density at 260 nm.

3.5. Gel Electrophoresis and Transmission Electron Microscopy

DNA nanotubes were analyzed by running samples in an agarose gel. For this, 2% agarose was dissolved in 0.5× TAE buffer by heating to boiling. $MgCl_2$ (11 mM) and ethidium bromide (0.5 µg/mL) were added after the cooling, and the solution was poured into a gel cask for solidification. Twenty microliters of each filter-purified DNA nanotube sample were mixed with 4 µL of 6× loading dye before loading into the gel pockets. Six microliters of 1 kb ladder were also loaded adjacent to the samples. The gel was run for 2 h at 70 V in an ice-cold water bath to prevent heat-induced denaturation of DNA nanotubes. To visualize DNA nanotubes, a JEM-1011 transmission electron microscope (JEOL GmbH, Eching, Germany) was used. DNA nanotubes were incubated on plasma-exposed (240 kV for 1 min) carbon-coated grids and then negatively stained with 2% uranyl formate for 10 s.

3.6. Stability of DNA Nanotubes

The stability of DNA nanotubes was tested in PBS buffer, DMEM and DMEM containing 10% FCS, separately. One microliter of DNA nanotubes (50 ng/µL) in 20 µL of buffer/medium was incubated at 37 °C for different time points. Two percent agarose gel with 11 mM $MgCl_2$ was prepared to analyze the samples, as mentioned in Experimental Section 3.5.

3.7. Cell Culture Experiments

HeLa cells were cultured at 37 °C, 5% CO_2 and 95% humidity in Dulbecco's modified Eagle's medium (Life Technologies Thermo Fischer, Waltham, MA, USA) supplemented with 10% heat-inactivated fetal calf serum (FCS, Invitrogen Thermo Fischer, Waltham, MA, USA), 2 mM L-glutamine, 100 U/mL penicillin and 100 µg/mL streptomycin. Stably GFP-transfected HeLa cell lines were generated by retroviral transduction using an eGFP containing pMP71 vector, as described previously [31,32]. To analyze uptake, DNA nanotubes, oligonucleotides and deoxynucleotide triphosphates were added to HeLa cells at a concentration between 10 and 40 nM for the indicated period of time in DMEM with L-glutamine, penicillin, streptomycin and either supplemented or not with 10% FCS. For siRNA-mediated knockdown experiments, GFP-expressing HeLa cells were seeded in 24-well plates and allowed to adhere overnight. On the next day, cells were either incubated with the indicated nanotubes coupled to GFP-targeting siRNAs or were transfected as a control with siRNA oligonucleotides (75 nM) using Lipofectamine RNAiMAX (Invitrogen). After 48 h, GFP-knockdown was measured by flow cytometry. The siRNA sequence used to target GFP (siGFP) was 5' GCCACAACGUCUAUAUCAU 3'. As a control (siCTRL), we used the non-targeting RNA sequence 5' GCGCUAUCCAGCUUACGUA 3' described previously [33]. SiRNAs were purchased from Eurofins and contained dTdT overhangs.

3.8. Flow Cytometry and Confocal Fluorescence Microscopy

Flow cytometry was used to determine the uptake of DNA nanotubes, oligonucleotides and deoxynucleotide triphosphates labeled with the fluorescent dyes, Atto488 or Atto647, into HeLa cells and to assess the knockdown efficiency of *GFP*-targeting siRNAs in stably GFP-expressing HeLa cells. For that, after the indicated time points, single-cell suspensions were prepared and washed several times before analyzing the cells on a FACS Calibur (Becton Dickinson, Franklin Lakes, NJ, USA). FlowJo software was used to analyze the data. GFP expression was depicted by median fluorescence intensity (MFI). For all experiments with fluorescent dye labeling, the data are represented as specific fluorescence intensity (SFI), which was calculated by dividing the MFI of the sample by the MFI of the control. Confocal fluorescence microscopy was used to determine the subcellular localization of nanotubes and RNAs taken up by HeLa cells. For that, HeLa cells were cultured in CELLview cell culture dishes with a glass bottom (Greiner Bio One). After incubation with Atto488- or Atto647-labeled nanotubes for the indicated time points, cells were washed three times with PBS and used for live-imaging on a Leica TCS SP5 confocal microscope (Leica Microsystems GmbH, Wetzlar, Germany). Zero-point-two micrograms per milliliter of Hoechst 33342 and MitoTracker Green (both from Life Technologies) were used according to the manufacturer's protocol to stain nuclei and mitochondria, respectively. In order to visualize endosomes, 20 μg/mL dextran labeled with Alexa Fluor 647 or Alexa Fluor 488 (Life Technologies Thermo Fischer) were added simultaneously with the DNA nanotubes.

4. Conclusions

In this study, we investigated the cellular delivery of tile-assembled DNA nanotubes carrying siRNAs using GFP-expressing HeLa cells via folate targeting. We observed that the nanostructures enter the cells via an endosomal pathway, but the nanostructures and their siRNA cargo are not capable of reaching the cytoplasm for knockdown and gene silencing. Contingently, no significant decrease in GFP expression levels was detectable, and folate modification did not change the uptake kinetics. The stability experiments revealed that unmodified DNA nanotubes are stable at 37 °C up to 8 h in the cell media and that they stay intact in PBS buffer containing 2 mM Mg^{2+} or more. However, the extension of the DNA tile strands with sequences that allow the hybridization of siRNA or dye-modified strands drastically decreases the construct's stability, a fact that may have contributed to the unsuccessful folate targeting experiments. Using DNA tiles that were 84-nt long drastically increased the stability in all cell media and buffers with low Mg^{2+} concentrations. Importantly, we observed that DNA strands alone and cleaved dyes are also uptaken by the cells, which can lead to the misinterpretation of recorded data. Overall, the results presented in this study demonstrate the importance of rigorously testing the stability of DNA nanostructures before applications *in vitro* and *in vivo*.

Supplementary Materials

Supplementary materials can be accessed at: http://www.mdpi.com/2079-4991/5/1/47/s1.

Acknowledgments

This work was supported by the European Commission under the Seventh Framework Programme (FP7), as part of the Marie Curie Initial Training Network, EScoDNA (No. 317110) and the ERC starting grant, ORCA, by the DFG Grant RO2525/5-1 to S.R. and by a Metiphys fellowship of the Medical Faculty of the Ludwig-Maximilian University to F.S.L.. H.M. is supported by the Molecular Medicine Program of the Medical Faculty of the Ludwig-Maximilian University (Förderprogramm für Forschung und Lehre) and DFG Grant GK 1202.

Author Contributions

S.K., S.R., T.L. and F.L. designed the experiments. S.K., H.M., I.S.M., V.C., A.M. and F.L. performed the experiments. S.K., A.M., T.L. and F.L. wrote the manuscript.

Conflicts of Interest

The authors declare no conflict of interest.

References

1. Bareford, L.M.; Swaan, P.W. Endocytic mechanisms for targeted drug delivery. *Adv. Drug Deliv. Rev.* **2007**, *59*, 748–758.
2. Smith, D.; Schüller, V.; Engst, C.; Radler, J.; Liedl, T. Nucleic acid nanostructures for biomedical applications. *Nanomedicine* **2013**, *8*, 105–121.
3. Czech, B.; Hannon, G.J. Small RNA sorting: Matchmaking for argonautes. *Nat. Rev. Genet.* **2011**, *12*, 19–31.
4. Kataoka, K.; Harada, A.; Nagasaki, Y. Block copolymer micelles for drug delivery: Design, characterization and biological significance. *Adv. Drug Deliv. Rev.* **2001**, *47*, 113–131.
5. Miller, A.D. Cationic liposomes for gene therapy. *Angew. Chem. Int. Ed.* **1998**, *37*, 1768–1785.
6. Zhou, J.; Rossi, J.J. Therapeutic potential of aptamer-siRNA conjugates for treatment of HIV-1. *BioDrugs* **2012**, *26*, 393–400.
7. Lee, H.; Lytton-Jean, A.K.; Chen, Y.; Love, K.T.; Park, A.I.; Karagiannis, E.D.; Sehgal, A.; Querbes, W.; Zurenko, C.S.; Jayaraman, M.; *et al.* Molecularly self-assembled nucleic acid nanoparticles for targeted *in vivo* siRNA delivery. *Nat. Nanotechnol.* **2012**, *7*, 389–393.
8. Douglas, S.M.; Bachelet, I.; Church, G.M. A logic-gated nanorobot for targeted transport of molecular payloads. *Science* **2012**, *335*, 831–834.
9. Li, J.; Pei, H.; Zhu, B.; Liang, L.; Wei, M.; He, Y.; Chen, N.; Li, D.; Huang, Q.; Fan, C. Self-assembled multivalent DNA nanostructures for noninvasive intracellular delivery of immunostimulatory cpg oligonucleotides. *ACS Nano* **2011**, *5*, 8783–8789.
10. Schüller, V.J.; Heidegger, S.; Sandholzer, N.; Nickels, P.C.; Suhartha, N.A.; Endres, S.; Bourquin, C.; Liedl, T. Cellular immunostimulation by cpg-sequence-coated DNA origami structures. *ACS Nano* **2011**, *5*, 9696–9702.
11. Zhao, Y.-X.; Shaw, A.; Zeng, X.; Benson, E.; Nyström, A.M.; Högberg, B. DNA origami delivery system for cancer therapy with tunable release properties. *ACS Nano* **2012**, *6*, 8684–8691.

12. Jiang, Q.; Song, C.; Nangreave, J.; Liu, X.; Lin, L.; Qiu, D.; Wang, Z.-G.; Zou, G.; Liang, X.; Yan, H.; *et al.* DNA origami as a carrier for circumvention of drug resistance. *J. Am. Chem. Soc.* **2012**, *134*, 13396–13403.
13. Voigt, N.V.; Torring, T.; Rotaru, A.; Jacobsen, M.F.; Ravnsbaek, J.B.; Subramani, R.; Mamdouh, W.; Kjems, J.; Mokhir, A.; Besenbacher, F.; *et al.* Single-molecule chemical reactions on DNA origami. *Nat. Nanotechnol.* **2010**, *5*, 200–203.
14. Rothemund, P.W. Folding DNA to create nanoscale shapes and patterns. *Nature* **2006**, *440*, 297–302.
15. Douglas, S.M.; Dietz, H.; Liedl, T.; Hogberg, B.; Graf, F.; Shih, W.M. Self-assembly of DNA into nanoscale three-dimensional shapes. *Nature* **2009**, *459*, 414–418.
16. Perrault, S.D.; Shih, W.M. Virus-inspired membrane encapsulation of DNA nanostructures to achieve *in vivo* stability. *ACS Nano* **2014**, *8*, 5132–5140.
17. Mikkilä, J.; Eskelinen, A.-P.; Niemelä, E.H.; Linko, V.; Frilander, M.J.; Törmä, P.; Kostiainen, M.A. Virus-encapsulated DNA origami nanostructures for cellular delivery. *Nano Lett.* **2014**, *14*, 2196–2200.
18. Okholm, A.H.; Nielsen, J.S.; Vinther, M.; Sorensen, R.S.; Schaffert, D.; Kjems, J. Quantification of cellular uptake of DNA nanostructures by qPCR. *Methods* **2014**, *67*, 193–197.
19. Ko, S.; Liu, H.; Chen, Y.; Mao, C. DNA nanotubes as combinatorial vehicles for cellular delivery. *Biomacromolecules* **2008**, *9*, 3039–3043.
20. Hong, C.A.; Jang, B.; Jeong, E.H.; Jeong, H.; Lee, H. Self-assembled DNA nanostructures prepared by rolling circle amplification for the delivery of sirna conjugates. *Chem. Comm.* **2014**, *50*, 13049–13051.
21. Hahn, J.; Wickham, S.F.; Shih, W.M.; Perrault, S.D. Addressing the instability of DNA nanostructures in tissue culture. *ACS Nano* **2014**, *8*, 8765–8775.
22. Seeman, N.C. Construction of three-dimensional stick figures from branched DNA. *DNA Cell Biol.* **1991**, *10*, 475–486.
23. Erben, C.M.; Goodman, R.P.; Turberfield, A.J. Single-molecule protein encapsulation in a rigid DNA cage. *Angew. Chem. Int. Ed.* **2006**, *45*, 7414–7417.
24. Shih, W.M.; Quispe, J.D.; Joyce, G.F. A 1.7-kilobase single-stranded DNA that folds into a nanoscale octahedron. *Nature* **2004**, *427*, 618–621.
25. Wei, B.; Dai, M.; Yin, P. Complex shapes self-assembled from single-stranded DNA tiles. *Nature* **2012**, *485*, 623–626.
26. Ke, Y.; Ong, L.L.; Shih, W.M.; Yin, P. Three-dimensional structures self-assembled from DNA bricks. *Science* **2012**, *338*, 1177–1183.
27. Yin, P.; Hariadi, R.F.; Sahu, S.; Choi, H.M.; Park, S.H.; Labean, T.H.; Reif, J.H. Programming DNA tube circumferences. *Science* **2008**, *321*, 824–826.
28. Schiffels, D.; Liedl, T.; Fygenson, D.K. Nanoscale structure and microscale stiffness of DNA nanotubes. *ACS Nano* **2013**, *7*, 6700–6710.
29. Martin, T.G.; Dietz, H. Magnesium-free self-assembly of multi-layer DNA objects. *Nat. Comm.* **2012**, *3*, doi:10.1038/ncomms2095.

30. Di Michele, L.; Mognetti, B.M.; Yanagishima, T.; Varilly, P.; Ruff, Z.; Frenkel, D.; Eiser, E. Effect of inert tails on the thermodynamics of DNA hybridization. *J. Am. Chem. Soc.* **2014**, *136*, 6538–6541.
31. Kobold, S.; Steffen, J.; Chaloupka, M.; Grassmann, S.; Henkel, J.; Castoldi, R.; Zeng, Y.; Chmielewski, M.; Schmollinger, J.C.; Schnurr, M.; *et al.* Selective bispecific T cell recruiting antibody enhances anti-tumor activity of adoptive T cell transfer. *J. Natl. Cancer Inst.* **2014**, *107*, doi:10.1093/jnci/dju364.
32. Engels, B.; Cam, H.; Schuler, T.; Indraccolo, S.; Gladow, M.; Baum, C.; Blankenstein, T.; Uckert, W. Retroviral vectors for high-level transgene expression in T lymphocytes. *Human Gene Ther.* **2003**, *14*, 1155–1168.
33. Besch, R.; Poeck, H.; Hohenauer, T.; Senft, D.; Hacker, G.; Berking, C.; Hornung, V.; Endres, S.; Ruzicka, T.; Rothenfusser, S.; *et al.* Proapoptotic signaling induced by RIG-I and MDA-5 results in type I interferon-independent apoptosis in human melanoma cells. *J. Clin. Invest.* **2009**, *119*, 2399–2411.

3 Hierarchical Assembly of DNA Nanostructures on Lipid Bilayer Membranes

3.1 Interaction of DNA Nanostructures with Lipid Membranes

Lipid membranes are functional interfacial barriers that allow the structural organization and compartmentalization of the cells. Many of the cellular processes such as signal transduction, energy conversion, intracellular and extracellular transportation are mediated by membrane-associated protein clusters [84-86]. Proteins that are involved in endocytosis such as clathrin and caveolin form self-assembled complexes upon receptor activation [87, 88]. As another example, FAS receptor, which is a transmembrane protein, can trigger apoptosis upon ligand activated multimerization [89]. All these processes require the interaction between protein components which is facilitated through their two-dimensional lateral diffusion within the lipid membranes of the cells. In order to mimic and potentially utilize similar membrane-based self-assembly mechanisms for nanotechnology applications such as targeted delivery or protein crystallization, we studied the self-assembly of membrane-bound DNA nanostructures which are inspired by and modeled after membrane-associated protein clusters.

Lipid membranes consist of different types of amphiphilic molecules such as glycerophospholipids, sphingophospholipids and cholesterol. (Figure 3.1A) Phospholipids are composed of hydrophobic alkyl tail, a linker molecule and a hydrophilic head group. The length of the alkyl tail and the charge of the hydrophilic head group, which could be neutral or charged, affect the structural organization and diffusion of the lipid bilayer [90]. The relative mobility of the individual lipid molecules in the lipid bilayer can be changed with the temperature. This response is known as the phase behavior of the lipid bilayer. At low temperatures, membranes are in a solid ordered gel (L_β) phase whereas at high temperatures liquid disordered phase (L_α) is adopted. The adopted phase also depends on lipid structure: long, saturated hydrocarbon chains are found in sphingomyelin (SM), so SM-rich mixtures tend to adopt solid-like phases; unsaturated hydrocarbon chains are found in most biomembrane glycerophospholipids, so these tend to be enriched in liquid phases [91]. Sterols by themselves do not form bilayer phases, but together with a bilayer-forming lipid, the liquid-ordered phase (L_o) can form. The liquid ordered phase has the high order of a solid but the high translational mobility of a liquid. Moreover, several phases could be exist simultaneously in mixture of lipids as depicted in the Figure 3.1B, two-phase or three-phase regions could be formed in the mixture of DOPC/SM/chol with different concentrations.

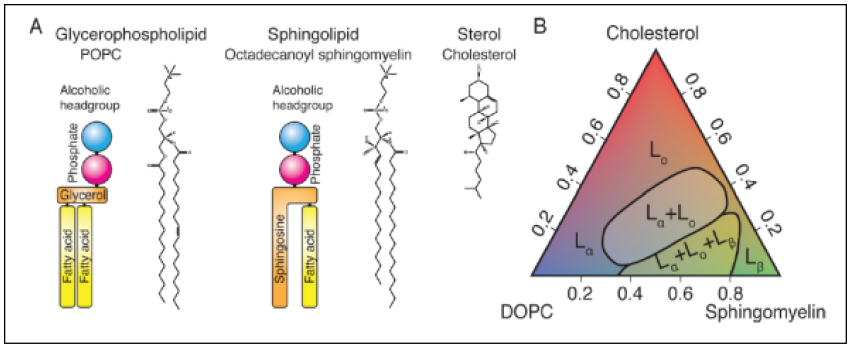

Figure 3.1: Lipids. A) Structures of lipid types. B) Phase diagram of a mixture of DOPC, sphingomyelin, and cholesterol. (L_α: Liquid crystalline, Lo: Liquid ordered, L_β: Solid ordered). Reprinted with permission from [90]. Copyright 2014 American Chemical Society.

Phospholipids self-assemble into lipid bilayers as in the form of a two-layered sheet with the hydrophobic tails pointing toward the center and hydrophilic head groups pointing towards the outside. The size of a typical lipid bilayer is around 5-6 nm. In order to form supported lipid bilayer a common technique was used which is based on the fusion of lipid molecules on the solid support such as glass or mica [92]. For this, lipids are first solubilized in organic solvent. After solvent evaporation under nitrogen and subsequent desiccation under vacuum, the dried lipid film is resuspended in aqueous buffer solution which yields a multilamellar vesicle (MLV) suspension. From this suspension, small unilamellar vesicles (SUVs) with the typical sizes of 25-100 nm can be obtained by sonication. The further addition of water to the SUV suspension induces the lipid bilayer formation.

There are several ways to enable the interaction of DNA nanostuctures with lipid membranes. One common way is the functionalization of DNA with hydrophobic molecules such as cholesterol, porhyrin, α-tocopherol or poly(propylene) oxide (PPO) [93-96]. Cholesterol-TEG (triethylene glycol) conjugation is mainly used for DNA lipid membrane interaction since it is commercially available and does not easily dissociate from the lipid membrane unless the hydrophobic interaction is weakened by the detergent molecules [93]. In addition to using hydrophobic molecules, charge interaction can also mediate the binding between DNA nanostructures and lipid membrane. Since DNA is highly negatively charged, it has high affinity to positively charged lipids such as DOTAP or DOTMA [97]. The interaction could be also established using divalent cations, Mg^{2+} or Ca^{2+}, together with zwitterionic lipids such as DOPC or POPC with zero net charge [98]. The mechanism for this interaction is divalent ion bridging the negative charge of DNA and lipid head group leading to the re-orientation of lipid molecules [99]. This divalent ion mediated interaction can be switched reversibly by changing divalent ion concentration [100].

It has been recently shown that DNA-based nanostructures conjugated with hydrophobic anchors can be used to mimic membrane-protein functions as occurred in the membrane ion channels [101]. Like natural pores, DNA based nanopores can control the transportation of waters soluble molecules. In 2012, the group of F. Simmel developed an artificial membrane channel with the scaffolded DNA origami method [102]. (Figure 3.2A) The structure is made of 54 parallel helices of which 6 inner helices were designed longer to penetrate the lipid membrane. The bottom of the cap structure was functionalized with cholesterol molecules in order to insert the structure inside the membrane. TEM images confirmed the insertion of DNA channels to the SUVs and the electrical measurements further proved the channel formation inside the membrane. The conductance of the DNA nanopore was around 1 nS, similar to the protein ion channels. In addition to ion transportation, DNA-based channels were also used for the selective transportation of other molecules such as fluorophores across lipid membranes [103]. (Figure 3.2B) For this, the group of S. Howorka was designed a 9 nm long 6-helix DNA bundle where the entrance of the pore is controlled by the molecular logic gate mechanism. The nanodevice is in closed state when the ´lock´ strand

is active which is a duplex formed by the hybridization of two docking sites at the entrance of the pore. Upon addition of the ´key´ strand the ´lock´ strand is preferentially hybridized with the ´key´ strand and removed from the entrance. The conductivity of the pore is shown in the presence and absence of the PEG molecules with different sizes to show that the transportation occurs only trough the pores. More strikingly, the selective and gate-depended transportation of charged molecules from lipid vesicles was indicated using flourophores as cargo molecules.

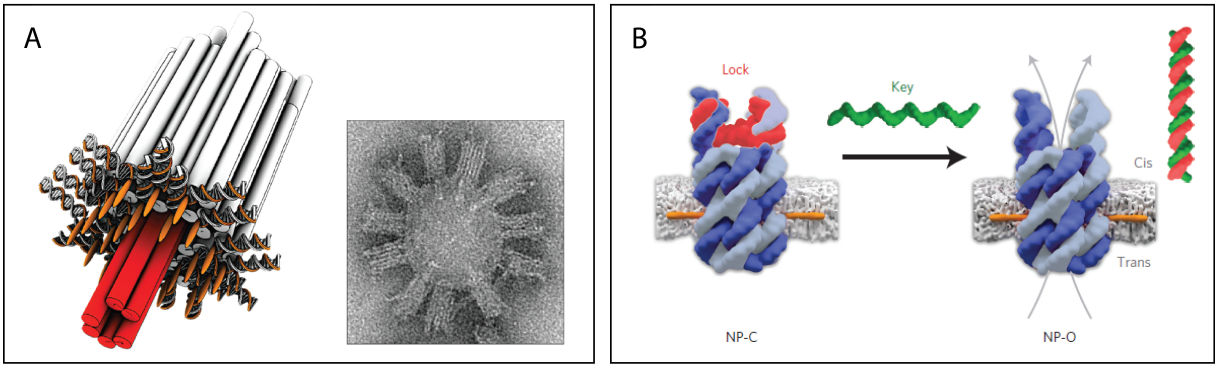

Figure 3.2: Synthetic DNA membrane channels. A) Left: Schematic illustration of DNA origami channel formed by 54 double helical domains packed on a honeycomb lattice. Red domains indicate transmembrane stem and orange ellipsoids indicate cholesterol molecules. Right: TEM image of DNA membrane channels adhered to a small unilamellar vesicle. From [102]. Reprinted with permission from AAAS. B) DNA nanopore features the selective transportation of molecules using logic-gate mechanism. Reprinted by permission from Macmillan Publishers Ltd: Nature Nanotechnology [103] Copyright 2016.

As an alternative to DNA origami nanopores, more cost-effective and simple designs with smaller pore size were also developed for the ion transportation across membranes using tile-based assembly. For this, we designed 4-helix tile DNA nanotubes with a length of 11 nm and a central channel with a nominal diameter of 0.8 nm assuming an anhydrated helix diameter of 2 nm [104]. Two of the tiles carry terminal cholesterol modifications for membrane insertion and two of the additional tiles carry Cy3 dyes for visualization by fluorescence microscopy. (Figure 3.3A) After only 60s, a bright ring around a GUV was appeared which indicates that tile based structures were incorporated on the membrane of the vesicle. (Figure 3.3B) These structures also showed the increased ionic conductivity on the GUVs. In order to check ion conductivity, the vesicles were suctioned onto the tip of a 200 nm diameter glass capillary where they burst and form lipid bilayer. (Figure 3.3C) This bilayer is then subjected to current-voltage (*IV*) recording protocol. Figure 3.3D shows the conductance of 170 independent *IV* recordings of plain GUVs (top) and GUVs incubated with DNA nanotubes (bottom). None of the plain GUVs showed a conductance above 0.3 nS. In contrast, 12 % of the GUVs incubated with DNA nanotubes showed elevated conductance.

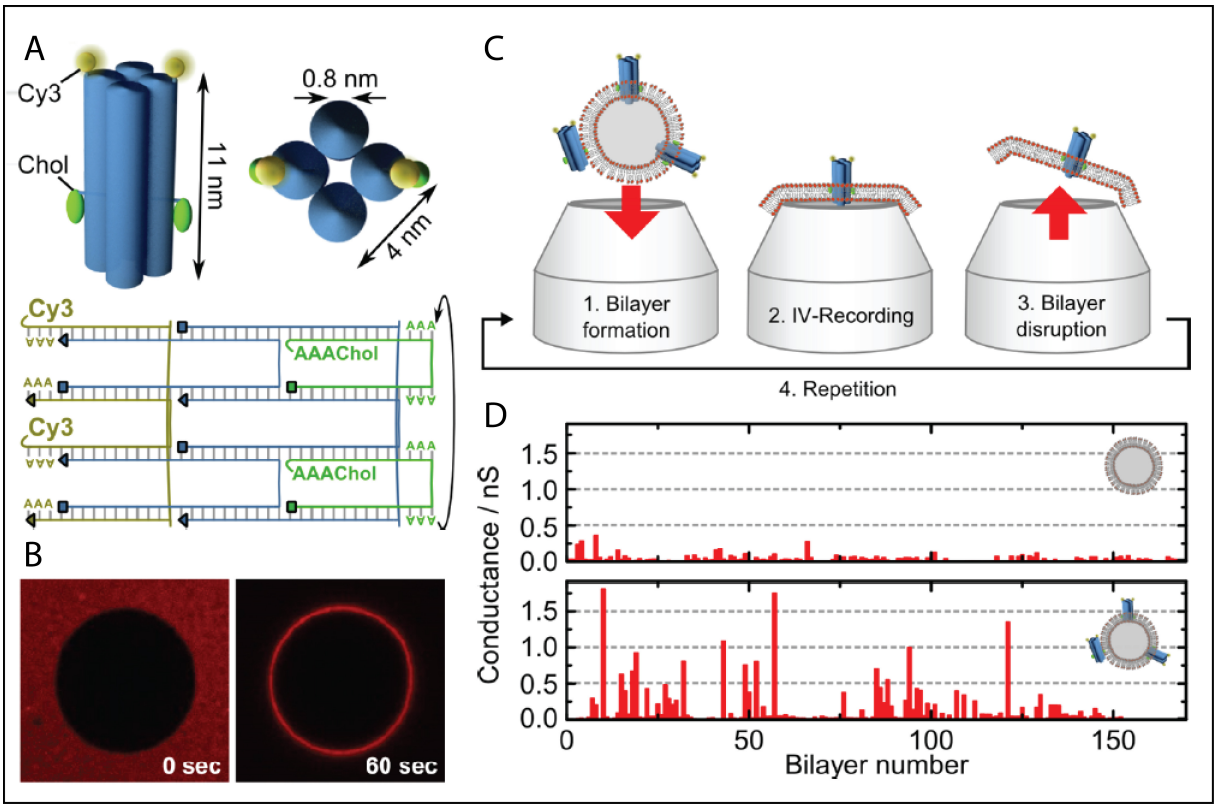

Figure 3.3: DNA tile-based membrane channels for ion conductivity. A) 4-helix DNA nanotubes carrying cholesterol molecules and Cy3 dyes. B) Giant unilamellar vesicle imaged in fluorescence mode (ex: 514 nm). C) Illustration of the ionic current measurement protocol on lipid bilayer setup. D) Conductances obtained for 170 independent *IV* recordings of plain GUVs (top) and GUVs with DNA nanotubes (bottom). Reprinted with permission from ref. [104] Copyright 2015 American Chemical Society.

DNA-based nanostructures have been also used to interact with cellular membranes. Burns and co-workers showed that 6-helix DNA nanopores which are modified with ethyl phosphorothioate (EP) groups can be used to target cancer cells [105]. (Figure 3.4A) They showed that these structures interacted with cancer cell membranes and cause cell death by possibly changing the influx/efflux of the critical ions or disrupting the membrane integrity by insertion. In another study, Li and co-workers developed DNA-conjugated gold nanoparticle networks (DNA-AuNP) on the cell membrane as a protective barrier against viral infection [106]. (Figure 3.4B) DNA-based networks inhibited the viral attachment, entry and budding up to 90% efficiency.

3.2 DNA Origami Growth and Clathrin Mimicking on Lipid Membranes

In the following study which the results were published in Associated Publication P3, we studied the hierarchical assembly of DNA origami nanostructure by mimicking the membrane-sculpting protein, clathrin [107]. Clathrin is a protein which forms coated vesicle complexes during endocytosis [87]. In order to mimic the function of clathrin we designed a truncated-Y shaped DNA origami. Upon addition of specific connector staples three of these structures form a trimer as in the formation of clathrin triskelion.

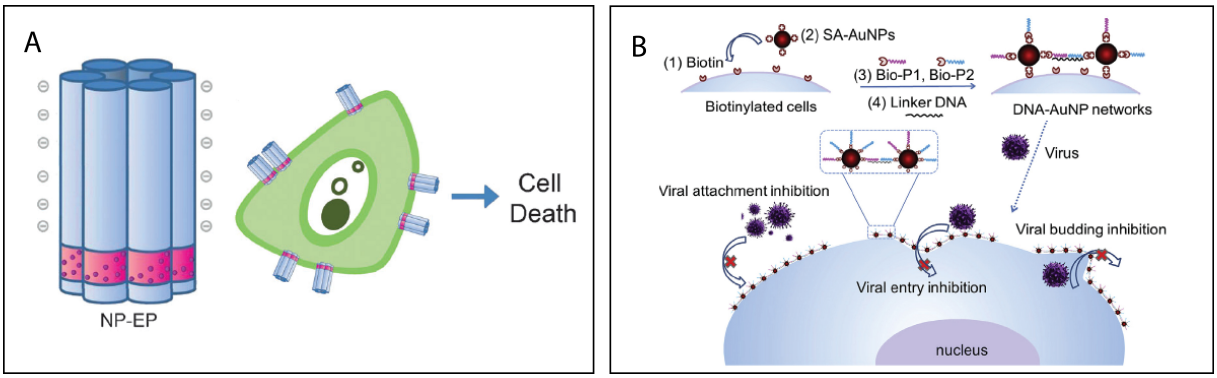

Figure 3.4: DNA nanostructures interact with cellular membranes**.** A) DNA nanopores interact with the membrane of cancer cells and cause cell death. Reprinted with permission from [105]. Copyright 2014 John Wiley and Sons. B) DNA-AuNP networks on the cellular membrane for the protection against viral infection. Reprinted with permission from [106]. Copyright 2016 Elsevier.

In order to understand the dynamics of DNA origami diffusion on the lipid membranes, first we designed a three-layer block origami structure to use as a model structure. Block origami structures were designed in a way that bottom layer was functionalized with 4 cholesterol molecules (Figure 3.5A) while the top layer was functionalized with the flourophore molecules to track the nanostructures using fluorescence microscopy. We realized that the diffusion coefficient of the DNA origami structures is depend on the number of cholesterol anchors and size of the structures. Upon addition of various sets of connector oligonucleotides we could able to grow either one-dimensional or two-dimensional hierarchical structures (Figure 3.5B and C) Here, lipid bilayers provide a two-dimensional confined space that increased the possibility of interaction of single DNA origami structures to form superlattices. We realized that it is not possible to form larger lattices in solution using the same conditions. One of the advantages of these lattices formed on the membranes is that they provide a two-dimensional platform where the proteins could be attached with nanometer spatial resolution for crystallization studies. For that, our lab is currently focusing on the positioning of gold nanoparticles on these DNA origami lattices which will be investigated using small angle x-ray scattering (SAXS).

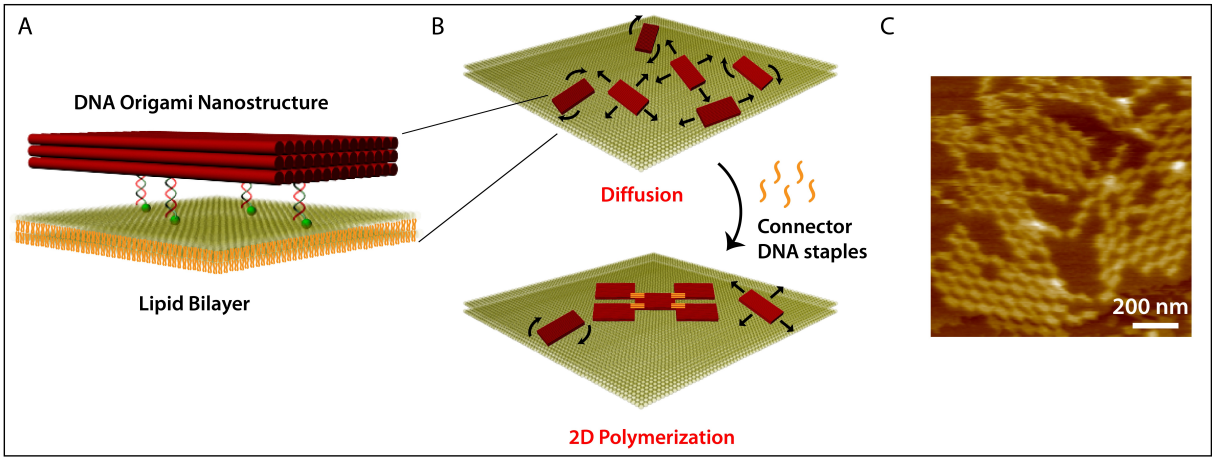

Figure 3.5: DNA origami polymerization on lipid membranes. A) Immobilization of DNA origami nanostructure onto lipid bilayer using 4 cholesterol molecules. B) Two-dimensional polymerization of diffusing DNA origami structures upon addition of connector DNA staples. C) AFM image of DNA origami lattices. Reprinted with permission from [107] Copyright 2015 American Chemical Society.

As mentioned earlier, another objective of the project was to mimic the clathrin using the DNA origami trimers. Upon hybridization on the membrane, the structures freely diffused and formed hexagonal lattices as in the formation of clathrin-coated pits. We also showed that 2D lattices formed by DNA origami structures could bend the membrane of SUVs. (see Associated Publication P2) The bending of the membrane using flat origami structures was also shown by the group of P.Schwille. In this work, they designed a DNA origami brick to investigate the membrane curvature and bending inspired by BAR proteins [108]. They showed that brick-like DNA origami structures can diffuse on freestanding GUV membranes and form 2D scaffolds which can promote deformation of membranes at high surface densities. (Figure 3.6A) DNA nanostructures have also been used recently to study the membrane fusion process of SNARE proteins [109]. (Figure 3.6B) In this study, DNA origami nanorings were designed to use as a template for v-SNARE-tethered SUV formation inside the ring. Formed SUVs then applied to lipid bilayers to study fusion process. With this platform they confirmed at the single molecule level that one to two SNARE pairs are sufficient to enable tethering and subsequent membrane fusion.

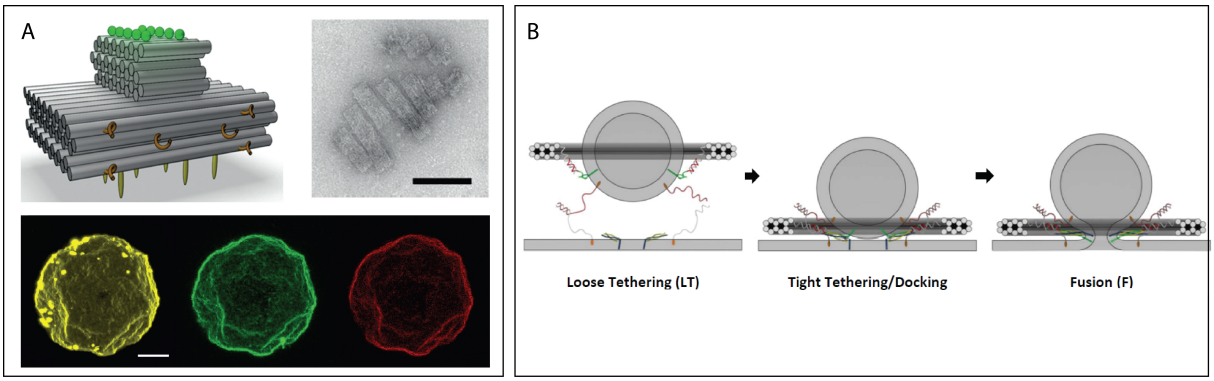

Figure 3.6: DNA nanostructures drive membrane bending and fusion**.** A) Amphiphatic DNA origami bricks labeled with Alexa-488 or Alexa-647 dyes form regular arrays as seen in the TEM image (scale bar: 100 nm) which at high surface densities deform a GUV. Reprinted with permission from [108] Copyright 2015 John Wiley and Sons. B) Templated SUVs fused with SLBs after capture mediated by tethered pairings. Reprinted with permission from [110] Copyright 2016 American Chemical Society.

To summarize, we showed that DNA origami structures can form 2D lattices on the membranes and these lattices can bend the membrane as in the formation of clathrin coated pits. The next step would be the design of curved DNA origami structures in order to shape the lipid membranes more precisely as observed in the membrane fusion processes by clathrin or BAR proteins. Moreover, inspired by these structures more sophisticated designs such as membrane-coated DNA origami vesicles in specific sizes and shapes or mechanical devices that can insert into membranes could be developed to use in drug delivery applications.

3.3 Associated Publication P2

Membrane-Assisted Growth of DNA Origami Nanostructure Arrays

by

Samet Kocabey, Susanne Kempter, Jonathan List, Yongzheng Xing, Wooli Bae, Daniel Schiffels, William M. Shih, Friedrich C. Simmel and Tim Liedl

published in

ACS Nano 2015, 9(4), 3530-39

Membrane-Assisted Growth of DNA Origami Nanostructure Arrays

Samet Kocabey,[†] Susanne Kempter,[†] Jonathan List,[‡] Yongzheng Xing,[†] Wooli Bae,[†] Daniel Schiffels,[†] William M. Shih,[§,∥] Friedrich C. Simmel,[‡] and Tim Liedl*[,†]

[†]Fakultät für Physik and Center for Nanoscience, Ludwig-Maximilians-Universität, Geschwister-Scholl-Platz 1, 80539 München, Germany, [‡]Physik-Department, Technische Universität München, Am Coulombwall 4a, 85748 Garching, Germany, and [§]Wyss Institute for Biologically Inspired Engineering and [∥]Biological Chemistry and Molecular Pharmacology, Harvard Medical School, Boston, Massachusetts 02115, United States

ABSTRACT Biological membranes fulfill many important tasks within living organisms. In addition to separating cellular volumes, membranes confine the space available to membrane-associated proteins to two dimensions (2D), which greatly increases their probability to interact with each other and assemble into multiprotein complexes. We here employed two DNA origami structures functionalized with cholesterol moieties as membrane anchors—a three-layered rectangular block and a Y-shaped DNA structure—to mimic membrane-assisted assembly into hierarchical superstructures on supported lipid bilayers and small unilamellar vesicles. As designed, the DNA constructs adhered to the lipid bilayers mediated by the cholesterol anchors and diffused freely in 2D with diffusion coefficients depending on their size and number of cholesterol modifications. Different sets of multimerization oligonucleotides added to bilayer-bound origami block structures induced the growth of either linear polymers or two-dimensional lattices on the membrane. Y-shaped DNA origami structures associated into triskelion homotrimers and further assembled into weakly ordered arrays of hexagons and pentagons, which resembled the geometry of clathrin-coated pits. Our results demonstrate the potential to realize artificial self-assembling systems that mimic the hierarchical formation of polyhedral lattices on cytoplasmic membranes.

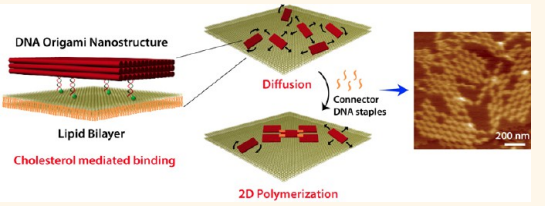

KEYWORDS: DNA origami · DNA nanotechnology · lipid membrane · diffusion · arrays · cholesterol · clathrin

Many of the cellular functions and processes such as trafficking of nutrients, compartmentalization, control of metabolic pathways, immune responses, cell adhesion, and transmembrane charge separation are mediated by the dynamic assembly of membrane-associated protein clusters.[1−3] The proteins clathrin and caveolin, for example, facilitate the formation of intracellular transport vesicles by forming self-assembled complexes upon receptor activation during endocytosis.[4,5] Other transmembrane proteins such as the FAS receptor, which can assemble into the death inducing signal complex, can trigger intracellular signaling pathways upon ligand-activated multimerization.[6,7] All these processes require the orchestrated interaction between various components, which is greatly facilitated through their lateral diffusion and two-dimensional confinement within the lipid membranes of the cells. In a different context, light-induced catalysis of water splitting in plants and bacteria relies on the concerted assembly of many active components into light-harvesting complexes within lipid bilayer membranes.[8,9] In chloroplasts, the membrane between the lumen and stroma fulfills several crucial roles to support efficient photosynthetic charge separation. In addition to the reduction of space and dimensions available to the reactants involved in photosynthesis, it acts as an efficient barrier for charges after they have been pumped across the membrane. Furthermore, it helps to organize the components of the photosynthetic complex with the correct orientation with respect to each other and the surrounding compartments in the first place.

In order to mimic and potentially utilize similar membrane-localized self-assembly mechanisms for nanotechnology applications, we here study the assembly of membrane-bound DNA nanostructures that are inspired by and modeled after membrane-associated protein complexes. DNA nanotechnology allows the construction of arbitrarily shaped objects at the same length scale as protein complexes, which can be

* Address correspondence to tim.liedl@physik.lmu.de.

Received for review January 9, 2015 and accepted March 3, 2015.

Published online March 03, 2015
10.1021/acsnano.5b00161

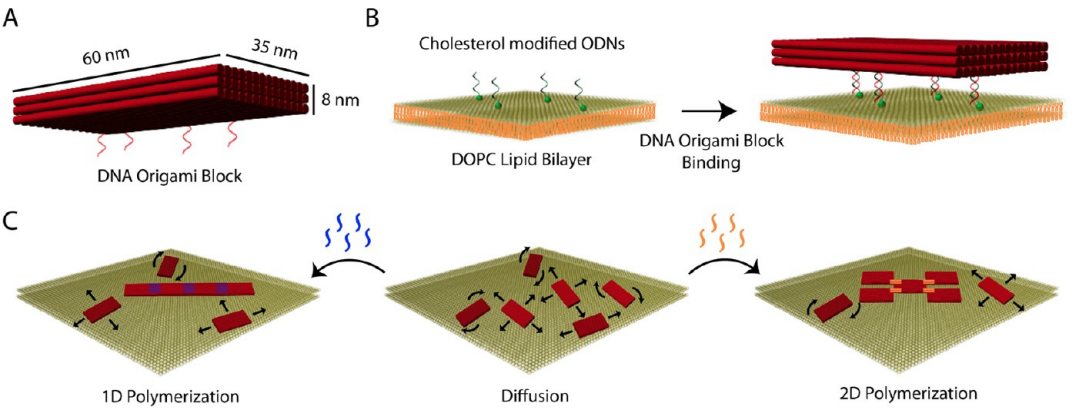

Figure 1. DNA origami block on lipid membrane. (A) DNA origami block structure consisting of three layers of 14 double helices each. The indicated dimensions assume a distance between the base pairs of 0.34 nm and an average distance between the centers of the helices of 2.5 nm. (B) Cholesterol-mediated binding of origami blocks to a lipid bilayer membrane (ODN: oligodeoxynucleotide; DOPC: 1,2-dioleoyl-*sn*-glycero-3-phosphocholine). (C) Programmed polymerization of DNA origami blocks into different superstructures following the addition of connector staples to structures diffusing on the membrane.

easily modified with organic molecules with nanometer precision, defined orientation, and fully controlled stoichiometry. Membrane-encapsulated DNA nanostructures and membrane-spanning DNA nanopores have already been constructed and have been introduced into artificial bilayers by functionalizing these DNA structures with hydrophobic moieties such as cholesterol, ethyl phosphorothioate, or porphyrin.[10−13]

Several characteristics of lipid bilayer membranes are particularly attractive for nanoscale assembly: membranes are extended, quasi two-dimensional structures, which naturally divide space into "cis" and "trans" membrane regions. This confers the possibility to create asymmetric assemblies with different components bound to only one side of a membrane or to embed transmembrane structures in distinct orientations. In addition, the flexibility and fluidity of lipid membranes facilitate the creation of potential nonplanar assemblies, which can change shape or dynamically assemble and disassemble. We here utilize these features to achieve hierarchical organization of DNA nanoobjects into extended superstructures on supported lipid bilayers (SLBs) and on small unilamellar vesicles (SUVs). We characterize the resulting dynamic assemblies by video fluorescence microscopy and high-speed atomic force microscopy (AFM) imaging.

In fact, until now only a few examples of DNA self-assembly across scales have been presented[14−17] even though many fields of research could benefit from large, self-assembled superstructures of molecules ordered in a defined orientation. For example, arrays of optically active subwavelength metamolecules could exhibit novel optical properties,[18] and molecular catalysts inserted into ion-impermeable membranes and assembled with light-funneling nanostructures could be used to create novel photocatalytic systems. Also structural biology could benefit from the arrangement of transmembrane proteins into two-dimensional lattices, which could ultimately be investigated in grazing incident X-ray experiments. Two important steps toward the realization of such applications are the orientation-controlled grafting of molecularly programmable building blocks in and on fluid membranes[19−22] and their subsequent assembly into superstructures of defined geometry.

RESULTS AND DISCUSSION

We built and studied two DNA origami structures: a rectangular, three-layered DNA origami block with dimensions of 60 nm × 35 nm × 8 nm (Figure 1) and a bent DNA origami structure with dimensions of 70 nm × 20 nm × 15 nm that mimics the triskelion assembly of clathrin. Both designs (details can be found in the Supporting Information, Figure S1) allow modification with up to 16 fluorescent dyes and four cholesterol moieties. To this end, we extended staple oligonucleotides with two 18-nt long sequences (anchor sequences), which are complementary to those of a cholesterol-TEG-labeled oligonucleotide and an Alexa488-labeled oligonucleotide (Figure 1A).

We first focus on the block structure in order to illustrate the basic principles of our approach. The three-layered DNA origami block was created as a sufficiently rigid structure that provided multiple positions for functionalization on its top and bottom layer. Structurally rigid building blocks are a necessary prerequisite for the assembly of extended lattices. This was particularly important in the initial phase of the project, when different lattice geometries were explored also in the absence of a supporting substrate. The positions of the cholesterol anchor extensions were chosen such that they were located close to the four edges of the bottom layer of the DNA origami block while the handle sites for the fluorophores were

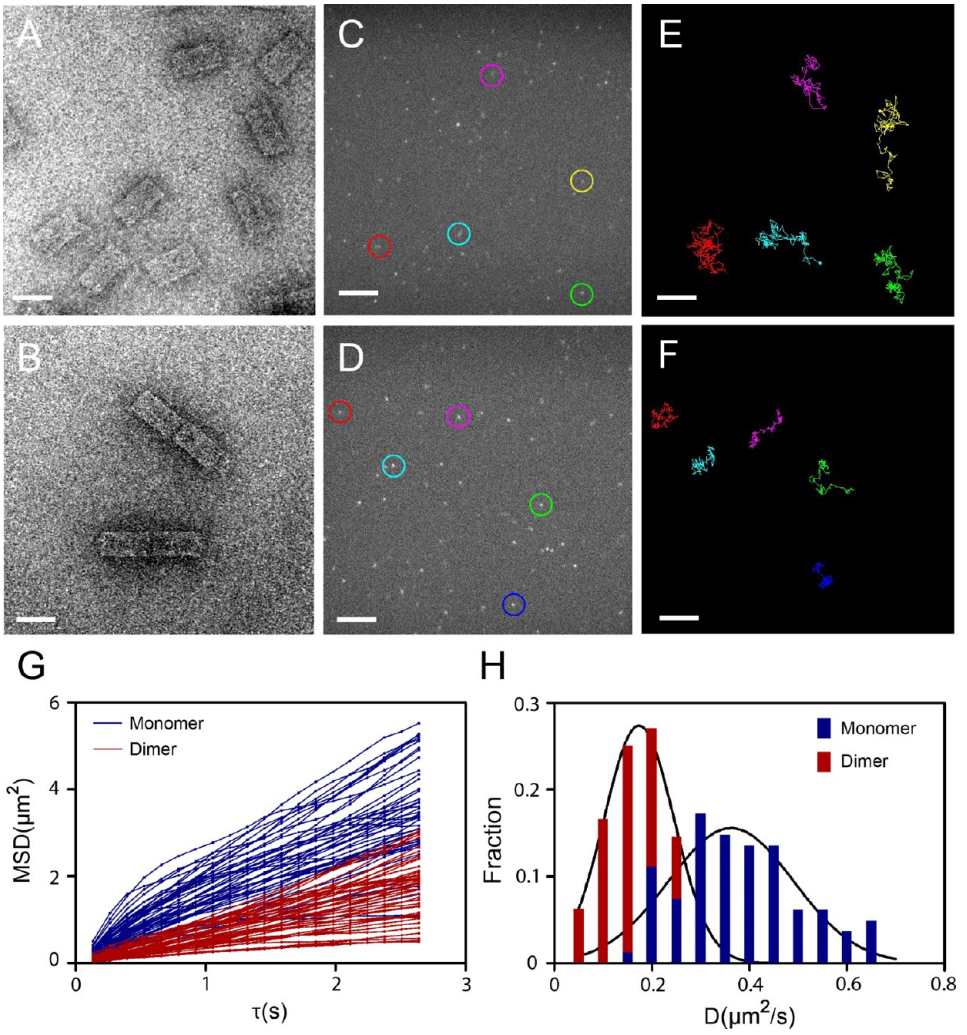

Figure 2. Lateral diffusion of origami block monomers and dimers on supported lipid bilayers. TEM images of DNA origami block monomers (A) and dimers (B) (scale bars: 50 nm). Fluorescence images of DNA origami block monomers (C) and dimers (D) on a DOPC lipid bilayer (scale bars: 5 μm). Example diffusion trajectories for five block monomers (E) and five dimers (F) (scale bars: 5 μm). (G) Time-dependent mean-square displacement (MSD) plot of monomers and dimers. (H) Distribution of diffusion coefficients obtained from single-particle tracking of origami block monomers and dimers. The black lines are Gaussian fits to the distributions.

evenly distributed over the top layer. First, we tested the assembly of DNA origami blocks in the presence of cholesterol-TEG-modified oligonucleotides. Cholesterol-modified structures have a strong tendency to form aggregates in aqueous solutions due to their hydrophobic interactions; in fact, the critical micelle concentration of cholesterol in solution is 25 to 40 nM,[23] which is below the concentration of cholesterol-modified DNA (>100 nM) in our assembly. Agarose gel analysis shows that the origami blocks that were modified with only two cholesterol moieties formed dimers and higher order aggregates (Supporting Information, Figure S2). For this reason, we folded the structures without cholesterol-modified strands and instead incorporated the cholesterol-bearing oligonucleotides into the lipid membrane during formation of the SLB as described below and in Figure 1B. For the sequence-controlled multimerization of the DNA structures we made use of a specific feature of DNA origami designs: single-stranded scaffold loops at the edges of origami structures can be cross-linked by appropriately chosen "multimerization staples", which results in the formation of long chains or structures extended in two dimensions.[14,24−28] In our origami block design we introduced sticky ends to induce end-to-end polymerization in one dimension and a corner-to-corner connection for the formation of a two-dimensional lattice where the nine helices of the front right corner of one block connect to the distant left corner of the next block and *vice versa*, as depicted in Figure 1A and C. DNA origami block dimers were fabricated by fusing two single DNA origami blocks using 12 staple strands as explained in the Supporting Information Figures S3 and S4. Agarose gel analysis and transmission electron microscopy (TEM) revealed the assembly of DNA

origami blocks (Figure 2A and Figure S5) and origami block dimers (Figure 2B and Figure S5) at high yields (93% and 94%, respectively).

To observe grafting of the DNA origami blocks and their subsequent lateral diffusion on artificial lipid membranes by fluorescence microscopy, we prepared lipid bilayers from a 99:1 mixture of 1,2-dioleoyl-*sn*-glycero-3-phosphocholine (DOPC) and 1,1′-dioctadecyl-3,3,3′,3′-tetramethylindodicarbocyanine perchlorate (DiD) inside a microscopy slide flow chamber (Sticky-Slide VI$^{0.4}$, Ibidi; *cf.* Materials and Methods). We then flushed a solution containing the cholesterol-modified oligonucleotides through the channel and incubated it for 1 h. The flow chamber was mounted on an inverted fluorescence microscope to image the membrane and the fluorescently labeled DNA structures that specifically hybridized to the cholesterol-anchored DNA handles. The fluidity of the bilayer was assessed in fluorescence recovery after photobleaching (FRAP) experiments with Texas Red-labeled 1,2-dihexadecanoyl-*sn*-glycero-3-phosphoethanolamine (DHPE) that was introduced at 1% into the membrane (Figure S6). Observation of diffusing DNA origami structures that were specifically attached to the cholesterol handles was crucially dependent on buffer composition. Divalent ions had to be omitted entirely, as the DNA structures stopped diffusing already at low Mg^{2+} concentrations, which we assume is a result of the DNA structures sticking to the glass substrate underneath the bilayer. We thus applied the DNA origami structures (10 pM) to the microscopic chamber in a HEPES buffer (10 mM, pH 7.6) containing only monovalent cations (150 mM NaCl). After 1 h of incubation and several washing steps, we observed adherence and two-dimensional diffusion of DNA origami structures in membranes that were prepared with the cholesterol handles (Figure 2C and D, Supplementary Movies S1 and S2). In control experiments with lipid membranes that lacked such cholesterol handles, in contrast, DNA structures did not adhere and the fluorescent objects moved in and out of the focal plane instead. Membrane-adherent particles were tracked with image analysis software, and 2D diffusion maps were generated as shown in Figure 2E and F. Analysis of single-particle tracks revealed that ~80% of the monomers (n = 748) and dimers (n = 762) were diffusing on the membrane, while the other particles remained stationary. Subdiffraction-sized holes in the membrane may account for the immobile objects, as DNA structures that encounter such a hole will permanently stick to the subjacent substrate.

In order to quantify the diffusive motion of DNA origami block monomers (Figure 2C and E) and dimers (Figure 2D and F) —each modified with either four or eight cholesterol handles—in DOPC lipid membranes, we tracked 84 single particles and 50 dimer particles over time. Examples of particle trajectories obtained from the sequential analysis of 200 frames are presented in Figure 2E and F. From these tracks we extracted the mean square displacement (MSD) of the particles over time using the two-dimensional diffusion equation $\langle \Delta x^2 \rangle = 4D\tau^{\alpha}$. Localization errors were accounted for by applying a confinement offset.[29] The resulting MSD plots displayed in Figure 2G reveal an almost linear increase over time for all tracked particles with a slight tendency for subdiffusional behavior, which may be attributed to occasional defects in the lipid bilayer. We then calculated the diffusion constant of single particles and plotted their relative frequency over D (Figure 2H). The average diffusion coefficients of the DNA origami block monomers were found to be $D_{M,4Chl} = 0.4 \pm 0.1\ \mu m^2/s$ ($\alpha_{M,\ 4Chl} = 0.9 \pm 0.1$, n = 84) and $D_{M,8Chl} = 0.26 \pm 0.1\ \mu m^2/s$ ($\alpha_{M,8Chl} = 1 \pm 0.1$, n = 49) for four and eight cholesterol anchors, respectively, while the dimer assemblies yielded $D_{D,4Chl} = 0.3 \pm 0.1\ \mu m^2/s$ ($\alpha_{D,4Chl} = 0.9 \pm 0.1$, n = 48) and $D_{D,8Chl} = 0.2 \pm 0.1\ \mu m^2/s$ ($\alpha_{D,8Chl} = 1 \pm 0.1$, n = 50). These values are in reasonable agreement with previous experiments, which were performed using other origami shapes and different experimental conditions. Single-particle tracking of single-layered rectangular DNA origami sheets on SLBs previously resulted in a diffusion coefficient of $D = 0.7\ \mu m^2/s$.[18] In fluorescence correlation spectroscopy experiments, DNA origami six-helix bundles were found to diffuse on lipid bilayer vesicles with a larger $D = 1.39\ \mu m^2/s$,[19] which may be expected for a membrane in which both lipid layers are fluid.

The standard theoretical model describing the diffusion of objects inside a lipid membrane originally developed by Saffman and Delbrück[30] cannot be directly applied to our experiments, as the DNA structures float on top of the membrane and only a finite number of anchoring cholesterols actually reside within the membrane. On the other hand, the Stokes–Einstein model for objects floating freely in solution predicts diffusion coefficients more than an order of magnitude larger than the observed values. This discrepancy indicates that the drag of the surrounding fluid is negligible and it is indeed the membrane that governs the behavior. Previous studies found that the frictional contributions of few lipid anchors that are coupled but well separated act additively. This is in good agreement with our observation that the measured diffusion constants of DNA structures that carry four cholesterol anchors are almost twice as large as those of the same structures with eight cholesterol anchors.[31,32]

Next, we tested the polymerization of DNA origami blocks on supported lipid bilayers. We used different sets of staples to polymerize DNA origami blocks either into 1D or 2D arrays (*cf.* Figure 1 and Figure S7). Multimerization staples were added to the fluid chamber 1 h after adsorption of the DNA origami blocks on

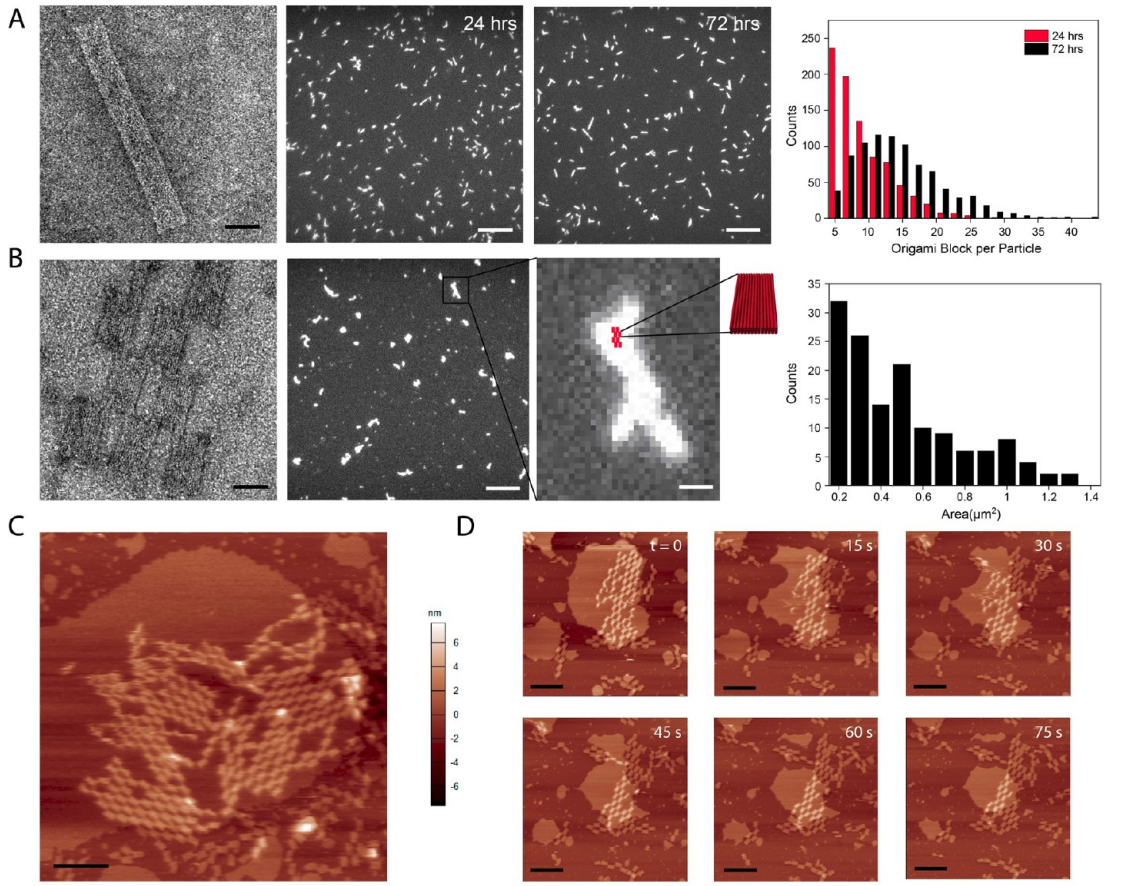

Figure 3. Programmable polymerization of DNA origami blocks on supported lipid bilayers. (A) One-dimensional polymerization. Left: TEM image of polymerized origami blocks after 24 h of incubation in TE buffer with 11 mM Mg^{2+} (scale bar: 50 nm). Middle: Fluorescence images of polymerized origami blocks after 24 and 72 h of incubation on DOPC lipid bilayers (scale bar: 5 μm). Right: Histogram of the estimated number of origami blocks per fluorescent particle after 24 and 72 h of incubation. (B) Two-dimensional polymerization. Left: TEM image of polymerized DNA origami blocks after 24 h of incubation in TE buffer with 11 mM Mg^{2+} (scale bar: 40 nm). Middle: Fluorescence image of polymerized DNA origami blocks after 72 h of incubation (scale bar: 5 μm). Inset: Magnified image of one of the particles including a scheme of a 2D origami lattice for size comparison (scale bar: 400 nm). Right: Histogram of the area of the lattices after 72 h of incubation. (C) AFM image demonstrating lattice formation on the lipid bilayer (scale bar: 300 nm, scan rate: 10 Hz, 512 × 512 pixels). (D) AFM images showing the decomposition of a lipid bilayer over a time interval of 75 s, which results in the adsorption of an origami lattice on the mica surface (scale bar: 300 nm, scan rate: 10 Hz, 1024 × 1024 pixels).

the DOPC lipid bilayer and after rigorous washing to flush out monomers that were not yet anchored to the membrane. In fluorescence images taken after 24 and 72 h of incubation time polymers of DNA origami blocks of submicrometer up to 1.5 μm (24 h) and 2.8 μm (72 h) length became visible (Figure 3A). The length distribution would be expected to follow a single exponential for 1D polymerization processes with fixed k_{on} and k_{off} rates if a constant supply of monomers were present in the chambers. Indeed, for the initial phase of the experiment (up to 24 h) we observe an approximately exponential length distribution (Figure 3A). Due to monomer depletion, however, the growth processes stalled and the final length histogram at 72 h deviates from an exponential. Note that we subsumed all particle sizes below the diffraction limit of the fluorescence microscope (~300 nm) into a single histogram bin. It is also noteworthy that we still observed rotational and lateral diffusion of the polymerized DNA origami blocks (Figure S8).

In order to form 2D arrays with the DNA origami blocks we employed a set of staples that pairwise connected the diagonally opposing corners of a block (*cf.* Figure 1 and Figure S9). When the monomer structures were incubated with the multimerization staples without the support of SLBs, TEM images revealed the formation of arrays containing ~10 monomers (Figure 3B). Even the addition of fresh monomers to the solution did not dramatically increase the size of the resulting arrays. In contrast, when the structures were incubated on the SLBs, the fluorescence images showed the formation of extended structures on the micrometer scale (Figure 3B). The area of the largest structure observed corresponds to an assembly of approximately 200 block monomers. High-speed AFM imaging on supported bilayers prepared on mica confirmed our assumptions. For this we

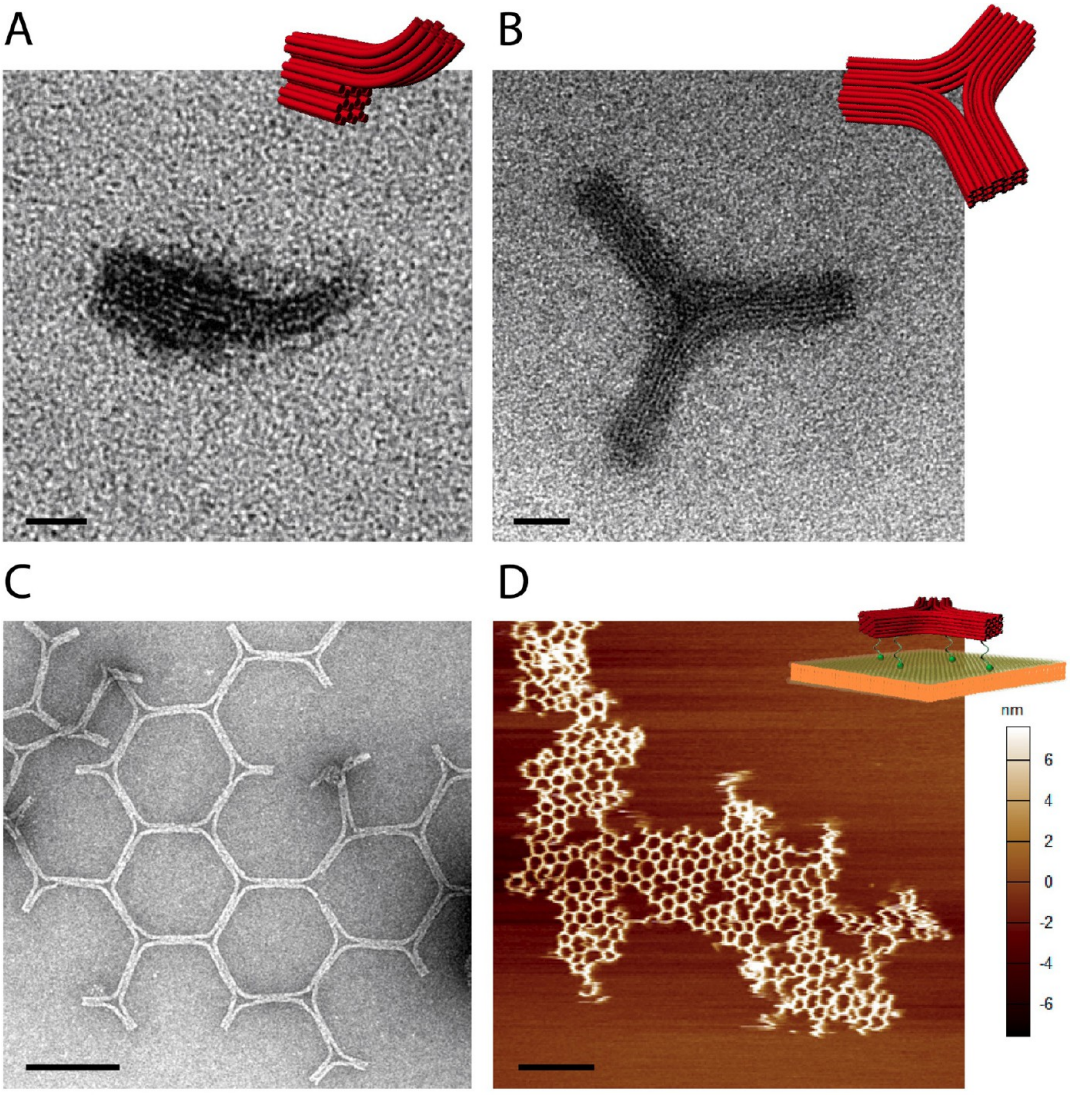

Figure 4. Programmable polymerization of DNA origami triskelions. (A) TEM image of a truncated Y-shaped DNA origami (scale bar: 20 nm). (B) TEM image of a triskelion DNA origami assembled from three truncated Y structures (scale bar: 20 nm). (C) TEM image showing the polymerization of DNA origami triskelions into hexagonal lattices in solution (scale bar: 200 nm). (D) AFM image demonstrating extended polymerization of DNA origami trimers into 2D arrays on supported lipid bilayer (scale bar: 2 μm, scan rate: 4 Hz, 1024 $\times$ 1024 pixels).

prepared lipid bilayers on a mica surface using a solution containing DOPC SUVs in water (*cf.* Materials and Methods). After binding of the DNA origami blocks on the bilayers and overnight incubation, we imaged the samples under various buffer conditions. Imaging in a "low-salt" HEPES buffer containing 150 mM NaCl was not successful, as the origami structures appeared to be too mobile and were pushed around on the bilayer by the AFM cantilever. In order to electrostatically fix the structures on the SLBs, we used an imaging buffer containing high concentrations of $MgCl_2$ (125 mM $MgCl_2$, 400 mM Tris, 200 mM acetic acid, and 10 mM EDTA, pH 8.5), which enabled the observation of DNA block arrays of up to 2 μm in diameter (Figure 3C). Arrays formed in solution, in contrast, were less ordered and far smaller in size (Figure S10). Even at such excessive Mg^{2+} concentrations, DNA nanostructures were still mobile on the mica-supported lipid bilayer during imaging. This resulted in a comparatively low imaging resolution, especially for arrays that were not immobilized at the edges of the bilayer patches. By contrast, DNA arrays touching the underlying mica substrate did not move. As an example, in Figure 3D a time-lapse image series is shown in which a DNA array has initially formed on top of a lipid bilayer. We speculate that due to the high $MgCl_2$ concentration and the repetitive imaging of the same area, the lipid bilayer is partly destroyed and thereby the substrate exposed, this way immobilizing the DNA lattice on the mica surface. At lower $MgCl_2$ concentrations, however, the lipid bilayer stayed intact over several imaging cycles (Figure S11).

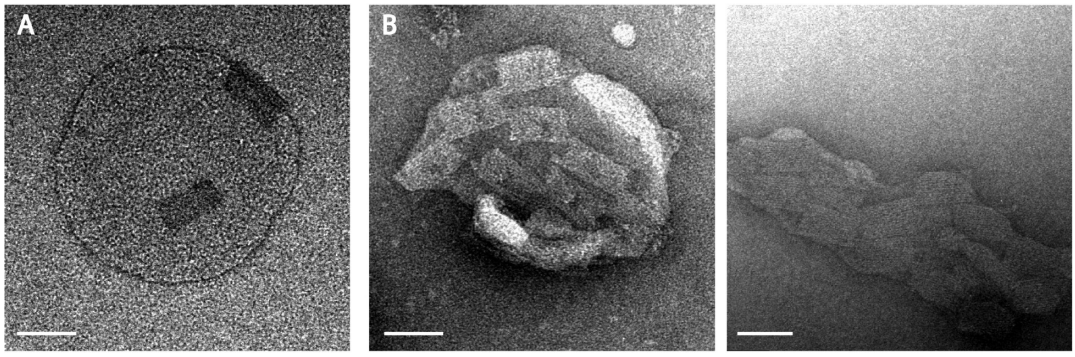

Figure 5. DNA origami block polymerization on SUVs. (A) TEM image of DNA origami block monomers on an SUV (scale bar: 60 nm). (B) 2D lattice formation of the DNA origami blocks on SUVs (scale bars: 60 nm). Interactions between origami lattices and SUVs apparently result in a shape deformation or even destruction of the vesicles.

To further illustrate the potential of our approach to mimic cellular self-assembly processes on artificial lipid bilayer membranes, we designed a second DNA origami structure that is inspired by the protein clathrin.[4] This protein has a three-legged shape (triskelion) and helps to bud off vesicles from the plasma membrane for internalization of molecules that adhered to a cell. The three arms of the triskelion form a 120° angle with respect to each other and furthermore bend slightly out of plane. During membrane budding, the clathrin molecules shape round vesicles by assembling into polyhedral networks consisting of pentagonal and hexagonal rings, the so-called clathrin-coated pits. Our DNA structure has the approximate shape of the letter Y, in which one of the arms has been truncated (Figure 4A). The remaining arm forms a 60° angle[25,33] with the vertical line, and the tip of this arm can be connected with a set of "trimerization" oligonucleotides to the recess of the truncated arm. Three truncated Y's thus form a homotrimer with three legs arranged in 3-fold rotational symmetry (Figure 4B). Upon addition of a set of multimerization oligonucleotides that connect these legs to each other, the homotrimers in turn can assemble into hexagonal arrays (Figure 4C). As the DNA-based structures still have some degree of angular flexibility, also the occasional formation of pentamers can be observed (Figure S12). When we anchored preassembled trimers *via* cholesterol linkers to SLBs on mica and then added the multimerization oligonucleotides, we were able to image arrays consisting of hexamers and pentamers that were several micrometers in diameter (Figure 4D).

Finally, we tested the formation of DNA origami lattices on SUVs in suspension. Following a standard SUV preparation protocol[34] involving tip sonication and extrusion, we obtained SUVs of up to 300 nm in diameter (Figure S13). We first incubated these SUVs with the cholesterol-modified oligonucleotides (HEPES buffer, 150 mM NaCl, pH 7.6) for 15 min, followed by incubation with DNA origami blocks for 1 h. TEM imaging revealed successful binding of DNA origami block monomers to the SUVs (Figure 5A). Subsequent addition of array-forming connector staples led to the formation of 2D array patches on the SUVs. TEM images suggest DNA origami-induced shape deformation of the SUVs, but further studies are required (Figure 5B).

CONCLUSIONS

In this study we explored cholesterol-mediated binding and diffusion of DNA origami structures on supported lipid bilayer membranes and utilized it to create hierarchical assemblies and arrays of such structures with sizes of several micrometers. We found that the measured diffusion coefficients of the individual membrane-anchored DNA structures scale both with the size of the object and with the number of cholesterol anchors that couple the objects to the lipid bilayers, which indicates that the coupled cholesterol moieties are spaced far enough apart to allow free draining of the lipid molecules in between. Importantly, the orientation of the DNA structures with respect to the bilayer is well-defined, as the anchoring is mediated exclusively through DNA anchors that extend from the DNA origami structures on a defined side and couple to cholesterol molecules embedded in the membrane. This predefined orientation of the objects and their confinement to diffuse in 2D allowed the growth of DNA origami arrays that were an order of magnitude larger than those assembled in solution and afterward deposited on a substrate. Arrays of oriented nanostructures tethered to artificial lipid bilayers could be employed to spatially order membrane-associated proteins in their native environment, which could help to study their structural properties with cryo-electron microscopy or X-ray diffraction methods. Moreover, we found that when the arrays were assembled on membranes of small unilamellar vesicles, the binding interactions appeared to be even strong enough to promote the deformation of these SUVs. Our results encourage us to

believe that it will be possible to build DNA objects that mimic biological building blocks such as clathrin or caveolin that play a crucial role in endocytotic processes.

MATERIALS AND METHODS

Preparation of DNA Origami Blocks and Triskelions. All unmodified DNA staple strands (HPSF purified) and dye-modified oligonucleotides (HPLC purified) were purchased from Eurofins MWG Operon (Ebersberg, Germany) (see the Supporting Information, Tables 1 and 2 for sequences) Cholesterol-modified DNA (HPLC purified) was purchased from Biomers (Ulm, Germany). DNA origami structures were designed using caDNAno[35] and prepared by mixing 10 nM M13 based dsDNA scaffold (p8064 for the block structure[36] and p7560 for the origami triskelion) with unmodified staple strands (100 nM each) and 1 μM fluorescently modified staple strands in 1× TE-Mg^{2+} buffer (10 mM Tris-HCl, 1 mM EDTA, 16 mM $MgCl_2$, pH 8.0). In the experiments, between 5 and 16 of the unmodified staple strands were extended at the 3′-end to facilitate hybridization of a fluorescently modified oligonucleotide (5′-Alexa488-GGAAGTTGATATGGTTGATG-3′) to the DNA origami structures. Either four or eight of the unmodified staple strands were extended at the 5′-end to enable hybridization to a cholesterol-modified oligonucleotide (5′-GGTAGTAATAGGAGAATG-CholTEG-3′). The solution was heated to 80 °C for 5 min, cooled to 65 °C over the course of 15 min, and cooled further to 25 °C in 16 h.

Purification and Characterization of DNA Origami Structures. Excess staple strands were removed from DNA origami blocks by agarose gel purification. For this 0.7% agarose was dissolved in 0.5× TBE buffer (pH 8.2) by heating until boiling. $MgCl_2$ (11 mM) was added after cooling, and the solution was poured into a gel cask for solidification. A 200 μL amount of sample solution containing the assembled DNA origami structures and excess staple strands was mixed with 40 μL of 6× loading dye and then loaded into the gel pockets. The gel was run for 2 h at 70 V in an ice-cold water bath to prevent heat-induced denaturation of DNA origami structures. After running, the corresponding band for fluorescently labeled DNA origami structures was cut out from the gel with a razor blade and extracted from the gel by running through spin columns (Freeze'n Squeeze spin columns, Biorad) at 8000*g* for 7 min. The typical concentration of DNA origami structures was 2 nM.

To characterize assembled DNA origami structures, samples were imaged using a JEM-1011 transmission electron microscope (JEOL). DNA origami structures were incubated on argon plasma-exposed (24 W for 1 min) Formvar/carbon-coated grids and then negatively stained with 1% uranyl acetate for 15 s.

Preparation of Lipid Bilayers and DNA Origami Structure Binding. 1,2-Dioleoyl-*sn*-glycero- 3-phosphocholine (Avanti Polar Lipids) and 1,1′-dioctadecyl-3,3,3′,3′-tetramethylindodicarbocyanine perchlorate (Life Technologies) were prepared with 25 and 1 mg/mL concentration in chloroform for supported lipid bilayer formation. DOPC and DiD were mixed at a 99:1 (w/w) ratio in a clean glass vial with a final concentration of 1 mg/mL DOPC. This solution was dried with nitrogen flow for 30 min and further dried in a vacuum oven overnight to make sure any trace chloroform was removed. Dried lipid film was resuspended in 1 mL of PBS buffer (pH 7.4) to obtain a 1 mg/mL lipid suspension. A stock of hydrated lipid suspension was stored at 4 °C for at most 2 weeks.

To prepare supported lipid bilayers, the hydrated lipid suspension stock was diluted to 0.1 mg/mL in 1× PBS buffer. A 100 μL portion of this suspension was injected into the fluidic chamber of a six-channel microscopic slide (Sticky Slide VI$^{0.4}$, Ibidi, Germany) and filled up with 1× PBS buffer. After 1 h incubation of lipid vesicles, the suspension was washed with double-distilled Milli-Q water to induce lipid bilayer formation by osmotic pressure and also to remove excess lipid vesicles. Then, 50 μL of 10 nM cholesterol-TEG-modified oligonucleotide was added to the chamber, and the mixture was incubated for 1 h to embed them into the lipid bilayers. A lipid buffer with monovalent cations (10 mM HEPES, 150 mM NaCl, pH 7.6) was used to dilute cholesterol-modified oligonucleotides and for further washing steps.[22] The stability of the DNA origami structures under these conditions was confirmed using TEM imaging and gel electrophoresis (Figure S14). After incubation for 1 h, unbound oligonucleotides were washed away using lipid buffer. Finally, DNA origami structures were added at a concentration of 10 pM.

Fluorescence Microscopy. Fluorescence images of DNA origami blocks were obtained on a fluorescence microscope (Olympus IX71) equipped with a CCD camera (Hamamatsu ORCA II) using a Olympus PlanApo 100×, 1.4 NA oil immersion objective. Lipid bilayer formation was checked at 647−670 nm (Ex/Em) wavelengths, and DNA origami blocks were visualized at 499−519 nm (Ex/Em) wavelengths.

Fluorescence Recovery after Photobleaching. For FRAP analysis, a DOPC-supported lipid bilayer was prepared as described above, but Texas Red-DHPE was used instead of DiD at the same molar ratio (99:1) for the dye labeling. FRAP was performed with a 532 nm laser (20 mW), and a circular bleach spot with a radius of 6.7 μm surrounding the bleached area was used for data collection and analysis. For the analysis, 20 images were acquired with an interval of 500 ms. The first image captured prior to photobleaching was used to calculate the initial fluorescence intensity followed by 19 consecutive images, in which bleaching and recovery were recorded. FRAP data were further processed using the ImageJ "FRAP Analyzer" plugin. The fluorescence signal was normalized to its respective initial fluorescence intensity prior to photobleaching, and the FRAP curve was constructed using the average fluorescence intensities of the recovery images. Then, the FRAP curve was fitted to a one-phase association fit model with the equation

$$f(t) = a + b \times (1 - e^{-\lambda t})$$

with the fit parameters $a = -0.116$, $b = 0.92$, and $\lambda = 0.2798$/s. To calculate the diffusion coefficient (D) for lateral diffusion of lipids within the lipid bilayer, the "characteristic" diffusion time ($\tau_{1/2} = \ln 2/\lambda$) required to recover 50% of the original fluorescence intensity was calculated from the equation above ($\tau_{1/2} = 2.477$ s) and inserted in the following equation:

$$D = 0.224w^2/\tau_{1/2}$$

where w is the radius of the photobleached spot.[37] The diffusion coefficient (D) of the lipid bilayer was found to be 4.1 μm^2/s.

Single-Particle Tracking and Mean Square Displacement Analysis. DNA origami blocks were added at 10 pM final concentration into a fluidic chamber containing a DOPC SLB. After 1 h of incubation, unbound origami structures were washed away using lipid buffer (10 mM HEPES, 150 mM NaCl, pH 7.6). Lateral diffusion of DNA origami blocks was monitored using mercury lamp excitation. To analyze diffusion, 100 frames from the same spot were acquired with 0.132 s exposure time per frame. At least 20 different fields of view were captured for analysis. Time-averaged mean square displacement analysis was performed using the ImageJ software plugin "Manuel Tracking". Only trajectories of the particles remaining within the frame and which could be tracked for all 100 frames (13.2 s) were analyzed.

To analyze the effect of the DNA origami block size on diffusion, we produced DNA origami block dimers from monomers by connecting them from the same side of two origami block monomers. Twelve connector staples were designed in such a way that half of them could bind to single-strand loops at the edge of one origami block, while the other half could bind to the same edge of another origami block. Each pair of connector staples could hybridize together over a length of 10 nt. Tracking and MSD analysis of block dimers were performed as mentioned above. In total, 81 block monomers and 49 block dimers were analyzed.

1D and 2D Polymerization of Membrane-Bound DNA Origami Blocks. To polymerize DNA origami blocks on DOPC-supported bilayers, DNA origami blocks were added into the fluidic chamber at 10 pM final concentration. After 1 h of incubation, connector staples were added at 100 pM final concentration. 1D polymerization was accomplished using 35 connector staples designed in such a way that every staple could bind to the single-stranded scaffold loop at the other end of the same helix (Figure S7). For 2D polymerization, 16 connector staples were designed to connect opposite corners of the structure by sticky end hybridization (Figure S9). Images were taken by fluorescence microscopy after 24 and 72 h of incubation. The characterization of the DNA block polymers was done using ImageJ software.

AFM Imaging. AFM measurements were performed in tapping mode with an Asylum Research Cypher ES and Olympus BioLever minicantilever (0.1 N/m spring constant) driven at its respective resonance frequency around 18 kHz. A DOPC-supported bilayer was formed on the mica surface by mixing a DOPC/DiD (99:1) solution and distilled water in 1:1 ratio directly after cleavage and incubating for at least 30 min at 37 °C. The sample was washed with distilled water to remove excess vesicles. In order to adsorb DNA nanostructures (500 pM) on the SLB and to facilitate the formation of lattices, the same protocol was applied as for the fluorescence microscopy samples on glass, followed by incubation for at least 12 h. The buffer (10 mM HEPES, 150 mM NaCl, pH 7.6) was then exchanged with a solution containing high concentrations of $MgCl_2$ (125 mM $MgCl_2$, 400 mM Tris, 200 mM acetic acid, and 10 mM EDTA, pH 8.5) to fix the DNA nanostructures to the substrate.

TEM Imaging of SUVs. To visualize DNA origami block polymerization on small unilamellar vesicles, a 1 mg/mL DOPC solution in 10 mM HEPES buffer (150 mM NaCl) was sonicated for 15 min with a tip sonicator. Then, a 0.25 mg/mL SUV suspension was mixed with 100 nM cholesterol-modified DNA in the same buffer. Thirty minutes after incubation, 100 pM DNA origami blocks were added. Finally, connector staples were added at 200 pM final concentration and incubated overnight. Samples were imaged using a JEM-1011 transmission electron microscope (JEOL). DNA origami blocks were incubated on argon plasma-exposed (24 W for 1 min) Formvar/carbon-coated grids and then negatively stained with 1% uranyl acetate for 20 s.

Conflict of Interest: The authors declare no competing financial interest.

Acknowledgment. This work was supported by the European Commission under the Seventh Framework Programme (FP7/2007-2013), as part of the Marie Curie Initial Training Network, EScoDNA (No. 317110) and the ERC grant ORCA, agreement n° 336440, and by the DFG through the SFB 1032 (TPA2 and TPA6) and the Cluster of Excellence Nanosystems Initiative Munich. We thank Prof. Deborah K. Fygenson, Alexander M. Maier, Philip Böhm, and Farzad Sekhavati for their help during DNA origami design, SLB experiments, and data analysis.

Supporting Information Available: Nanostructure design schematics, additional data, and oligonucleotide sequences are available as Supporting Information. This material is available free of charge *via* the Internet at http://pubs.acs.org.

REFERENCES AND NOTES

1. Axelrod, D. Lateral Motion of Membrane Proteins and Biological Function. *J. Membr. Biol.* **1983**, *75*, 1–10.
2. Heldin, C. H. Dimerization of Cell Surface Receptors in Signal Transduction. *Cell* **1995**, *80*, 213–223.
3. Lamb, T. D. Gain and Kinetics of Activation in the G-Protein Cascade of Phototransduction. *Proc. Natl. Acad. Sci. U.S.A.* **1996**, *93*, 566–570.
4. Pearse, B. M. Clathrin: A Unique Protein Associated with Intracellular Transfer of Membrane by Coated Vesicles. *Proc. Natl. Acad. Sci. U.S.A.* **1976**, *73*, 1255–1259.
5. Doherty, G. J.; McMahon, H. T. Mechanisms of Endocytosis. *Annu. Rev. Biochem.* **2009**, *78*, 857–902.
6. Kischkel, F. C.; Hellbardt, S.; Behrmann, I.; Germer, M.; Pawlita, M.; Krammer, P. H.; Peter, M. E. Cytotoxicity-Dependent APO-1 (Fas/CD95)-Associated Proteins Form a Death-Inducing Signaling Complex (DISC) with the Receptor. *EMBO J.* **1995**, *14*, 5579–5588.
7. Ashkenazi, A.; Dixit, V. M. Death Receptors: Signaling and Modulation. *Science* **1998**, *281*, 1305–1308.
8. Deisenhofer, J.; Epp, O.; Miki, K.; Huber, R.; Michel, H. X-ray Structure Analysis of a Membrane Protein Complex. *J. Mol. Biol.* **1984**, *180*, 385–398.
9. Liu, Z.; Yan, H.; Wang, K.; Kuang, T.; Zhang, J.; Gui, L.; An, X.; Chang, W. Crystal Structure of Spinach Major Light-Harvesting Complex at 2.72 A Resolution. *Nature* **2004**, *428*, 287–292.
10. Langecker, M.; Arnaut, V.; Martin, T. G.; List, J.; Renner, S.; Mayer, M.; Dietz, H.; Simmel, F. C. Synthetic Lipid Membrane Channels Formed by Designed DNA Nanostructures. *Science* **2012**, *338*, 932–936.
11. Burns, J. R.; Stulz, E.; Howorka, S. Self-Assembled DNA Nanopores That Span Lipid Bilayers. *Nano Lett.* **2013**, *13*, 2351–2356.
12. Burns, J. R.; Gopfrich, K.; Wood, J. W.; Thacker, V. V.; Stulz, E.; Keyser, U. F.; Howorka, S. Lipid-Bilayer-Spanning DNA Nanopores with a Bifunctional Porphyrin Anchor. *Angew. Chem., Int. Ed.* **2013**, *52*, 12069–12072.
13. Perrault, S. D.; Shih, W. M. Virus-Inspired Membrane Encapsulation of DNA Nanostructures to Achieve *in Vivo* Stability. *ACS Nano* **2014**, *8*, 5132–5140.
14. Zheng, J.; Birktoft, J. J.; Chen, Y.; Wang, T.; Sha, R.; Constantinou, P. E.; Ginell, S. L.; Mao, C.; Seeman, N. C. From Molecular to Macroscopic *via* the Rational Design of a Self-Assembled 3D DNA Crystal. *Nature* **2009**, *461*, 74–77.
15. Liu, W.; Zhong, H.; Wang, R.; Seeman, N. C. Crystalline Two-Dimensional DNA-Origami Arrays. *Angew. Chem., Int. Ed.* **2011**, *50*, 264–267.
16. Schreiber, R.; Do, J.; Roller, E.-M.; Zhang, T.; Schuller, V. J.; Nickels, P. C.; Feldmann, J.; Liedl, T. Hierarchical Assembly of Metal Nanoparticles, Quantum Dots and Organic Dyes Using DNA Origami Scaffolds. *Nat. Nanotechnol.* **2014**, *9*, 74–78.
17. Aghebat Rafat, A.; Pirzer, T.; Scheible, M. B.; Kostina, A.; Simmel, F. C. Surface-Assisted Large-Scale Ordering of DNA Origami Tiles. *Angew. Chem., Int. Ed.* **2014**, *53*, 7665–7668.
18. Zheludev, N. I.; Kivshar, Y. S. From Metamaterials to Metadevices. *Nat. Mater.* **2012**, *11*, 917–924.
19. Suzuki, Y.; Endo, M.; Yang, Y.; Sugiyama, H. Dynamic Assembly/Disassembly Processes of Photoresponsive DNA Origami Nanostructures Directly Visualized on a Lipid Membrane Surface. *J. Am. Chem. Soc.* **2014**, *136*, 1714–1717.
20. List, J.; Weber, M.; Simmel, F. C. Hydrophobic Actuation of a DNA Origami Bilayer Structure. *Angew. Chem., Int. Ed.* **2014**, *53*, 4236–4239.
21. Johnson-Buck, A.; Jiang, S.; Yan, H.; Walter, N. G. DNA-Cholesterol Barges as Programmable Membrane-Exploring Agents. *ACS Nano* **2014**, *8*, 5641–5649.
22. Czogalla, A.; Petrov, E. P.; Kauert, D. J.; Uzunova, V.; Zhang, Y.; Seidel, R.; Schwille, P. Switchable Domain Partitioning and Diffusion of DNA Origami Rods on Membranes. *Faraday Discuss.* **2013**, *161*, 31–43.
23. Haberland, M. E.; Reynolds, J. A. Self-Association of Cholesterol in Aqueous Solution. *Proc. Natl. Acad. Sci. U.S.A.* **1973**, *70*, 2313–2316.
24. Douglas, S. M.; Dietz, H.; Liedl, T.; Hogberg, B.; Graf, F.; Shih, W. M. Self-Assembly of DNA into Nanoscale Three-Dimensional Shapes. *Nature* **2009**, *459*, 414–418.
25. Dietz, H.; Douglas, S. M.; Shih, W. M. *Folding DNA into Twisted and Curved Nanoscale Shapes* **2009**, *325*, 725–730.
26. Rothemund, P. W. Folding DNA to Create Nanoscale Shapes and Patterns. *Nature* **2006**, *440*, 297–302.
27. Jungmann, R.; Scheible, M.; Kuzyk, A.; Pardatscher, G.; Castro, C. E.; Simmel, F. C. DNA Origami-Based Nanoribbons: Assembly, Length Distribution, and Twist. *Nanotechnology* **2011**, *22*, 275301.
28. Woo, S.; Rothemund, P. W. Programmable Molecular Recognition Based on the Geometry of DNA Nanostructures. *Nat. Chem.* **2011**, *3*, 620–627.

29. Wieser, S.; Schutz, G. J. Tracking Single Molecules in the Live Cell Plasma Membrane-Do's and Don't's. *Methods* **2008**, *46*, 131–140.
30. Saffman, P. G.; Delbruck, M. Brownian Motion in Biological Membranes. *Proc. Natl. Acad. Sci. U.S.A.* **1975**, *72*, 3111–3113.
31. Knight, J. D.; Lerner, M. G.; Marcano-Velazquez, J. G.; Pastor, R. W.; Falke, J. J. Single Molecule Diffusion of Membrane-Bound Proteins: Window into Lipid Contacts and Bilayer Dynamics. *Biophys. J.* **2010**, *99*, 2879–2887.
32. Tamm, L. K. Lateral Diffusion and Fluorescence Microscope Studies on a Monoclonal Antibody Specifically Bound to Supported Phospholipid Bilayers. *Biochemistry* **1988**, *27*, 1450–1457.
33. Castro, C. E.; Kilchherr, F.; Kim, D. N.; Shiao, E. L.; Wauer, T.; Wortmann, P.; Bathe, M.; Dietz, H. A Primer to Scaffolded DNA Origami. *Nat. Methods* **2011**, *8*, 221–229.
34. Mingeot-Leclercq, M. P.; Deleu, M.; Brasseur, R.; Dufrene, Y. F. Atomic Force Microscopy of Supported Lipid Bilayers. *Nat. Protoc.* **2008**, *3*, 1654–1659.
35. Douglas, S. M.; Marblestone, A. H.; Teerapittayanon, S.; Vazquez, A.; Church, G. M.; Shih, W. M. Rapid Prototyping of 3D DNA-Origami Shapes with caDNAno. *Nucleic Acids Res.* **2009**, *37*, 5001–5006.
36. Stein, I. H.; Schuller, V.; Bohm, P.; Tinnefeld, P.; Liedl, T. Single-Molecule FRET Ruler Based on Rigid DNA Origami Blocks. *ChemPhysChem* **2011**, *12*, 689–695.
37. Soumpasis, D. M. Theoretical Analysis of Fluorescence Photobleaching Recovery Experiments. *Biophys. J.* **1983**, *41*, 95–97.

4 DNA-based Nanostructures as Immune-Modulatory Agents *in vivo*

4.1 DNA-based Nanostructures for Immune-Stimulation and Vaccination

DNA based nanostructures can also be used for immune stimulation and vaccination through the hybridization with immunoactive oligonucleotides. In eukaryotic cells, DNA molecules outside of the nucleus or mitochondria are considered as pathogen-associated molecular patterns (PAMPs) which alerts the host cell against pathogen invasion or in the presence of damaged cells around [111, 112]. This induces the activation of innate immune system by the production of pre-inflammatory cytokines which recruit the leukocytes to remove the infectious microbes and clear the damaged cells. One of the main signaling pathways sensing foreign DNA is through unmethylated cytosine-phosphate-guanine (CpG) motifs. These motifs are highly specific to bacterial or viral DNA and rarely found in the mammalian genome are recognized by Toll-like receptor 9 (TLR9) localized in the endosome [113, 114]. Upon interaction with the internalized CpG motif, TLR9 is translocated to endolysosomal complex and activates downstream myeloid differentiation primary response 88 (MYD88)-mediated signaling pathway [115]. The activation of this pathway leads the production of proinflammatory cytokines such as type I interferon (IFN) and interleukin 6 (IL-6) in phagocytic and antigen presenting cells (APCs). For this reason, synthetic oligonucleotides containing CpG motifs are commonly used as vaccine adjuvants to improve APC funtion and co-administered with antigens to induce adaptive immune system for the therapy of cancer, allergy and infectious diseases [116].

Since DNA nanostructures are more stable in compare to free oligonucleotides, several groups have developed DNA carriers decorated with CpG motifs. Takakura et al. developed Y-shaped DNA structure consisted of 3 CpG motifs where the halves of each ODN are partially complementary to the half of the other 2 ODNs [117]. These structures induced increased amount of tumor necrosis factor α (TNF- α) and IL-6 in macrophage-like RAW264.7 cells compared to the single stranded or double stranded ODNs due to the increased amount of uptake by the cells. More branched structures such as polypod-like and dendrimer-like structures or rolling circle amplification (RCA) products with high CpG density showed the further enhanced efficiency of immune stimulation *in vitro* [118-120]. (Figure 4.1A and B) Schüller et al. showed that 30-helix DNA origami tubes covered with 62 individual CpG sequences induced the immune response in freshly isolated spleen cells especially when the CpG motifs partially phosphorothioate (PTO) modified [121]. (Figure 4.1C) It is highlighted that DNA origami tubes carrying CpG motifs induced higher IL-6, IL-12 and C-type lectin 69 (CD69) expression in compare to bare DNA origami structures and free oligonucleotides with CpG or GpC motifs. Liu et al. showed for the first time in vivo application of a DNA tetrahedron containing CpG motifs [122]. (Figure 4.1D) Functionalization of biotinylated CpG sequences with a model antigen, phycoerythrin-conjugated streptavidin a synthetic vaccine construct was developed. Immunization of the mices with this constructs showed the enhanced antibody production over time.

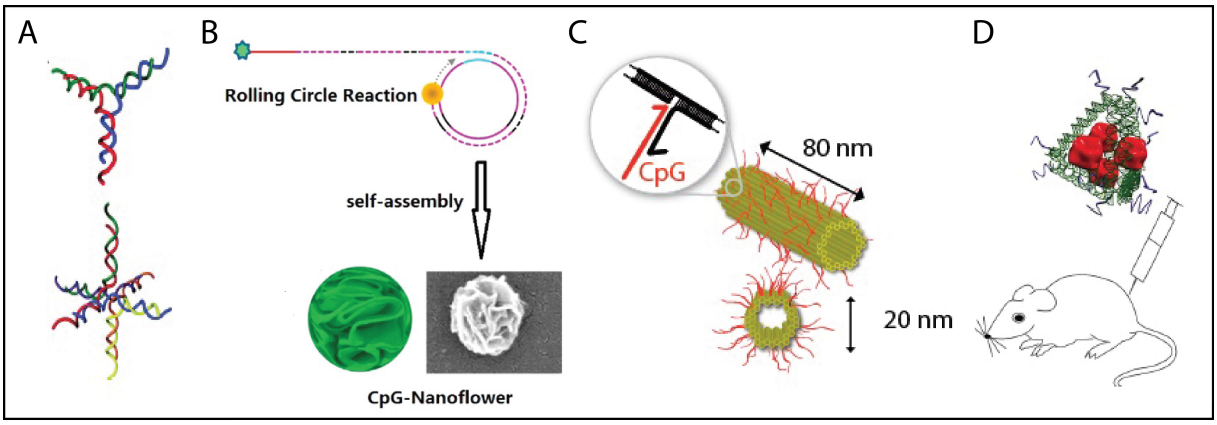

Figure 4.1: Immune stimulation by CpG ODNs using various DNA nanostructure designs. A) Polypod-like DNA nanostructures with 3 or 6 CpG oligonucleotides per particle. Reprinted with permission from [118] Copyright 2012 American Chemical Society. B) CpG nanoflower self-assembled from RCA reaction. Reprinted with permission from [120] Copyright 2015 American Chemical Society. C) DNA origami tube-like structure decorated with 62 CpG oligonucleotides. Reprinted with permission from [121] Copyright 2011 American Chemical Society. D) CpG-ODN containing DNA tetrahedron-vaccine complex for *in vivo* immune stimulation. Reprinted with permission from [122] Copyright 2012 American Chemical Society.

4.2 CpG-Decorated DNA Nanotubes as Immune-Stimulatory Agents *in vivo*

In this study, we investigated the effect of DNA nanotubes carrying CpG sequences in real time using in vivo microscopy where the results were presented in associated publication P3.[1] 8-helix DNA nanotubes were formed using single stranded tile assembly method as seen in the electron micrograph image. (Figure 4.2A and B) To investigate the uptake and inflammation in vivo microscopy setup was used as depicted in Figure 4.2C. DNA nanostructures were microinjected locally to the cremaster muscle of the anesthetized mice. (Figure 4.2D) The initiation of the inflammatory response is started upon the uptake of the DNA nanostructures by tissue macrophages or mast cells. The uptake of the structures by these cells was seen in Figure 4.2E. These cells then release pro-inflammatory cytokines that results with the activation of the endothelial cells.

[1] Portions of Chapter 4.2 is reprinted (adapted) with permission from Sellner, S., Kocabey, S., Nekolla, K., Krombach, F., Liedl, T., and Rehberg, M. DNA Nanotubes as Intracellular Delivery Vehicles *in vivo*. Biomaterials, 2015, 53, 453-463. Copyright 2015 Elsevier. Contributions to the Chapter 4.2 were as follows: DNA nanostructure design and characterization experiments were performed by S.K. and supervised by T.L. Microinjection of DNA nanostructures into anesthesized mice, flourescence microscopy experiments and leukocyte recruitment analysis were performed by S.S. and supervised by M.R. The images used in Figure 4.2 C-E and Figure 4.3 B were kindly adapted from S.S and M.R.

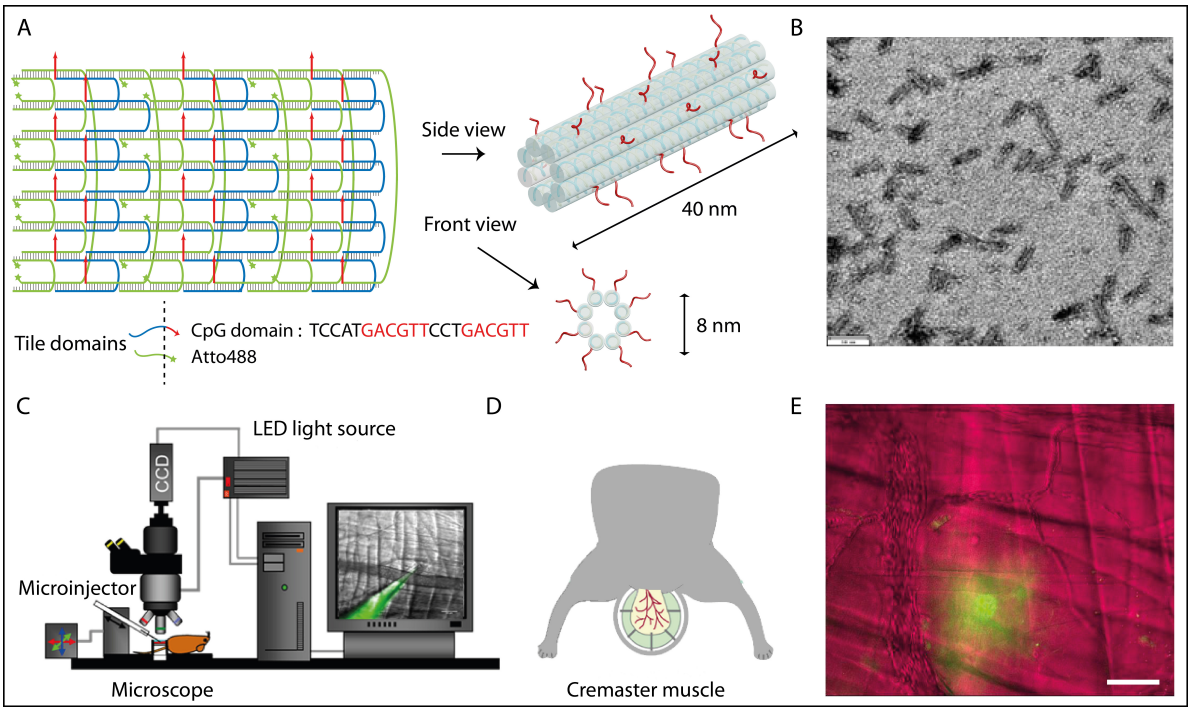

Figure 4.2: Injection of CpG decorated DNA nanotubes. A) Design of 8-helix nanotubes with CpG motifs. B) TEM image of CpG nanotubes. (scale bar: 50 nm) C) Microscopy setup. D) Cremaster muscle of the mice. E) Distribution of Atto-488 labeled CpG nanotubes around the muscle tissue. (scale bar: 50 μm)

Leukocytes are regularly rolling inside the blood vessels via continuous binding and unbinding of the selectins to their glycosilated ligands expressed on the endothelial cells [123]. When the cytokines released by tissue macrophages they bind to the cytokine receptors of the endothelial cells located in the basement membrane and this mediates the activation of rolling leukocytes to arrest and strong adhesion on the endothelium. (Figure 4.3A) The adhesion of the leukocytes is regulated by the expression of integrins and vascular cell adhesion molecules (VCAMs) which is the result of G-protein coupled receptors (GPCRs)-triggered signaling by cytokines [124, 125]. In the last step, strongly adhered leukocytes extend membrane protrusions into the endothelial cell bodies and cell junctions by expressing several adhesion molecules such as intercellular cell adhesion molecule 1 (ICAM1) and platelet/endothelial cell adhesion molecule 1 (PECAM1) which trigger paracellular or transcelluar migration to the tissue side [126, 127]. In our experiments, the leukocyte recruitment was investigated by counting the adhered and transmigrated cells in 100 μm^2 area including the both sides of the blood vessel. (Figure 4.3B) (ipsilateral: is the area next to the injection side, contralateral: the opposite side of the vessel) We observed that DNA nanostructures were rapidly uptaken by tissue macrophages and localized in the endosome which induce the release of cytokines to activate rolling leukocytes. The number of adhered and transmigrated leukocytes were significantly higher for CpG nanotubes in compare the plain nanotubes and CpG oligonucleotides. As mentioned also in previous section, CpG-mediated TLR9 activation induces MYD88-mediated signaling pathway which results in the acetylation and translocation of p65, a subunit of the NF-κB transcription factor complex, to the nucleus to start NF-κB pro-inflammatory gene expression. (Figure 4.3C) In our

experiments, immunohistochemistry results showed that only CpG decorated DNA nanotubes showed the p65 translocation which is the indicator of NF-κB activation.

It is important to note that the *in vivo* conditions are totally different than the *in vitro* conditions which tile-based DNA nanotubes are tested for the uptake experiments in section 2.2 although the same tile assembly method was used to fold 8-helix tubes for CpG delivery experiments. The stability experiments for CpG nanotubes were performed by considering the DNAse concentration and distribution over the muscle tissue. In these conditions, by incubating DNA nanotubes in the DNAse containing buffer and the diluted mice serum we observed that the structures are stable at least for 2 hrs. Moreover, the structures were rapidly uptaken by tissue resident macrophages and CpG mediated inflammation and leukocyte recruitment was clearly showed.

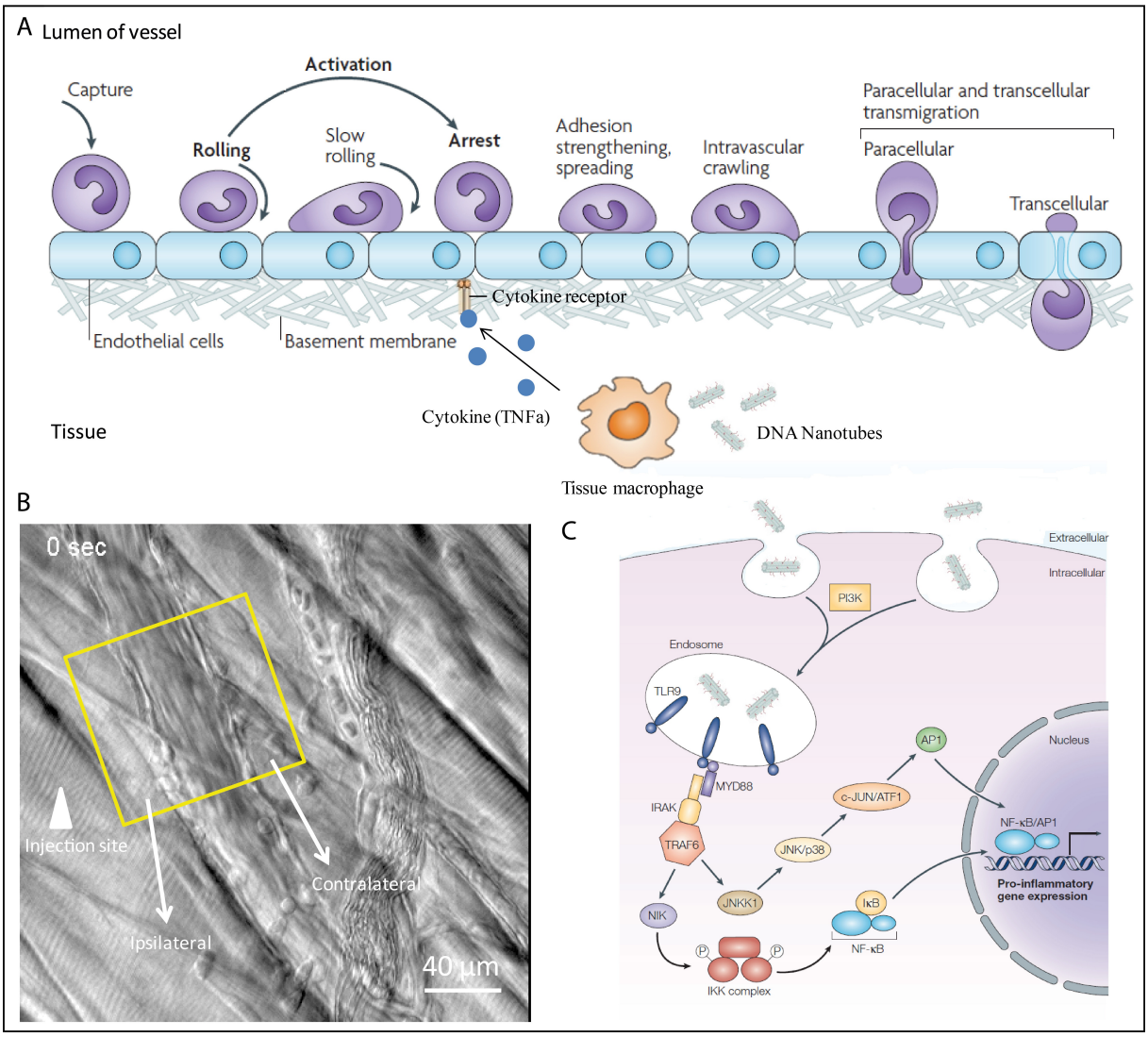

Figure 4.3: CpG mediated leukocyte recruitment and NF-κB activation. A) Leukocyte rolling and adhesion cascade. Reprinted with permission from [123] B) The area showing the leukocytes adhered and transmigrated to the both sides of the blood vessel. C) CpG nanotube-TLR9 mediated cell signaling. Reprinted with permission from [116] Copyright 2004 Nature Publishing group.

To summarize, we demonstrated an efficient delivery system using CpG decorated DNA nanotubes in vivo. Using this approach, we showed that tissue macrophages could be targeted and leukocyte recruitment could be induced in a really short time. Most importantly, the elevation of inflammation is only possible by the conjugation of CpG sequences on the structure, plain nanotubes do not induce inflammation.

4.3 Dexamethasone-Conjugated DNA Nanotubes as Anti-Inflammatory Agents *in vivo*

The balance of the immune system is severely important for the host system during the abnormal auto-immune responses. In this kind of cases, the manipulation of the immune system could be required with an external agent. The ease of fabrication of DNA-based nanostructures allow designing of such agents to use as drug carriers. The synthetic glucocorticoid drug known as dexamethasone is commonly used to treat inflammatory and autoimmune disorders such as rheumatoid arthritis, asthma and severe allergies [128, 129]. It has the ability to penetrate into cell nuclei via intracellular glucocorticoid receptors thereby suppressing immune response by binding to glucocorticoid responsive elements (GREs) [130, 131].

In this study, we investigated the effect of dexamethasone conjugated DNA nanotubes in real time using in vivo microscopy. We designed 6-helix DNA nanotubes using single stranded tile assembly method where each tile has 21 base-long domains to hybridize with 4 adjacent tiles. (Figure 4.4A) Longer single stranded tiles were used in order to increase the stability and resistance to low Mg conditions as discussed in the section 2.2. As illustrated in the Figure 4.4A, dexamethasone was conjugated to the nanotubes using i-motif sequence. The electon micrograph image shows the folded structure in figure 4.4B. The i-motif structure is a four-stranded DNA structure that can be formed in sequences contain stretches of cytosine residues [132, 133]. In this structure, when the pH is low, cytosines are protonated and form noncanonical base pairs with an unprotonated cytosine which leads the formation of quadruple helix. This motif is commonly used for pH-dependent dynamic studies and drug delivery applications. Krishnan group recently showed that i-motif based DNA nanodevices could be used to map temporal pH changes during endosomal maturation in living cells [59, 134]. Our purpose was the use of this pH dependent release mechanism to increase the rate of endosomal escape in the macrophages to induce the anti-inflammatory responses.

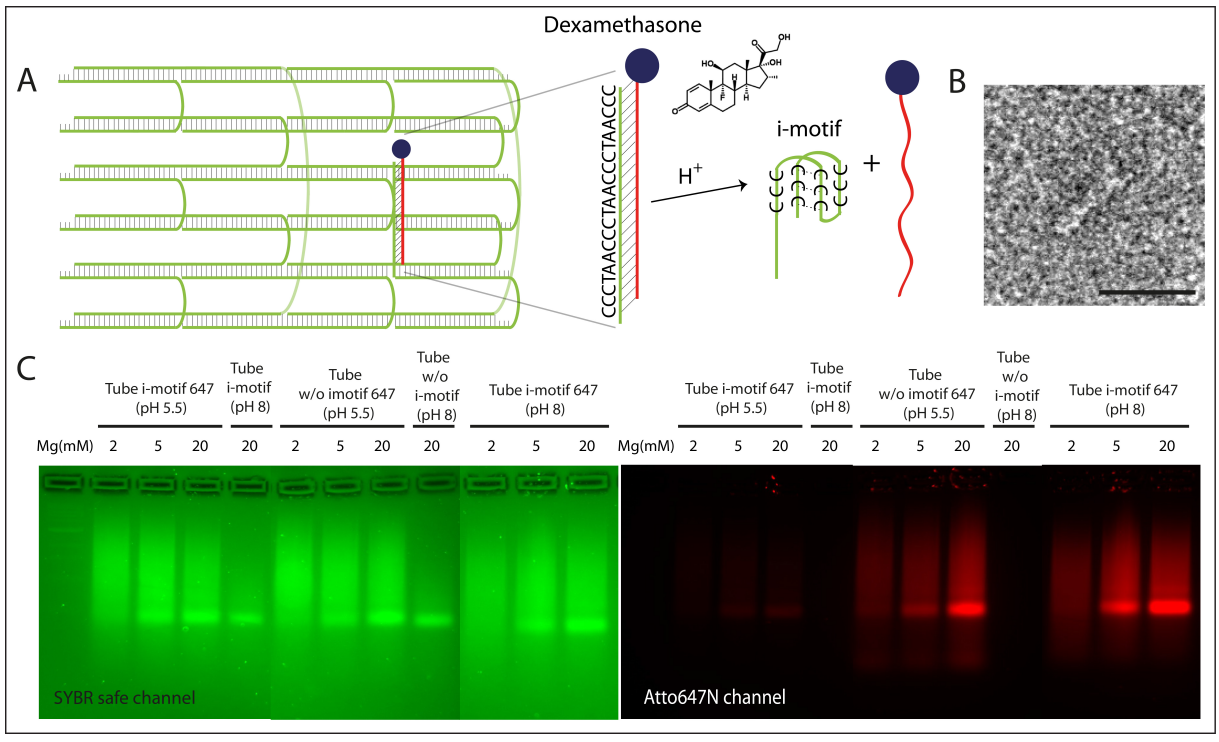

Figure 4.4: Dexamethasone conjugated DNA nanotubes. A) 6-helix DNA nanotube design carrying i-motif sequence and i-motif dependent release mechanism of dexamethasone conjugated ssDNA oligonucleotide. B) TEM image of a single DNA nanotube. (Scale bar: 30 nm) C) Gel analysis showing i-motif dependent release of the hybridized oligonucleotides labeled with Alexa647N at pH 5.5 at 37 °C.

First we showed that pH dependent release mechanism is working at pH 5.5 only when the nanotubes are carrying i-motif sequence. (Figure 4.4C) It is important to note that the structures were incubated and filtered at physiological temperature, 37 °C, in order to observe the release of dye-modified oligonucleotides. Then, we investigated the anti-inflammatory effect of the nanotubes using the injection method shown in section 3.2. DNA nanotubes were similarly uptaken by tissue macrophages and localized in the endosome. The number of adhered and transmigrated leukocytes was decreased for the nanotubes conjugated with dexamethasone via i-motif sequence in compare to the plain nanotubes, nanotubes without i-motif sequence and dexamethasone conjugated ODNs that were not folded into structure. (Figure 4.5) The anti-inflammatory effect, particularly the number of transmigrated leukocytes, for dexamethasone-conjugated nanotubes was almost similar with the treatment of high dose dexamethasone (1 µg/ml), which demonstrates the potential of DNA-based drug carriers with targeting molecules.

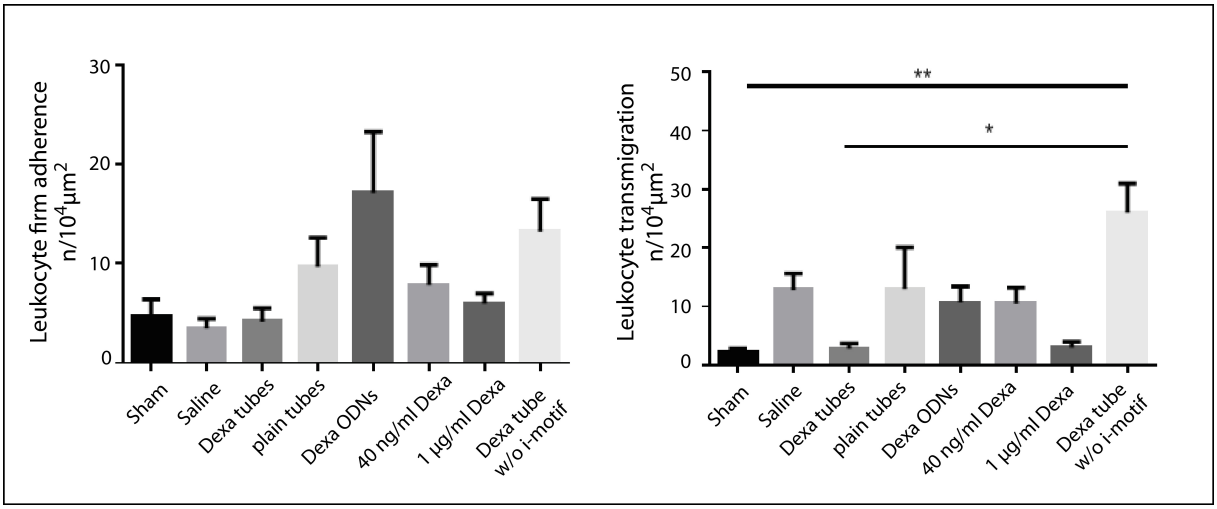

Figure 4.5: Quantitative analysis of intravascular adherence and transmigration of leukocytes after microinjection of DNA nanotubes. Leukocyte adherence and transmigration were quantified in postcapillary venules in the cremaster muscle using *in vivo* transillumination microscopy at 60 min upon microinjection of Dexa tubes, plain tubes, Dexa ODNs, Dexa tubes w/o imotif, dexamethasone or saline into postischemic cremaster tissue at onset of reperfusion.

It has been shown that Dexamethasone mediates the immunosuppressive effect by inhibiting the recruitment of leukocytes [135]. In order to understand the mechanism behind the inhibition of leukocyte recruitment we checked the expression levels of several cellular adhesion molecules such as VCAM and PECAM [136]. Immunohistochemistry analysis showed that expression levels of these cell adhesion molecules were significantly decreased for dexamethasone conjugated nanotubes in compare to the other controls. (Figure 4.6)

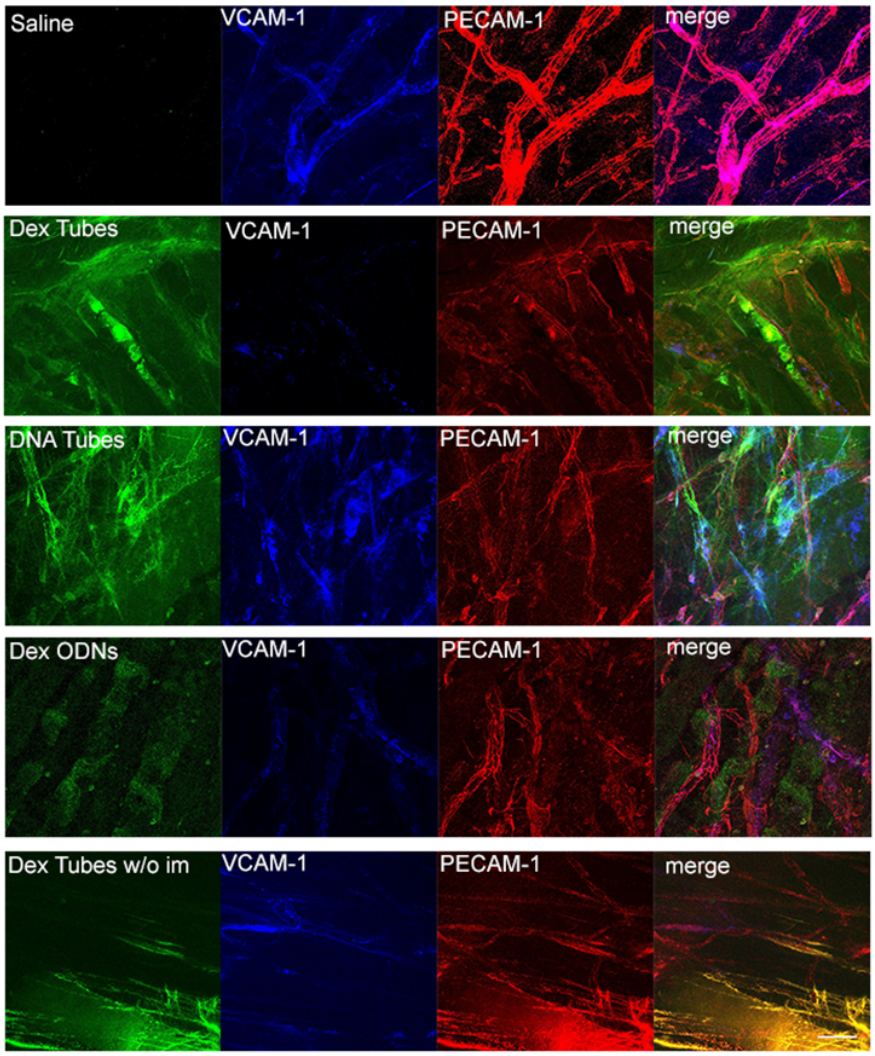

Figure 4.6: Expression patterns of VCAM-1 after the treatment of DNA nanotubes into postischemic cremaster tissue. Confocal immunofluorescence of DNA nanotubes (green), VCAM-1 (blue), and PECAM-1 (red) showed significant lower VCAM-1 signal in vessels next to the injection site of Dexamethasone conjugated DNA nanotubes compared to saline after the treatment. Injection of DNA tubes, Dexamethasone DNA nanotubes w/o i-motif as well as of Dexa-ODNs into the cremaster tissue led to equivalent VCAM-1 expression levels 60 min after the treatment. Scale bar: 50 µm.

In summary, we demonstrated the effective use of DNA nanotubes as drug carriers to inhibit the inflammation *in vivo*.[2] The conjugation of dexamethasone to the nanotubes and i-motif dependent release from the structures were successfully indicated. Although endosomal escape of dexamethasone could not be proven *in vivo* by using confocal microscopy, the quantitative data clearly indicates that dexamethasone conjugated DNA nanotubes effectively blocked the recruitment of leukocytes by inhibiting the expression of cell adhesion molecules on the endothelial cells.

[2] Portions of Chapter 4.3 is reprinted (adapted) with permission from Sellner, S., Kocabey, S., Zhang, T., Nekolla, K., Hutten, S., Krombach, F., Liedl, T., and Rehberg, M. Dexamethasone-conjugated DNA nanotubes as anti-inflammatory agents *in vivo*. (manuscript in revision) Contributions to the Chapter 4.3 were as follows: DNA nanostructure design and i-motif dependent release experiments were performed by S.K. and supervised by T.L. Microinjection of DNA nanostructures into anesthesized mice, flourescence microscopy experiments and leukocyte recruitment analysis were performed by S.S. and supervised by M.R. The images used in Figure 4.5 and Figure 4.6 were kindly adapted from S.S and M.R.

4.4 Associated Publication P3

DNA Nanotubes as Intracellular Delivery Vehicles *in vivo*

by

Sabine Sellner*, Samet Kocabey*, Katharina Nekolla, Fritz Krombach,

Tim Liedl and Markus Rehberg

*equal contribution

published in

Biomaterials 2015, 53, 453-463

Biomaterials 53 (2015) 453–463

Contents lists available at ScienceDirect

Biomaterials

journal homepage: www.elsevier.com/locate/biomaterials

DNA nanotubes as intracellular delivery vehicles *in vivo*

Sabine Sellner [a, 1], Samet Kocabey [b, 1], Katharina Nekolla [a], Fritz Krombach [a], Tim Liedl [b], Markus Rehberg [a, *]

[a] Walter Brendel Centre of Experimental Medicine, Ludwig-Maximilians-Universität München, Marchioninistr. 15, 81377 Munich, Germany
[b] Department of Physics & Center for NanoScience, Ludwig-Maximilians-Universität München, Geschwister-Scholl-Platz 1, 80539 Munich, Germany

ARTICLE INFO

Article history:
Received 11 December 2014
Received in revised form
19 February 2015
Accepted 21 February 2015
Available online 19 March 2015

Keywords:
DNA nanotechnology
Self assembly
Single stranded tile
Delivery
CpG
Macrophage

ABSTRACT

DNA-based nanoconstructs possess great potential for biomedical applications. However, the *in vivo* behavior of such constructs at the microscopic tissue/cell level as well as their inflammatory potential is largely unknown.

Unmethylated CpG sequences of DNA are recognized by Toll-like receptor 9 (TLR9), and thus initiate an innate immune response. In this study, we investigated the use of DNA-based nanotubes as carrier systems for CpG delivery and their effect on immune cells *in vivo* and in real time. DNA nanotubes were microinjected into skeletal muscle of anesthetized mice. Using *in vivo* microscopy, we observed that the DNA tubes were internalized within minutes by tissue-resident macrophages and localized in their endosomes. Only microinjection of CpG-decorated DNA nanotubes but not of plain DNA nanotubes or CpG oligonucleotides induced a significant recruitment of leukocytes into the muscle tissue as well as activation of the NF-κB pathway in surrounding cells.

These results suggest that DNA nanotubes are promising delivery vehicles to target tissue macrophages, whereupon the immunogenic potential depends on the decoration with CpG oligonucleotides.

1. Introduction

All mammals (and many other living organisms) have developed complex mechanisms to fight off pathogens or foreign substances entering their bodies [1]. Importantly, the physical introduction of the critical substance into the body marks the beginning of an immune response. Despite the fact that our immune system evolved several effective mechanisms against foreign substances, external manipulation and modulation of the immune system is required in the case of severe conditions such as viral and bacterial infections, immune deficiency-related diseases (genetic or acquired, e.g. AIDS), and cancer. Since conventional therapies including the application of cytostatic and (anti)inflammatory drugs mainly act non-specifically and systemically, they might cause serious adverse reactions. In addition, antimicrobial drugs used against infections cause the emergence of drug-resistant pathogens over time. For this reason, functionalized nanoscale carriers have been developed for the targeted delivery of drugs with the aim to reduce the quantity and the adverse reactions of therapeutics [2,3]. After the introduction of the concept of DNA-based nanostructures over three decades ago, the field of DNA nanotechnology has now reached a level where it enables advanced technology in a variety of research fields [4–6]. The use of DNA structures in biological and biomedical studies is particularly promising due to a number of advantages: DNA structures can be modified with a plethora of (bio)chemical moieties with nanoscale precision [7], there is full control over stoichiometry [8,9], they are non-cytotoxic [10,11], they can survive in cell media, blood serum and cultured cells for extended periods of time [12–14] and they can be used as carriers for immune-stimulatory motifs including unmethylated CpG sequences [10,15]. Particularly the recently introduced DNA tile-assembly method [16,17] could foster biomedical applications, as the tile-assembly method is extremely versatile, easy to apply, results in high yields of folded structures, and different than in DNA origami applications, no virus-derived scaffold is needed for assembly of DNA nanotubes.

Unmethylated CpG sequences have immunogenic properties and are used as adjuvant in vaccination [18] or to overcome tumor-associated immunosuppression [19]. These sequences, that are highly specific for bacterial DNA, are recognized by a specialized receptor of the innate immune system localized in the endosome,

* Corresponding author.
E-mail address: markus.rehberg@lrz.uni-muenchen.de (M. Rehberg).
[1] These authors contributed equally to this work.

http://dx.doi.org/10.1016/j.biomaterials.2015.02.099
0142-9612/

the Toll-like receptor 9 (TLR9), causing production and secretion of inflammatory mediators [20,21].

The initiation of an inflammatory response by macrophages - which are phagocytic cells along with monocytes, dendritic cells, and mast cells - is accompanied by the activation of other immune cell populations as well as clearance of cellular debris to maintain tissue homeostasis [22–24]. On the other hand, they contribute to a tumorigenic environment by the release of proangiogenic mediators [25] and suppression of adaptive immunity [26] in cancer-related inflammation. The acute inflammatory response is associated with the release of soluble proinflammatory mediators, e.g. by tissue macrophages or mast cells, resulting in the activation of the endothelium. This includes the expression of endothelial adhesion molecules that facilitate capture and rolling of leukocytes along the vessel wall. Rolling leukocytes are then activated by the interaction with chemokines presented or secreted by endothelial cells leading to arrest and firm adhesion of leukocytes. Subsequently, leukocytes emigrate through the vascular wall into the interstitial tissue [27]. To directly observe this immediate response of immune cells, attracted by chemical signaling in living tissue, can help to understand and circumvent those aspects of the immune system if needed. Since macrophages are major players, not only in inflammatory diseases, but also in antimicrobial defense, autoimmunity, allergy and asthma, antitumor immune responses, tumorigenesis, metabolic disorders, atherosclerosis, fibrosis and wound healing, there is great interest in being able to effectively target these cells [28,29].

In this study we therefore investigated the use of DNA-based nanotubes as carrier systems for CpG sequences *in vivo*. To analyze the uptake of plain as well as CpG sequence-decorated DNA nanotubes by tissue macrophages and to monitor their effect on immune cells in real time, we applied *in vivo* fluorescence microscopy upon local microinjection of DNA nanoconstructs in intact muscle tissue of healthy mice.

2. Materials and methods

2.1. DNA nanotubes

DNA nanotubes were designed using the single stranded tile (SST) method, where each tile oligonucleotide is 42 bases long and consists of four domains with 10 or 11 bases. Each domain is complementary to one domain on the neighboring tiles [17,30]. We designed 8-helix tubes consisting of 48 individual tile oligonucleotides folding into 8 parallel double helices. Tile strands located at the ends of the tube contain non-pairing poly-A sequences in order to prevent sticky end formation and polymerization. For CpG labeling, the 3′ ends of 24 tiles (every second tile in each helices) were extended by 20 bases containing the immune stimulatory CpG motif, GACGTT, twice (CpG 1826: TCCATGACGTTCCTGACGTT). For the control tubes that do not carry the CpG motif, tiles without CpG extension were used. All oligonucleotides were purchased from Eurofins Operon MWG (Ebersberg, Germany) with HPSF purification.

2.2. Enzymatic dye labeling of tiles

To visualize the DNA nanotubes *in vivo*, the 3′ ends of some of the tile strands were enzymatically labeled with Atto488-dUTP or Cy3-dUTP [31]. For this, Atto488-dUTP or Cy3-dUTP (80 μM, purchased from Jena Bioscience, Jena, Germany), $CoCl_2$ (5 mM), terminal transferase enzyme (16 U/μl, Roche, Penzberg, Germany), and all DNA tiles (400 pmol) were mixed in a 20 μl, 1× TdT reaction buffer. The solution was incubated at 37 °C for 30 min. Then, 2.5 μl of NaOAc (3 M) was added and the solution was filled up to 80 μl with ice-cooled ethanol (99%). After 1 h incubation at −20 °C, samples were centrifuged at 13,000 g for 30 min. Then, samples were washed with 70% ethanol for 10 min again and the supernatant was discarded. The remaining pellet was redissolved in distilled water. For CpG-labeled tubes, 24 of the unmodified tiles and for the control tubes, 40 of the core tiles were used for dye labeling. For CpG ODNs, 24 of the tiles with CpG sequence were labeled with dye.

2.3. DNA nanotube assembly and purification

For the annealing of DNA nanotubes, 800 nM of each tile (dye-modified and unmodified) were mixed with folding buffer (10 mM Tris–HCl, 1 mM EDTA, pH 8.0, 20 mM $MgCl_2$). The DNA nanotubes were folded over the course of 16 h (5 min at 80 °C, cooling down to 65 °C at 1 °C/min, cooling down to 25 °C at 2.5 °C/h). The assembled DNA nanotubes were then purified using 30 K Amicon Ultra 0.5 ml centrifuge filters (30,000 MWCO, Millipore, Schwalbach, Germany) in order to remove excess strands that were not folded into the structures. 100 μl of assembled DNA tube solution was mixed with 400 μl of folding buffer, filled into the centrifuge filter, and centrifuged 3 times at 13,000 g for 6 min. After every centrifuge step, the flow-through was removed and the filter was refilled up to 500 μl with buffer. After final centrifugation, the remaining solution at the bottom of the filter (~50 μl) was pipetted out and the concentration of tubes was determined by measuring the optical density at 260 nm. Overall, 50–60 % of the initial amount of DNA nanotubes was obtained after purification.

2.4. Gel electrophoresis and transmission electron microscopy

To analyze DNA nanotubes, the samples were run in an agarose gel. 2% agarose was dissolved in 0.5× TBE buffer by heating to boiling. After cooling, $MgCl_2$ was added to 11 mM final concentration and the solution was poured into a gel cask for solidification. 10 μl of each filter-purified DNA tube sample were mixed with 2 μl of 6× loading dye before loading into the gel pockets. 6 μl of 1 kb ladder was also loaded adjacent to the samples. The gel was run for 2 h at 70 V in an ice-cold water bath to prevent heat induced denaturation of DNA nanotubes. After running, the gel was stained with ethidium bromide (0.5 μg/ml) for 30 min.

DNA nanotubes were visualized by electron microscopy using a JEM-1011 transmission electron microscope (JEOL). The DNA nanotubes were incubated on plasma-exposed (240 kV for 1 min) carbon-coated grids and then negatively stained with 1% uranyl acetate for 15 s.

2.5. Stability of DNA nanotubes

Stability of DNA nanotubes and pUC 18 double stranded plasmid were tested in DNAse I-containing buffer, mice serum and FCS separately. For DNAse I experiments, 50 ng/μl of each sample was incubated in buffer at 37 °C for different time periods. To emulate *in vivo* conditions, the DNAse I concentration was adjusted to 1.97 U × 10^{-4} U/g wet weight [32]. For some experiments, also the mice serum was diluted 37 times to mimic conditions prevalent in the skeletal muscle [32]. The DNA nanotubes were also incubated in pure FCS (not heat-inactivated) for up to 2 h. Zeta potential and size measurements were performed with a Malvern Zetasizer at 100 nM nanotube concentration.

2.6. Animals

Male C57BL/6 mice at the age of 10–12 weeks were purchased from Charles River (Sulzfeld, Germany), MacGreen mice (JAX, Stock Number: 018549) were obtained from The Jackson Laboratory. Animals were housed under conventional conditions with free access to food and water. All experiments were performed according to German legislation for the protection of animals.

2.7. Experimental groups

In a first set of experiments, mice (n = 6 each group) received saline, DNA nanotubes, CpG-decorated DNA nanotubes, or CpG oligonucleotides via microinjection 20 min after the preparation of the cremaster muscle. Additional experiments were performed in mice (n = 6) receiving cromolyn (0.2 mg/kg), an inhibitor of mast cell degranulation, as a bolus via intra-arterial injection 30 min before cremaster preparation and subsequent application of CpG-decorated DNA nanotubes. The animals were randomly assigned to the experimental groups.

2.8. Surgical procedure

The surgical preparation was performed as described by Baez with minor modifications [33]. Briefly, mice were anesthetized by i.p. injection of a ketamine/xylazine mixture (100 mg/kg ketamine and 10 mg/kg xylazine). The left femoral artery was cannulated in a retrograde manner for administration of 2 μm FluoSpheres (Invitrogen, Carlsbad, CA, USA) for measurement of blood flow velocities. The right cremaster muscle was exposed through a ventral incision of the scrotum. The muscle was opened ventrally in a relatively avascular zone, using careful electrocautery to stop any bleeding, and spread over the pedestal of a custom-made microscopy stage. Epididymis and testicle were detached from the cremaster muscle and placed into the abdominal cavity. Throughout the procedure as well as after surgical preparation during *in vivo* microscopy, the muscle was superfused with warm buffered saline. The body temperature was maintained at 37 °C using a heating pad placed under the mouse. After *in vivo* microscopy, tissue samples of the cremaster muscle were prepared for immunohistochemistry. Blood samples were collected by cardiac puncture for the determination of systemic leukocyte counts using a Coulter ACT Counter (Coulter Corp., Miami, FL, USA). Anaesthetized animals were then euthanized by an intra-arterial pentobarbital overdose (Narcoren, Merial, Hallbergmoos, Germany).

2.9. In vivo microscopy

The setup for *in vivo* microscopy was centered around a VisiScope.A1 imaging system (Visitron Systems GmbH, Puchheim, Germany), equipped with an LED light source for fluorescence epi-illumination. For DNA nanotubes or oligonucleotide

excitation the 470 nm or 550 nm LED modules (exposure time 700 ms), and for transillumination the 655 nm LED module (exposure time 10 ms) were used in a fast simultaneous mode. Light was directed onto the specimen via a triple dichroic filter NC316973 (z 405/488/561 rpc; Chroma Technology Corp., Bellows Falls, VT, USA). Microscopic images were obtained with a water dipping objective (20×, NA 1.0). Light from the specimen was separated with a beam splitter (T 580 lpxxr Chroma Technology Corp., Bellows Falls, VT, USA) and acquired with two Rolera EM^2 cameras and VisiView Imaging software (Visitron). Oblique transillumination was obtained by positioning a mirroring surface (reflector) directly below the specimen and tilting its angle relative to the horizontal plane as described previously [34].

2.10. Microinjection of DNA nanotubes and LysoTracker dye

Local administration of 250 ± 100 pl of fluorescently labeled DNA nanotubes (500 nM), CpG-decorated DNA nanotubes (500 nM), CpG oligonucleotides (12 μM), or saline into the cremaster muscle was performed via perivenular microinjection in regions at a distance of 25–75 μm from a postcapillary venule. Venules with diameters ranging between 25 and 35 μm were selected for the experiments. Microinjection was performed under visual control of the intravital microscope, with a long distance air objective (20×, NA 0.4 Olympus), using borosilicate glass micropipettes (GB150TF-8P, Science Products GmbH, Hofheim, Germany) - pulled with a micropipette puller (PC 10, Narishige, London, United Kingdom) - which were connected to the injection system consisting of a micromanipulator (PatchStar Micromanipulator, Scientifica, Uckfield, United Kingdom) and a microinjector (FemtoJet, Eppendorf, Hamburg, Germany). The tip pressure during injection was 3000 hPa and the tip diameter <1 μm. The vessel and the surrounding tissue were visualized during a time period of 1 min at baseline conditions before injection and up to 90 min after injection. For LysoTracker Red DND-99 (Invitrogen, Carlsbad, CA, USA) co-microinjection, the stock solution was diluted to a concentration of 750 nM in saline and further diluted to an end concentration of 75 nM in the respective DNA nanotube sample. Different fluorescent labels (as described above) did not affect the distribution and localization of DNA nanoconstructs.

2.11. Quantification of leukocyte kinetics and microhemodynamic parameters

To quantify the sequential steps of leukocyte extravasation, *in vivo* microscopy records were analyzed offline using ImageJ software (National Institutes of Health, Bethesda, MD). Firmly adherent cells were determined as those resting in the associated blood flow for more than 30 s and related to the luminal surface per 100 μm vessel length. Transmigrated cells were counted in regions of interest, covering 75 μm on both sides of a vessel over 100 μm vessel length, and are presented per 10^4 μm^2. Green fluorescent beads (FluoSpheres 2 μm, Invitrogen, Carlsbad, CA, USA) were injected via the femoral artery catheter and their passage through the vessels of interest was recorded (filter T580lpxxr, LED 470 nm, exposure 50 ms, cycle time 1 min). Centerline blood flow velocity was determined by measuring the progression of free flowing fluorescent beads in subsequent images in the blood stream.

2.12. Immunostaining

To determine NF-κB activation after microinjection of DNA nanotube constructs or CpG ODNs, immunostaining of the cremaster muscle was performed. After dissection, the tissue was fixed with 2% paraformaldehyde for 15 min at room temperature, then blocked and permeabilized in PBS, supplemented with 2% bovine serum albumin (Sigma Aldrich, Munich, Germany) and 0.5% Triton X-100 (Sigma Aldrich, Munich, Germany) for 1 h at room temperature. After incubation with a rabbit anti-mouse anti-NF-κB p65 (acetyl K310) antibody (Abcam, Cambrige, UK) at room temperature for 2 h, the tissue was washed with PBS and incubated with an Alexa-Fluor 546-linked goat anti-rabbit antibody and TO-PRO3®-Iodide (Invitrogen, Carlsbad, CA, USA) for another 2 h at room temperature. Immunostained cremaster muscles were mounted in PermaFlour (Thermo Fisher Scientific Inc, Braunschweig, Germany) on glass slides. For localization of microinjected DNA constructs in Csfr1-EGFP mice as well as colocalization with LysoTracker dye, the dissected cremaster muscle was mounted in a custom-made imaging chamber and immediately viewed. Images were obtained using a Leica SP5 confocal laser-scanning microscope – equipped with a Leica HyD GaAsP hybrid detection system – with an oil-immersion lens (63×; NA 1.40; Leica Microsystems, Wetzlar, Germany), as previously described [35]. Images were processed with ImageJ software and figures for publication were assembled in Photoshop 9 (Adobe Systems, Mountain View, California, US).

2.13. Stimulation of RAW 264.7 cells

RAW 264.7 macrophage-like cells were grown in Gibco DMEM medium (Life technologies, Darmstadt, Germany) supplemented with 10% fetal calf serum (Biochrom, Merck Millipore, Berlin, Germany), 4 mM L-Glutamin and 1 g/L D-Glucose at 37 °C and 5% CO_2. Cells were seeded on 24-well culture plates at a density of 4×10^5 cells and cultivated for 24 h. For stimulation, RAW 264.7 cells were incubated with DNA nanotube constructs or CPG ODNs for 18 h. Culture supernatants were collected and stored at −80 °C for further analysis. Cells were washed and resuspended in DMEM medium, and uptake of DNA constructs and oligonucleotides was visualized using a confocal laser scanning microscope (Leica SP5, Leica Microsystems, Wetzlar, Germany) equipped with a GaAsP hybrid detection system (Leica HyD).

2.14. Flow cytometry

Upon incubation with DNA nanoconstructs, RAW 264.7 cells were washed with DMEM and transferred into FACS tubes. The fluorescence intensity of incorporated Cy3 coupled DNA constructs was determined by a Gallios flow cytometer (Beckmann Coulter, Krefeld, Germany), in order to quantify the uptake of DNA nanoconstructs. Post-acquisition analysis was performed using FlowJo software (Tree Star, Ashland, US).

2.14.1. ELISA

The concentration of TNF-α in culture supernatants was determined by enzyme-linked immunosorbent assay (ELISA) according to the manufacturer's instructions (R&D Systems, Wiesbaden, Germany).

2.15. Statistical analysis

GraphPad Prism 6 (GraphPad Software Inc., La Jolla, USA) was used for statistical analysis. Groups were compared with one-way ANOVA followed by a multiple comparison test (Tukey's test). In all cases, p values of $p < 0.05$ were considered to be significant.

3. Results

3.1. Design, assembly, and characterization of DNA nanotubes

To test the potential immunostimulatory effects of CpG-decorated DNA nanostructures (CpG tubes) *in vivo,* we designed DNA nanotubes consisting of 48 different oligonucleotides, each of which is 42 base pairs long. During a temperature-controlled annealing these oligonucleotides assemble into eight parallel double helices that form a DNA tube with a designed length of ~40 nm and a diameter of ~8 nm (Fig. 1) [17,30]. To trigger TLR9-mediated activation of an immune response, the well-characterized 20-nt long CpG oligodeoxynucleotide (ODN) CpG 1826 was conjugated to the DNA tube. This B type CpG sequence includes two highly stimulative GACGTT motifs, which are recognized by murine TLR9 receptors [10,20].

In order to present the CpG 1826 sequence on the surface of the DNA nanotubes, 24 of the 48 tile strands were extended on their 3′ ends with the ODN 1826 sequence (Fig. 1). DNA nanotubes without CpG extensions (plain tubes) and oligonucleotides carrying CpG motifs (CpG ODNs), which are not folded into a structure, served as control samples in all experiments. Gel electrophoresis analysis revealed prominent bands for the folded structures (Lane 2 + 3 in Fig. 2A). Note the lower mobility of the CpG-decorated tubes (Lane 2) compared with the plain tubes (Lane 3). Characterization by transmission electron microscopy (TEM) clearly showed the correct assembly of the nanotubes and the monodispersity of the samples. The measured length of 41 ± 1 nm and the measured diameter of 8 ± 1 nm are in perfect agreement with the designed dimensions (Fig. 2B and C).

To test the stability of DNA nanotubes, they were treated with DNAse I and incubated in different serum conditions for various incubation times. A double-stranded plasmid (pUC 18) was used as a control sample. If the DNAse concentration was adjusted to concentrations that are prevalent in murine tissues such as liver, testis or pancreas (0.5 U/ml) which is 40 times higher than the DNAse amount in skeletal muscle [32], no degradation of DNA tubes was observed for 2 h while the plasmid pUC18 degraded completely within 30 min (Fig. S1A) Also at high DNAse I concentrations (10 U/ml) the DNA tubes survived for up to 15 min while the double-stranded plasmid was instantaneously degraded (Fig. S1B). When adjusting serum concentrations to conditions prevalent in the muscle tissue only little degradation of DNA nanotubes was observed over 24 h (Fig. S1C). However it has to be noted that all samples are degrading over the course of hours in pure serum (Fig. S1D).

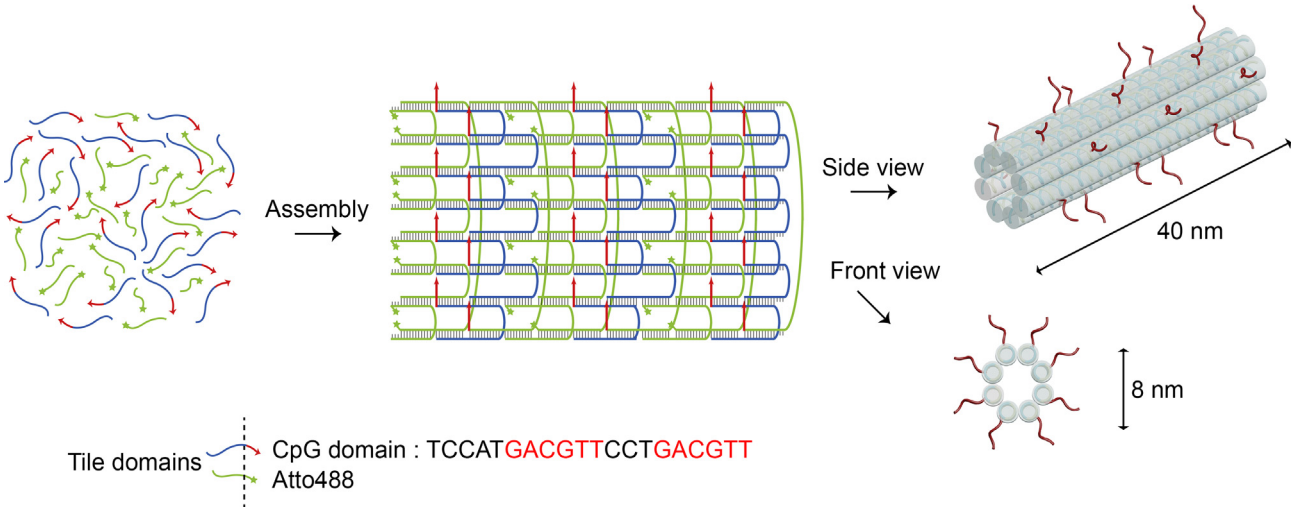

Fig. 1. *Design of CpG-decorated DNA nanotubes.* Left: Mixture of 48 different DNA tiles. Middle: Secondary structure of assembled tiles. Red arrows represent CpG domains, blue and green tile domains contain random sequences, stars at the 3′ ends represent Atto488 dye and vertical lines indicate the base pairing. Left: 3D side and front views of 8-helix tube. Transparent cylinders indicate double helices and red extensions represent CpG domains. (For interpretation of the references to color in this figure legend, the reader is referred to the web version of this article.)

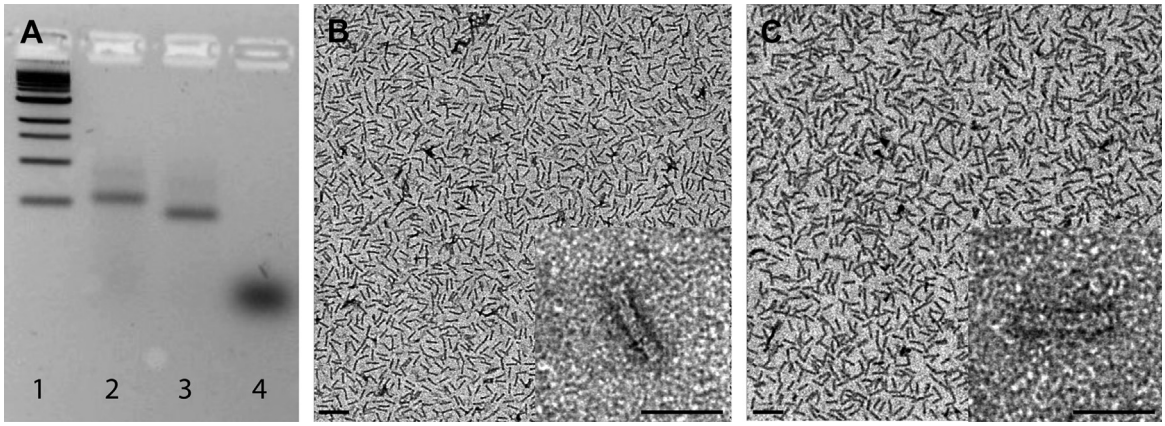

Fig. 2. *Characterization of DNA nanotubes.* (**A**) Gel electrophoresis analysis of assembled nanotubes after purification. 1) 1 kb ladder, 2) CpG tube 3) plain tube and 4) CpG ODNs. Electron micrographs of (**B**) CpG tubes and (**C**) plain tubes. Scale bars: 100 nm (left) and 40 nm (inset).

3.2. Release of inflammatory cytokines after stimulation with DNA nanotubes and oligonucleotides in vitro

To test whether the DNA nanotubes induce a cytokine response in immune cells, macrophage-like RAW 264.7 cells were incubated either with CpG-decorated DNA nanotubes, plain DNA nanotubes, CpG oligonucleotides, CpG oligonucleotides mixed with plain tubes or lipopolysaccharide (LPS), which served as positive control.

All constructs localized in vesicular structures of RAW 264.7 cells after 1 h of incubation (Fig. 3). The cellular uptake of fluorescently labeled CpG tubes, plain tubes, plain tubes + CpG ODNs and CpG ODNs constructs was further analyzed by flow cytometry and revealed no apparent differences in the uptake of these constructs (Fig. S2), as well as the viability of the RAW 264.7 cells (up to 18 h of incubation) (Fig. S3). The concentration of secreted tumor necrosis factor alpha (TNF-α) in culture supernatants was measured by ELISA. CpG tubes induced at 1 h of incubation a 3-fold and at 3 h a 5-fold induction of TNF-α release in RAW 264.7 macrophages as compared to unstimulated cells (Fig. 3D, E). Interestingly, incubation with plain tubes, CpG ODNs and CpG ODNs + plain tubes elicited only a slight increase in TNF-α production at 3 h (Fig. 3E). From this we conclude that the complexation of CpG oligonucleotides with the DNA tubes is of critical importance for the TNF-α production and that the CpG-DNA tube complexes withstand degradation within the first 3 h of incubation.

3.3. Localization of DNA nanotubes in skeletal muscle tissue after microinjection

Next, we performed *in vivo* fluorescence microscopy to explore the behavior of DNA nanotubes in the mouse cremaster muscle. Accordingly, fluorescently labeled CpG tubes, plain tubes, and CpG ODNs were microinjected 25 μm–50 μm distant to a venule into the muscle tissue. Within five minutes after microinjection, we observed rapid internalization of all DNA nanoconstructs by perivascular and tissue resident cells in the vicinity of the injection site (Fig. 4A and B) (Supporting Information, Movie S1).

Supplementary video related to this article can be found at http://dx.doi.org/10.1016/j.biomaterials.2015.02.099.

In order to characterize these cells, we repeated the microinjection of the DNA nanoconstructs in the cremaster muscle of Csf1r-EGFP transgenic (MacGreen) mice [36]. In MacGreen mice, cells of

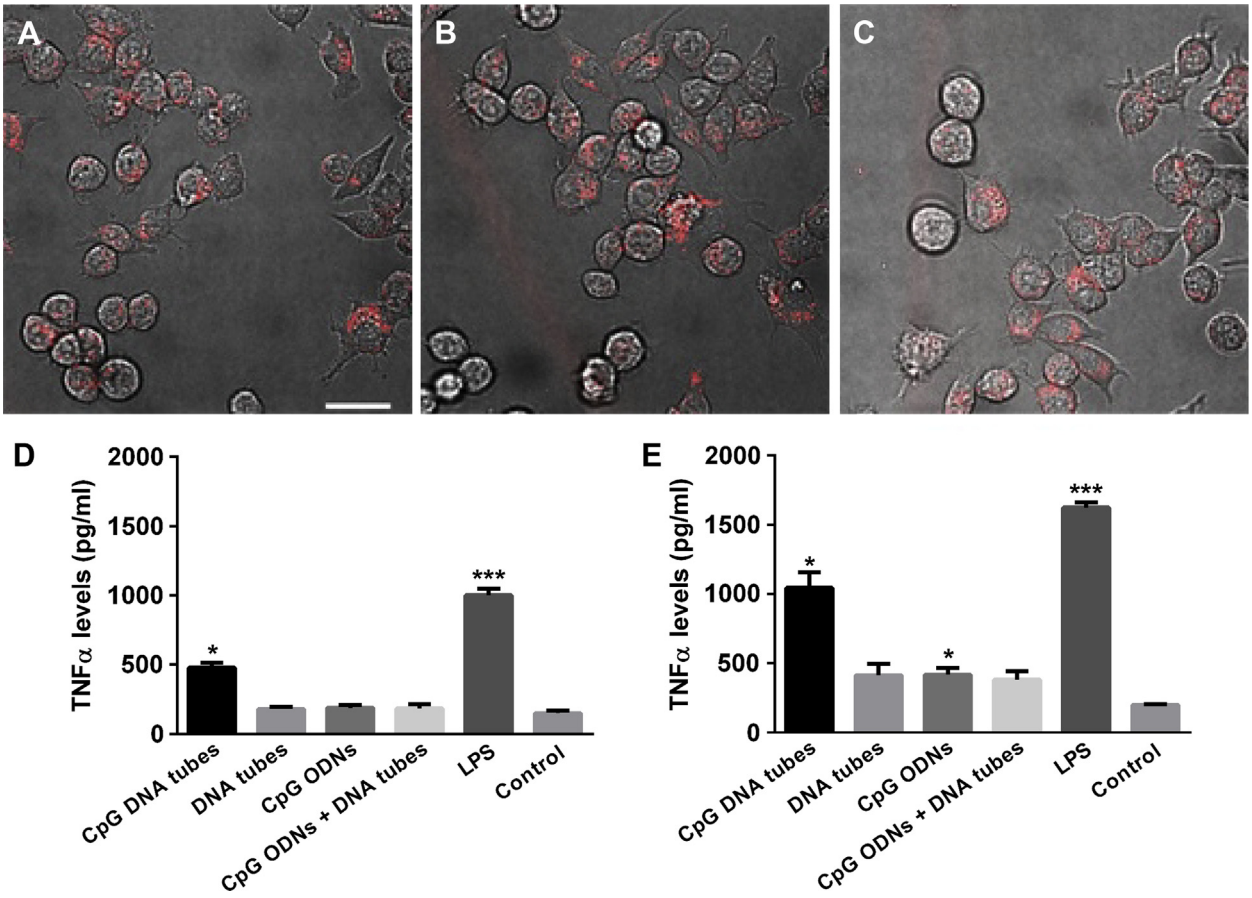

Fig. 3. *Uptake of DNA nanoconstructs and TNF-α response by RAW 264.7 cells.* RAW 264.7 cells were incubated with 5 nM of (**A**) plain tubes, (**B**) CpG tubes, and (**C**) CpG ODNs for 3 h at 37 °C. The different DNA nanotubes (red) were internalized by RAW 264.7 cells. (**D, E**) ELISA analysis of TNF-α levels in supernatants of 4×10^5 RAW 264.7 cells incubated for (**D**)1 h and (**E**) 3 h with 5 nM CpG tubes, plain tubes, CpG ODNs, CpG ODNs + DNA tubes, LPS (10 nM) which served as positive control or without additive (control) (n = 3, mean ± SEM; *p < 0.05, ***p < 0.001 vs. control). Scale bar: 20 μm. (For interpretation of the references to color in this figure legend, the reader is referred to the web version of this article.)

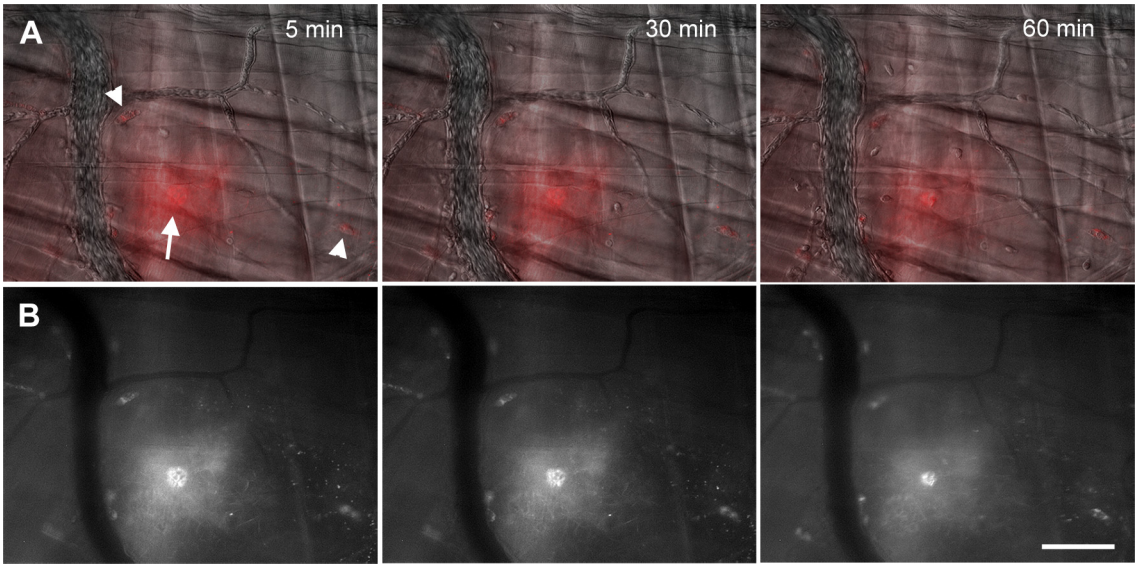

Fig. 4. *Distribution of CpG-decorated DNA nanotubes in the cremaster tissue. In vivo* fluorescence microscopy images of CpG tube (red) distribution after microinjection into the cremaster muscle revealed a rapid uptake of CpG tubes by tissue-resident cells (arrowheads) in the vicinity of the application site (arrow). At 30 min and 60 min, transmigrated leukocytes are visible in the tissue adjacent to the postcapillary venule (**A, B**) to the injection site. The fluorescence channel images (**B**) are merged with the corresponding transmitted light images from the cremaster tissue (**A**). Images were taken at the indicated time points after microinjection of 250 pl of CpG tubes and selected from a movie (Supplementary Movie 1.) Scale bar: 50 μm. (For interpretation of the references to color in this figure legend, the reader is referred to the web version of this article.)

the myeloid lineage, in particular macrophages and to some extent polymorphonuclear leukocytes, can be identified by the expression of green fluorescent protein under the control of the CSF-1R (c-fms) promotor. Microinjected CpG or plain DNA nanotubes as well as CpG ODNs were present in intracellular vesicles of $EGFP^+$ tissue resident macrophages (Fig. 5A–I). Moreover, concomitant microinjection of LysoTracker dye and DNA nanotubes revealed that internalized nanotubes accumulated in the late endosomes/lysosomes of these phagocytic cells (Fig. 5G–L).

Overall, the distribution pattern did not differ between CpG tubes, plain tubes, and CpG ODNs. DNA nanotubes also accumulated in muscle fibers, if these have been pierced by the glass capillaries during the microinjection process (Fig. 7). Furthermore, CpG tubes as well as plain DNA tubes were attached to tissue structures, presumably collagen fibers (Figs. 4 and 7).

3.4. Microinjection of CpG tubes induced leukocyte adhesion and transmigration

To assess the immunogenic potential of the DNA nanotubes, the extent of local inflammation upon perivenular microinjection in the cremaster muscle was analyzed by means of *in vivo*

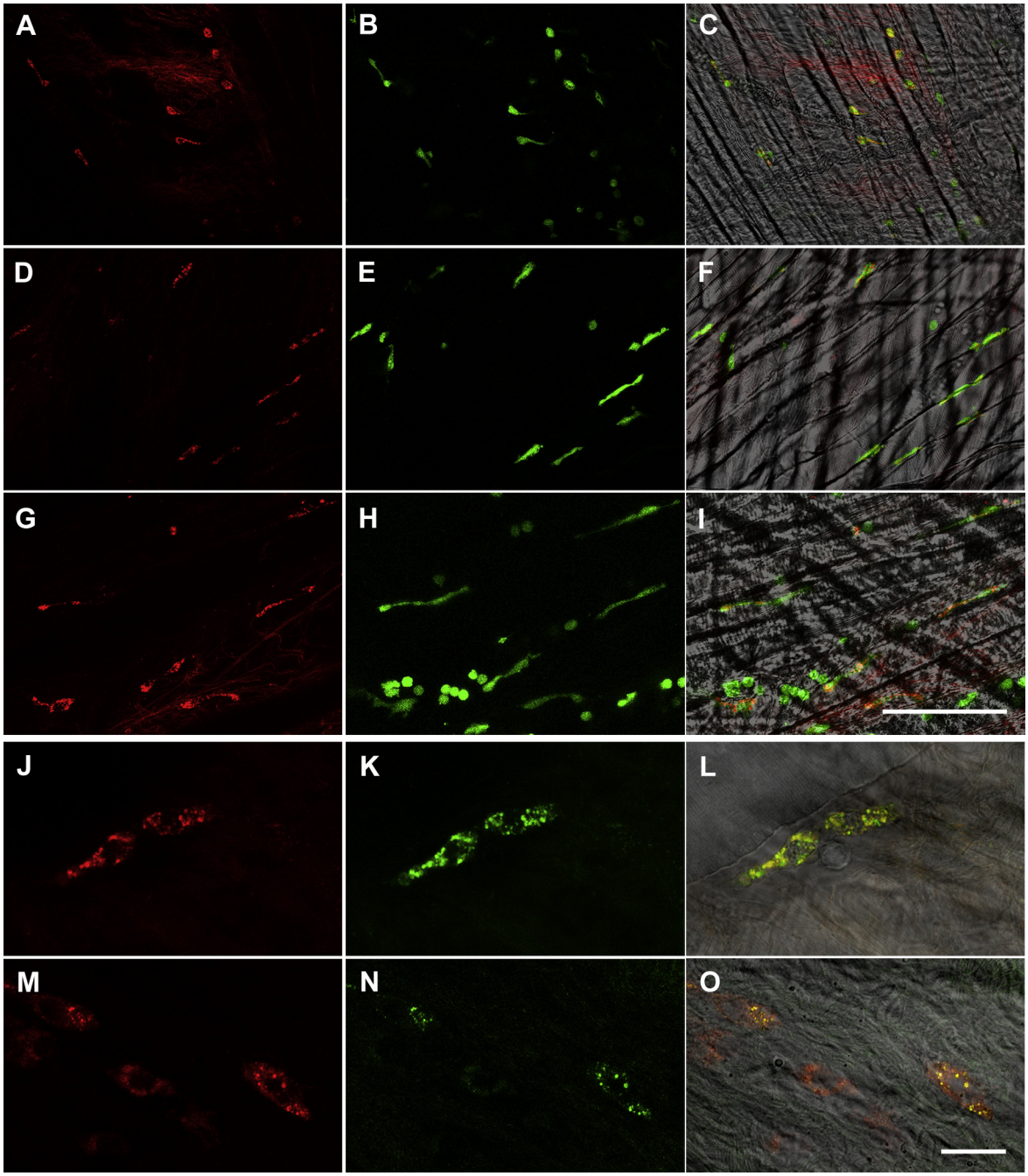

Fig. 5. *DNA nanotubes are localized in the endolysosomes of tissue macrophages*. Confocal imaging of CpG-decorated (**A-C**), plain tubes (**D-F**) and CpG ODNs (**G-I**) microinjected in the cremaster muscle of Csfr1-EGFP (MacGreen) mice. Images show that DNA nanotubes (**A**, **D**, red) as well as CpG ODNs (**G**) were internalized by EGFP positive macrophages (**B**, **E**, **H**, green). The fluorescence channel images (**A**, **B**, **D**, **E, G, H**) are merged with the corresponding transmitted light images depicting the muscle tissue (**C**, **F, I**). Scale bar: 50 μm. Confocal imaging of co-microinjected DNA nanotubes (red) and LysoTracker (green) showing the presence of plain tubes (**J**) as well as CpG tubes (**M**) in the late endolysosome (**K**, **N**). Merged image (**L**, **O**). Scale bar: 30 μm. (For interpretation of the references to color in this figure legend, the reader is referred to the web version of this article.)

transillumination microscopy. The preparation of the mouse cremaster muscle is a well-defined and widely used model system to study inflammation-related events and the associated recruitment of leukocytes [27,34,37].

No statistically significant differences in microhemodynamic parameters and systemic leukocyte counts were detected among experimental groups upon microinjection of CpG tubes, plain tubes, CpG ODNs, or vehicle control (Supporting Information, Table S1), thus assuring intergroup comparability.

As shown in Fig. 6A, microinjection of CpG ODNs or plain tubes did not affect leukocyte recruitment, whereas a significant increase in numbers of firmly adherent leukocytes ($3.5 \pm 0.31/10^4$ μm^2) at the vessel walls of postcapillary venules was found 30 min upon application of CpG tubes as compared to the injection of plain tubes ($0.75 \pm 0.35/10^4$ μm^2). 60 min post microinjection of CpG nanotubes, the number of adherent leukocytes was increased by a factor of five in postcapillary venules ($2.89 \pm 0.23/10^4$ μm^2) compared to the experimental group receiving saline ($0.67 \pm 0.31/10^4$ μm^2) and a factor of two or four compared to the group receiving plain tubes or CpG ODNs, respectively (Fig. 6B). In accordance with the typical length of time for the different steps of leukocyte recruitment upon application of inflammatory mediators [38] the effect of CpG nanotubes on leukocyte adherence ceased 90 min after injection (data not shown).

To test whether local microinjection of the different constructs resulted in a directed transmigration of leukocytes into the adjacent tissue, we compared the numbers of transmigrated cells on the vessel side ipsilateral to the application site with those on the contralateral side.

Consistent with the results obtained for leukocyte firm adherence, the number of transmigrated leukocytes detected within the perivascular tissue on the ipsilateral side was significantly elevated after microinjection of CpG tubes (Fig. 6D, 60 min, $7.3 \pm 0.32/10^4$ μm^2) as compared to saline (Fig. 6D, 60 min, $1.3 \pm 0.51/10^4$ μm^2) at all investigated time points (Fig. 6C and D), but not after microinjection of CpG ODNs or plain DNA tubes.

Taken together, these data indicate that only CpG-decorated DNA tubes, but neither plain DNA tubes nor CpG ODNs, elicit leukocyte recruitment in the cremaster muscle preparation.

3.5. Mast cell inhibition abolishes CpG tube-evoked leukocyte adhesion and transmigration

Mast cells are another important key player in the initiation of inflammation as well as in the recognition of pathogens and the modulation of appropriate immune responses [39]. These cells are able to facilitate the exit of leukocytes from postcapillary venules by rapid degranulation and the release of proinflammatory mediators [40]. Mast cells are not affected by the microsurgical preparation and do not contribute to the low baseline levels of preparation-induced leukocyte recruitment as we and others have reported previously [35,41]. To test whether mast cells are involved in the local recruitment of leukocytes after microinjection of CpG tubes, mice were pretreated with cromolyn, an inhibitor of mast cell degranulation, prior to microinjection.

CpG tube-elicited leukocyte adherence (Fig. 6B, 60 min, $1.3 \pm 0.33/10^4$ μm^2) as well as transmigration to the injection side (Fig. 6D, 60 min, $1.7 \pm 0.71/10^4$ μm^2) were significantly diminished in cromolyn pre-treated animals as compared to non-treated mice (Fig. 6B, adherence 60 min $2.8 \pm 0.24/10^4$ μm^2, Fig. 6D, transmigration 60 min, $7.3 \pm 0.48/10^4$ μm^2) and matched almost the values obtained in the control group (Fig. 6B, adherence 60 min, $0.7 \pm 0.32/10^4$ μm^2, Fig. 6D, transmigration 60 min, $1.3 \pm 0.62/10^4$ μm^2).

3.6. CpG tube microinjection results in NF-κB pathway activation

Activation of the TLR9 signaling cascade induces a translocation of the transcription factor NF-κB from the cytoplasm into the nucleus and thus regulates a broad range of genes expressed during inflammatory and immune responses [42,43], such as the expression of the inflammatory mediators TNF-α and IL-1 in macrophages [44].

To examine whether the injection of CpG nanotubes promotes NF-κB activation, we stained the muscle tissue for phosphorylated p65, a subunit of the NF-κB complex, which indicates nuclear NF-κB [45].

Remarkably, 90 min upon microinjection, almost all cell nuclei adjacent to the CpG tube application site in the tissue (Fig. 7B and E) were phospho-p65 positive, which was not the case in plain tube (Fig. 7A and D) and CpG ODN (Fig. 7C and F) injected tissues. A high proportion of phospho-p65 positive cells that accumulated at the injection site exhibited roundish nuclei, reminiscent of multi-lobed granulocyte nuclei (Fig. 7B and E), whereas p65 positive cells with elongated nuclei are tissue resident cells, contributing to the inflammatory process.

4. Discussion

Schueller et al. previously showed *in vitro* that splenocytes moderately expressed IL-6 and CD69 after exposure to CpG ODNs, whereas exposure to CpG-decorated DNA nanotubes led to a considerably enhanced expression [10]. In our experiments, RAW 264.7 cells responded to CpG DNA nanotubes in a similar manner, in which the release of TNF-α is low after incubation with CpG ODNs and markedly increased upon incubation with CpG-decorated DNA tubes, although the amount of CpGs was equal for all samples. Thereby the firm attachment of CpG-sequences to the DNA nanotubes is a prerequisite, since coincubation of RAW 264.7 macrophages with plain DNA tubes mixed with CpG ODNs failed to induce TNF-α production. These findings and our stability analysis allow the conclusion that the DNA tubes are stable over the course of our experiments.

In line with our *in vitro* findings, CpG ODNs did not exhibit immunostimulatory effects in the skeletal muscle during the observation time. It has been previously shown by Kiemer et al. that ISS 1018 (B type CpG ODNs) only weakly induced TNF-α production in human monocyte-derived macrophages compared to genomic DNA isolated from an attenuated *Mycobacterium bovis* BCG strain [46]. Wu et al. also described that a high aggregation of CpG ODNs is essential to crosslink and activate TLR9 [47]. Hence, the activation of TLR9 seems to depend on structural parameters of its agonist. Our experiments also clearly show that the conjugation of CpG ODNs to DNA tubes – which is equivalent to forming a high local density of CpG sequences – strongly enhances the release of immunostimulatory reagents *in vitro*, possibly by effectively crosslinking TLR9 receptors. This is in accordance with recent studies, where it has been shown that particulate- or aggregated CpG evoke strong immune responses via TLR9 activation [48,49].

Perivascular as well as tissue-resident macrophages are professional phagocytes and fulfill fundamental homeostatic and immune functions, such as clearance of cellular debris and pathogens [22]. It is well documented that the phagocytosis of different nanoparticles by alveolar macrophages is crucial for the production and release of cytokines [50,51], as well as the production of inflammatory mediators in monocytes [52] and macrophages [53]. Moreover, we have previously reported that the surface chemistry of quantum dot nanoparticles determines their uptake by perivascular macrophages as well as their proinflammatory properties upon systemic injection [35,54]. We found in these studies that solely negatively charged

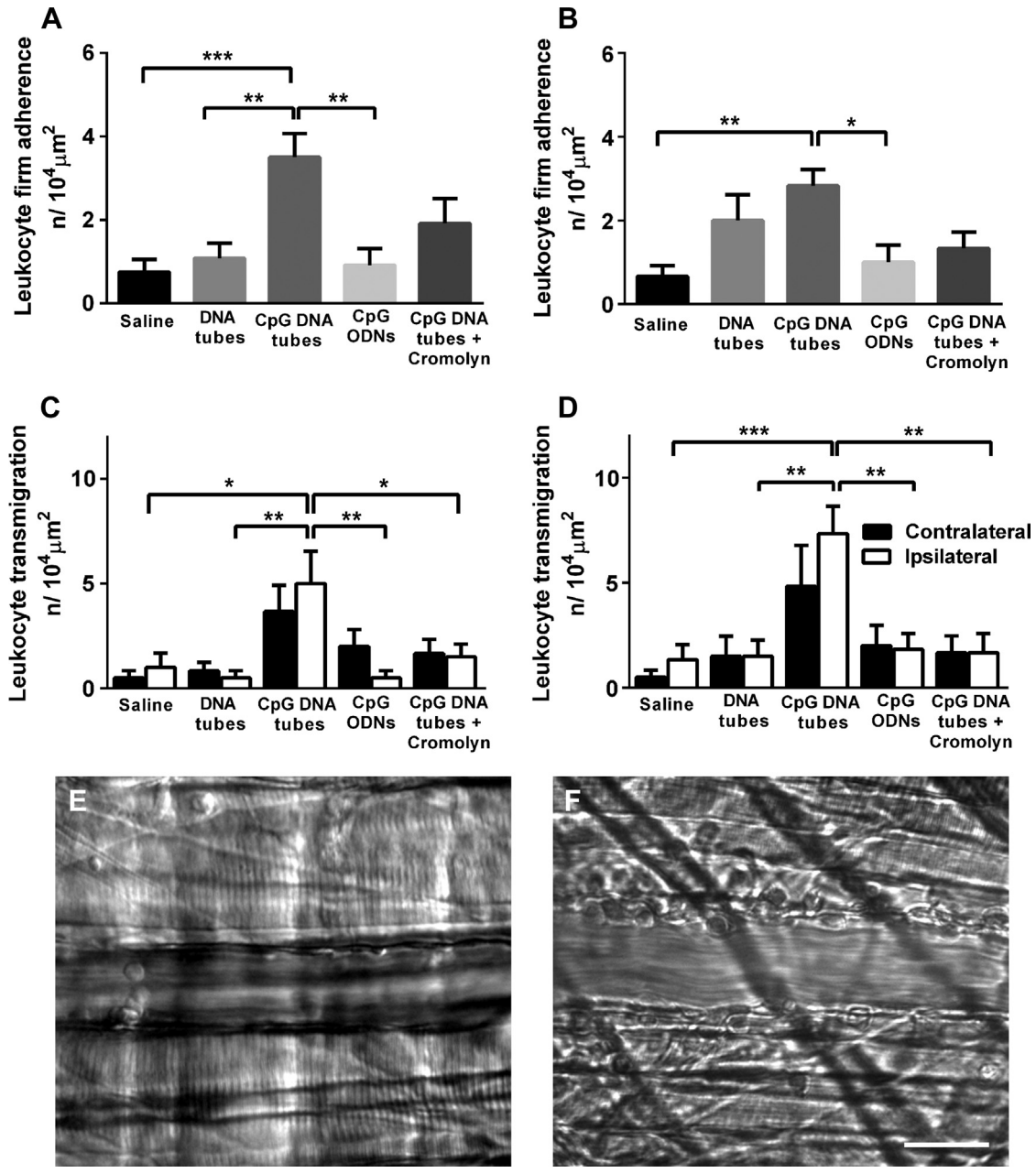

Fig. 6. Quantitative analysis of intravascular adherence and transmigration of leukocytes after microinjection of DNA nanotubes. Leukocyte adherence was quantified in post-capillary venules in the cremaster muscle using *in vivo* transillumination microscopy at 30 min (**A**) and 60 min (**B**) upon microinjection of CpG tubes, DNA tubes, CpG ODNs, or saline. The numbers of adherent leukocytes were significantly increased at 30 min and 60 min after CpG tube injection. Pretreatment with cromolyn prior to CpG tube injection diminished leukocyte adherence. Leukocyte transmigration was quantified on the vessel side ipsilateral to the microinjection site (white bars) and on the contralateral side (black bars) at 30 min (**C**) and 60 min (**D**) after microinjection. CpG tube injection elicited leukocyte transmigration into the tissue. Cromolyn pretreatment attenuated the leukocyte transmigration induced by microinjection of CpG tubes ($n = 6$, mean ± SEM; $^{*}p < 0.05$, $^{**}p < 0.01$, $^{***}p < 0.001$ vs. all groups). (E, F) depicts representative *in vivo* microscopy images of postcapillary venules in the cremaster muscle 30 min after microinjection of either saline (**E**) or CpG tubes (**F**) with adherent as well as transmigrated leukocytes. Scale bar, 25 µm.

quantum dots (with carboxyl-surface modifications) were rapidly taken up by perivascular macrophages upon systemic injection and subsequently elicited leukocyte recruitment in a mast cell-dependent manner. In remarkable accordance with these results, we found in the present study that the negatively charged DNA nanotubes (zeta potential; CpG tube: −13.2 ± 0.4 mV and plain tube: −11.4 ± 0.2 mV) were rapidly localized in the endolysosomal system of tissue-resident macrophages upon microinjection. Most recently, King et al. described that negatively charged, immune-modifying microparticles are readily taken up by inflammatory monocytes, mediated via the macrophage receptor with collagenous structure (MARCO) [55]. Since the observed cellular localization and uptake pattern of CpG-decorated as well as plain DNA nanotubes were indistinguishable (Fig. 4A and B), it seems that the absorption route from the extracellular space into the endosome is independent of the CpG motif present on the DNA tube surface. The rapid intracellular localization of the DNA nanotubes argues for an active uptake, which could possibly be mediated by scavenger receptors. In this regard, Minchin et al. recently demonstrated, that macrophage scavenger receptor A1 (SR-A1) and MARCO mediated the clearance of

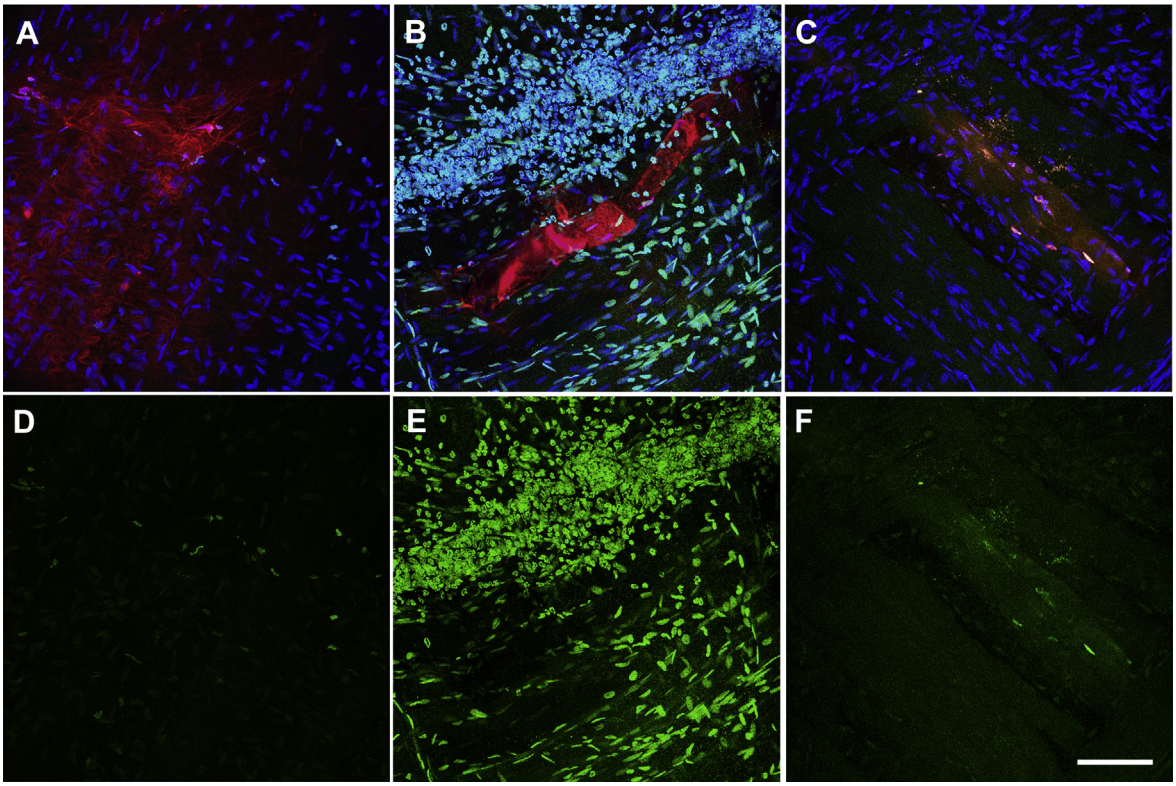

Fig. 7. *NF-κB p65 translocation occurs in the vicinity of microinjected CpG-decorated DNA nanotubes*. Confocal immunofluorescence of DNA nanotubes (red), NF-κB p65 (green), and TO-PRO (blue) counterstaining showed marked NF-κB p65 nuclear staining of cells adjacent to the injection site of CpG tubes (**B**, **E**). Injection of plain tube (**A**, **D**) as well as of CpG ODNs into the cremasteric tissue (**C**, **F**) caused only weak nuclear p65 staining. Scale bar: 50 μm. (For interpretation of the references to color in this figure legend, the reader is referred to the web version of this article.)

albumin-covered nanomaterials by macrophages [56]. Furthermore, Latz et al. have previously shown that the receptor for advanced glycation end products (RAGE) directly binds DNA and promotes its uptake via the endocytic pathway [57]. It has also been proposed, that TLR9 activation by DNA-containing immune complexes is mediated partly by RAGE [58]. In general, macrophages can internalize nanoparticles via several pathways, including constitutive macropinocytosis, phagocytosis, as well as clathrin-mediated pathways [59,60]. Although, we clearly observed internalized DNA tubes within the endosomal/lysosomal compartment, the precise details of uptake and the subsequent compartmentalization of DNA tubes need to be addressed in future studies, since this is pivotal for intracellular targeting as well as payload release. For some applications of DNA nanotubes as *in vivo* carriers, endosomal escape of the therapeutics has to be ensured. In this regard it seems promising to tune DNA secondary structure by pH change (i.e. by using i-motifs), in order to enable the release of DNA bound molecules [61].

The inflammatory response and the extent of leukocyte transmigration upon microinjection of CpG nanotubes was considerable and highly dependent on the activation of mast cells as judged by the reduction of CpG nanotubes-elicited leukocyte transmigration to control levels in the presence of the mast cell stabilisator cromolyn [62,63]. Surface-localized cytokine receptors enable mast cells to respond to macrophage-released cytokines [39,64]. Therefore, it is possible that mast cells, which are predominantly located in close vicinity to the abluminal side of the vessel walls [65], were stimulated by macrophage-released cytokines [66,67] during the CpG nanotube-elicited inflammatory response. Although we were not able to detect CpG nanotubes by means of confocal microscopy in mast cells in the cremaster muscle (data not shown), we cannot exclude direct mast cell activation (e.g. via activated complement factors). In any case, activated mast cells amplify the proinflammatory cascade via the release of inflammatory mediators, such as histamine, platelet-activating factor, or TNF-α from their intracellular granula by rapid exocytosis [68] which in turn rapidly (within 10 min) increases leukocyte adherence [35,69,70]. The considerable increase of adherent leukocytes already 30 min after microinjection of CpG nanotubes could likewise be explained by mast cell activation.

5. Conclusion

Taken together, we demonstrated an effective delivery system *in vivo* using CpG-decorated DNA nanotubes. With this DNA nanotube *in vivo* approach, we have observed that tissue-resident macrophages can be targeted and that these cells are reached in intact muscle tissue almost immediately upon application. Most important, plain DNA nanotubes on the other hand do not induce an immune response. However, the attachment of conjugating ligands allows gearing the tissue homeostasis in a certain direction, since modification of nanotubes with CpG sequences induced a strongly elevated immune response, particularly the recruitment of leukocytes from postcapillary venules to the tissue and nuclear translocation of p65, a subunit of the NF-κB transcription factor complex, which is commonly used as an indicator of NF-κB activation. Inhibition of mast cells with cromolyn also revealed that CpG-dependent immune stimulation requires mast cell degranulation. Additionally, the stability of DNA nanotubes against DNAse I under conditions present in muscle tissue is promising for further *in vivo* applications of DNA-based nanostructures. So far, DNA nanostructures have been used to successfully deliver different

cargos to cells *in vitro*, such as apoptosis-inducing antibodies [11] or anticancer drugs such as anthracyclines or doxorubicin [71].

Our results encourage further research to use DNA nanotubes to effectively target macrophages *in vivo*, thus facilitating versatile applications.

Acknowledgments

We thank C. Fahney, S. Kempter, G. Adams and B. Uhl for excellent technical assistance and J. O. Rädler for helpful discussions. Funding: This work was supported by the Deutsche Forschungsgemeinschaft (SFB 1032, Teilprojekte A6 and B10) and the EU (ITN EScoDNA). Author contributions: S.S., S.K., T.L. and M.R. designed the research, S.K. and T.L. designed, characterized and produced the nanoconstructs. S.S. performed *in vitro* and *in vivo* experiments. S.S., S.K., A.K.N., and M.R. did the imaging and prepared the figures. S.S., S.K., A.K.N., F.K., T.L. and M.R. critically evaluated the results and finalized the manuscript. S.S., S.K., T.L. and M.R. wrote the manuscript.

Appendix A. Supplementary data

Supplementary data related to this article can be found at http://dx.doi.org/10.1016/j.biomaterials.2015.02.099

References

[1] Beck G, Habicht GS. Immunity and the invertebrates. Sci Am 1996;275:60–3. 6.
[2] Bao G, Mitragotri S, Tong S. Multifunctional nanoparticles for drug delivery and molecular imaging. Annu Rev Biomed Eng 2013;15:253–82.
[3] Bareford LM, Swaan PW. Endocytic mechanisms for targeted drug delivery. Adv Drug Deliv Rev 2007;59:748–58.
[4] Seeman NC. Nucleic acid junctions and lattices. J Theor Biol 1982;99:237–47.
[5] Seeman NC. At the crossroads of chemistry, biology, and materials: structural DNA nanotechnology. Chem Biol 2003;10:1151–9.
[6] Pinheiro AV, Han D, Shih WM, Yan H. Challenges and opportunities for structural DNA nanotechnology. Nat Nanotechnol 2011;6:763–72.
[7] Voigt NV, Torring T, Rotaru A, Jacobsen MF, Ravnsbaek JB, Subramani R, et al. Single-molecule chemical reactions on DNA origami. Nat Nanotechnol 2010;5:200–3.
[8] Rothemund PW. Folding DNA to create nanoscale shapes and patterns. Nature 2006;440:297–302.
[9] Douglas SM, Dietz H, Liedl T, Hogberg B, Graf F, Shih WM. Self-assembly of DNA into nanoscale three-dimensional shapes. Nature 2009;459:414–8.
[10] Schuller VJ, Heidegger S, Sandholzer N, Nickels PC, Suhartha NA, Endres S, et al. Cellular immunostimulation by CpG-sequence-coated DNA origami structures. ACS Nano 2011;5:9696–702.
[11] Douglas SM, Bachelet I, Church GM. A logic-gated nanorobot for targeted transport of molecular payloads. Science 2012;335:831–4.
[12] Castro CE, Kilchherr F, Kim DN, Shiao EL, Wauer T, Wortmann P, et al. A primer to scaffolded DNA origami. Nat Methods 2011;8:221–9.
[13] Hahn J, Wickham SF, Shih WM, Perrault SD. Addressing the instability of DNA nanostructures in tissue culture. ACS Nano 2014;8:8765–75.
[14] Walsh AS, Yin H, Erben CM, Wood MJ, Turberfield AJ. DNA cage delivery to mammalian cells. ACS Nano 2011;5:5427–32.
[15] Li J, Pei H, Zhu B, Liang L, Wei M, He Y, et al. Self-assembled multivalent DNA nanostructures for noninvasive intracellular delivery of immunostimulatory CpG oligonucleotides. ACS Nano 2011;5:8783–9.
[16] Ke Y, Ong LL, Shih WM, Yin P. Three-dimensional structures self-assembled from DNA bricks. Science 2012;338:1177–83.
[17] Wei B, Dai M, Yin P. Complex shapes self-assembled from single-stranded DNA tiles. Nature 2012;485:623–6.
[18] Klinman DM, Klaschik S, Sato T, Tross D. CpG oligonucleotides as adjuvants for vaccines targeting infectious diseases. Adv Drug Deliv Rev 2009;61:248–55.
[19] Zoglmeier C, Bauer H, Norenberg D, Wedekind G, Bittner P, Sandholzer N, et al. CpG blocks immunosuppression by myeloid-derived suppressor cells in tumor-bearing mice. Clin Cancer Res – Off J Am Assoc Cancer Res 2011;17:1765–75.
[20] Krieg AM, Yi AK, Matson S, Waldschmidt TJ, Bishop GA, Teasdale R, et al. CpG motifs in bacterial DNA trigger direct B-cell activation. Nature 1995;374:546–9.
[21] Hemmi H, Takeuchi O, Kawai T, Kaisho T, Sato S, Sanjo H, et al. A Toll-like receptor recognizes bacterial DNA. Nature 2000;408:740–5.
[22] Davies LC, Jenkins SJ, Allen JE, Taylor PR. Tissue-resident macrophages. Nat Immunol 2013;14:986–95.
[23] Ajuebor MN, Das AM, Virag L, Flower RJ, Szabo C, Perretti M. Role of resident peritoneal macrophages and mast cells in chemokine production and neutrophil migration in acute inflammation: evidence for an inhibitory loop involving endogenous IL-10. J Immunol 1999;162:1685–91.
[24] Cailhier JF, Partolina M, Vuthoori S, Wu S, Ko K, Watson S, et al. Conditional macrophage ablation demonstrates that resident macrophages initiate acute peritoneal inflammation. J Immunol 2005;174:2336–42.
[25] Biswas SK, Gangi L, Paul S, Schioppa T, Saccani A, Sironi M, et al. A distinct and unique transcriptional program expressed by tumor-associated macrophages (defective NF-kappaB and enhanced IRF-3/STAT1 activation). Blood 2006;107:2112–22.
[26] Kuang DM, Zhao Q, Peng C, Xu J, Zhang JP, Wu C, et al. Activated monocytes in peritumoral stroma of hepatocellular carcinoma foster immune privilege and disease progression through PD-L1. J Exp Med 2009;206:1327–37.
[27] Ley K, Laudanna C, Cybulsky MI, Nourshargh S. Getting to the site of inflammation: the leukocyte adhesion cascade updated. Nat Rev Immunol 2007;7:678–89.
[28] Mantovani A, Vecchi A, Allavena P. Pharmacological modulation of monocytes and macrophages. Curr Opin Pharmacol 2014;17C:38–44.
[29] Murray PJ, Wynn TA. Protective and pathogenic functions of macrophage subsets. Nat Rev Immunol 2011;11:723–37.
[30] Yin P, Hariadi RF, Sahu S, Choi HM, Park SH, Labean TH, et al. Programming DNA tube circumferences. Science 2008;321:824–6.
[31] Sorensen RS, Okholm AH, Schaffert D, Kodal AL, Gothelf KV, Kjems J. Enzymatic ligation of large biomolecules to DNA. ACS Nano 2013;7:8098–104.
[32] Takeshita H, Yasuda T, Nakajima T, Hosomi O, Nakashima Y, Kishi K. Mouse deoxyribonuclease I (DNase I): biochemical and immunological characterization, cDNA structure and tissue distribution. Biochem Mol Biol Int 1997;42:65–75.
[33] Baez S. An open cremaster muscle preparation for the study of blood vessels by in vivo microscopy. Microvasc Res 1973;5:384–94.
[34] Mempel TR, Moser C, Hutter J, Kuebler WM, Krombach F. Visualization of leukocyte transendothelial and interstitial migration using reflected light oblique transillumination in intravital video microscopy. J Vasc Res 2003;40:435–41.
[35] Rehberg M, Praetner M, Leite CF, Reichel CA, Bihari P, Mildner K, et al. Quantum dots modulate leukocyte adhesion and transmigration depending on their surface modification. Nano Lett 2010;10:3656–64.
[36] Sasmono RT, Williams E. Generation and characterization of MacGreen mice, the Cfs1r-EGFP transgenic mice. Methods Mol Biol 2012;844:157–76.
[37] Hughes EL, Gavins FN. Troubleshooting methods: using intravital microscopy in drug research. J Pharmacol Toxicol Methods 2010;61:102–12.
[38] Khandoga AG, Khandoga A, Reichel CA, Bihari P, Rehberg M, Krombach F. In vivo imaging and quantitative analysis of leukocyte directional migration and polarization in inflamed tissue. PloS One 2009;4:e4693.
[39] Abraham SN, St John AL. Mast cell-orchestrated immunity to pathogens. Nat Rev Immunol 2010;10:440–52.
[40] Kunder CA, St John AL, Abraham SN. Mast cell modulation of the vascular and lymphatic endothelium. Blood 2011;118:5383–93.
[41] Guo Y, Lindbom L, Hedqvist P. Spontaneous leukocyte rolling in rat and mouse microvessels is independent of mast cell activity. Inflamm Res – Off J Eur Histamine Res Soc [et al] 2000;49:325–9.
[42] Zhang G, Ghosh S. Toll-like receptor-mediated NF-kappaB activation: a phylogenetically conserved paradigm in innate immunity. J Clin Investig 2001;107:13–9.
[43] Tak PP, Firestein GS. NF-kappaB: a key role in inflammatory diseases. J Clin investig 2001;107:7–11.
[44] Coussens LM, Werb Z. Inflammation and cancer. Nature 2002;420:860–7.
[45] Maguire O, Collins C, O'Loughlin K, Miecznikowski J, Minderman H. Quantifying nuclear p65 as a parameter for NF-kappaB activation: correlation between ImageStream cytometry, microscopy, and Western blot. Cytom Part A – J Int Soc Anal Cytol 2011;79:461–9.
[46] Kiemer AK, Senaratne RH, Hoppstadter J, Diesel B, Riley LW, Tabeta K, et al. Attenuated activation of macrophage TLR9 by DNA from virulent mycobacteria. J Innate Immun 2009;1:29–45.
[47] Wu CC, Lee J, Raz E, Corr M, Carson DA. Necessity of oligonucleotide aggregation for toll-like receptor 9 activation. J Biol Chem 2004;279:33071–8.
[48] Gungor B, Yagci FC, Tincer G, Bayyurt B, Alpdundar E, Yildiz S, et al. CpG ODN nanorings induce IFNalpha from plasmacytoid dendritic cells and demonstrate potent vaccine adjuvant activity. Sci Transl Med 2014;6:235ra61.
[49] Kobiyama K, Aoshi T, Narita H, Kuroda E, Hayashi M, Tetsutani K, et al. Nonagonistic Dectin-1 ligand transforms CpG into a multitask nanoparticulate TLR9 agonist. Proc Natl Acad Sci U S A 2014;111:3086–91.
[50] Haberzettl P, Duffin R, Kramer U, Hohr D, Schins RP, Borm PJ, et al. Actin plays a crucial role in the phagocytosis and biological response to respirable quartz particles in macrophages. Arch Toxicol 2007;81:459–70.
[51] Scherbart AM, Langer J, Bushmelev A, van Berlo D, Haberzettl P, van Schooten FJ, et al. Contrasting macrophage activation by fine and ultrafine titanium dioxide particles is associated with different uptake mechanisms. Part Fibre Toxicol 2011;8:31.
[52] Lee HM, Shin DM, Song HM, Yuk JM, Lee ZW, Lee SH, et al. Nanoparticles up-regulate tumor necrosis factor-alpha and CXCL8 via reactive oxygen species and mitogen-activated protein kinase activation. Toxicol Appl Pharmacol 2009;238:160–9.

[53] Kang CM, Jang AS, Ahn MH, Shin JA, Kim JH, Choi YS, et al. Interleukin-25 and interleukin-13 production by alveolar macrophages in response to particles. Am J Respir Cell Mol Biol 2005;33:290–6.
[54] Rehberg M, Leite CF, Mildner K, Horstkotte J, Zeuschner D, Krombach F. Surface chemistry of quantum dots determines their behavior in postischemic tissue. ACS Nano 2012;6:1370–9.
[55] Getts DR, Terry RL, Getts MT, Deffrasnes C, Muller M, van Vreden C, et al. Therapeutic inflammatory monocyte modulation using immune-modifying microparticles. Sci Transl Med 2014;6:219ra7.
[56] Mortimer GM, Butcher NJ, Musumeci AW, Deng ZJ, Martin DJ, Minchin RF. Cryptic epitopes of albumin determine mononuclear phagocyte system clearance of nanomaterials. ACS Nano 2014;8(4):3357–66.
[57] Sirois CM, Jin T, Miller AL, Bertheloot D, Nakamura H, Horvath GL, et al. RAGE is a nucleic acid receptor that promotes inflammatory responses to DNA. J Exp Med 2013;210:2447–63.
[58] Tian J, Avalos AM, Mao SY, Chen B, Senthil K, Wu H, et al. Toll-like receptor 9-dependent activation by DNA-containing immune complexes is mediated by HMGB1 and RAGE. Nat Immunol 2007;8:487–96.
[59] Weissleder R, Nahrendorf M, Pittet MJ. Imaging macrophages with nanoparticles. Nat Mater 2014;13:125–38.
[60] Kuhn DA, Vanhecke D, Michen B, Blank F, Gehr P, Petri-Fink A, et al. Different endocytotic uptake mechanisms for nanoparticles in epithelial cells and macrophages. Beilstein J Nanotechnol 2014;5:1625–36.
[61] Son S, Nam J, Kim J, Kim S, Kim WJ. i-motif-driven Au nanomachines in programmed siRNA delivery for gene-silencing and photothermal ablation. ACS Nano 2014;8:5574–84.
[62] Mazurek N, Berger G, Pecht I. A binding site on mast cells and basophils for the anti-allergic drug cromolyn. Nature 1980;286:722–3.
[63] Mazurek N, Bashkin P, Petrank A, Pecht I. Basophil variants with impaired cromoglycate binding do not respond to an immunological degranulation stimulus. Nature 1983;303:528–30.
[64] Schramm R, Thorlacius H. Neutrophil recruitment in mast cell-dependent inflammation: inhibitory mechanisms of glucocorticoids. Inflamm Res – Off J Eur Histamine Res Soc [et al] 2004;53:644–52.
[65] Galli SJ, Tsai M. Mast cells in allergy and infection: versatile effector and regulatory cells in innate and adaptive immunity. Eur J Immunol 2010;40:1843–51.
[66] Alam R, Forsythe PA, Stafford S, Lett-Brown MA, Grant JA. Macrophage inflammatory protein-1 alpha activates basophils and mast cells. J Exp Med 1992;176:781–6.
[67] Galli SJ, Tsai M. IgE and mast cells in allergic disease. Nat Med 2012;18:693–704.
[68] Piliponsky AM, Chen CC, Grimbaldeston MA, Burns-Guydish SM, Hardy J, Kalesnikoff J, et al. Mast cell-derived TNF can exacerbate mortality during severe bacterial infections in C57BL/6-KitW-sh/W-sh mice. Am J Pathol 2010;176:926–38.
[69] Foy DS, Ley K. Intercellular adhesion molecule-1 is required for chemoattractant-induced leukocyte adhesion in resting, but not inflamed, venules in vivo. Microvasc Res 2000;60:249–60.
[70] Thorlacius H, Raud J, Rosengren-Beezley S, Forrest MJ, Hedqvist P, Lindbom L. Mast cell activation induces P-selectin-dependent leukocyte rolling and adhesion in postcapillary venules in vivo. Biochem Biophys Res Commun 1994;203:1043–9.
[71] Zhao YX, Shaw A, Zeng X, Benson E, Nystrom AM, Hogberg B. DNA origami delivery system for cancer therapy with tunable release properties. ACS Nano 2012;6:8684–91.

Appendix

Supporting Information for Associated Publication P1

Supporting Information for Associated Publication P2

Supporting Information for Associated Publication P3

Supporting Information for Chapter 4.3

Supporting Information for Associated Publication P1

Cellular Uptake of Tile-Assembled DNA Nanotubes

by

Samet Kocabey, Hanna Meinl, Iain S. MacPherson, Valentina Cassinelli, Antonio Manetto, Simon Rothenfusser, Tim Liedl and Felix S. Lichtenegger

published in

Nanomaterials 2015, 5(1), 47-60

Supporting Information

Table S1. The list of oligonucleotide sequences used in the 6-helix tile-tube assembly.

(**A**) Oligonucleotides for folate conjugation. X: C8-Alkyne-dU.

ODN-1	XAAAACGCTAAGCCACCTTTAGATCCAAA
ODN-2	XGGATCTAAAGGACTTCTATCAAAGACGGGACGACTCCGGGAG
ODN-3	XAAACTCCCGGAGTCCGCTGCTGATCAAA
ODN-4	XGATCAGCAGCGCCCGTCTCGACTGCAGAAATAGGACCCCCAG
ODN-5	XAAACTGGGGGTCCTCGAGGCGAAACAAA
ODN-6	XGTTTCGCCTCGTAGCCTTCGCCCGCACGACCTGGCTTAGCGT

(**B**) Oligonucleotides for fluorescent dye labeling. Z: Atto488-dUTP or overhang sequence for Atto647 modified oligonucleotide (GGTAGTAATAGGAGAATG).

GGTCGTGCGGACTGTCGAACACCAACGATGCCTGATAGAAGTZ
GCGTGGCAATTGCCATAAATTCATACATAACGGCGCCAGACGZ
TTTCAAGACCGGCACTTGTATGGCGTAGGGCGGGTTTAGCGGZ
CGTTATGTATGCCGCTAAACCTTGCAATGACTGAACTCGAACZ
GTCCCGTCTTTGGATCCGAAAGCCATAATATATCGAGACGGGZ
TCGAAGTCGTGTTCGAGTTCAAATGTCTATGCGATGCAGCAGZ
GTCATTGCAATAGCTCCCATCATTTAATGTCGTTTACAGTAAZ
GCATAGACATTTTACTGTAAAACCTTACGTAACTTACAGCCAZ
ATTTCTGCAGGGAATTCAGCCTATTCACATAGGCGAAGGCTAZ
ATGCCAGGAATGGCTGTAAGTTGCATCATGGGGGTCCTCAATZ
TACGTAAGGTCAATACTCATCCCTGAGTGATCCATGACCCTTZ
CCCATGATGCAAAGGGTCATGGGTCTTGAAAAATTTATGGCAZ

(**C**) Oligonucleotides for siRNA labeling.

GGCATCGTTGGCGTCTGGCGCACGACTTCGATTTCGGATCCAAGGATGTAGGTGGTAGAG
CGCCCTACGCCAAAAAAGATGGGAGCTAAGGATGTAGGTGGTAGAG
TATATTATGGCCTGCTGCATCTTCCTGGCATGGCTGAATTCCAGGATGTAGGTGGTAGAG
CGACATTAAATAAAAAAGATGAGTATTGAGGATGTAGGTGGTAGAG
CTATGTGAATAATTGAGGACCATTGCCACGCTGTTCGACAGTAGGATGTAGGTGGTAGAG
GATCACTCAGGAAAAAAATACAAGTGCCAGGATGTAGGTGGTAGAG

Table S2. Molecular weights of 6 oligonucleotides before and after folate conjugation.

Samples	**MW (g/mol)**		**MW (g/mol) after reaction**	
	expected	**experimental**	**expected**	**experimental**
ODN-1	8913	8920,382	9554,64	9547,765
ODN-2	14355	14602,380	14996,64	14992,571
ODN-3	8937	8931,952	9578,64	9574,670
ODN-4	14197	14195,535	14838,64	14842,370
ODN-5	9075	9071,732	9716,64	9710,265
ODN-6	14119	14142,973	14760,64	14759,459
Folate-PEG3-Azide	641,64			

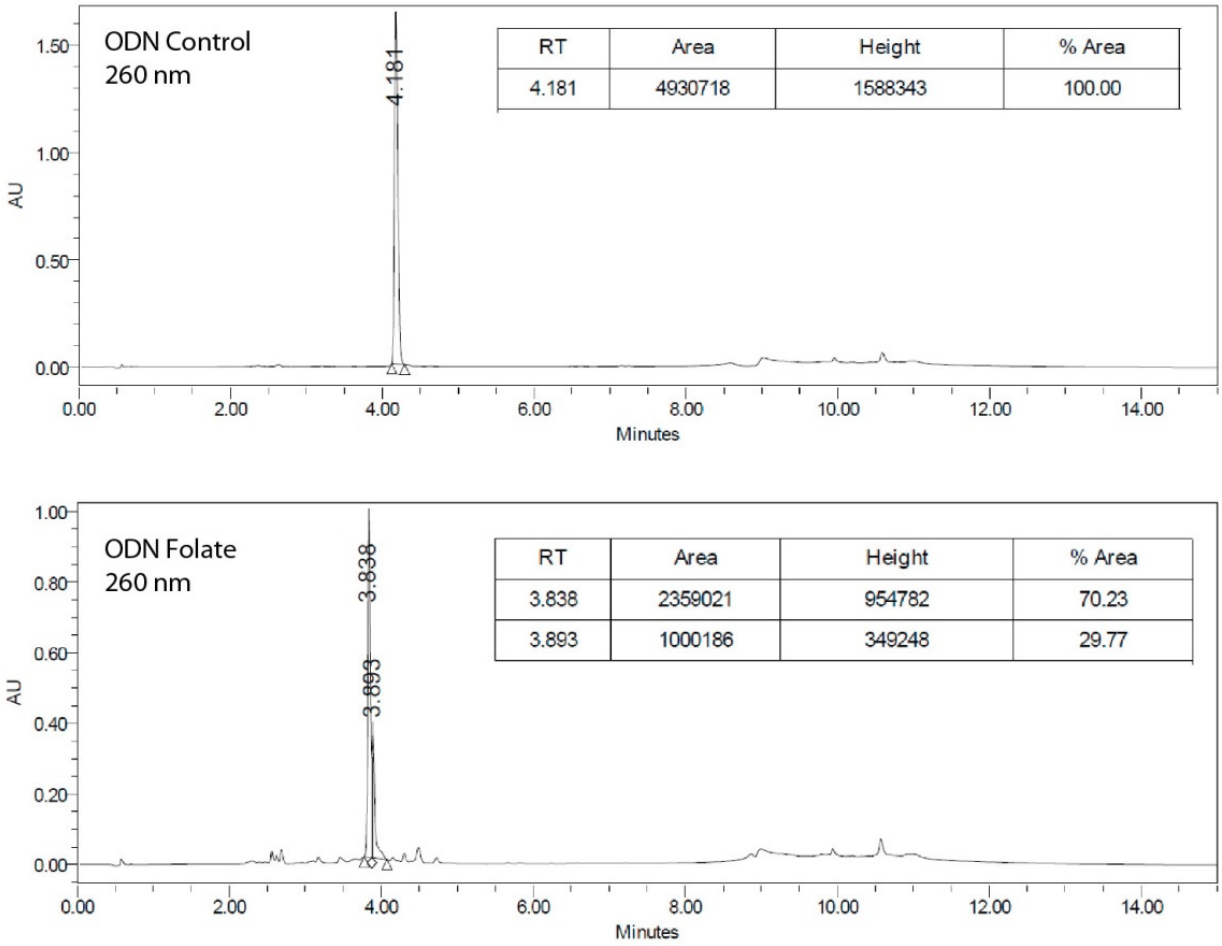

Figure S1. RP-HPLC chromotogram of a single DNA oligonucleotide before (upper chromatogram) and after (bottom chromatogram) folate conjugation.

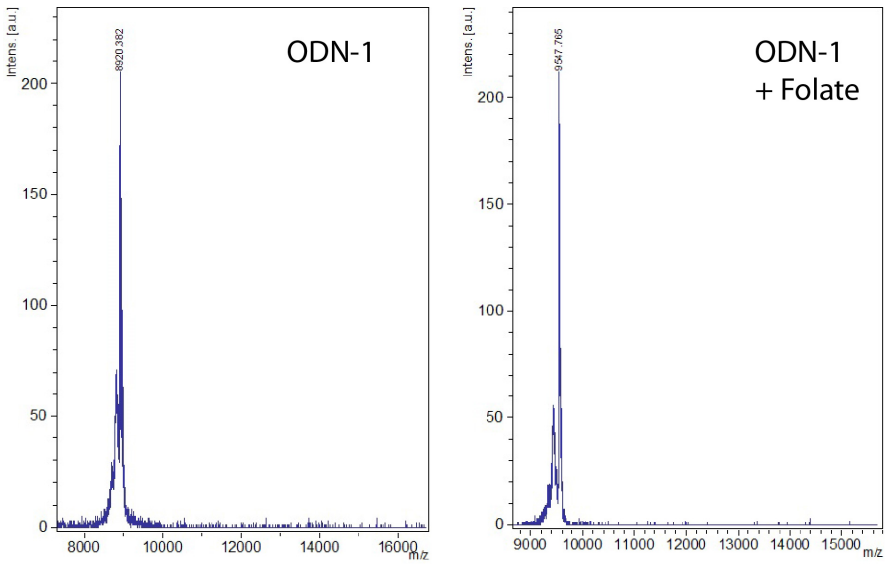

Figure S2. *Cont.*

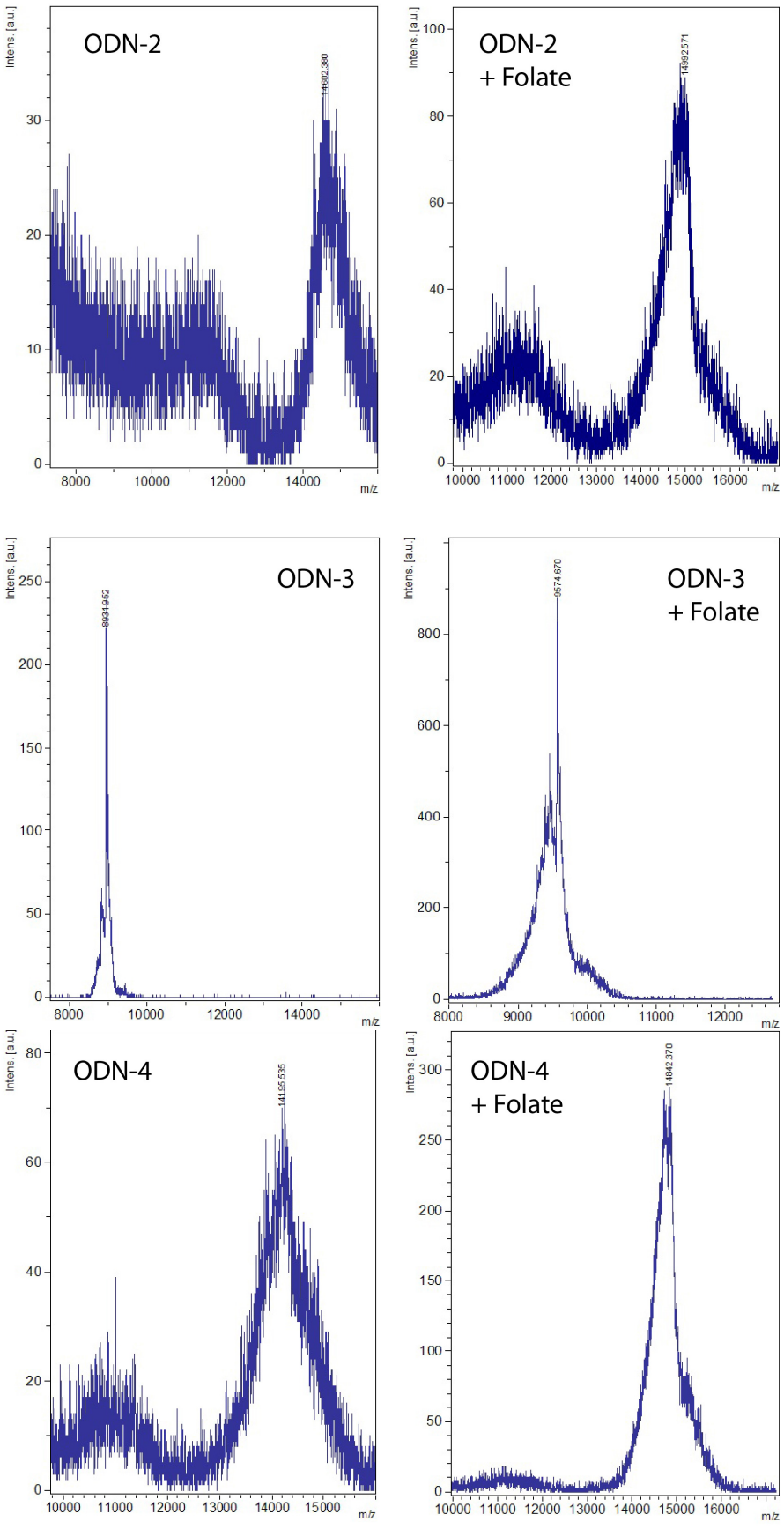

Figure S2. *Cont.*

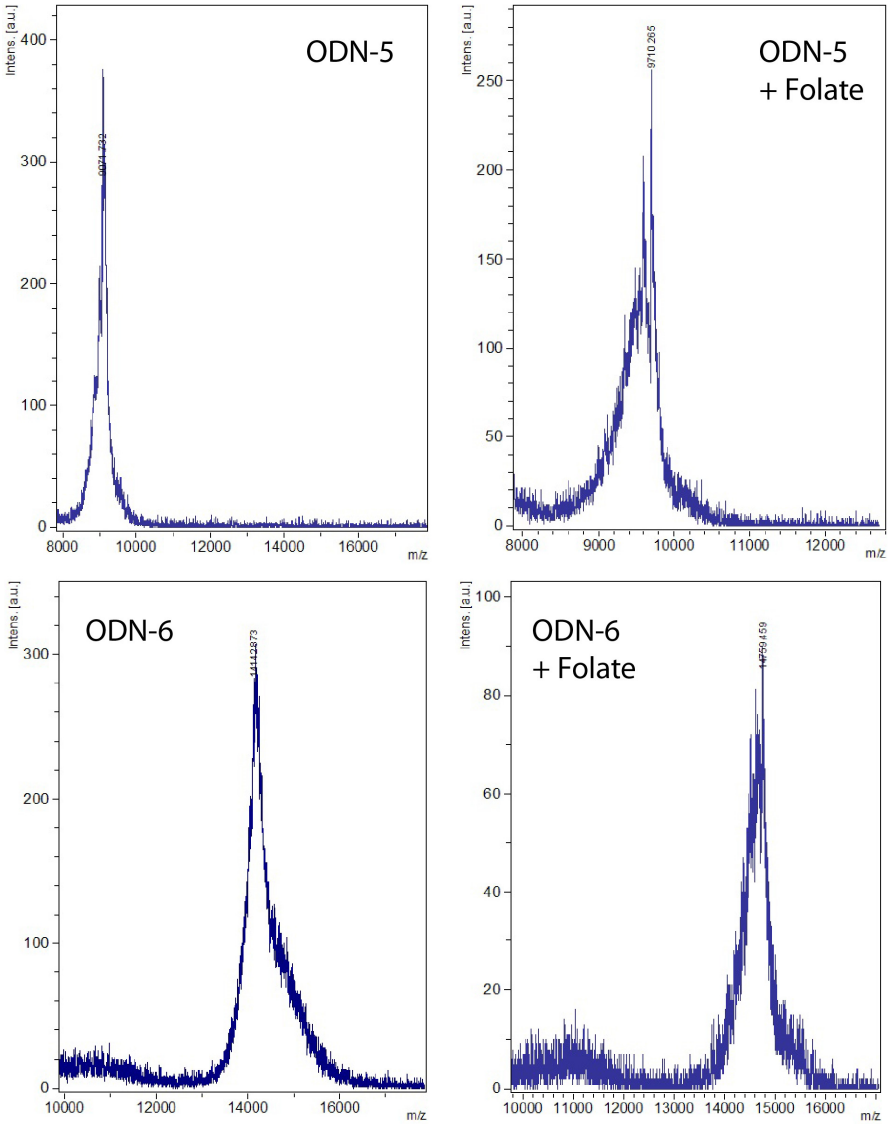

Figure S2. Mass spectrometry analysis of 6 oligonucleotides before and after folate conjugation.

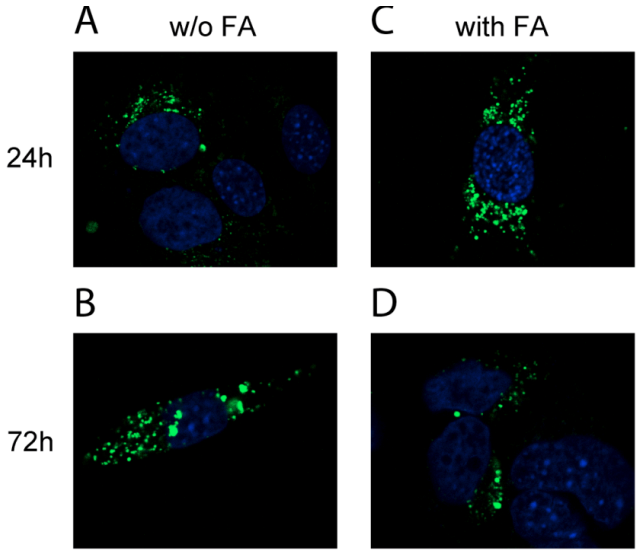

Figure S3. Endosomal uptake of unmodified (**a**,**b**) and folate-modified (**c**,**d**) DNA nanotubes after 24 h and 72 h of incubation.

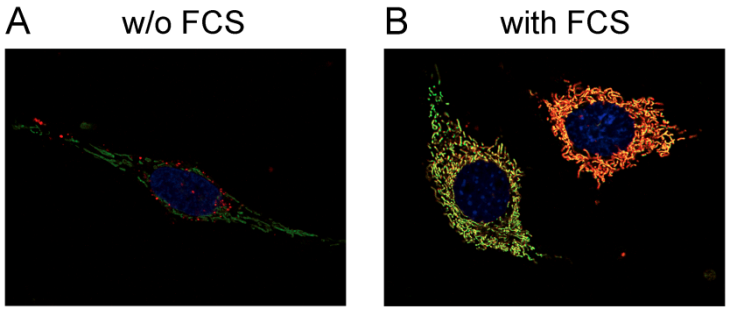

Figure S4. Mitochondrial colocalization of the mitochondrial dye Mito-tracker green (shown in green) and DNA nanotubes coupled to Atto 647 (shown in Red) after culture medium (**a**) without FCS and (**b**) with FCS.

Supporting Information for Associated Publication P2

Membrane-Assisted Growth of DNA Origami Nanostructure Arrays

by

Samet Kocabey, Susanne Kempter, Jonathan List, Yongzheng Xing, Wooli Bae, Daniel Schiffels, William M. Shih, Friedrich C. Simmel and Tim Liedl

published in

ACS Nano 2015, 9(4), 3530-39

Supporting Information

Membrane-Assisted Growth of DNA Origami Nanostructure Arrays

Samet Kocabey[1], Susanne Kempter[1], Jonathan List[2], Yongzheng Xing[1], Wooli Bae[1], Daniel Schiffels[1], William M. Shih[3,4], Friedrich C. Simmel[2], Tim Liedl[1]

[1]Fakultät für Physik and Center for Nanoscience, Ludwig-Maximilians-Universität, Geschwister-Scholl-Platz 1, 80539 München, Germany;

[2]Physik-Department, Technische Universität München, Am Coulombwall 4a, 85748 Garching, Germany;

[3]Wyss Institute for Biologically Inspired Engineering and [4]Biological Chemistry and Molecular Pharmacology, Harvard Medical School, Boston, MA, 02115, United States

Figure S1. Schematic design of DNA origami block. Scaffold routing and staple design in two-dimensional representation. Graphics and sequences were created using caDNAno software package.[1] Black staples show the staples chosen for cholesterol labeling and dark green staples show the staples chosen for dye labeling.

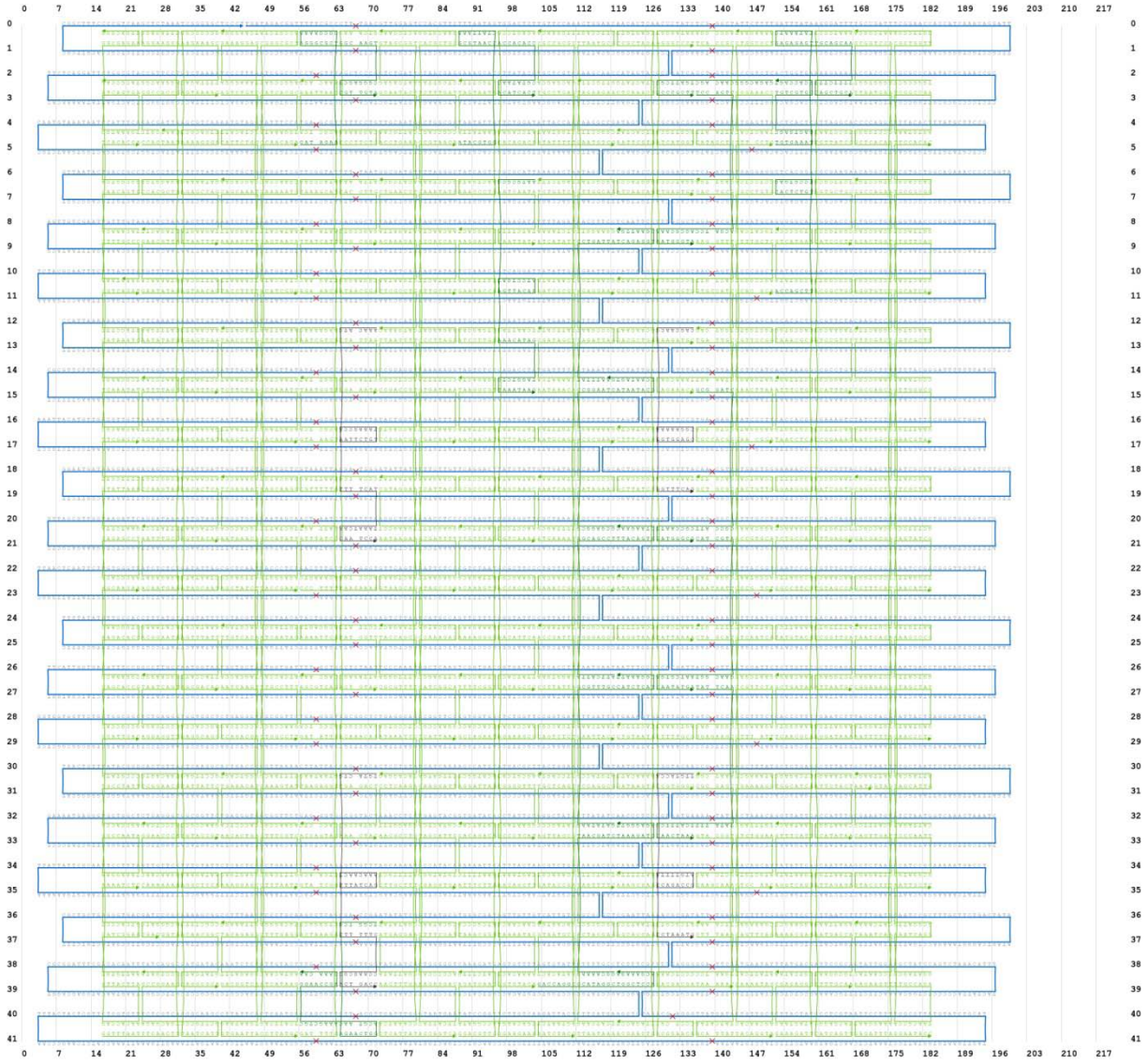

Schematic design of DNA origami triskelion. Scaffold routing and staple design in two-dimensional representation. Graphics and sequences were created using caDNAno software package.[1] Black staples indicate the staples chosen for cholesterol labeling, dark green staples for dye labeling, grey staples were used for trimer formation and blue staples were used for lattice formation.

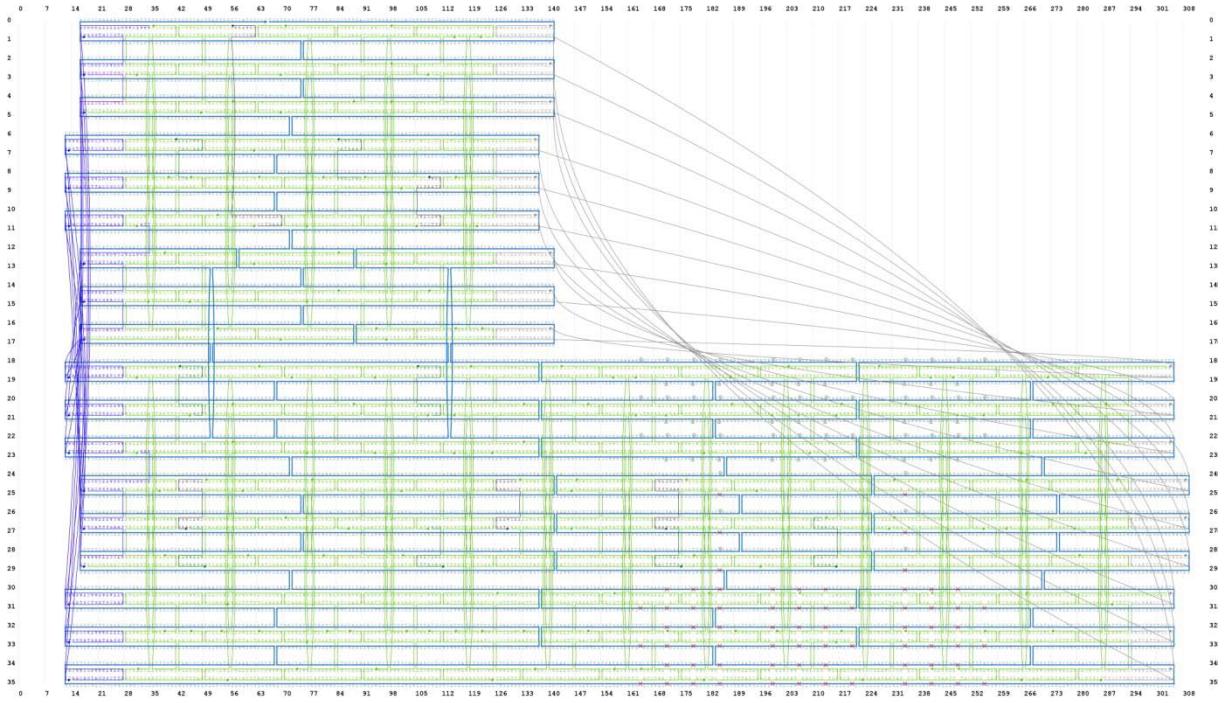

Figure S2. Gel Analysis of DNA Origami Blocks Folded with Cholesterol. 2 % Agarose gel, 1x TAE buffer 11 mM Mg^{2+}. 1) 1 kb ladder 2) p8064 scaffold 3) Block with 1 cholesterol 4) Block with 2 cholesterol 5) Block with 3 cholesterol 6) Block with 4 cholesterol 7) Block without cholesterol.

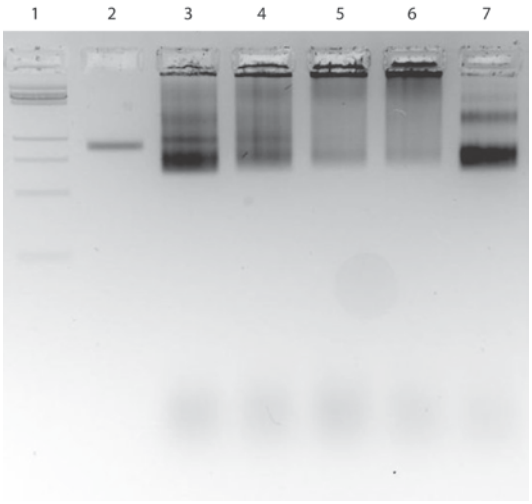

Figure S3. Schematic design of DNA origami block dimer (right edge). Scheme showing DNA origami block dimer formation. 6 pairs of complementary staples at the right edge of the origami were used. Arrows indicate the hybridization of 10 nt-long complementary regions. The helix numbers and their positions within the square lattice orientations are depicted at the bottom right corner.

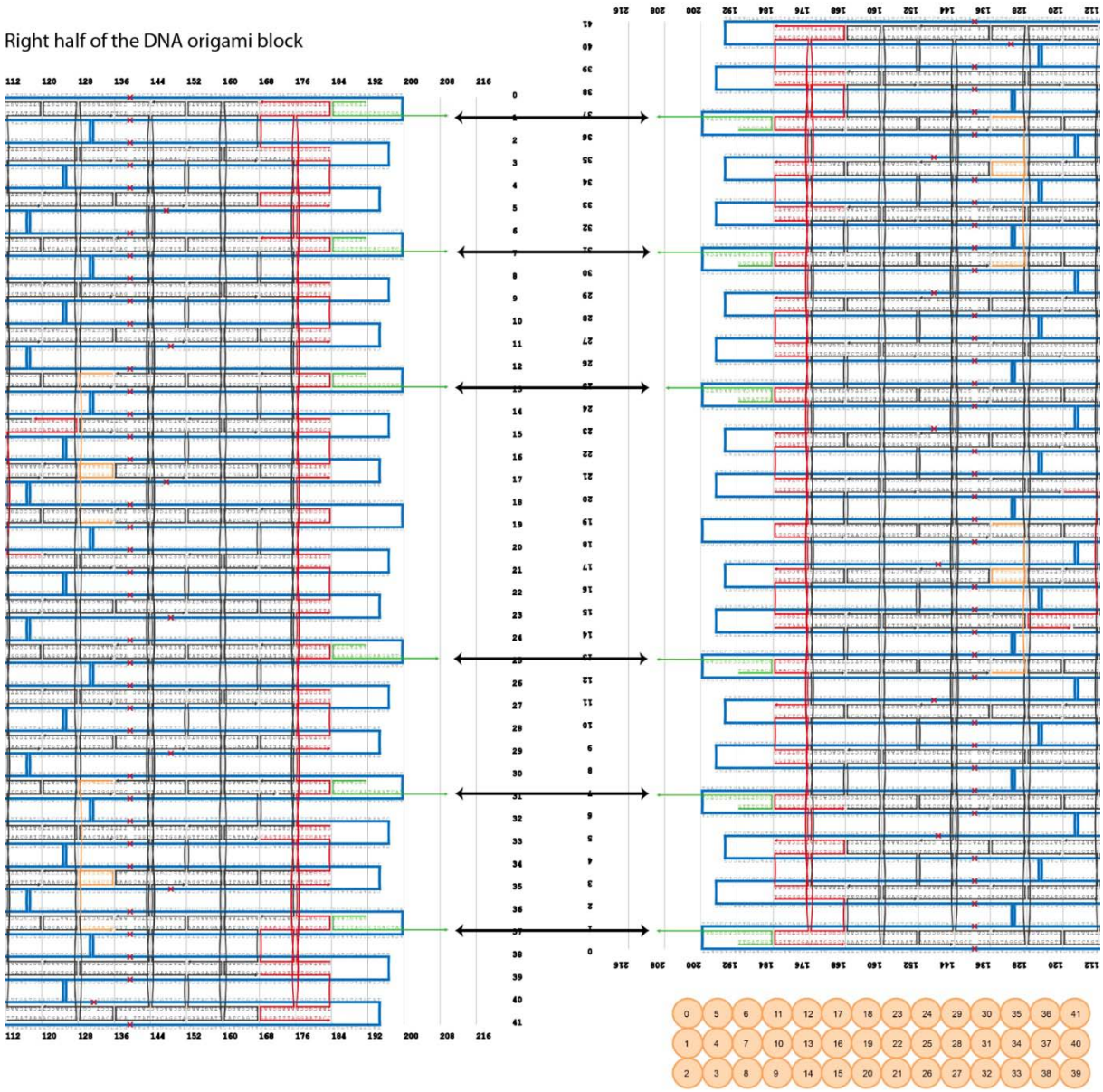

Figure S4. Schematic design of alternative DNA origami block dimer (left edge). Scheme showing DNA origami block dimer formation. 6 pairs of complementary staples at the left edge of the origami were used. Arrows indicate the hybridization of 10 nt-long complementary regions. The helix numbers and their positions within the square lattice are depicted at the bottom right corner.

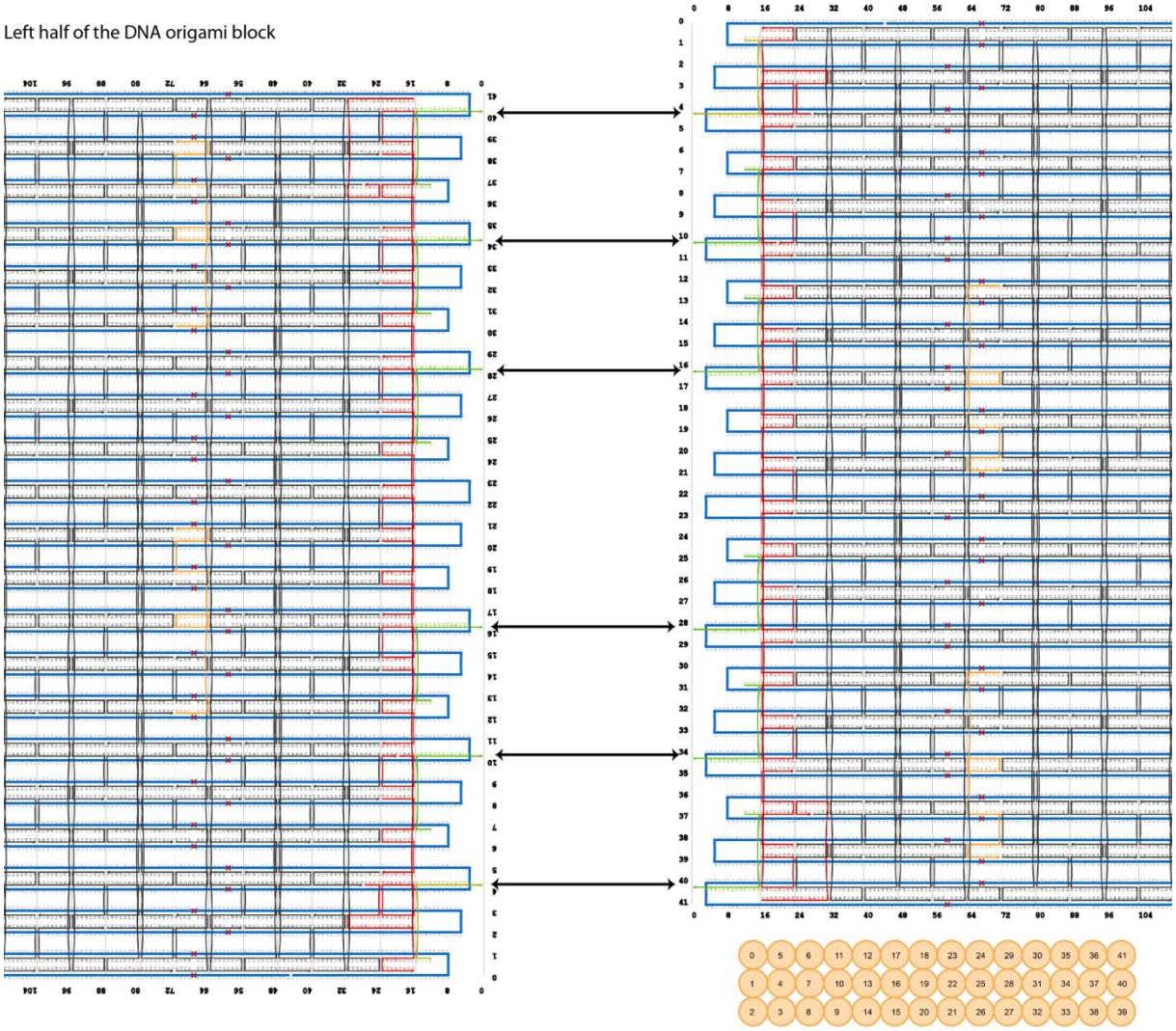

Figure S5. Gel Analysis of DNA Origami Block Monomers and Dimers. 2 % Agarose gel, 1x TAE buffer 11 mM Mg^{2+}. 1) 1 kb ladder 2) Block monomer 3) Block dimer assembled from the left side 4) Block monomer 5) Block dimer assembled from the right side.

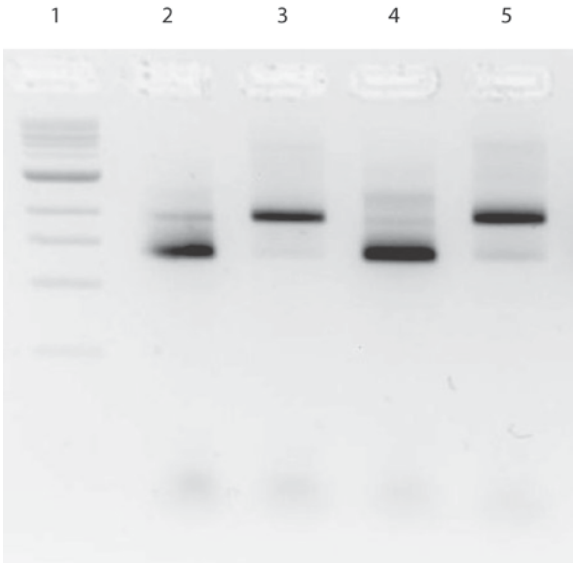

Figure S6. FRAP Analysis of DOPC/Texas Red Membrane. Left: Representative fluorescence images of DOPC bilayer before and after photobleaching. 20 frame were captured over the course of 14 s. For clarity, only 6 frames are depicted here. Right: Time (in s) *vs.* Intensity plot acquired from the images shown in the left panel. A one-phase association approach was used for curve fitting.[2]

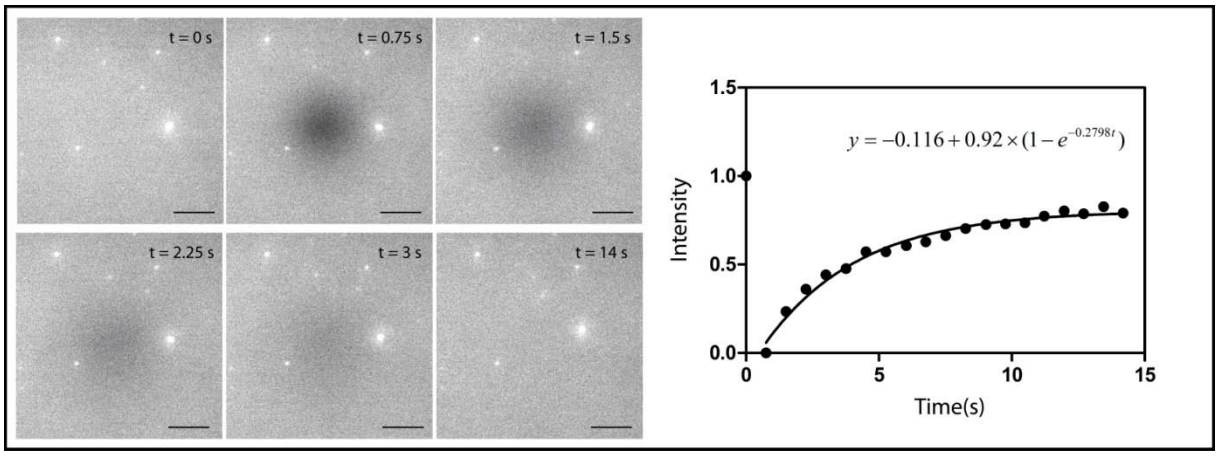

Figure S7. Schematic design of DNA origami block for 1D polymerization. The connector staples for 1D polymerization are depicted in orange.

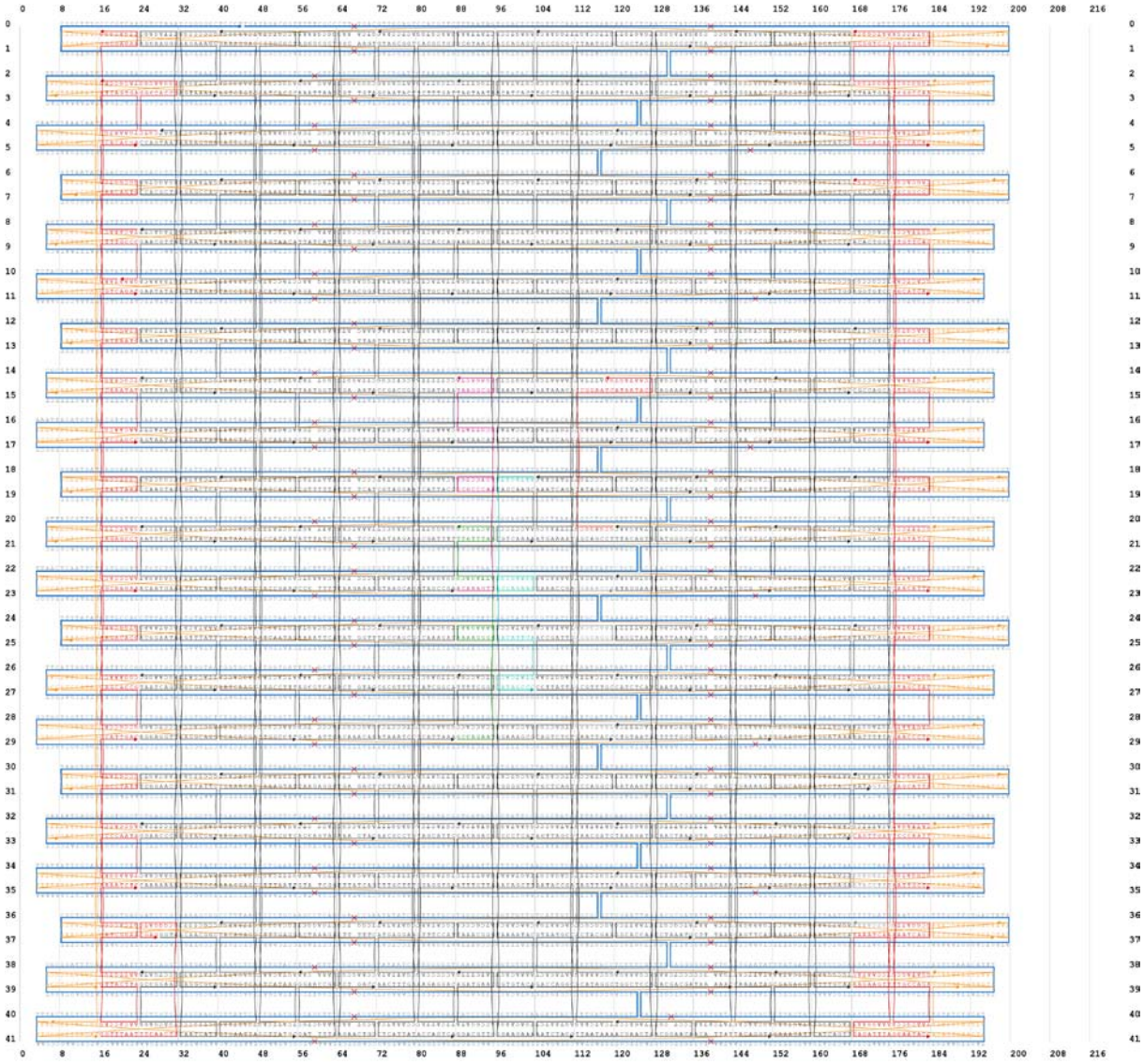

Figure S8. Fluorescence images of DNA origami arrays. Images show the 1D polymerization of DNA origami blocks. The same region on the SLB was captured with 1 h intervals. (scale bars: 5 µm)

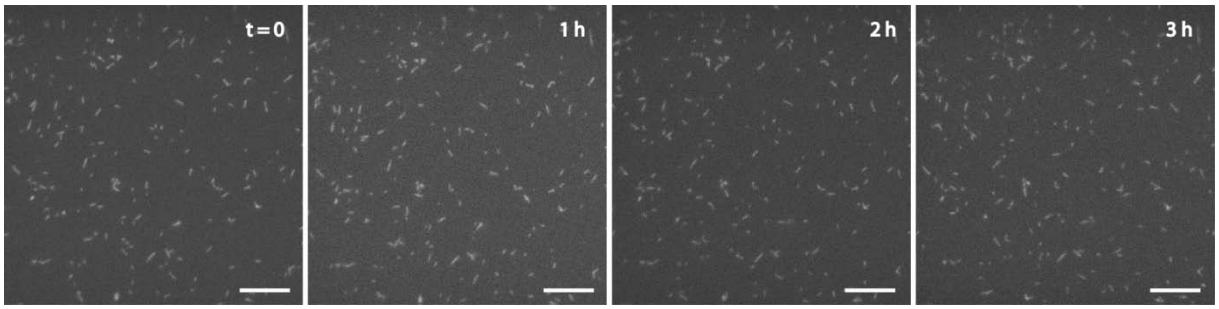

Figure S9. Schematic design of DNA origami block for 2D polymerization. The connector staples for 2D polymerization are depicted in pink and turquise for the each two opposite corners.

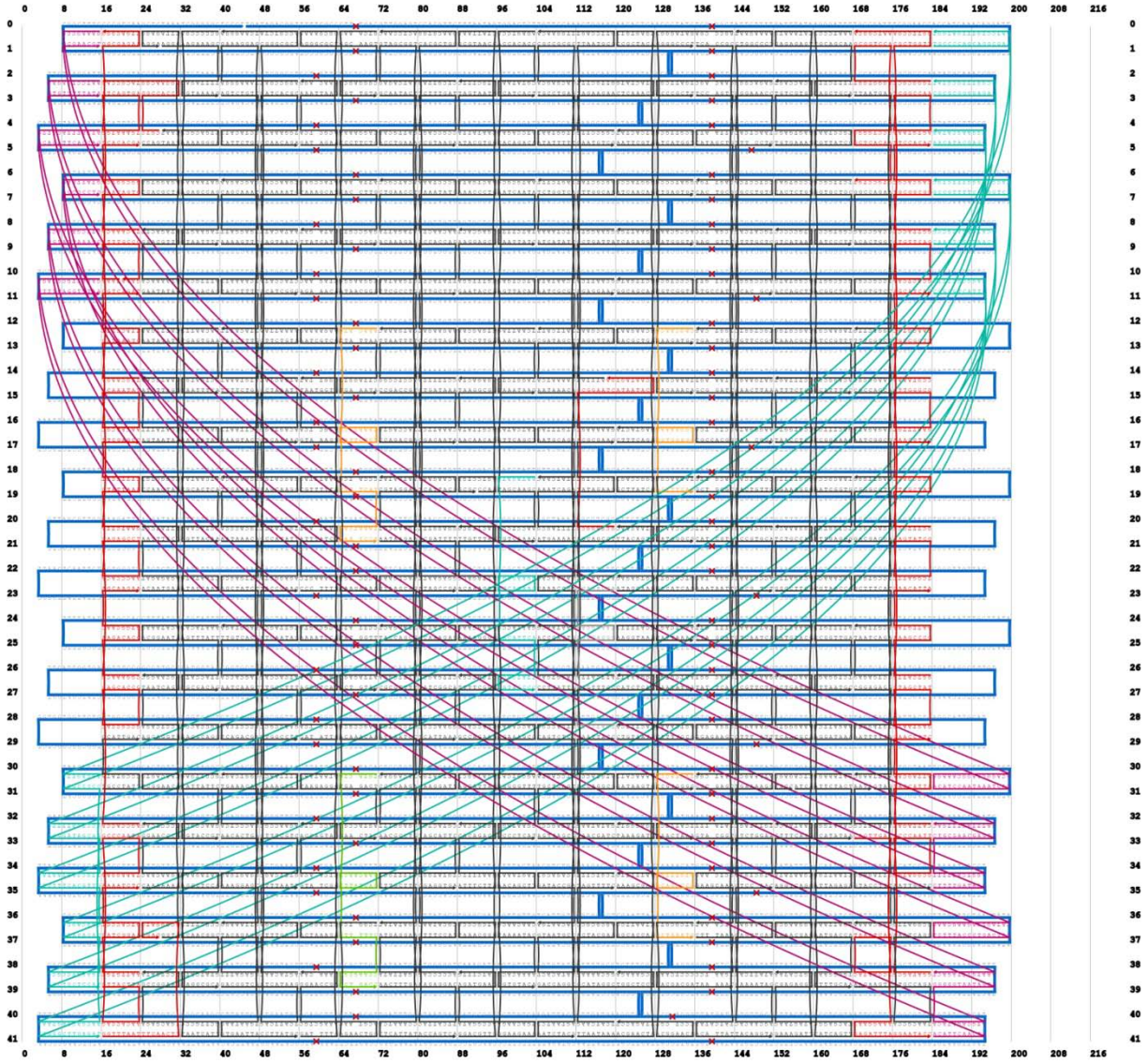

Figure S10. AFM images of DNA origami block arrays formed without SLB support. The DNA structures were assembled in solution and then deposited on the mica using high Mg^{2+} concentration (125mM $MgCl_2$, 400mM Tris, 200mM acetic acid, and 10mM EDTA, pH 8.5). The scan rate of the images is 5 Hz and the scan size of the images is 512x512 pixels.

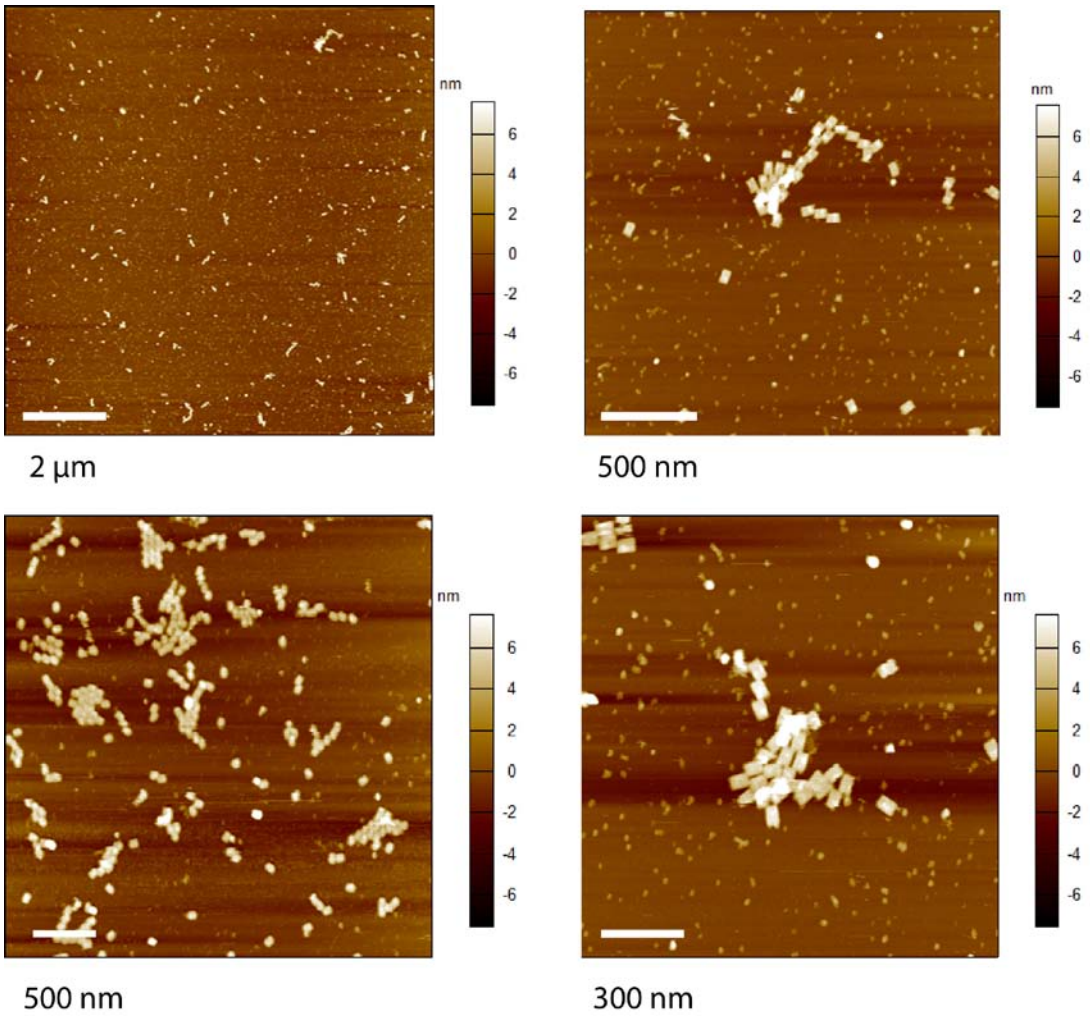

Figure S11. AFM images of the lipid bilayer at low salt concentration (10 mM HEPES, 150 mM NaCl, 0 mM Mg^{2+}, pH 7.6). The scan rate of the images is 6.5 Hz and the scan size of the images is 512x512 pixels.

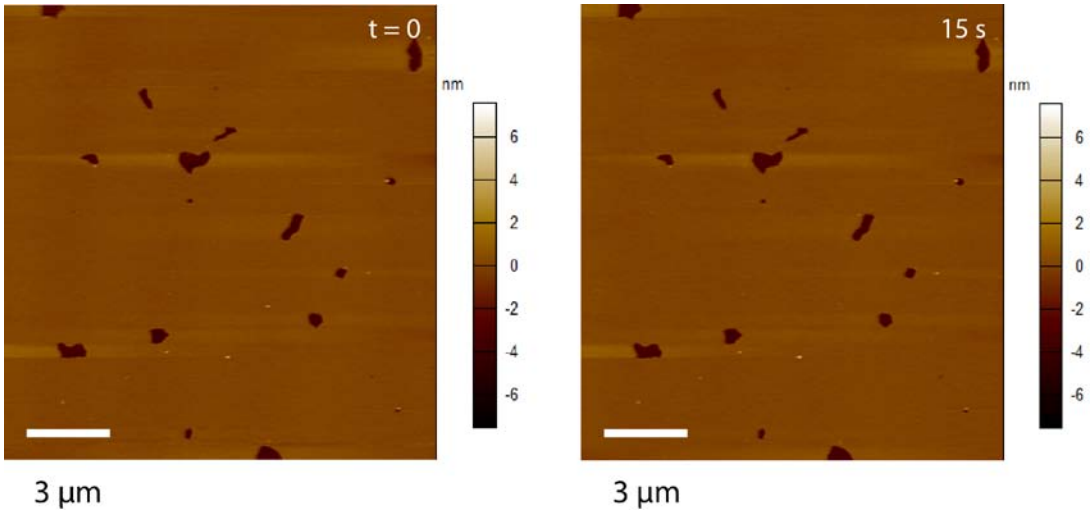

Figure S12. TEM image of triskelion arrays. Both hexagons and pentagons form during the assembly. Clusters and multiple layers of lattices were also observed. The triskelion lattices were assembled in solution (without SLB support) and deposited on the carbon-coated EM grids. (scale bars: 100 nm)

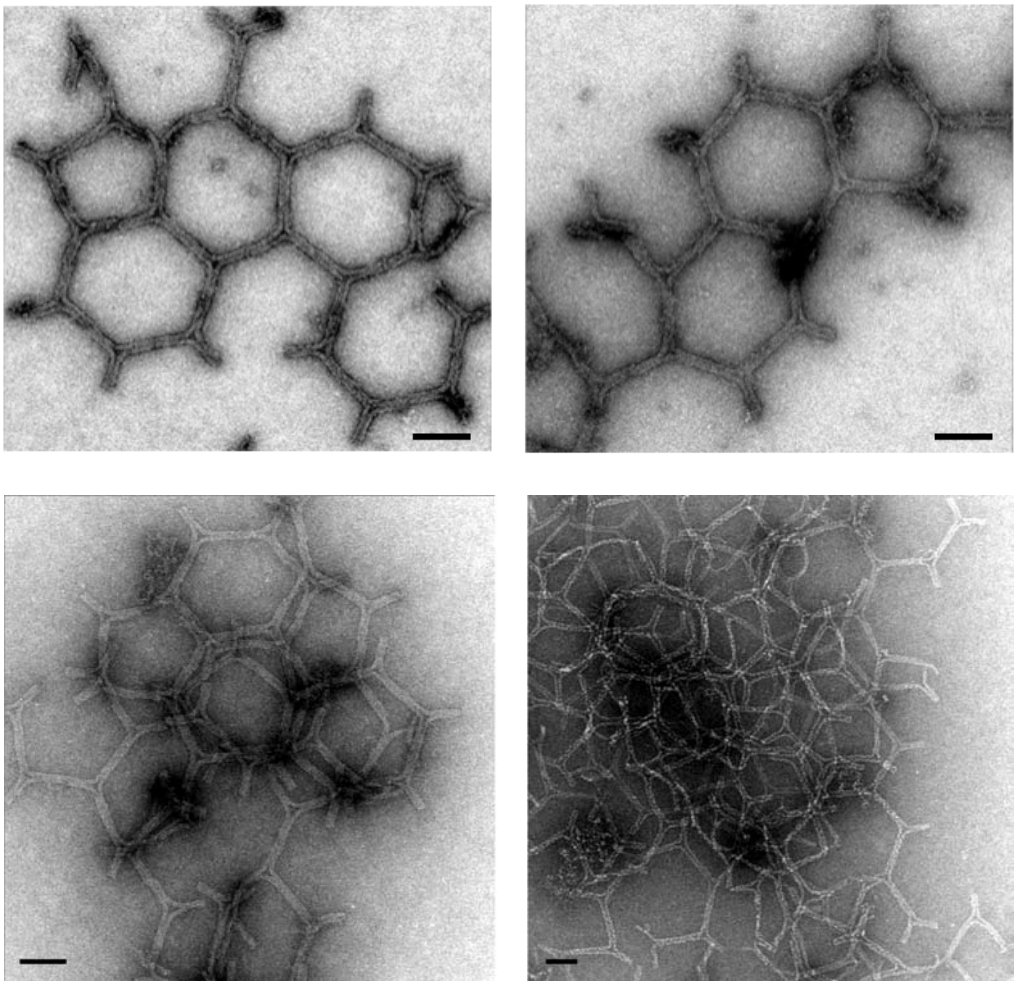

Figure S13. SUVs without DNA origami nanostructures. Left: TEM image of SUVs without DNA origami nanostructures. Right: DLS measurements of SUVs without DNA origami nanostructures.

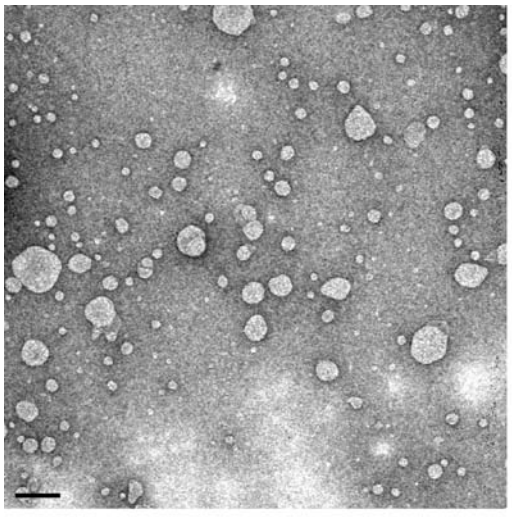

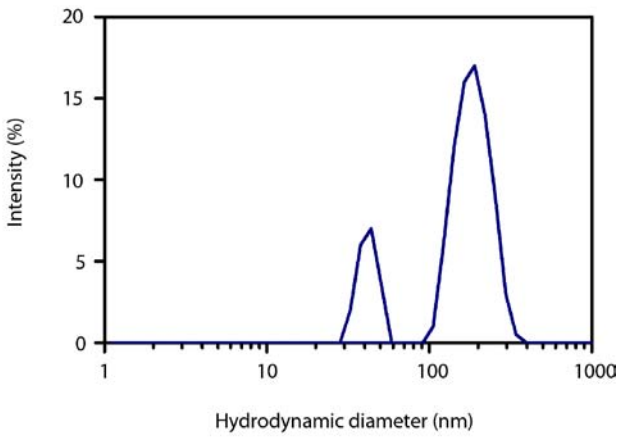

Figure S14. Stability of DNA Origami Block Nanostructures in Mg^{2+}-free buffer (10 mM HEPES, 150 mM NaCl, pH 7.6). Left: TEM images of DNA origami blocks after 24 hrs of incubation. Middle: TEM images of DNA origami blocks after 72 hrs of incubation. Right: Agarose gel analysis of DNA origami blocks after 72 hrs of incubation in Mg^{2+}-free buffer**.** (2 % Agarose gel with 11 mM Mg^{2+})

Amicon 100K Filter (Millipore) was used for buffer exchange. To 100 µl of solution containing DNA origami after folding (with 100 nM staple strands and 10 nM scaffold strand) 400 µl of Mg2+-free buffer was added. The solution was centrifuged at 13000 g for 6 min. The centrifugal steps were repeated 3 times with fresh Mg2+-free buffer added in every step. The final solution (~30 µl) was used for TEM imaging and gel electrophoresis after 72 hrs of incubation at room temperature.

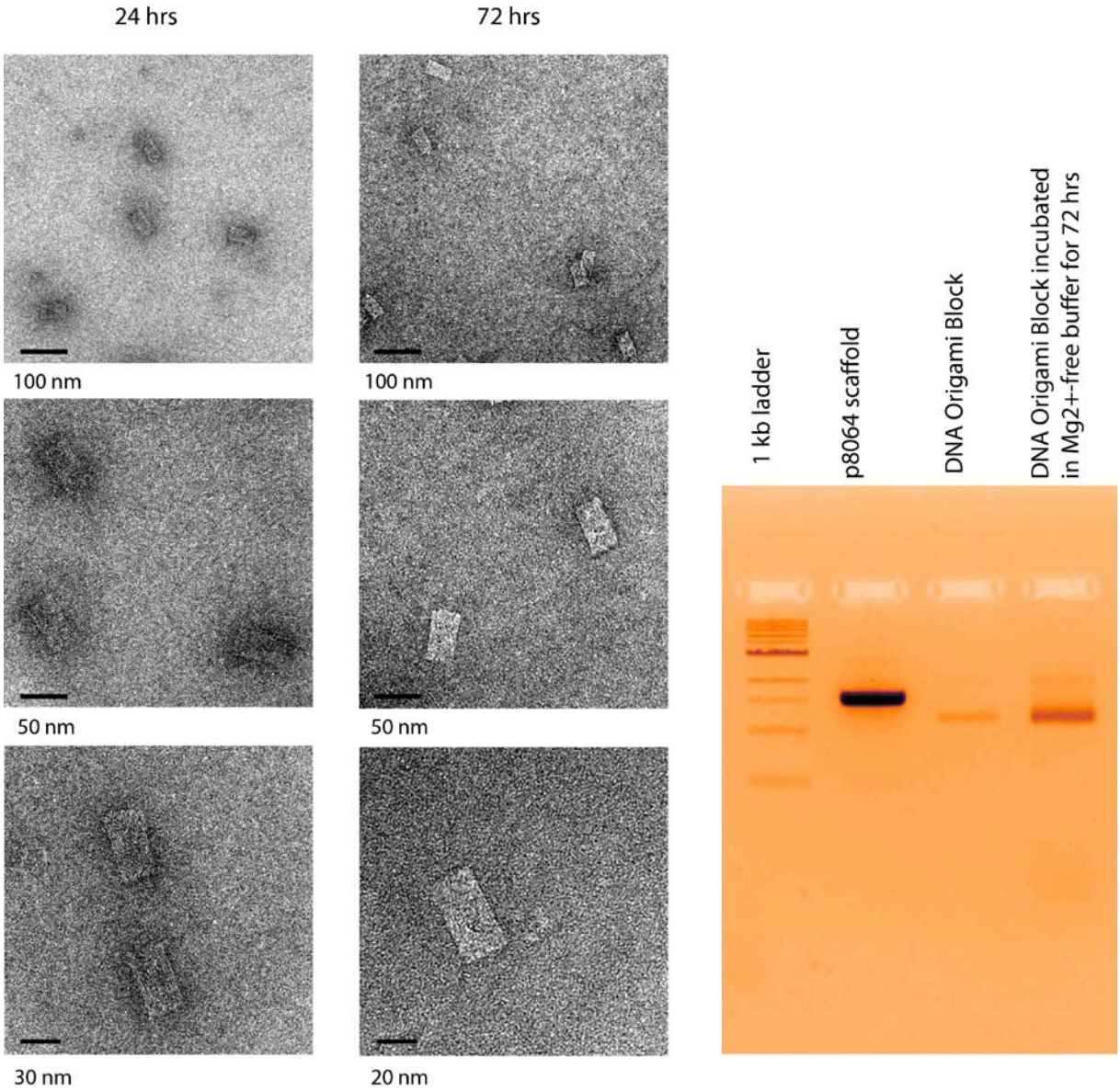

Table S1. Staple sequences for DNA Origami Block Assembly and Polymerization

	Unmodified Staples
Oligo1	GCCCCCGAAAAAGGGATTGACGCTAGAGCCAGTAGAAGTATTAATTTT
Oligo2	GTCAAAGCCCTTCTGCAGGAAAACACCTTGGAGCCGTCTTGCGGA
Oligo3	AGCCCGAGATAGGGTATCATGGTGCGTTGCGTTGAGTGT
Oligo4	AAATCCCTTGTTATCCTGCCTAATGGTGCTGCCGGTGCCGCATCCCTT
Oligo5	TCACCGCATTAATTCATAGCTGCAGTTGA
Oligo6	AGGCCGATTAAAGGGAGAAAGGAGCCTACATTCATTCTGGCAGCAGAA
Oligo7	CTCGTTAGAATCAGAGGTAGCGGTCATTGCAAACCTGAAAACATCGCC
Oligo8	GACGAGCACGCCGCGCCTGGTAATATATTTTTGAATGTCG
Oligo9	GAGACGGGCAACAGCTGATTCGCGCCCGCTT
Oligo10	AGTCTGTCTGAGGATTCAGCAAATTCAAAATTTACCTTTTTTACATTT
Oligo11	GCAATACTATAGATTACTGAACCTCTGAATAATTCGCCTGGATGAAAC
Oligo12	TCCAGTCACGATCCAGCGCAAAAATGGGTA
Oligo13	TTAATGAAGCAGCCAGGGCCAGAATCCGCCGGAGGTGTCCCGGACTTG
Oligo14	CGGCCTTGTTAATGCGGTTCCAGTTTGGAACA
Oligo15	CCAGTAATTTTAGAGCAGGAAGGGAAGAAAGCTTTTAGACAGTAAAAG
Oligo16	GATAGAAGGCGAAAAAGGGCGCTGGCAAGTCGGGAGCTCGTTGTA
Oligo17	ATACGTGGCTATTAAAGCGTAACCACCACACCCGTATAACACATCACT
Oligo18	AATTCGTATGAGTGTTCCGCTACAGGGGCCCT
Oligo19	TGTGAAATTATAAATCGAGAGAGTTGCAGCAATTTTCTTTCAGCTGCA
Oligo20	GATAAAACAGTAACAGATTTGCACTGAGTGAAGCTGATGCTAATTTCA
Oligo21	ATTAAAAATAACGGATGGAAGGGCTATTAACTTAGGTTTGAAATA
Oligo22	GGATCCCCCGTCGGTGGCCCTGCGGAAGATGC
Oligo23	TCTTCGCGACGGCTGGGCGCGGTTGTCCGTTTACAGGCGGTCATTTGC
Oligo24	CACTGCGCACTGTTGTGCCATCTGGTCAG
Oligo25	AATACATTCATCACGCTGGAAATACGGGCGCTACCGTCTATCAAGGGA
Oligo26	AACAACTATCTTTGATCCGCCAGCCACGCTGCGAACGTGGACTCCAAC
Oligo27	GGAAGGTTTAGAAGAACTCAAACTGTACTATGGTTGCTTT
Oligo28	TGCATCAGGGGAAACCTAACTCACCTGGCCCTAAAAGAAT
Oligo29	AAAAGTTTATGTAAATTAACCTTGGCTTAATTAAAGTACCAGAAACCA
Oligo30	ACAAAGAAACCTCCGGTTAATTTTTACCAGTACCAGACGAAATAATAT
Oligo31	ATCATATTCAAAATCACGATAGCTCTGTTTAGAATGCAGATTATCAAC
Oligo32	AAGGTTTGTAAAGTTAAACGAGCAGAAACA
Oligo33	ACACTGGTAAAGCCGCTTTCGTCTGAGAGATAAATCGGCGAAGTTGGG
Oligo34	GCAATTCAGTTGGCAAAGCGCTATTAGTCTTT
Oligo35	GAATATACAGAGGTGACCACGCTGCAAT
Oligo36	AGAAACAATACCGAATAAAGCATACGCTCAAAATTAACAAACAGG
Oligo37	GAATACCAAACTGATAAAACCCTCCAATATTATAGTAATAGTGCTTTC
Oligo38	GGCAGCACGGGTACCGATCAACAGCTCACTAT
Oligo39	ACCAGCTTTCCGTGAGCACTCTGTGAGTGAGCTGTCGTGCTCACCAGT
Oligo40	AACAATTTGAGAATATGAGAATCGCGCACTCAGCTACAATAGTTACAA
Oligo41	AAACATCAATTCTGTTAAAGCCATTTTCATTAAATCAACAATCCA
Oligo42	CAGCAACCGGTGGAGCCGGAAAAAGGTTTCAG
Oligo43	TAGAACGTCCGGAAACGACTTTCTGATCGGTGTCTGGTGCTTTGAGGG
Oligo44	TGATTGCGCTCTCACGCCACGGGACGTTG

Oligo45	ATAACTATGAGTAACACTACCATAGAAAAATCCGAACCACCCAACAGA
Oligo46	CCTTTTTAACCACCAGTTATACTTCAAATATCGCCCTAAAGCGTAAGA
Oligo47	ATTTATCCTGATTATCAGAGGTGGAATTGA
Oligo48	GATGAAGGCTTTGCTCAGCCGGGTCGCCTGTGCCTCCTCATTTCCTG
Oligo49	TCTTCTGATGCACCCATCGAGAACATTGAGCGAGCTATCTAACGTAGA
Oligo50	CCGACCGTTGAAGCCTCGTAGGAAAACTGAACGTAAGCAGTTAAGACT
Oligo51	AATAAACATTTTAGCGAAATCAGAAAAAACAGGAAACCGATAATAACG
Oligo52	GCGGATCCGCCATTCGCCAATTGATGGGCG
Oligo53	CGCCAGCAGCACCGCTCGGGCCTCTCCGTGGGGCTTTCATACGTTAAT
Oligo54	GAAAAAGCTAGATTAAGCCCGAATAGAGGAAC
Oligo55	AGTAATAACATTTGAAAATATATGGTAAAACAGAACGTTATTAGACTT
Oligo56	GTAAAGTAAGAAAACAATCGTCGTTAGAACTTATCATTAATAGAT
Oligo57	AACAACATCTGAGCAAATCCTTGATGTTTGGAAAGGAGCGGGAGCACT
Oligo58	CTTTCAGAGCAAGAATGACGCTGAGCTTGATG
Oligo59	TAACCTCACAGCGTGGCAAACGCGGCGGTATGGTCATAAAGTGCCCCC
Oligo60	ATCAATAAATAGCAATCTAATATCAGTTTATTTTACCATTAGCGACAG
Oligo61	CCCATCCTAAGAAAAACCCTGATATGGTTATTAGAGCACTGTAG
Oligo62	TAAAACGAGCCATCAAGTCACGTTTATTAAAA
Oligo63	TAACGCCATGTAGCCAAACAAACGCCGGTTGATCTGGAGCATTAATGC
Oligo64	GCTGCGCGGGATAGAAATAATTTTTTGTT
Oligo65	TGCTATTTCCTAAATTACAGTAGGCTTCTGTAAAAATTAAACATCGGG
Oligo66	GGAGGTTTGTGATAAACAAATTCTCCCTTAGAAAGAAGATATTGCTTT
Oligo67	AGGCAAAGAAACTTAAAAGGGATACGTTCCGGTGCTGGTCCCACGCA
Oligo68	AATAAACATAGCACCATTGTCACAACCCTCAGTCAGACGAGGGTCAGT
Oligo69	AATAAGAAATTTGGGATACCAGCGCTCCCTCAATAAATCCTACAGGAG
Oligo70	ATGAAAATAAGGTGAAACCGATTGATCACCGGCAGTCTCTTTCCAGTA
Oligo71	CATCGTAGAACGGTAATCGTGACAATATGA
Oligo72	GACGACGACCTGAGAGTAATCAGATGTAGGTAAATTTTTAAATTAAGC
Oligo73	AATAACATTATAGAAGGCCCCTGTACGCGAAG
Oligo74	ACAATGAATCGGCTGTCCAAGTACCCATATTTATTTTAGTAAATCCAA
Oligo75	CCCTTTTTAATTTACCGTTTTTAACGCTCATAATGGTTGGGTTAT
Oligo76	ATAGGAACCGGCCAGTGCTTATCCGAGTACTA
Oligo77	GGCCTTCCGGGTTTTCGGAAGGGCCCGTGGTGATTTCTGCCCTTTAGT
Oligo78	AAATACATGAGGCAGGAGCCACCATATTATTCGAACCGCCTGTACCGT
Oligo79	CCTTATTACAAACAAGAGCCGCCTGAGACTAGTACCGCAAACTAC
Oligo80	GAATACCCGGAAAGCGAACCAGAGCGGGGTTTGGAATAGGGCCCTCAT
Oligo81	AAATCAGCCTTTTGCGAGTCAAATCCGTGGGG
Oligo82	ATTTTGTTAGGATAAAAAGATTCAATTCTACTCAAATGGTCCATATAA
Oligo83	CTAGCATCGGAGACGGAGAAGCAAATCGG
Oligo84	ATCACCAGGCCATATTAGAGGGTAAAGCAAGCGAGCATGTGACAAAAG
Oligo85	CTTGAGCCACGATTTTGGAGAATTTCATTACCACAAGAAACGACAATA
Oligo86	ATTCATTAAGCAGCCTTTACAGTACTAAGAAC
Oligo87	GAATCGATACCGTGCAACCGTAATAACTGTTGCCAGTCACGAACGGA
Oligo88	AATCAAGTCACCCTCATGAAACATGGAGTGAGAAAGGAGCGTTAAAGG
Oligo89	CGCGTTTTGGAGGTTTCCTCAAGAATTTTGCTCTTGCTTTCGATATAT
Oligo90	CCTTATTATATAGCCCTGCTCAGTCCAGACGTGATACCGAGACAATGA
Oligo91	TATTCAATATATTTTCATTTCGCAACTAAA

Oligo92	CGGAGAGGACATTTCGAATA
Oligo93	AGGAGGTTACATAAAGACGGAATAAGAGAGATAATTTGCCTTTATCCT
Oligo94	GATATTCACGCAGTAAAAATTCAACAAAGTCATTTATCCGATTAGT
Oligo95	CTGTAATATCATTTTTAAGGTAAAGGTGAGAG
Oligo96	TCAACGCAAAAATTCGTATGTACCGCGGATTGTCTGCCAGCGGAAACC
Oligo97	GCCTTGAGAGGCTCCAAATAGAAAGCAACGGCGTATCATCGAGGCGCA
Oligo98	TGTACTGTTTATCAGAAACAACTCTTTTTCCCAAGCGCACTGACC
Oligo99	AGCGTCATAACAGCTTTAGTAAATTAAAATACAAAACACTGGTGTACA
Oligo100	TTGTACCACCAGACCGATGTTTTACCTAAATG
Oligo101	AATAAAGCATTAGAGATTAATTGCAATGACCATGCGGAATTTTTGCAA
Oligo102	CGCGAGCGCTCAACGAAGCAAATTCAAAT
Oligo103	AGAACCGCTTGCCTTTGAACCGCCATCAATAGTGTTAGCATACCGAAG
Oligo104	GATATAAGGCGTTTGCCATCTCATCGGAAATT
Oligo105	TGTTTAGCCCGTTCTAAGAAAGGCGTCAATCACATTAAATCGCGTCT
Oligo106	AACACTGAGGAGATTTTACAGAGGTGAATAAGGTGAATTACCTTATGC
Oligo107	AACGCCTGCGATTATAATGAGGAACCAAATCACTCATTATACCAGTCA
Oligo108	AGTTAGCGAATACACTGTAATGCCAGTAATCTAATCTACG
Oligo109	GTACGGTTGAATCCCCCTCAAAGACGACGATAAAAAC
Oligo110	TCGTCTTTACCAGGCGATGTACCGGAATTACC
Oligo111	CAAAAAAATAACAGTGTCGGAACCCCCTCAGATAATCAGTAGCAAGGC
Oligo112	GTATCGGGTAATAAGTAAGAGGCACCCTCAAGCGTCAGCAGCAAA
Oligo113	AAAGCGAAAAAACATTGATAAGTGCACTTTCA
Oligo114	AGGTCAGGCTCAGAGCTGGCATCAAAAGGGTGGCTGATAAAAACAAGA
Oligo115	CCGCTTTTTAATCATTGCTTGCCCTGACGAGAGCCGGAACGCCTGATA
Oligo116	TCGGTCGAGAACTGGACGTAACAAAGCTGCGGAACCGAGAAACAA
Oligo117	CAACAACCGGAAGAAATGACAAGAACCGGATAAGATGAACCATCTTTG
Oligo118	ATCGCGTTACGGAACACCCTCGTTTAGACCT
Oligo119	AGATTAAGCATCAGTTTACGAGGCATAGTAAGCGAGAGGCCGTCATAA
Oligo120	GGTAGGAACAACGGAACCCAACCCTCAG
Oligo121	CTTTAAATATCATAAACATTATTACAGGTA
Oligo122	AGTACAACGTTTCGTCGTTTCAGCGAAAGTATTTTTAACGTTGGCCTT
Oligo123	ACCCCCAGTAGCATTCTGTATGGGGAAGGATTTTTGATGATCATTAAA
Oligo124	GGCAAAAGTAACGATCTAAAGATGAGAGGGTT
Oligo125	ATATTCATGTCTGGAAATGCTGTATGAAAAGGATAAAGCTCTTTATT
Oligo126	GACGGTCAATCATAAGTCATTCAGCTTTGAGGTGCAGGGACTTTAATT
Oligo127	AACTTTGAAAGAGGACTTCATTACGTTTCCATCGCATAACCGAGGTGA
Oligo128	GACCAGGCGCATAGGCTGGCTCCAACGAAAGA
Oligo129	CAAAATAGAGCAACACCAGTTCAGCGAAAGACCTCCAAC
Oligo130	TCATCAAGACTACGAAAGCGCGCCTAGTTTTC
Oligo131	GATTTTACTGAGGCTACTAAAGATTCAACAACCAGTACCACCCTC
Oligo132	GGACGTTGATCGCCCATAAACGGGGAATTTTCCACAGACATGTATCAC
Oligo133	TTAATAAAACGAACTATTAATTCGGGCACCAAAATTTTTG
Oligo134	GAAAGATTAGGAAGCCAAAACGAGTGAATATAGTTTCATTCAATAACC
Oligo135	TGGGCGCCAGGGTGGTGCGGTCCAGCCTGGGGGCTCACAAGTGCCTGT
Oligo136	CGTCGGCCACCGAGGAACGGTACGCCAG
Oligo137	TACAAACAATCAGTGATGAAATGGGGCGAGAATTGACGGG
Oligo138	GGTTACCTTCGGCCAAAGTGTAAACGCTGGTTGGTTCCGAAATCGGCA

Oligo139	TCGCAAGACTTTGCCCGAAA
Oligo140	CCGTAAAAGTGTTCAGGCACTCAATGCGGCGGCAGCACGCTTCCACAC
Oligo141	GAATCTTATCAAATATAACAACGCCATAAATCTTACCTTTCGTCAGAT
Oligo142	GCTTTCCGGTTGGGCGGAATTTGTCGTCGCTGGAACGTGCAGCATCAG
Oligo143	CGGAAACGCAGAGCCTAACCCACAGTATTAAACTTTCCTTTTCGAGCC
Oligo144	GGTCATTGCAGTATCGTCGGATTCTTCGCTATAGGCGATTAAACGTAC
Oligo145	AGCCACCACAGCACCGGCCGCCACAAGACACCGTGGCAACAGCAAGAA
Oligo146	CATTAGATGTAGCTATGAGTAATGAAAGCCCCAATTGTAACAACATTA
Oligo147	CAGTTGATTCCAATACTAAATCAAAAAGGAATGAGATTTAGGAATACC
Oligo148	AATTGTGTGCCCAATATAAAGGAATGCCTATTCCCGTATAGCATTGAC
Oligo149	GGATAGCGTCCCAATTGCGGATGGTAGCATTAATTAGCAAGAACCCTC
Oligo150	GTTACTTAAACACCAGCATCGGAAGTCACCCTAAAATCTC
Oligo151	AAGAAGTTTTGCCAGATAACGCCAAAATCAGGGCGGATTGAATTGCTC
Oligo152	GGTTTAATTTCAACTTGCGGGATCCGAG
Oligo153	AATGCGCGAGTTACAAATCCTGATAAACATAGTAGGTCTGTAAATAAG
Oligo154	AGAGTCCACACAGACAATCCAGAAAATCAATATATCTTTAGAATTATC
Oligo155	ACAAAGTTAGTCCTGAGCGCCCAAGCGTTATATAAGGCGTAGAGACTA
Oligo156	TCAATTACGTTCAGCTTATCATATTAGCAAGCAACCTCCCCGTCAAAA
Oligo157	TGCCTGAGATCTAAAATCTGGTCATCAATATAAATCGCGCTATTCATT
Oligo158	GCCAGAATAAAAGAACAAAAGGGCATTAGACGTTGTTTAAGACTTGCG
Oligo159	GCGAGGCGCCGGAATCATAATACGTCAATAGTGA
Oligo160	AATAGATAACCAGAAGGGAAGCGCGACATTCATTATCACCCATAGCCC
Oligo161	ATTTCTTAACATGGCTAGGATTAGCCACCACCTTTTCGGTGTCACCGA
Oligo162	CGTACTCACATCGGCAGGAACCGCCCAAAGACTGGCATGAATAGCCGA
	Staples for Cholesterol labeling
	(Anchor sequences for cholesterol labeling were shown with orange color)
Oligo1	CATTCTCCTATTACTACCTTTAAACATCAATTCTGTTAAAGCCATTT
Oligo2	TCATTAAATCAACAATCCA
Oligo3	CATTCTCCTATTACTACCTTCAGCAACCGGTGGAGCCGGAAAAAGGTTTCAG
Oligo4	CATTCTCCTATTACTACCTTTTGTACTGTTTATCAGAAACAACTCTT
Oligo5	TTTCCCAAGCGCACTGACC
Oligo6	CATTCTCCTATTACTACCTTGTACCACCAGACCGATGTTTTACCTAAATG
Oligo7	CATTCTCCTATTACTACCTTTACAAAGAAACCTCCGGTTAATTTTTACC
Oligo8	AGTACCAGACGAAATAATAT
Oligo9	CATTCTCCTATTACTACCTTAAGGTTTGTAAAGTTAAACGAGCAGAAACA
Oligo10	CATTCTCCTATTACTACCTTTCGCGTTTTGGAGGTTTCCTCAAGAATTT
Oligo11	TGCTCTTGCTTTCGATATAT
Oligo12	CATTCTCCTATTACTACCTTTATTCAATATATTTTCATTTCGCAACTAAA
	Staples for dye labeling
	(Anchor sequences for dye labeling were shown with green color)
Oligo1	GAGACGGGCAACAGCTGATTCGCGCCCGCTTCATCAACCATATCAACTTCC
Oligo2	ATTTATCCTGATTATCAGAGGTGGAATTGACATCAACCATATCAACTTCC
Oligo3	GCGGATCCGCCATTCGCCAATTGATGGGCGCATCAACCATATCAACTTCC
Oligo4	GATATAAGGCGTTTGCCATCTCATCGGAAATTCATCAACCATATCAACTTCC
Oligo5	GGCAAAAGTAACGATCTAAAGATGAGAGGGTTCATCAACCATATCAACTTCC

Oligo6	ACCAGCTTTCCGTGAGCACTCTGT
Oligo7	GAGTGAGCTGTCGTGCTCACCAGTCATCAACCATATCAACTTCC
Oligo8	TGTGAAATTATAAATCGAGAGAGT
Oligo9	TGCAGCAATTTTCTTTCAGCTGCACATCAACCATATCAACTTCC
Oligo10	ATACGTGGCTATTAAAGCGTAACC
Oligo11	ACCACACCCGTATAACACATCACTCATCAACCATATCAACTTCC
Oligo12	GATAGAAGGCGAAAAAGGGCGCT
Oligo13	GGCAAGTCGGGAGCTCGTTGTACATCAACCATATCAACTTCC
Oligo14	TCCAGTCACGATCCAGCGCAAAAATGGGTACATCAACCATATCAACTTCC
Oligo15	GCGAGGCGCCGGAATCATAATACGTCAATAGTGACATCAACCATATCAACTTCC
Oligo16	ATTCATTAAGCAGCCTTTACAGTACTAAGAACCATCAACCATATCAACTTCC
Oligo17	CATCGTAGAACGGTAATCGTGACAATATGACATCAACCATATCAACTTCC
Oligo18	TATTCAATATATTTTCATTTCGCAACTAAACATCAACCATATCAACTTCC
Oligo19	GACCAGGCGCATAGGCTGGCTCCAACGAAAGACATCAACCATATCAACTTCC
Oligo20	TCGGTCGAGAACTGGACGTAAC
Oligo21	AAAGCTGCGGAACCGAGAAACAACATCAACCATATCAACTTCC
	Connector Staples for dimerization (right side)
	(Complementary sequences for dimerization were shown with the same colors)
Oligo1	TTGATGGTTGCCCCAGCAGGCGAATACGCATGAT
Oligo2	GAAGCAAATCTTTACCCTGACTATGCTAAATTTA
Oligo3	GTTTCTGCGCCGTTTTCACGGTCACCGTAAGTAC
Oligo4	GGCAAAGAACATCCAATAAATCATCCCGTATTGG
Oligo5	TCATAACGGCAGCCTCCGGCCAGAAACTGACCTC
Oligo6	AATATTTAAAAAACAGGAAGATTGCAACTATGGA
Oligo7	GAAGCAAATCTTTACCCTGACTATATCATGCGTA
Oligo8	TTGATGGTTGCCCCAGCAGGCGAATAAATTTAGC
Oligo9	GGCAAAGAACATCCAATAAATCATGTACTTACGG
Oligo10	GTTTCTGCGCCGTTTTCACGGTCACCAATACGGG
Oligo11	AATATTTAAAAAACAGGAAGATTGGAGGTCAGTT
Oligo12	TCATAACGGCAGCCTCCGGCCAGATCCATAGTTG
	Connector Staples for dimerization (left side)
	(Complementary sequences for dimerization were shown with the same colors)
Oligo1	ACGTATTATTTACATTGAAATGTAACT
Oligo2	ACAGAACGAGTAGTAAACCGAATACGA
Oligo3	CCTGGAAATTGCGTAGAATTCTAAGGA
Oligo4	CCCCTTGCGAATAATATTTCGGAGGTC
Oligo5	AGTACAACATGTAATTTTATAGGCCCT
Oligo6	CGCACAGAACCACCACGATAAAACACC
Oligo7	ACAGAACGAGTAGTAAAAGTTACATTT
Oligo8	ACGTATTATTTACATTGTCGTATTCGG
Oligo9	CCCCTTGCGAATAATATTCCTTAGAAT
Oligo10	CCTGGAAATTGCGTAGAGACCTCCGAA
Oligo11	CGCACAGAACCACCACGAGGGCCTATA
Oligo12	AGTACAACATGTAATTTGGTGTTTTAT

	Connector Staples for 1D polymerization
Oligo1	GAAAGCCGAATCCTGTTTGATGGTTGCCCCAGCAGG
Oligo2	GCGCTTTCCAAATCGTTAACGCGT
Oligo3	CATCCTCATAACGGCAGCCTCCGGCCAGAAAA
Oligo4	CAGTACAACATGTAATTTTACCAGTCCCGGTTGTGTACATCGAGA
Oligo5	GGGATGTGCTGCATACGCCAGCTGGCGAAAAG
Oligo6	ACAACCCGGCCTCAGGAAGATGAG
Oligo7	AAGCAAATATTTAAAAAACAGGAAGATTGGAA
Oligo8	CAATGCCTTTTTGAGAGATCTACC
Oligo9	GGCAAGGCAAAGAACATCCAATAAATCATATG
Oligo10	TCATTTTTCTGCGAACGAGTAAGG
Oligo11	AGTCAGAAGCAAATCTTTACCCTGAC
Oligo12	AAGCATAACGCGCGGGGAGAGGTG
Oligo13	AAAATGCAGATACAGGGGGT
Oligo14	GGGGGTTTCTGCGCCGTTTTCACGGTCAACCG
Oligo15	CGAAGCGAACGTATTATTTACATTGCGG
Oligo16	CGGGGTCATTGTTTTCAGGTTTAATTTAATGGGCA
Oligo17	AACGGAGAATTGAGTTAAGTA
Oligo18	AGCGCCATGTTAGGCAGAGGCATTATCATTCCAGG
Oligo19	AATGTGAGCGAGCCCAATAATAAGATATAAAATAT
Oligo20	ACGCACAGAACCACCACCATG
Oligo21	ATATATTTTAAAGAGCCGCCGCCAAACAGTTAACA
Oligo22	CCCCCTTGCGAATAATAAAGG
Oligo23	CTTTTGATAAGTTTTTTCACGTTGCAGCAGCGTAT
Oligo24	TATAAAGACAGAACGAGTAGT
Oligo25	AATAGTAACCTGCTCCAT
Oligo26	AACATACGAGCGCAGATTCACCAGGTATTAACTACC
Oligo27	CCTGGAAATTGCGTAGACAG
Oligo28	AAACTTTTCCAACGCTAACCGCACTCCAGCCA
Oligo29	CGTCTTTCTCACCAATGAAACAAAGGCTATCA
Oligo30	AATCCTGAGAAGCGGTTTGCGTAT
Oligo31	ATCGATAGCCCTCATTTTCGATTTAGTTTGAC
Oligo32	TTTTTATAATTCGACAACTGCATCAGATGCCG
Oligo33	GATAGCAACGAAATCCGCGAAATGTTTAGACT
Oligo34	ACATTCAACTATTGGGCTTGAGAT
Oligo35	ATTAAATCCAAAGAACGCGACATAAAAAAATC
	Connector Staples for 2D polymerization
Oligo1	GAAAGCCGACAGGCAAGGCAAAGAACATCCAATAAATCATGCGAACGT
Oligo2	AATCCTGAGAAGATTTAGTTTGAC
Oligo3	ATTATTTACATTGAGGTCATTTTTCTGCGAACGAGTAGTGTTTTTATA
Oligo4	GTATTAACTATAGTCAGAAGCAAATCTTTACCCTGACTATACCGCCTG
Oligo5	ATTCGACAACTAAATGTTTAGACT
Oligo6	GAAATTGCGTAGAATGCAGATACAGGGGGTAATAGTACGTATTAAATC
Oligo7	CTTTTGATAAGGCAGATTCACCAG

Oligo8	ACATTCAACTATTTTCAGGTTTAA
Oligo9	TGCCCCAGCAGGCGAAATGCCCCCTTGCGAATAATAACGGAAGCATAA
Oligo10	CGCGCGGGGAGAGAGGGATAGCAACGAAATCCGCGGCATCAGATGCCG
Oligo11	AACATACGAGCTTTTTTCACGTTGCAGCAGCGTACCGGGGGTTTCTGC
Oligo12	GCCGTTTTCACGGTCAAAAGACAGAACGAGTAGTAAACAGGCGCTTTC
Oligo13	CAAATCGTTAACGACCTGCTCCAT
Oligo14	CGGGGTCATTGTTGGGCTTGAGAT
Oligo15	AACAGTTAAATCCTGTTTGATGGT
Oligo16	CCCTCATTTTCGCGGTTTGCGTAT

Table S2. Staple sequences for DNA Origami Triskelion Assembly and Polymerization

	Unmodified Staples
Oligo 1	CCACTACGTGAACCAACCCTAAAAGGAACGCTGCGGGTTGCTACAGGAG
Oligo 2	ATCAGGGTTTAGAGCTTGAGATACCGACGCAAGTG
Oligo 3	TCCAACGTCAAAGGTCCGAAAGGCGAAAGCCAGGGGGG
Oligo 4	AGACGCTTCTGTGCTGAATTAATGCCGGAGAATCAGGTGTCA
Oligo 5	CCCCAAGAGTCCACTATTAAAGAATATAAATCCACGCTACCA
Oligo 6	CCCAGCATCGGCAACGCCCTGCGCACGATATTTTTGAAGGGT
Oligo 7	GTATCGGCCTGCCATTGAACATCGTAATCCTGATTGTTCATA
Oligo 8	GCTTAGTTAAGCTACGGCCCTTTAATGGCTATTAGATTAACACCGCCAA
Oligo 9	GTGTAATGAAACTCACATTAATTGTGTTATCAGCTCGAGGTC
Oligo 10	GTACTATCGTAACCTGAGTAGCTCATGGTGCGCGATAACCAGAACACAG
Oligo 11	AGAGGGGTGCCTAATGAGCACAACAACGGAGGCGCA
Oligo 12	ACGCGCGTGGTTTTGTGTAAT
Oligo 13	CGTTAGAATCAGAGCGGATCAGTGCAAATTATCTAAAGCCAGCAG
Oligo 14	GCCGATTATCCTGAACTTCTTGAGC
Oligo 15	CAGTGTAAAGCCTGGCGGTTTGCATGCGCCGCTACTTTTAGA
Oligo 16	TTTATAGAGCTAATTGACGAGCACGTAAAGT
Oligo 17	CGGAAGCATAAAGGGTGCTTGGGTGCAACAGTGCCGCAAAGC
Oligo 18	TGTTTCCTGTGTGAAATCGTTGCGCGTGCCAGCTGCATAGACGGGCGAA
Oligo 19	TAATATGAACGGTACGCCAGAAAAGGGAAGGGCGC
Oligo 20	ACTAGCGGTCAGGGAAGAAAGCGAAAAGCACTCATTGGCGGAC
Oligo 21	ACTTGCCACCACACGCGAACGTGGCGAGAAGGGAGTCGT
Oligo 22	GCTATTGGGCATCCTGTTTCGGGGAAAGCCGCCGCCGC
Oligo 23	CTCGGTACCGCGCTCACAATTCCATGAGCTATCGGCCA
Oligo 24	CTCTAGGGGCTTTCCCACAGGAGACAGTCAACTGATAAATT
Oligo 25	GGCTTACGCTAATCCCTCGTGGAC
Oligo 26	CTGTAGAACCAGCGGAATTATCATTGGATTAACTGATAAACA
Oligo 27	GTTGTGAATTCATGGAGTGACGTAAGCAACTCGTCAAACGACGATCTAC
Oligo 28	TTCCTGGCCAACAGAGAAAATGGAAAAAACGAAGA
Oligo 29	GGATGTTCTTCTGTAAGAATACGTGGGGCTTCTGA
Oligo 30	ACAATATTTTTGTCTCAGGAGAAGCCGAGGCCAGT
Oligo 31	AAAGGCTGGGTAGCCTTAAGTG
Oligo 32	GCCAAGCGCCATCTTCTATGATGGTGGTGCGAAAAACCGTCT
Oligo 33	CGATACGCCATTGGTGTTTTGAGGGGACCCGTCGGATTTGGG
Oligo 34	AAGATAAGCCCTAACAACAGGTTATTTAAAATCGGATCACCC
Oligo 35	GAGCAGCAAAAATATCTGGGCCGGAAACCAGACGCTGATGATTAG
Oligo 36	GGGCGATCGGTGCGTAGCGCAACTGTTGTTACCTCCAGG
Oligo 37	CAGGTGAGGCGGTCAGTTCTTTAAAAATACCTACATTGCGACATC
Oligo 38	TCGGGCCTCTTCGCTATCGTTGTAGGTG
Oligo 39	ACGGCTGGCGAAAGGGGCCAGGGTCTTGAATATAACCCATAG
Oligo 40	ATAATTCGTAATTTCTCCAACAGCTTGCAGCAAGCGGTCAAA

Oligo 41	ACCTCAAATATCAAACCCTCAATCTGAAAAAACCGTTGCAA
Oligo 42	GCCATTCGCCATTCAGGCTACCGTGCAT
Oligo 43	CTGCCAGAGATGGGATCCCCGCTGGTTGTCTTTTCGGTTTGC
Oligo 44	AAATCAACAGTTGATAGG
Oligo 45	ACCGCTTCTGGTTCGATTAGACGTCGCTTACATAAAAT
Oligo 46	GTATCGGCCTCAGGCCAT
Oligo 47	TAACAACTGGCCTTAGTACGGTACATTTAGAA
Oligo 48	CAGCAAACATTAAATGTGAGCGAG
Oligo 49	ACCGATATCTTGATACGGATAGCAAGCCCACACCCTCA
Oligo 50	ACATACAACAACCATCGCCCACGCATA
Oligo 51	ACGCAATAATAACGGAATACCCAAACAAAGTTTTCCAG
Oligo 52	AGCCCTTAGATACCTTTTTTAATGGTTAAATAAGAATATACAAATTAC
Oligo 53	TTTTCCTAACCTTGCTTCTATCAAAATCTCCTTTTGATATTGA
Oligo 54	CAAATTCCATAGATTTATCAGGTCATACTGCGGAATCGTTGCAAAAGGC
Oligo 55	GAGAACACCAGATATTCATTCATCTGCAGATACATAAGAGC
Oligo 56	AGCAATGAGGAAGTTTCCAAGGCACCCCTTCATACCGAACACTA
Oligo 57	TAAACAGATTCGGTCGCTGAGGCTTGCAGGAGAGGCTTATAA
Oligo 58	AGAGAGCCACACCGGAAATGGCTGTTTTAACGGGGCAG
Oligo 59	GCAAAAATAGAAAATTCATATCAACCGATTAGCGTTTCAAGTTATG
Oligo 60	TAGCCGAAAGAACTGGCATGATTAAGACCGGAATACCCTCAGGGA
Oligo 61	GGATTTATTGAGTAAAACAAAGAGGCGATATCATACAACGCC
Oligo 62	TAAAAGGAACGAAGATCGCACTCCAGCCAGCTATT
Oligo 63	CAAATATCCAGCTTTCATCGCATGTTTTAACCTGTAATTAAA
Oligo 64	ACGAGCATCGATCGTCACCCT
Oligo 65	GGTGAAGGACTAAAGAGGCAAAACCAGGCGAGAGGACGAGGCAAGAACG
Oligo 66	TTAATTGTGCGCCGACAATGACAAGCCACCTGAGTTTGAGGGGT
Oligo 67	ACCGGCAACATAACGTAGAAAAT
Oligo 68	AGTAATTTATTTTGAAATATTTTTCGGTGACTGTAAGTGCCCGTAGAAA
Oligo 69	CCCTTTTATAAGAGATTTTTTGTTTACACAAATTT
Oligo 70	GCCGAGCTGACAAAATTATAGCGACGACAAAAGGTAAA
Oligo 71	CTAACTTTGACCCCCAGCGGATTTGTGAACGAGGCGCAGA
Oligo 72	AAGACTTTTTCACGGCTACGAGTTAAAGGCCGCTTTTGCGGGGAAC
Oligo 73	TCTTGTAGCATTCCAGGCTCAATAGGAACCCCAG
Oligo 74	AAAAGGAACAACTAAAGGATTGCTAAAGTAAATGAATTTTCACCAGAC
Oligo 75	AAAAGGAACCAGTAGATCTAAGAACCTAACAAGA
Oligo 76	GAGAGGTGAATTATCACCGCAAAATCAGATAGCAGCACCGTA
Oligo 77	GGTTCACAATCGACACCATCCTTATTACGCAGTATGTTAGCAATAAA
Oligo 78	AAACCCTAGATTTTGTACCTT
Oligo 79	CAAAAGGCAGGAAGATTGTCGCTATATTCAGAGCACAGA
Oligo 80	GATAAAAATTTTTAAAGAGAAAATCATACAT
Oligo 81	CCTTTTGCGGGAGAAGCAAATCATAATAGTAAACG
Oligo 82	TGCACATTATGACCCTGGAATTAGAAAGGTGCATT
Oligo 83	ATGTGTAGGTAAAAGCTAAATC
Oligo 84	GAAATCTATGGGATTATTGCGAATAATAATACACTAAAATTGTGTC

Oligo 85	AACAGTTTCAGCGTTTTGTCGTCTTTCCAGCGTAACCAAA
Oligo 86	CAAGGTAACTGAACACAAGAATTGAGCGGAAATTACCATTAG
Oligo 87	CTGACATTAGACGGGAGATTACGTCAAAAATGCGCACTCGCTGTCT
Oligo 88	TCAACTGAATATACATTTCAATTACCACAATA
Oligo 89	CGGTCAACAAAGTACAACGGAATTATACACTACGATTAA
Oligo 90	ATCAGTTGGGAATTAGAGCCAGTCACCGACGCGACATTGGTTT
Oligo 91	AACGTCACCAATGAAGCGTCACATAGCCCACC
Oligo 92	AAAAGGGAGAATAAAGAAATTGCGTTCTGAATTAAA
Oligo 93	TTCAGTAACACAGGTTTAACGTCATCTGCGGAACAAAG
Oligo 94	AAATAATACTCATATATTTTAAATGCCTGAGTAAT
Oligo 95	TAAGGGACAAGAGTAATCTAGTAATGCCCAAGCGCGAAGATT
Oligo 96	AGCCCTCATGAAAACAATAGATAAGTCCTGATTATTCTAGGAT
Oligo 97	AAAAGAATATGTGAGTGAAAATATAGTCGTTTAGA
Oligo 98	TTTCATCCAAAAGGTTGAGCCATGAGTGAGAATAGAAAAGGCTCC
Oligo 99	AGTATAACAGAGAGGTCATTTTTGTCAGGATAGATTAAGAGGAAGTCA
Oligo 100	AATAAATATGATAATGCTGTAGCTACAGCTTCAAAGCG
Oligo 101	AGAACCGGAACGAGTAGTAACGAAAGACGGTAAAATAATAAG
Oligo 102	AAAATCCACCCTCAGAGCCAGTAAAGGTAGCGCCAAAGAGCCT
Oligo 103	ACCAACCGCCCCGCCAGCATTGACAGGAGTAGCCGCCAAGGCAGA
Oligo 104	ACCGCGTTCCACCTTGAGTACAAGCCGTTTTTGAAGGCT
Oligo 105	GCCAGTTAGATATAATTTTCATCGTAGGCAAGTACAAAATAGGGAA
Oligo 106	TTCACTAACATAGACTTTACAAACAACGTTAAATTAATACCAAGTTCTT
Oligo 107	AAATGCCGTCAATAGATCTTCCGGC
Oligo 108	TTCAACCAATTTTTTGTTAAATCAAAAACTATATGAGC
Oligo 109	TTCAAATAATTTTGTTAAAATTCGTGTACCCTTCTACTACAGGCAAGAA
Oligo 110	GGCCGTAACACATTATAAGGAATTCTGAGACTCCTGATAAGT
Oligo 111	AGCCTGAGTTGCTATTTTGCAAGCCTTAACGCGAGGCG
Oligo 112	AGCGATAGCTTAGATTAAGGTTGGTCCAATCGCAAGACACCT
Oligo 113	TCAATATACCTTTGCGAGAA
Oligo 114	TTAATTCCGGAAGGACTTCAAATATCGGAAA
Oligo 115	TCATTGTGAAGCTTCAGTGATGATTTCT
Oligo 116	GAACCGAGGAGGGATATAAGTATACAGTACATGTACCCAACGCCCCAAA
Oligo 117	GCCACCCAAGGTGTATCACCGTA
Oligo 118	AACCAGAGCTGAATCAACTAACCTGTAGTTAAATTGTAAACGAAAA
Oligo 119	TCATACGTTAATAAAATAGAAAGATTACCCTGGCTGAAAC
Oligo 120	CTTATGAACGGAACTCGAGAGGGTTTTTAGTACCTTAC
Oligo 121	CTCCCACCCTTTTTCAGCGATAGTTATCGGTTTATCAGCTTGAAAA
Oligo 122	ATAAGAATGGAAAGCTCATACCCAGAGCCCCTTATTGAGG
Oligo 123	GGCAGGTTCTGAATTTGGTATTCTAAGAAATCAAGATGTTGA
Oligo 124	CTTGCGGGAGGTTTTGACCCAGCTGAGCGTCTACCAGAACCGAAG
Oligo 125	AACTTTTTCAAAAATAGGTCTGAGAGACGTGAATTTGT
Oligo 126	TTTTGCAAATCACAAAATAGAAACGCAAGAAACAGAGAGATAACCCACC
Oligo 127	AAATTTAATGAAAACAATTAATTTAATGGAAGGGTTAGACAG
Oligo 128	CTGAAAGAACTTAACCTCCGGCTTAGACGCTAATT

Oligo 129	TTCAGAATCATAATTACTAGAAAATAGTATAT
Oligo 130	TTTAGTTATCAATAGATGATGACATTATCATTTGTGCTAATACATTTGA
Oligo 131	CTATTTCTGCGGTAGCATGCATGTCTCGATGAACGGTAAGAGCAAG
Oligo 132	CCCATCAAAATAGAGAGTACCTTTAATTGCAGCAAAGCGGATTGCTGA
Oligo 133	AAAAGTTTGACGCATCAACGGTTGAAGTCTGGAGCAAACGAAC
Oligo 134	AAACCCGAAACAAACTCCAACAGGCGGATGGAAGT
Oligo 135	TGATATTCATTGAATCCAACCAAAAAGCAATACCAAAACTGAGTA
Oligo 136	ACGCGCAAATGGGGCGCCCAAAAAGTGAGAAAGGCCTTGCAA
Oligo 137	CAGTTCACGTTTTAATTCGGTTGGGAAGATTTAGGTTTGACA
Oligo 138	GAGAAAAATCTTATACCAGTCAGGCAAATTGGGCTTGAGATGGTTTGGC
Oligo 139	AGGCGAACTCGATTTTAAGAACTAATTTCGACGAGAGGT
Oligo 140	GCCGAAAAGCTGTGTACAGAGAATTTTTTCACGTTGCTTTCGA
Oligo 141	GCGCAAGAGAAGGATTGAAACATAGTTAGACGTTACAACTTTC
Oligo 142	TTTGCTGCCCGGAATAATCCTCATTGATACAGCGTAATC
Oligo 143	GATAAAGCCTTCACAAACAAATTCGCCACCAGAACCACCACCTTG
Oligo 144	GCGGCAGTCCAGACGATTGGCCAGAGCCGACCCTCAAAC
Oligo 145	TATCCACCCTCCCTTCGGCATGATTAAGCCCAATATAAGAAA
Oligo 146	CTGGATAAGGGGGTATCCAATCTTTATT
Oligo 147	TAGCGTGTACTGGTATTTCGAGTAGCGACAGAATGCCATCT
Oligo 148	ACCATTGAGAATCGCCATATTTAATGCGTTAAACACCGTCTT
Oligo 149	GTAGCAGAGGCATTTTCGAGCCAGTTGCCAGGCGTCCATTTA
Oligo 150	GTTTAATAAGAGAATATAAAGTACGAGGCTTTCATAAACCAT
Oligo 151	CGATGTCCAGACGACGACAATAAATAACCCTCAACTAAAGTT
Oligo 152	TCACAACATGTTCAGCTAATGCTAGTAACGCCAATAC
Oligo 153	AACTGACCAATTAGCCGATCATCGCCTGATAAACACTCATAACGA
Oligo 154	CCCATCCTAATTTACGAGCATGTATAAATCAGTGGTAA
Oligo 155	TTATGCCTTTAACCATCCCAGTAGCACCATTATTCATTAAGGAA
Oligo 156	AACATGTAATTTAGAAAAGCCTGTTTAGATTA
Oligo 157	GTAATTCCGATAAACCCTCAAATGCTTACCACATTCGTTTACTAAATCA
Oligo 158	CGCCTGTTTATCAGTATTAAGAGGACAGATGATGCGCGACCTGCTC
Oligo 159	AAAATAATATCCCCCTGCCTAATAATTT
Oligo 160	CCAATCAATAATCGATCGAGAACAAGACGCGCGTTATCCGGA
Oligo 161	GGGCGCTGGCTAACGTGCTTTCTA
	Staples for Cholesterol Labeling
	(Anchor sequences for cholesterol labeling were shown with orange color)
Oligo 1	CATTCTCCTATTACTACCCCTGAAAAGTTTGACGCTCAACCCCCGACGATGGC
Oligo 2	CATTCTCCTATTACTACCTCCTTAAATCTATACGAATATGAC
Oligo 3	CATTCTCCTATTACTACCTTACATCTCGCGCACATCAAGGAA
Oligo 4	CATTCTCCTATTACTACCGGTTGTAAAGCCTTTCATTTGGTC
Oligo 5	CATTCTCCTATTACTACCCATGTTACCTTTGAACATAGGCAAAT
	Staples for Dye Labeling
	(Anchor sequences for cholesterol labeling were shown with orange color)

Oligo 1	ACTTAGCAATGAAGTGTTTTCCTCTACCACCTACAT
Oligo 2	GAGTAAAGATAAAGTACGAGCTTCCTCTACCACCTACAT
Oligo 3	AGTGAAGTATACTAATAAGTTGGCTTCCTCTACCACCTACAT
Oligo 4	CAGTTAATATTCGCGTCGACGACATTCCTCTACCACCTACAT
Oligo 5	CTAGTAACACACCCTCACAGAACCTTCCTCTACCACCTACAT
Oligo 6	ACAGATTAATTGAGAAGAGTTCCTCTACCACCTACAT
Oligo 7	AGATGTCTGGCTTAGAGCTTCCTCTACCACCTACAT
Oligo 8	CAATTGCCCTAACTTTAATTCCTCTACCACCTACAT
	Connector Staples for Trimer Formation
Oligo 1	GTTCCAGTTTGGAAGAGATAGGGTTGAGTGCG
Oligo 2	TGGCCCTGAGAGAGTGATTGCCCTTCACCGGC
Oligo 3	GTCGGGAAACCTGTCTCACTGCCCGCTTTCGA
Oligo 4	CACATAAATCATCATGGTCATATC
Oligo 5	TCCCGCCAAACGGCTGACGCATTA
Oligo 6	GTCAACCTTATGACAAAA
Oligo 7	TTCAACCGTTCTAGATCACCATCAATATGAGA
Oligo 8	TAAGTTGGGTAACGGATGTGCTGCAAGGCGAA
Oligo 9	CGGATTGACCGTAACTCCGTGGGAACAAACAA
Oligo 10	TAGCTATCTTAGGAAACCGAGGGG
Oligo 11	GCGCTAATATCAATGAAATAGCAT
Oligo 12	GCGACAAAGTCAGAGGGTAATTTA
Oligo 13	TAACATAAAAACAGCAGCCTTTACAGAGAGTG
Oligo 14	TCCCAATCCAAATAAAACAGCCATATTATTTT
Oligo 15	TTACCAACGCTAACACAATTTTATCCTGAAGC
Oligo 16	CCAATAGCAAAGCGAACCTCCCCA
Oligo 17	GGTATTAAACAATCATTACCGCCC
Oligo 18	TTCCTTATCATTCCAAGAATT
	Connector Staples for Polymerization
Oligo 1	AAATCAAGTTTTTTGGGGTTC
Oligo 2	AGGTGCCGTAAGGAGCGGGCGCGT
Oligo 3	GTCTGTCCATCACGAGGCCACCGAGTAAAAAT
Oligo 4	CAATATTACCGCCATGCTGGTAATATCCAGTT
Oligo 5	ACCAGTAATAAAAGAGATTCACCAGTCACAAT
Oligo 6	ATTCTGATTATCAGATGATGGCAT
Oligo 7	TTCATCAATACCATTAAAAATATT
Oligo 8	GAACGAACCACATCACCTTGCTTT
Oligo 9	ATCTAAAATATCTTAAGGAATTGAGGAAGGGA
Oligo 10	AAATCCTTTGCCCGAATTCGACAACTCGTACC
Oligo 11	TATTTGCACGTAAAAACCTACCATATCAAAAA
Oligo 12	AAAACAATAACGGATTCGCCTGCG

Oligo 13	TGCTTTGAATTACATTTAACAAAA
Oligo 14	TCATTTGAATATCCTTGAAAACGA
Oligo 15	AATGCTGATGCAAAGTTATATAACTATATGCT
Oligo 16	GTGATAAATAAGGCGTTTGAAATACCGACCTA
Oligo 17	AACAGTAGGGCTTAAGTATAAAGCCAACGCCG

REFERENCES

1. Douglas, S. M.; Marblestone, A. H.; Teerapittayanon, S.; Vazquez, A.; Church, G. M.; Shih, W. M. Rapid Prototyping of 3D DNA-Origami Shapes with caDNAno. *Nucleic Acids Res.* **2009,** *37*, 5001-5006.
2. Soumpasis, D. M. Theoretical Analysis of Fluorescence Photobleaching Recovery Experiments. *Biophys. J.* **1983,** *41*, 95-97.

Supporting Information for Associated Publication P3

DNA Nanotubes as Intracellular Delivery Vehicles *in vivo*

by

Sabine Sellner*, Samet Kocabey*, Katharina Nekolla, Fritz Krombach,

Tim Liedl and Markus Rehberg

*equal contribution

published in

Biomaterials 2015, 53, 453-463

DNA Nanotubes as Intracellular Delivery Vehicles *in vivo*

Sabine Sellner, Samet Kocabey, Anna K. Nekolla, Fritz Krombach, Tim Liedl, Markus Rehberg*

Supplementary Information

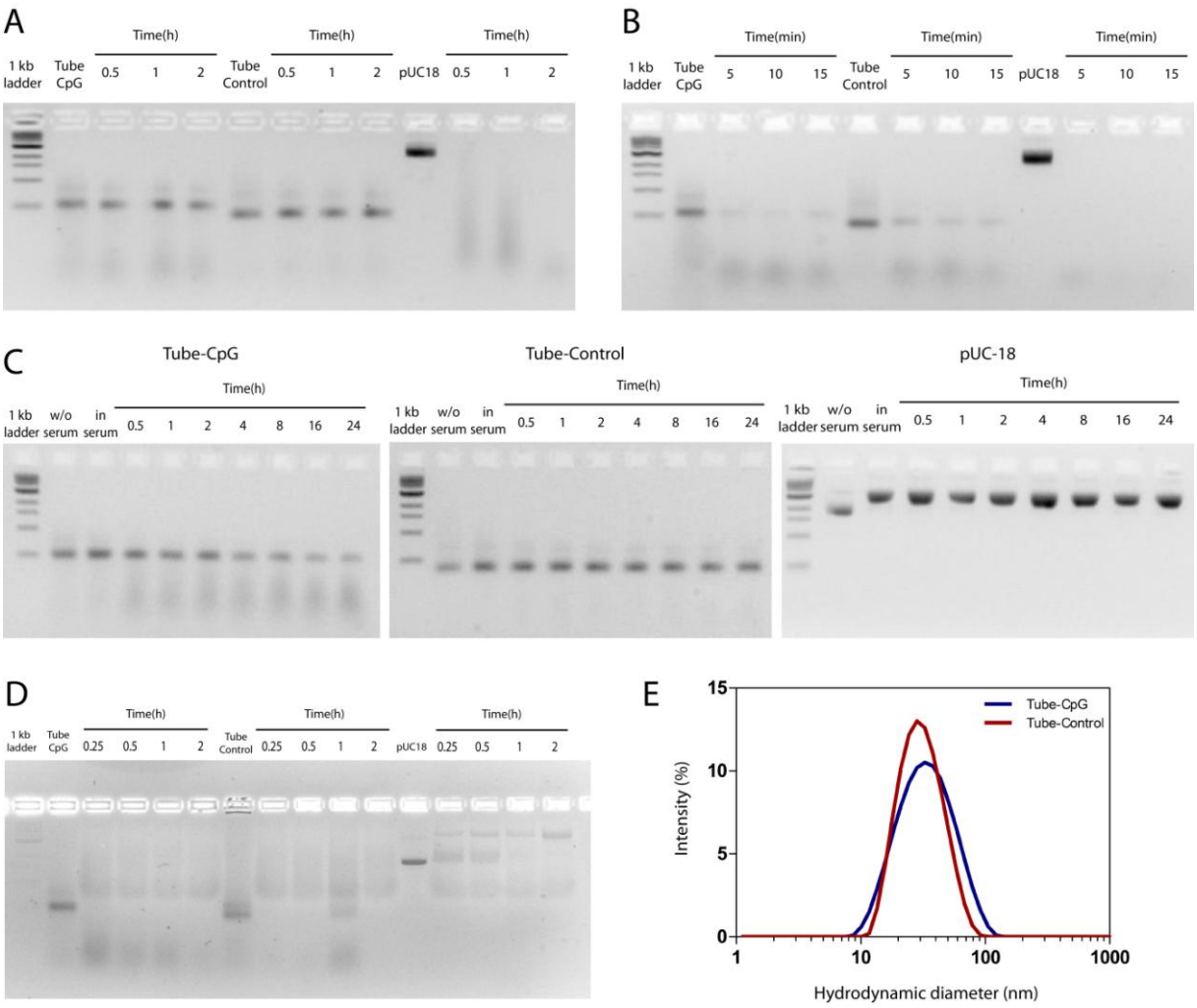

Fig. S1. *Stability of DNA nanotubes*. (A) Gel analysis of CpG tube, plain tube, and pUC 18 (left to right) incubated in the reaction buffer containing 5 x 10^{-1} U / ml DNAse I at 37°C for 2 h. (B) Gel analysis of CpG tube, plain tube, and pUC 18 (left to right) incubated in reaction buffer containing high concentration of DNAse I (10 U/ml) at 37°C for 15 min. (C) Gel analysis of CpG tube, plain tube and pUC 18 (left to right) incubated in 37x diluted mice serum. (D) Gel analysis of CpG tube, plain tube and pUC 18 (left to right) incubated in pure FCS (not heat-inactivated) for 2 hrs. E) DLS analysis of CpG tube and plain tube.

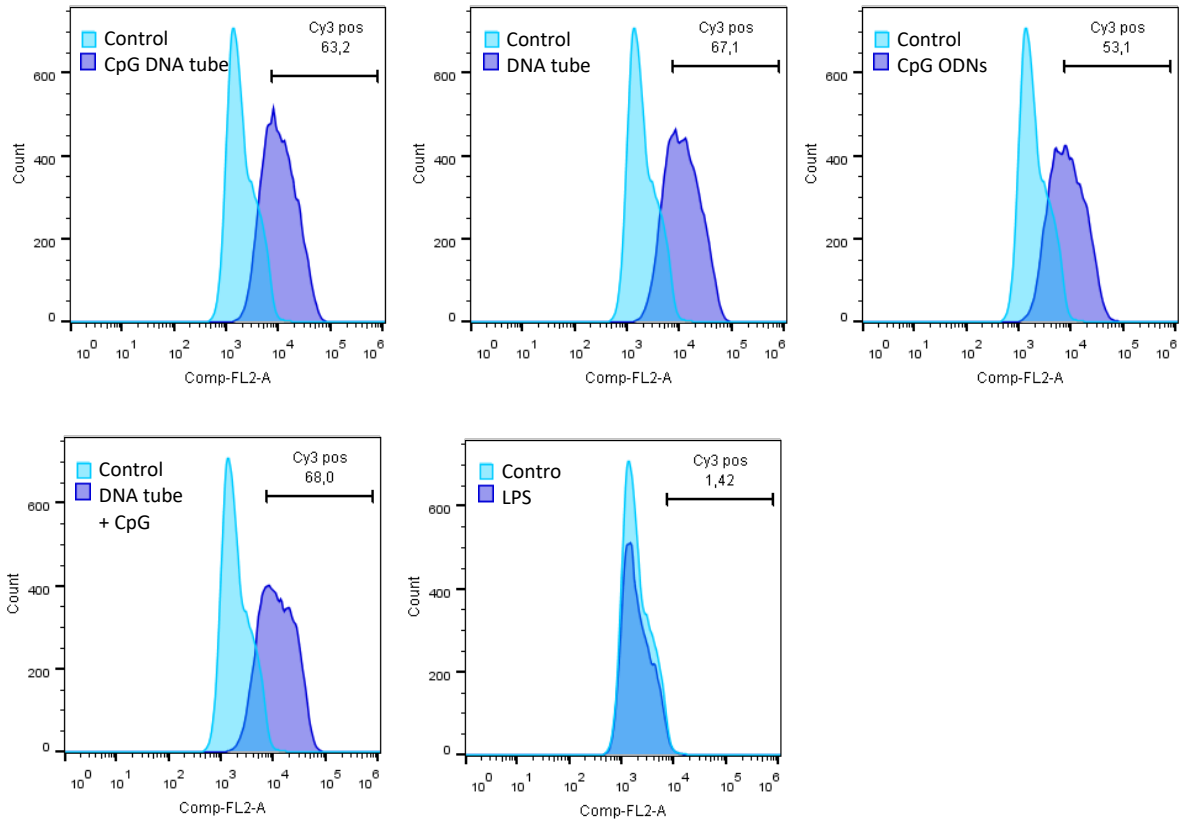

Fig. S2. *Uptake of DNA nanoconstructs by RAW 264.7 macrophages after 1 h of incubation.* Representative histograms show fluorescence shift indicating the uptake of Cy3 coupled DNA nanoconstructs by RAW 264.7 macrophages. Cells were incubated with 5 nM of different DNA nanoconstructs (CpG DNA tubes, DNA tubes, CpG ODNs, DNA tubes + CpG ODNs), LPS (10 ng/ml) or without additive for 1 h at 37°C.

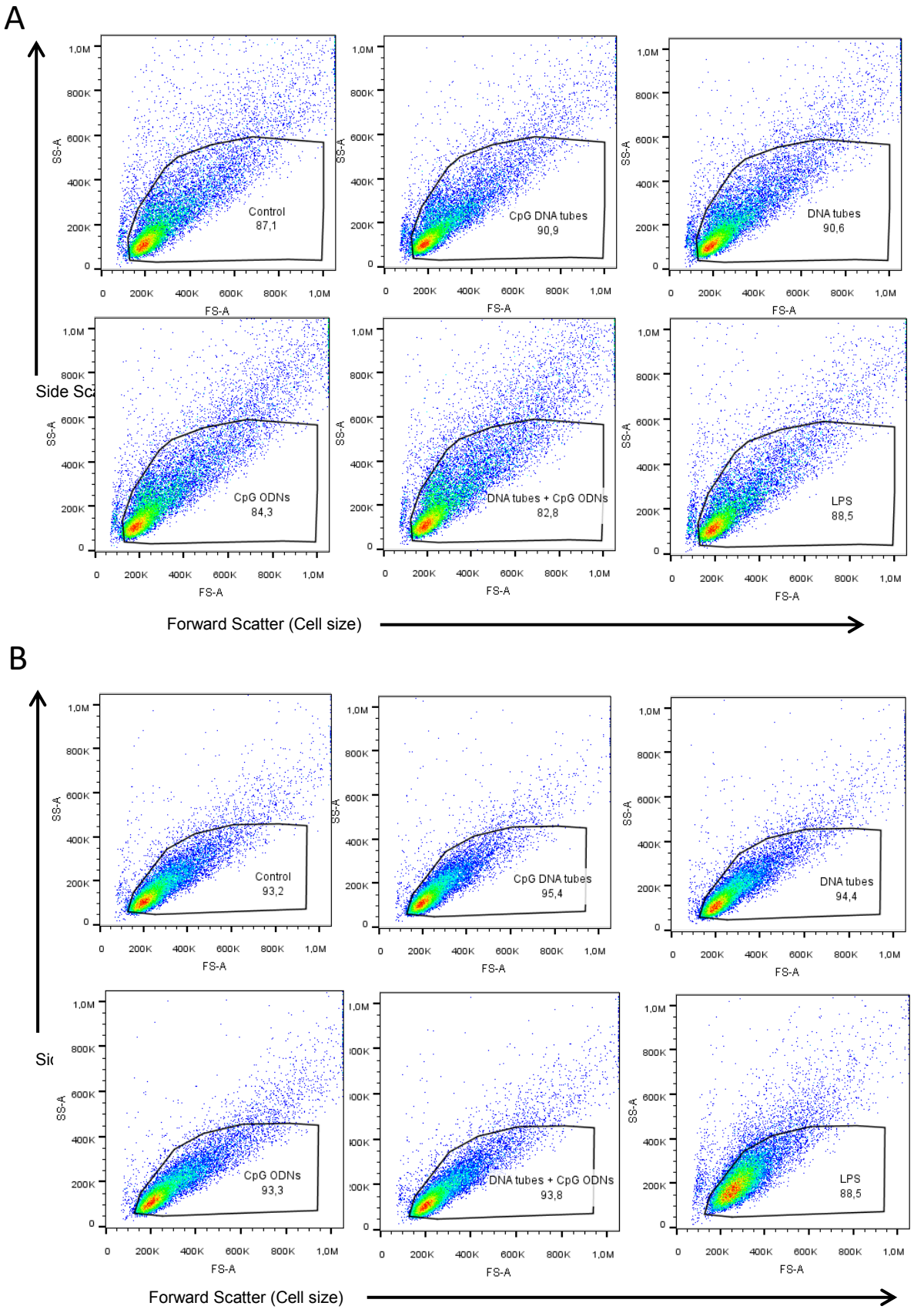

Fig. S3. *Cell viability after incubation with DNA nanoconstructs.* FACS analysis of RAW 264.7 macrophage viability after incubation with 5 nM of different DNA nanoconstructs (CpG DNA tubes, DNA tubes, CpG ODNs, DNA tubes + CpG ODNs), LPS (10 ng/ml) or without additive for 1 h (**A**) and 18 h (**B**) at 37°C. The numbers indicate the percentage of viable cells within the sample.

Table S1. *Systemic leukocyte counts and microhemodynamic parameters*

Experimental group	Inner vessel diameter [µm]	Blood flow velocity [mm/s]	Wall shear rate [s^{-1}]	Systemic leukocyte counts [x 10^6 ml^{-1}]
Saline	26.7 ± 1,2	2.4 ± 0.2	3489.0 ± 129.7	2.6 ± 0.5
Plain tubes	26.7 ± 2.8	2.3 ± 0.7	3683.6 ± 1554.6	1.5 ± 0.3
CpG tubes	30.6 ± 3.8	2.1 ± 0.3	2969.6 ± 550.5	1.8 ± 0.2
CpG ODN	26.0 ± 2.3	1.9 ± 0.4	2848.3 ± 483.7	2.8 ± 0.8
Cromolyn + CpG tubes	24.8 ± 1.5	2.0 ± 0.3	3408.7 ± 659.7	2.7 ± 0.4

Systemic leukocyte counts as well as microhemodynamic parameters, including inner vessel diameter, blood flow velocity, and wall shear rate, were obtained as detailed in *Materials and Methods* (mean+/-SEM for n=3 per group).

Supporting Information for Chapter 4.3

DNA Nanotube Design

DNA nanotubes were designed using single stranded tiles, where each single stranded tile oligonucleotide has 21-base long (2 full turn) domains complementary to the adjacent domains on the neighbouring tiles. 15 individual single stranded tiles were used to fold 6-helix nanotubes. The domains at the ends of the nanotube contain non-pairing poly-A sequences to prevent polymerization. For i-motif formation, 3 of the tiles were extended with the i-motif sequence. (CCCTAACCCTAACCCTAACCC). For Dexamethasone labeling, 3 of the tile oligonucleotides extended with either i-motif sequence or random sequence were hybridized with Dexamethasone-conjugated single stranded oligonucleotides. All unmodified oligonucleotides (HPSF purified) and amine modified oligonucleotides (HPLC purified) were purchased from Eurofins Operon MWG (Ebersberg, Germany) (see the Supporting Information, Table S1 for the sequences).

Dexamethasone Conjugation

Amine modified single stranded oligonucleotides were conjugated with Dexamethasone using the method developed by Acedo et al.[6] In brief, Dexamethasone (0.4 g, 1 mmol, Sigma) was reacted with succinid anhydride (0.15 g, 1.5 mmol) and DMAP (0.13 g, 1 mmol) in pyridine at room temperature for 20 hrs. The reaction mixture was concentrated by drying in vacuum evaporator and then dissolved in 150 ml of DCM/MeOH(4:1) and washed twice with 75 ml of 1 M sulfuric acid and water. The organic white solid formed after the reaction, dexamethasone succinic acid (0.25 g, 0.5 mmol), was reacted with N-hydroxysuccinimide (70 mg, 0.6 mmol) and DCC (125 mg, 0.6 mmol) in 5 ml of THF at room temperature for 20 hrs. After several filtration and washing steps, the final residue was dissolved in 5 ml DMF (10 mM) and stored at 4 °C for months. For DNA coupling, 10 µl of 5´amine-labeled oligonucleotide (100 µM) and 10 µl of Dexamethasone-NHS (10 mM) were mixed in Tris buffer (50 mM, pH 7.4) and incubated at room temperature overnight. Next day, the solution was centrifuged at 13000 g for 5 min and supernatant was collected. The solution was evaporated to remove DMF in vacuum centrifuge and redissolved in water. The centrifuge and evaporation steps were repeated several times. At the end, Dexamethasone-conjugated oligonucleotides were purified using 3K Amicon Ultra 0.5 ml centrifuge filters to further use in dye labeling and assembly.

Enzymatic Dye Labeling of Tiles

To visualize the DNA nanotubes *in vivo*, 6 of the tiles at the middle part of the structure and dexamethasone-conjugated oligonucleotide were enzymatically labeled with Atto488-dUTP and Atto647N-dUTP respectively. Atto488-dUTP or Atto647N-dUTP (80 µM, purchased from Jena Bioscience, Jena, Germany), CoCl2 (5 mM), terminal transferase enzyme (16 U/µl, Roche, Penzberg, Germany), and all DNA tiles (1 nmol) were mixed in a 20 µl, 1x TdT reaction buffer. The solution was incubated at 37°C for 1 h. Then, 2.5 µl of NaOAc (3 M) was added and the solution was filled up to 80 µl with ice-cooled ethanol (99 %). After 1 h incubation at -20°C, samples were centrifuged at 13000 g for 30 min. Then, samples were washed with 70 % ethanol for 10 min again and the supernatant was discarded. The remaining pellet was redissolved in distilled water.

DNA nanotube assembly and purification

DNA nanotubes were assembled by mixing 1 µM of each tile with folding buffer (10 mM Tris-HCl, 1 mM EDTA, pH 8.0, 20 mM $MgCl_2$). The folding was completed over the course of 16 h (5 min at 80°C, cooling down to 65°C at 1 °C/min, cooling down to 25°C at 2.5 °C/h). The assembled DNA nanotubes were then purified using 100K Amicon Ultra 0.5 ml centrifuge filters (Millipore,

Schwalbach, Germany) in order to remove excess strands. 100 µl of assembled DNA nanotube solution was completed up to 500 µl with folding buffer in the centrifuge filter, and centrifuged 3 times at 13000 g for 6 min. After every centrifuge step, the flow-through was removed and the filter was refilled up to 500 µl with buffer. After final centrifugation, the remaining solution at the bottom of the filter (~ 50 µl) was pipetted out and the concentration of tubes was determined by measuring the optical density at 260 nm.

Gel electrophoresis analysis of i-motif formation and transmission electron microscopy

DNA nanotubes were analyzed by running the samples in a 2 % agarose gel (0.5 x TBE, 11 mM $MgCl_2$). 10 µl of each filter-purified DNA tube sample were mixed with 2 µl of 6x loading dye before loading into the gel pockets. 6 µl of 1 kb ladder was also loaded adjacent to the samples. The gel was run for 2 h at 70 V in an ice-cold water bath to prevent heat induced denaturation of DNA nanotubes. To test the i-motif dependent release of single stranded oligonucleotides, DNA nanotubes were assembled with varying $MgCl_2$ concentrations, 2 mM, 5 mM or 20 mM respectively. After assembly, 100 µl of folded DNA nanotubes were filled up to 500 µl in 50 mM MES buffer (pH 5.5) and incubated at 37 °C for 30 min. Then, the samples were centrifuged 3 times at 13000 g at 37 °C for 6 min using 100K Amicon filters. DNA nanotubes were also visualized by electron microscopy using a JEM-1011 transmission electron microscope (JEOL). Prior to imaging, DNA nanotubes were incubated on plasma-exposed (240 kV for 1 min) carbon-coated grids and then negatively stained with 1% uranyl acetate for 15s.

1. Yin, P., et al., *Programming DNA tube circumferences.* Science, 2008. **321**(5890): p. 824-6.
2. Kocabey, S., et al., *Cellular Uptake of Tile-Assembled DNA Nanotubes.* Nanomaterials, 2015. **5**(1): p. 47-60.
3. Gehring, K., J.L. Leroy, and M. Gueron, *A tetrameric DNA structure with protonated cytosine.cytosine base pairs.* Nature, 1993. **363**(6429): p. 561-5.
4. Leroy, J.L., et al., *Acid multimers of oligodeoxycytidine strands: stoichiometry, base-pair characterization, and proton exchange properties.* Biochemistry, 1993. **32**(23): p. 6019-31.
5. Liu, D. and S. Balasubramanian, *A proton-fuelled DNA nanomachine.* Angew Chem Int Ed Engl, 2003. **42**(46): p. 5734-6.
6. Acedo, M., et al., *Preparation of Oligonucleotide-Dexamethasone Conjugates.* Bioorganic & Medicinal Chemistry Letters, 1995. **5**(15): p. 1577-1580.

Table S1. The list of oligonucleotide sequences used in the 6-helix tile-tube assembly.

Unmodified Oligonucleotides

U1R1	AAAAACTTACTGAGGATATTGCCTGAAGCTGTACCGTTTTAGGGGAAA
U2R1	CCCCTAAAACGGTACAGCTTCGGTACGTGCGGTACTAAGACTGGGGCGAATAGACAGGCTCCCCTCTCACTCGCTAGGAGGCAA
U3R1	AAATTGCCTCCTAGCGAGTGAGAGGTTTCCCGCATATTAACGCCTAAA
U4R1	AGGCGTTAATATGCGGGAAACGACGCTGACTCAACCACGGTACGTTAGATGCCTCGCTGTACTAATAGTTGTCGACAGATCGTC
U5R1	AAAGACGATCTGTCGACAACTATTGGTCGGATCTGAGTCGACCAAAAA
U6R1	TTGGTCGACTCAGATCCGACCGCTCCATGATACTCAAAGAGCTCGCCCCGAGTCTGGAGTTCAAGGCAATATCCTCAGTAAGTT

Oligonucleotides for Atto488 dye labeling

U1R2	TGAACTCCAGACTCGGGGCGACAACTCTTCATACATAGAGCAAGGGCGTCGAACGGTCGTGAAAGTCTTAGTACCGCACGTACC
U2R2	TTCACGACCGTTCGACGCCCTTCGCGAGTTCAGTCATGAGAAATCGCTTGCCCAAGTTGTGAAGTGTCTATCACCCCTAGGCCC
U3R2	GGGAGCCTGTCTATTCGCCCCGGGCCTAGGGGTGATAGACACGATTGTATCCGCATTTGATGCTACCGTGGTTGAGTCAGCGTC
U4R2	GCATCAAATGCGGATACAATCGCTCTTAGTCAACTCTACTCACACTGTGCTGCGGCTACCCATCACGTTCGTCGGGTTCACCCG
U5R2	AGTACAGCGAGGCATCTAACGCGGGTGAACCCGACGAACGTGGGACACACTCGAGCTCCGATCGCTCTTTGAGTATCATGGAGC
U6R2	GATCGGAGCTCGAGTGTGTCCATTGGACTCATTCAACCATGGGAGGAGATCTTCAACCTTCCCTGCTCTATGTATGAAGAGTTG

Oligonucleotides for Dexamethasone labeling

U1R3-i-motif	GGGAAGGTTGAAGATCTCCTCAAAAAATTCTCATGACTGAACTCGCGACCCCTAACCCTAACCCTAACCC
U3R3-i-motif	TTCACAACTTGGGCAAGCGATAAAAAATGAGTAGAGTTGACTAAGAGCCCCTAACCCTAACCCTAACCC
U5R3-i-motif	ATGGGTAGCCGCAGCACAGTGAAAAAACCATGGTTGAATGAGTCCAATCCCTAACCCTAACCCTAACCC
U1R3-control	GGGAAGGTTGAAGATCTCCTCAAAAAATTCTCATGACTGAACTCGCGAAAAAAAAAAAAAAAAAAAA
U3R3-control	TTCACAACTTGGGCAAGCGATAAAAAATGAGTAGAGTTGACTAAGAGCAAAAAAAAAAAAAAAAAAA
U5R3-control	ATGGGTAGCCGCAGCACAGTGAAAAAACCATGGTTGAATGAGTCCAATAAAAAAAAAAAAAAAAAAA

Oligonucleotides for Dexamethasone conjugation

Dexa i-motif	NH_2-GGGTTAGGGTTAGGGTTAGGG
Dexa control	NH_2-TTTTTTTTTTTTTTTTTT

Figure S1. HPLC chromotogram of a single DNA oligonucleotide before and after dexamethasone conjugation**.** The peak shifted to 7.1 min after dexamethasone conjugation.

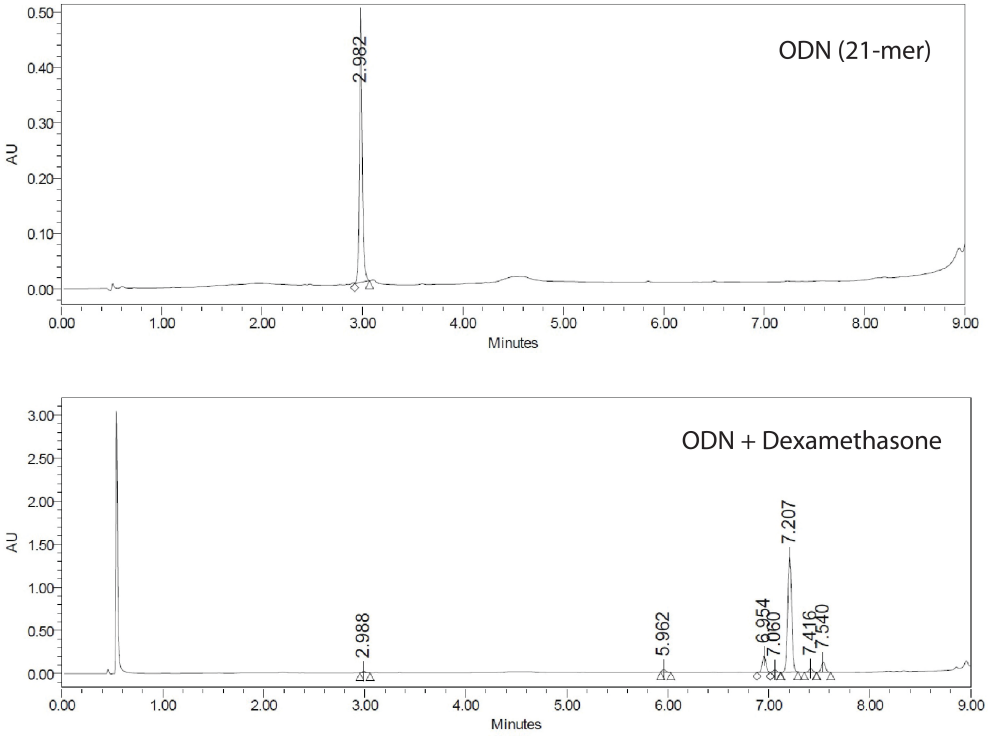

Figure S2. Mass spectrometry analysis of a single oligonucleotide before and after dexamethasone conjugation.

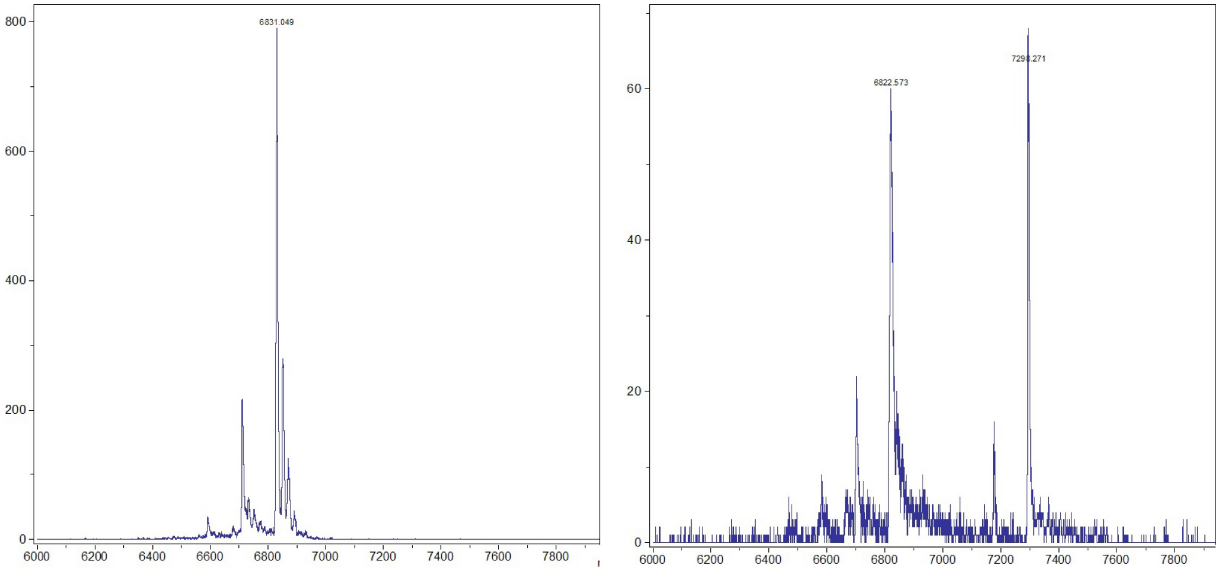

Bibliography

1. Dahm, R., *Discovering DNA: Friedrich Miescher and the early years of nucleic acid research.* Human Genetics, 2008. **122**(6): p. 565-581.
2. Hershey, A.D. and M. Chase, *Independent functions of viral protein and nucleic acid in growth of bacteriophage.* J Gen Physiol, 1952. **36**(1): p. 39-56.
3. Watson, J.D. and F.H.C. Crick, *Molecular Structure of Nucleic Acids: A Structure for Deoxyribose Nucleic Acid.* Nature, 1953. **171**(4356): p. 737-738.
4. Franklin, R.E. and R.G. Gosling, *Molecular configuration in sodium thymonucleate.* Nature, 1953. **171**(4356): p. 740-1.
5. Mandelkern, M., et al., *The dimensions of DNA in solution.* J Mol Biol, 1981. **152**(1): p. 153-61.
6. Ghosh, A. and M. Bansal, *A glossary of DNA structures from A to Z.* Acta Crystallogr D Biol Crystallogr, 2003. **59**(Pt 4): p. 620-6.
7. Watson, J.D., *The double helix; a personal account of the discovery of the structure of DNA*. 1968, New York: Atheneum.
8. Crick, F.H.C. and J.D. Watson, *The Complementary Structure of Deoxyribonucleic Acid.* Proceedings of the Royal Society of London A: Mathematical, Physical and Engineering Sciences, 1954. **223**(1152): p. 80-96.
9. Klug, A., *The discovery of the DNA double helix.* J Mol Biol, 2004. **335**(1): p. 3-26.
10. Sponer, J., J. Leszczynski, and P. Hobza, *Hydrogen bonding and stacking of DNA bases: a review of quantum-chemical ab initio studies.* J Biomol Struct Dyn, 1996. **14**(1): p. 117-35.
11. Yakovchuk, P., E. Protozanova, and M.D. Frank-Kamenetskii, *Base-stacking and base-pairing contributions into thermal stability of the DNA double helix.* Nucleic Acids Res, 2006. **34**(2): p. 564-74.
12. Seeman, N.C., *Nucleic acid junctions and lattices.* J Theor Biol, 1982. **99**(2): p. 237-47.
13. Seeman, N.C., *DNA in a material world.* Nature, 2003. **421**(6921): p. 427-431.
14. Chen, J.H. and N.C. Seeman, *Synthesis from DNA of a molecule with the connectivity of a cube.* Nature, 1991. **350**(6319): p. 631-3.
15. Bustamante, C., et al., *Entropic elasticity of lambda-phage DNA.* Science, 1994. **265**(5178): p. 1599-600.
16. Holliday, R., *A mechanism for gene conversion in fungi.* Genetics Research, 1964. **5**(02): p. 282-304.
17. Panyutin, I.G. and P. Hsieh, *The kinetics of spontaneous DNA branch migration.* Proc Natl Acad Sci U S A, 1994. **91**(6): p. 2021-5.
18. Ma, R.I., et al., *Three-arm nucleic acid junctions are flexible.* Nucleic Acids Res, 1986. **14**(24): p. 9745-53.
19. Wang, Y.L., et al., *Assembly and characterization of five-arm and six-arm DNA branched junctions.* Biochemistry, 1991. **30**(23): p. 5667-74.
20. Fu, T.J. and N.C. Seeman, *DNA double-crossover molecules.* Biochemistry, 1993. **32**(13): p. 3211-20.
21. Li, X., et al., *Antiparallel DNA Double Crossover Molecules As Components for Nanoconstruction.* Journal of the American Chemical Society, 1996. **118**(26): p. 6131-6140.
22. Sa-Ardyen, P., A.V. Vologodskii, and N.C. Seeman, *The flexibility of DNA double crossover molecules.* Biophys J, 2003. **84**(6): p. 3829-37.
23. Mao, C., et al., *Logical computation using algorithmic self-assembly of DNA triple-crossover molecules.* Nature, 2000. **407**(6803): p. 493-6.

24. Winfree, E., et al., *Design and self-assembly of two-dimensional DNA crystals.* Nature, 1998. **394**(6693): p. 539-44.
25. Liu, F., R. Sha, and N.C. Seeman, *Modifying the Surface Features of Two-Dimensional DNA Crystals.* Journal of the American Chemical Society, 1999. **121**(5): p. 917-922.
26. LaBean, T.H., et al., *Construction, Analysis, Ligation, and Self-Assembly of DNA Triple Crossover Complexes.* Journal of the American Chemical Society, 2000. **122**(9): p. 1848-1860.
27. Reishus, D., et al., *Self-assembly of DNA double-double crossover complexes into high-density, doubly connected, planar structures.* J Am Chem Soc, 2005. **127**(50): p. 17590-1.
28. Ke, Y., et al., *A Study of DNA Tube Formation Mechanisms Using 4-, 8-, and 12-Helix DNA Nanostructures.* Journal of the American Chemical Society, 2006. **128**(13): p. 4414-4421.
29. He, Y., et al., *Sequence Symmetry as a Tool for Designing DNA Nanostructures.* Angewandte Chemie, 2005. **117**(41): p. 6852-6854.
30. Yan, H., et al., *Directed nucleation assembly of DNA tile complexes for barcode-patterned lattices.* Proceedings of the National Academy of Sciences, 2003. **100**(14): p. 8103-8108.
31. Zhang, Y. and N.C. Seeman, *Construction of a DNA-Truncated Octahedron.* Journal of the American Chemical Society, 1994. **116**(5): p. 1661-1669.
32. Goodman, R.P., R.M. Berry, and A.J. Turberfield, *The single-step synthesis of a DNA tetrahedron.* Chem Commun (Camb), 2004(12): p. 1372-3.
33. Shih, W.M., J.D. Quispe, and G.F. Joyce, *A 1.7-kilobase single-stranded DNA that folds into a nanoscale octahedron.* Nature, 2004. **427**(6975): p. 618-21.
34. Goodman, R.P., et al., *Rapid chiral assembly of rigid DNA building blocks for molecular nanofabrication.* Science, 2005. **310**(5754): p. 1661-5.
35. He, Y., et al., *Hierarchical self-assembly of DNA into symmetric supramolecular polyhedra.* Nature, 2008. **452**(7184): p. 198-201.
36. Yin, P., et al., *Programming DNA tube circumferences.* Science, 2008. **321**(5890): p. 824-6.
37. Wei, B., M. Dai, and P. Yin, *Complex shapes self-assembled from single-stranded DNA tiles.* Nature, 2012. **485**(7400): p. 623-6.
38. Ke, Y., et al., *Three-dimensional structures self-assembled from DNA bricks.* Science, 2012. **338**(6111): p. 1177-83.
39. Yang, Y., et al., *Self-Assembly of DNA Rings from Scaffold-Free DNA Tiles.* Nano Letters, 2013. **13**(4): p. 1862-1866.
40. Rothemund, P.W., *Folding DNA to create nanoscale shapes and patterns.* Nature, 2006. **440**(7082): p. 297-302.
41. Douglas, S.M., et al., *Self-assembly of DNA into nanoscale three-dimensional shapes.* Nature, 2009. **459**(7245): p. 414-8.
42. Ke, Y., et al., *Multilayer DNA origami packed on a square lattice.* J Am Chem Soc, 2009. **131**(43): p. 15903-8.
43. Douglas, S.M., et al., *Rapid prototyping of 3D DNA-origami shapes with caDNAno.* Nucleic Acids Res, 2009. **37**(15): p. 5001-6.
44. Dietz, H., S.M. Douglas, and W.M. Shih, *Folding DNA into twisted and curved nanoscale shapes.* Science, 2009. **325**(5941): p. 725-30.
45. Han, D., et al., *DNA gridiron nanostructures based on four-arm junctions.* Science, 2013. **339**(6126): p. 1412-5.
46. Andersen, E.S., et al., *Self-assembly of a nanoscale DNA box with a controllable lid.* Nature, 2009. **459**(7243): p. 73-6.
47. Liedl, T., et al., *Self-assembly of three-dimensional prestressed tensegrity structures from DNA.* Nat Nanotechnol, 2010. **5**(7): p. 520-4.
48. Benson, E., et al., *DNA rendering of polyhedral meshes at the nanoscale.* Nature, 2015. **523**(7561): p. 441-4.
49. Stein, I.H., et al., *Single-molecule FRET ruler based on rigid DNA origami blocks.* Chemphyschem, 2011. **12**(3): p. 689-95.

50. Kuzyk, A., et al., *DNA-based self-assembly of chiral plasmonic nanostructures with tailored optical response.* Nature, 2012. **483**(7389): p. 311-4.
51. Schreiber, R., et al., *Hierarchical assembly of metal nanoparticles, quantum dots and organic dyes using DNA origami scaffolds.* Nat Nanotechnol, 2014. **9**(1): p. 74-8.
52. Knudsen, J.B., et al., *Routing of individual polymers in designed patterns.* Nat Nanotechnol, 2015. **10**(10): p. 892-8.
53. Rosen, C.B., et al., *Template-directed covalent conjugation of DNA to native antibodies, transferrin and other metal-binding proteins.* Nat Chem, 2014. **6**(9): p. 804-9.
54. Stein, C.A., et al., *Dynamics of the internalization of phosphodiester oligodeoxynucleotides in HL60 cells.* Biochemistry, 1993. **32**(18): p. 4855-61.
55. Hanss, B., et al., *Identification and characterization of a cell membrane nucleic acid channel.* Proc Natl Acad Sci U S A, 1998. **95**(4): p. 1921-6.
56. Ko, S., et al., *DNA Nanotubes as Combinatorial Vehicles for Cellular Delivery.* Biomacromolecules, 2008. **9**(11): p. 3039-3043.
57. Modi, S., et al., *Two DNA nanomachines map pH changes along intersecting endocytic pathways inside the same cell.* Nat Nano, 2013. **8**(6): p. 459-467.
58. Schaffert, D.H., et al., *Intracellular Delivery of a Planar DNA Origami Structure by the Transferrin-Receptor Internalization Pathway.* Small, 2016. **12**(19): p. 2634-40.
59. Surana, S., et al., *An autonomous DNA nanomachine maps spatiotemporal pH changes in a multicellular living organism.* Nat Commun, 2011. **2**: p. 340.
60. Douglas, S.M., I. Bachelet, and G.M. Church, *A logic-gated nanorobot for targeted transport of molecular payloads.* Science, 2012. **335**(6070): p. 831-4.
61. Shaw, A., et al., *Spatial control of membrane receptor function using ligand nanocalipers.* Nat Methods, 2014. **11**(8): p. 841-6.
62. Akkus Sut, P., C.U. Tunc, and M. Culha, *Lactose-modified DNA tile nanostructures as drug carriers.* Journal of Drug Targeting, 2016. **24**(8): p. 709-719.
63. Zhao, Y.X., et al., *DNA origami delivery system for cancer therapy with tunable release properties.* ACS Nano, 2012. **6**(10): p. 8684-91.
64. Chang, M., C.-S. Yang, and D.-M. Huang, *Aptamer-Conjugated DNA Icosahedral Nanoparticles As a Carrier of Doxorubicin for Cancer Therapy.* ACS Nano, 2011. **5**(8): p. 6156-6163.
65. Jiang, Q., et al., *DNA Origami as a Carrier for Circumvention of Drug Resistance.* Journal of the American Chemical Society, 2012. **134**(32): p. 13396-13403.
66. Halley, P.D., et al., *Daunorubicin-Loaded DNA Origami Nanostructures Circumvent Drug-Resistance Mechanisms in a Leukemia Model.* Small, 2016. **12**(3): p. 308-20.
67. Zhang, Q., et al., *DNA Origami as an In Vivo Drug Delivery Vehicle for Cancer Therapy.* ACS Nano, 2014. **8**(7): p. 6633-6643.
68. Toffoli, G., et al., *Overexpression of folate binding protein in ovarian cancers.* Int J Cancer, 1997. **74**(2): p. 193-8.
69. Lu, Y. and P.S. Low, *Folate-mediated delivery of macromolecular anticancer therapeutic agents.* Adv Drug Deliv Rev, 2002. **54**(5): p. 675-93.
70. Reddy, J.A. and P.S. Low, *Folate-mediated targeting of therapeutic and imaging agents to cancers.* Crit Rev Ther Drug Carrier Syst, 1998. **15**(6): p. 587-627.
71. Antony, A.C., *The biological chemistry of folate receptors.* Blood, 1992. **79**(11): p. 2807-20.
72. Fire, A., et al., *Potent and specific genetic interference by double-stranded RNA in Caenorhabditis elegans.* Nature, 1998. **391**(6669): p. 806-11.
73. Hahn, J., et al., *Addressing the instability of DNA nanostructures in tissue culture.* ACS Nano, 2014. **8**(9): p. 8765-75.
74. Fischer, S., et al., *Shape and Interhelical Spacing of DNA Origami Nanostructures Studied by Small-Angle X-ray Scattering.* Nano Lett, 2016. **16**(7): p. 4282-7.
75. Castro, C.E., et al., *A primer to scaffolded DNA origami.* Nat Meth, 2011. **8**(3): p. 221-229.
76. Okholm, A.H., et al., *Quantification of cellular uptake of DNA nanostructures by qPCR.* Methods, 2014. **67**(2): p. 193-7.

77. Perrault, S.D. and W.M. Shih, *Virus-inspired membrane encapsulation of DNA nanostructures to achieve in vivo stability.* ACS Nano, 2014. **8**(5): p. 5132-40.
78. Mikkila, J., et al., *Virus-encapsulated DNA origami nanostructures for cellular delivery.* Nano Lett, 2014. **14**(4): p. 2196-200.
79. Cassinelli, V., et al., *One-Step Formation of "Chain-Armor"-Stabilized DNA Nanostructures.* Angew Chem Int Ed Engl, 2015. **54**(27): p. 7795-8.
80. De Stefano, M. and K. Vesterager Gothelf, *Dynamic Chemistry of Disulfide Terminated Oligonucleotides in Duplexes and Double-Crossover Tiles.* Chembiochem, 2016. **17**(12): p. 1122-6.
81. Kiviaho, J.K., et al., *Cationic polymers for DNA origami coating - examining their binding efficiency and tuning the enzymatic reaction rates.* Nanoscale, 2016. **8**(22): p. 11674-80.
82. Chopra, A., S. Krishnan, and F.C. Simmel, *Electrotransfection of Polyamine Folded DNA Origami Structures.* Nano Lett, 2016.
83. Kocabey, S., et al., *Cellular Uptake of Tile-Assembled DNA Nanotubes.* Nanomaterials, 2015. **5**(1): p. 47.
84. Axelrod, D., *Lateral motion of membrane proteins and biological function.* J Membr Biol, 1983. **75**(1): p. 1-10.
85. Heldin, C.H., *Dimerization of cell surface receptors in signal transduction.* Cell, 1995. **80**(2): p. 213-23.
86. Lamb, T.D., *Gain and kinetics of activation in the G-protein cascade of phototransduction.* Proc Natl Acad Sci U S A, 1996. **93**(2): p. 566-70.
87. Pearse, B.M., *Clathrin: a unique protein associated with intracellular transfer of membrane by coated vesicles.* Proc Natl Acad Sci U S A, 1976. **73**(4): p. 1255-9.
88. Doherty, G.J. and H.T. McMahon, *Mechanisms of endocytosis.* Annu Rev Biochem, 2009. **78**: p. 857-902.
89. Ashkenazi, A. and V.M. Dixit, *Death receptors: signaling and modulation.* Science, 1998. **281**(5381): p. 1305-8.
90. Langecker, M., et al., *DNA nanostructures interacting with lipid bilayer membranes.* Acc Chem Res, 2014. **47**(6): p. 1807-15.
91. van Meer, G., D.R. Voelker, and G.W. Feigenson, *Membrane lipids: where they are and how they behave.* Nat Rev Mol Cell Biol, 2008. **9**(2): p. 112-24.
92. Mingeot-Leclercq, M.P., et al., *Atomic force microscopy of supported lipid bilayers.* Nat Protoc, 2008. **3**(10): p. 1654-9.
93. Pfeiffer, I. and F. Hook, *Bivalent cholesterol-based coupling of oligonucletides to lipid membrane assemblies.* J Am Chem Soc, 2004. **126**(33): p. 10224-5.
94. Borjesson, K., et al., *Functionalized nanostructures: redox-active porphyrin anchors for supramolecular DNA assemblies.* ACS Nano, 2010. **4**(9): p. 5037-46.
95. Kurz, A., et al., *Lipid-anchored oligonucleotides for stable double-helix formation in distinct membrane domains.* Angew Chem Int Ed Engl, 2006. **45**(27): p. 4440-4.
96. Rodriguez-Pulido, A., et al., *Light-triggered sequence-specific cargo release from DNA block copolymer-lipid vesicles.* Angew Chem Int Ed Engl, 2013. **52**(3): p. 1008-12.
97. Jaaskelainen, I., J. Monkkonen, and A. Urtti, *Oligonucleotide-cationic liposome interactions. A physicochemical study.* Biochim Biophys Acta, 1994. **1195**(1): p. 115-23.
98. Gromelski, S. and G. Brezesinski, *DNA condensation and interaction with zwitterionic phospholipids mediated by divalent cations.* Langmuir, 2006. **22**(14): p. 6293-301.
99. Mengistu, D.H., K. Bohinc, and S. May, *Binding of DNA to zwitterionic lipid layers mediated by divalent cations.* J Phys Chem B, 2009. **113**(36): p. 12277-82.
100. Czogalla, A., et al., *Switchable domain partitioning and diffusion of DNA origami rods on membranes.* Faraday Discuss, 2013. **161**: p. 31-43; discussion 113-50.
101. Howorka, S., *NANOTECHNOLOGY. Changing of the guard.* Science, 2016. **352**(6288): p. 890-1.
102. Langecker, M., et al., *Synthetic lipid membrane channels formed by designed DNA nanostructures.* Science, 2012. **338**(6109): p. 932-6.

103. Burns, J.R., et al., *A biomimetic DNA-based channel for the ligand-controlled transport of charged molecular cargo across a biological membrane.* Nat Nanotechnol, 2016. **11**(2): p. 152-6.
104. Gopfrich, K., et al., *DNA-Tile Structures Induce Ionic Currents through Lipid Membranes.* Nano Lett, 2015. **15**(5): p. 3134-8.
105. Burns, J.R., et al., *Membrane-spanning DNA nanopores with cytotoxic effect.* Angew Chem Int Ed Engl, 2014. **53**(46): p. 12466-70.
106. Li, C.M., et al., *DNA-AuNP networks on cell membranes as a protective barrier to inhibit viral attachment, entry and budding.* Biomaterials, 2016. **77**: p. 216-26.
107. Kocabey, S., et al., *Membrane-assisted growth of DNA origami nanostructure arrays.* ACS Nano, 2015. **9**(4): p. 3530-9.
108. Czogalla, A., et al., *Amphipathic DNA origami nanoparticles to scaffold and deform lipid membrane vesicles.* Angew Chem Int Ed Engl, 2015. **54**(22): p. 6501-5.
109. Xu, W., et al., *A Programmable DNA Origami Platform to Organize SNAREs for Membrane Fusion.* Journal of the American Chemical Society, 2016. **138**(13): p. 4439-4447.
110. Xu, W., et al., *A Programmable DNA Origami Platform to Organize SNAREs for Membrane Fusion.* J Am Chem Soc, 2016. **138**(13): p. 4439-47.
111. Barber, G.N., *Cytoplasmic DNA innate immune pathways.* Immunol Rev, 2011. **243**(1): p. 99-108.
112. Desmet, C.J. and K.J. Ishii, *Nucleic acid sensing at the interface between innate and adaptive immunity in vaccination.* Nat Rev Immunol, 2012. **12**(7): p. 479-91.
113. Vollmer, J. and A.M. Krieg, *Immunotherapeutic applications of CpG oligodeoxynucleotide TLR9 agonists.* Adv Drug Deliv Rev, 2009. **61**(3): p. 195-204.
114. Krieg, A.M., et al., *CpG motifs in bacterial DNA trigger direct B-cell activation.* Nature, 1995. **374**(6522): p. 546-9.
115. Latz, E., et al., *TLR9 signals after translocating from the ER to CpG DNA in the lysosome.* Nat Immunol, 2004. **5**(2): p. 190-8.
116. Klinman, D.M., *Immunotherapeutic uses of CpG oligodeoxynucleotides.* Nat Rev Immunol, 2004. **4**(4): p. 249-58.
117. Nishikawa, M., et al., *Enhanced immunostimulatory activity of oligodeoxynucleotides by Y-shape formation.* Immunology, 2008. **124**(2): p. 247-255.
118. Mohri, K., et al., *Design and development of nanosized DNA assemblies in polypod-like structures as efficient vehicles for immunostimulatory CpG motifs to immune cells.* ACS Nano, 2012. **6**(7): p. 5931-40.
119. Mohri, K., et al., *Self-assembling DNA dendrimer for effective delivery of immunostimulatory CpG DNA to immune cells.* Biomacromolecules, 2015. **16**(4): p. 1095-101.
120. Zhang, L., et al., *Self-Assembled DNA Immunonanoflowers as Multivalent CpG Nanoagents.* ACS Appl Mater Interfaces, 2015. **7**(43): p. 24069-74.
121. Schuller, V.J., et al., *Cellular immunostimulation by CpG-sequence-coated DNA origami structures.* ACS Nano, 2011. **5**(12): p. 9696-702.
122. Liu, X., et al., *A DNA nanostructure platform for directed assembly of synthetic vaccines.* Nano Lett, 2012. **12**(8): p. 4254-9.
123. Ley, K., et al., *Getting to the site of inflammation: the leukocyte adhesion cascade updated.* Nat Rev Immunol, 2007. **7**(9): p. 678-89.
124. Campbell, J.J., et al., *Chemokines and the arrest of lymphocytes rolling under flow conditions.* Science, 1998. **279**(5349): p. 381-4.
125. Constantin, G., et al., *Chemokines trigger immediate beta2 integrin affinity and mobility changes: differential regulation and roles in lymphocyte arrest under flow.* Immunity, 2000. **13**(6): p. 759-69.
126. Barreiro, O., et al., *Dynamic interaction of VCAM-1 and ICAM-1 with moesin and ezrin in a novel endothelial docking structure for adherent leukocytes.* J Cell Biol, 2002. **157**(7): p. 1233-45.

127. Mamdouh, Z., et al., *Targeted recycling of PECAM from endothelial surface-connected compartments during diapedesis.* Nature, 2003. **421**(6924): p. 748-53.
128. Kroot, E.-J.A., et al., *Oral Pulsed Dexamethasone Therapy in Early Rheumatoid Arthritis.* Annals of the New York Academy of Sciences, 2006. **1069**(1): p. 300-306.
129. Keeney, G.E., et al., *Dexamethasone for Acute Asthma Exacerbations in Children: A Meta-analysis.* Pediatrics, 2014.
130. Evans, R.M., *The steroid and thyroid hormone receptor superfamily.* Science, 1988. **240**(4854): p. 889-95.
131. Beato, M., *Gene regulation by steroid hormones.* Cell, 1989. **56**(3): p. 335-44.
132. Gehring, K., J.L. Leroy, and M. Gueron, *A tetrameric DNA structure with protonated cytosine.cytosine base pairs.* Nature, 1993. **363**(6429): p. 561-5.
133. Leroy, J.L., et al., *Acid multimers of oligodeoxycytidine strands: stoichiometry, base-pair characterization, and proton exchange properties.* Biochemistry, 1993. **32**(23): p. 6019-31.
134. Modi, S., et al., *A DNA nanomachine that maps spatial and temporal pH changes inside living cells.* Nat Nanotechnol, 2009. **4**(5): p. 325-30.
135. Mancuso, F., R.J. Flower, and M. Perretti, *Leukocyte transmigration, but not rolling or adhesion, is selectively inhibited by dexamethasone in the hamster post-capillary venule. Involvement of endogenous lipocortin 1.* J Immunol, 1995. **155**(1): p. 377-86.
136. Ito, A., et al., *Dexamethasone reduces lung eosinophilia, and VCAM-1 and ICAM-1 expression induced by Sephadex beads in rats.* Eur J Pharmacol, 2003. **468**(1): p. 59-66.
137. Sellner, S., et al., *DNA nanotubes as intracellular delivery vehicles in vivo.* Biomaterials, 2015. **53**: p. 453-63.

Acknowledgements

I would like to thank my PhD advisor, Prof. Tim Liedl, for giving me the opportunity to work in his group and all the support during the course of my studies. I really enjoyed the time in your group. I also thank you to let me be part of the international DNA Nanotechnology network, EScoDNA (European School of DNA Nanotechnology).

Thank you to Prof. Joachim Rädler, for establishing friendly and lovely chair atmosphere.

Thank you to all my colleagues for the fruitful collaborations: Sabine Sellner and Dr. Markus Rehberg for the perfect collaboration in the immune-modulation projects. Jonathan List and Prof. Friedrich Simmel for AFM imaging in the membrane project. Hanna Meinl and Dr. Felix Lichtenegger for their collaboration in the folate-mediated uptake project.

Thanks to all my colleagues from Liedl group for their support and all scientific discussions: Tao Zhang, Eva-Maria Roller, Dr. Wooli Bae, Dr. Susanne Kempter, Dr. Yongzheng Xing, Alex Maier, Luisa Kneer, Philipp Nickels, Caroline Hartl, Dr. Ian MacPherson, Timon Funck, Francesca Nicoli, Andrea Cooke, Dr. Mauricio Pilo-Pais, Thomas Zettl, Dr. David Smith, Dr. Daniel Schiffels, Dr. Robert Scheriber, Dr. Verena Schüller, Philip Böhm. Thanks to Gerlinde Schwake for the technical support and my office mates: Rafal Krzyszton and Alexandra Murschhauser for their help. And thanks to all the people from the chair of Prof. Joachim Rädler.

Thanks to EScoDNA for the funding and all EScoDNA members for the scientific discussions, collaborations, secondments and good time at conferences.

Thanks to my mother, my father, my brother and my sister. Their supports are invaluable for me!

Finally, thanks to my beautiful wife for everything!

List of Publications

Göpfrich, K., Zettl, T., Meijering, A.E.C., Hernandez, S.A., Kocabey, S., Liedl, T., Keyser, U.
DNA-Tile Structures Induce Ionic Currents through Lipid Membranes.
Nano Letters, 15(5), 3134-3138, (2015)

Kocabey, S., Kempter, S., List, J., Xing, Y., Bae, W., Schiffels, D., Shih, W.M., Simmel, F.C., Liedl, T.
Membrane-Assisted Growth of DNA Origami Nanostructure Arrays.
ACS Nano, 9(4), 3530-3539, (2015)

Sellner, S.*, Kocabey, S.*, Nekolla, A.K., Krombach, F., Liedl,T., Rehberg, M.
DNA Nanotubes as Intracellular Delivery Vehicles in vivo.
Biomaterials, 53, 453-463, (2015)
***** These authors contributed equally to this work

Kocabey, S., Meinl, H., MacPherson, I. S., Cassinelli, V., Manetto, A., Rothenfusser, S., Liedl, T., Lichtenegger, F.S.
Cellular Uptake of Tile-Assembled DNA Nanotubes.
Nanomaterials, 5(1), 47-60, (2015)

Sellner, S.*, Kocabey, S.*, Zhang, T., Nekolla, A.K., Hutten, S., Krombach, F., Liedl,T., Rehberg, M.
Dexamethasone-conjugated DNA Nanotubes as anti-inflammatory agents in vivo.
Submitted to Biomaterials.
***** These authors contributed equally to this work